

Nanocatalytic materials against multidrug-resistant bacterial infection

Inaugural-Dissertation

to obtain the academic degree

Doctor rerum naturalium (Dr. rer. nat.)

submitted to the Department of Biology, Chemistry,

Pharmacy

of Freie Universität Berlin

by

Xin Fan

from Fujian, China

2023

The work presented in this thesis was conducted in the research group of Prof. Dr. Rainer Haag from **September 2019** until **April 2023** at the Department of Biology, Chemistry, Pharmacy of the Freie Universität Berlin.

1st Reviewer: Prof. Dr. Rainer Haag, Freie Universität Berlin

2nd Reviewer: Prof. Dr. Andrej Trampuz, Charité – Universitätsmedizin Berlin

Day of defense: 11.Oct.2023

Acknowledgement

First of all, I would like to thank my supervisor Prof. Dr. Rainer Haag, who offered me the internship and PhD position in his group and always supports my research projects.

I am so grateful to learn so many experiments, instruments and research skills in AG Haag. I appreciate the all-inclusive research facilities and supportive colleagues in AG Haag, so that I never think about “what can we do?” but “how can we do it better?”.

I would like to thank my second supervisor, Prof. Dr. Andrej Trampuz for hosting me in his group for antibacterial experiments and all the supports to my research projects. Over the last 4 years working in his lab, he treated me as a part of AG Trampuz. I learned a lot about antibiotics and bacteriophage in his lab.

I would like to thank Dr. Chuanxiong Nie for all the scientific and mental supports. He is like my older brother, who always ready to help me solve the problems. It seems like he is omnipotent, I can always have right answers after discussing with him.

I would like to thank Dr. Yang Gao, Xizheng Wu and Prof. Dr. Chong Cheng for supporting my animal experiments and material characterizations from China.

I would like to thank Dr. Lei Wang, who selflessly taught me the experiments and knowledge regarding bacteriophage.

I would like to thank my bro Alphonse Fiebor and his sweet family for all the company and joy they brought over the last four years.

I would like to thank Dr. Wiebke Fisher, Cathleen Hudziak, Marleen Selent and Alexandros Mavroskoufis to be my German teachers and help me improve my speaking from time to time.

I would like to thank Benjamin Allen for the language polishing.

I would like to thank all members in AG Haag and AG Trampuz.

I am grateful for the financial support afforded by China Scholarship Council (CSC) during my PhD thesis.

I would like to thank the core facility BioSupraMol for offering diverse characterization instruments.

Finally, I would like to thank my family for all the supports and encouragement during last four years. Especially, many thanks to my wife Fan Yang, for your scientific supports, amazing delicious comfort food and unconditional love!

Table of Contents

1. Introduction	1
1.1. Bacterial and biofilm infection	1
1.1.1. Multidrug-resistant (MDR) bacteria and their biofilm	1
1.1.2. Limitations of current clinical antimicrobial treatments	3
1.1.3. Nanomaterials as a new strategy against MDR bacterial infection	4
1.2. Antibacterial nanocatalytic materials (NCMs)	6
1.2.1. Intrinsically reactive-oxygen-species-producing NCMs	6
1.2.2. Chemical-responsive NCMs	8
1.2.3. Energy-responsive NCMs	10
1.2.4. Quorum-sensing-blocking NCMs	13
1.2.5. Extracellular-DNA-cleaving NCMs	14
1.2.6. Biofilm-microenvironment (BME)-responsive NCMs	16
1.2.7. Challenges	18
1.3. Further functionalization of antibacterial NCMs	19
1.3.1. Structure and reaction path innovation	19
1.3.2. Enhancing bacterial binding	22
2. Scientific goals	26
3. Publications	28
3.1. A Nanohook-equipped bionanocatalyst for localized near-infrared-enhanced catalytic bacterial disinfection	28
3.2. Photocatalytic quantum dot-armed bacteriophage for combating drug-resistant bacterial infection	74
3.3. A copper single-atom cascade bionanocatalyst for treating multidrug-resistant bacterial diabetic ulcer	102
4. Summary and outlook	136
5. Zusammenfassung und Ausblick	138
6. References	141
7. Appendix	146
7.1. Publications	146
7.2. Curriculum Vitae	147

1. Introduction

1.1. Bacterial and biofilm infection

1.1.1. Multidrug-resistant (MDR) bacteria and their biofilm

Bacteria are single-celled microorganisms that can be found almost everywhere in the earth. The pathogenic ones are able to cause infections by various ways like invading cells or bloodstream, producing toxins, and disrupting normal microbial flora.^[1-2] These infections can range from mild to severe, with symptoms ranging from fever to severe pain, organ damage, and even life-threatening organ failure and tissue necrosis.^[1] The discovery of penicillin in 1928 has opened a new era for combating bacterial infection.^[3] Since then, numerous antibiotics were successfully developed. It was considered the bacterial-related disease can be thoroughly eliminated with the assistance of antibiotics. However, over decades of abusing and misusing antibiotics, some mutative strains with certain antibiotic-resistant gene, which are also known as drug-resistant bacteria, have emerged and become a new threat to public health since they are no longer sensitive to the certain antibiotic under clinical dosage (Figure 1). Thus, other kinds of antibiotics were applied to control these drug-resistant bacterial infections, which provides the selective environment and evolution pressure for the bacteria to obtain multidrug-resistance. Up to now, the infection caused by multidrug-resistant (MDR) bacteria has led to millions of deaths and it is predicted that over 10 million of people will die of it annually by 2050.^[4]

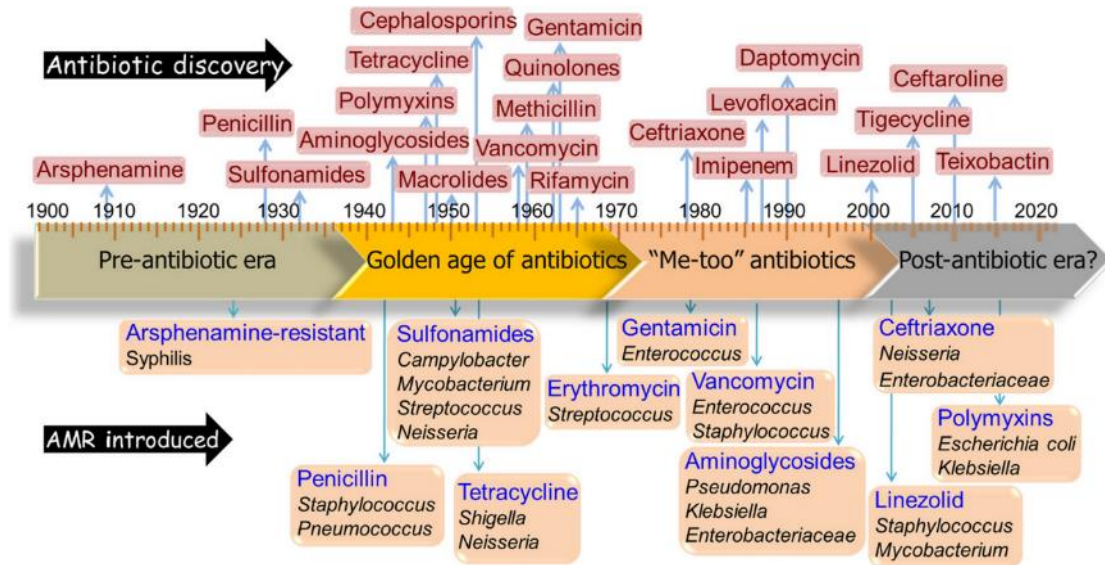


Figure 1. Timeline of the discovery and resistance for the most common-use antibiotics. Reprinted with permission from Ref.^[5] Copyright 2022, Springer.

Apart from genetically, the bacterial drug-resistance can be physically obtained or further strengthened. Typically, during colonization, the aggregated bacteria are able to adhere in inert or living surfaces and secrete extracellular polymeric substance (EPS), which encapsulates them to form a complex community, i.e., the biofilm (Figure 2). The dense EPS can serve as a safety shield, which not only prevent the attack from host immune cells, but also significantly minimize the penetration of antibiotics, resulting in a drug resistance increase by several orders of magnitude. Moreover, the planktonic bacteria can be continuously released from the biofilm, leading to chronic and recurrent infections.^[6] Nowadays, over 60% of infectious disease can be attributed to biofilm-related infections,^[7-8] and the approaches against biofilms are still very limited in clinic.

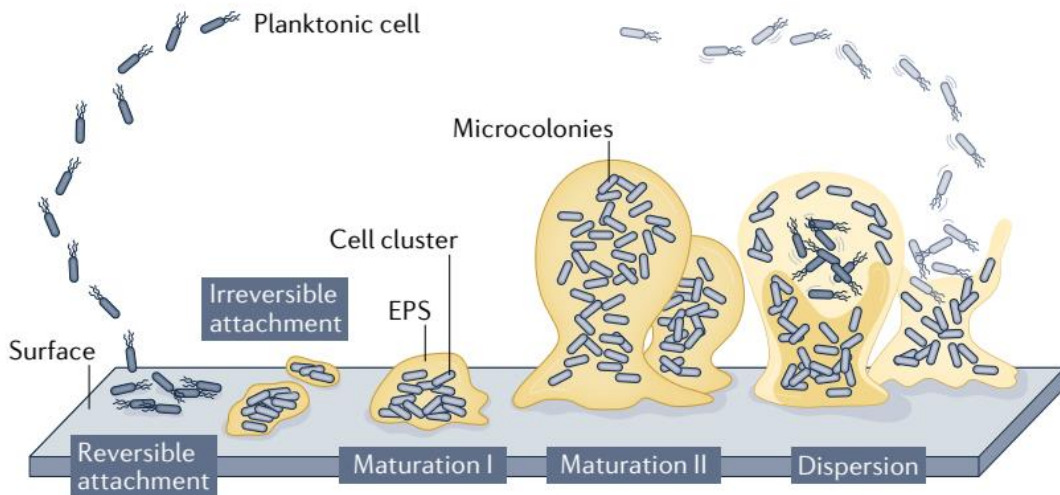


Figure 2. The lifecycle of biofilm. Reprinted with permission from Ref.^[6] Copyright 2022, Springer Nature.

1.1.2. Limitations of current clinical antimicrobial treatments

Clinically, the current antibacterial treatments still highly rely on antibiotics.^[9] Apart from the potential risk for inducing strong and multiple drug-resistance we have mentioned above, the antibiotics-based therapies also face other limitations: (a) limited spectrum of activity: for example, common-used antibiotics like vancomycin only shows activity against gram-positive bacteria. When MDR bacterial infections happen, it becomes even more tricky to select the antibiotics. Thus, it usually requires an extra bacterial identification before antibiotics administration, which causes a delayed treatment; (b) lack of highly targeted property: even if the pathogenic bacteria have been identified, it is difficult to achieve the certain-strain targeted killing via antibiotics. As a consequence, the microbial flora might be disrupted and the overgrowth of other pathogenic bacteria can lead to the secondary infection;^[10] (c) poor efficiency against mature biofilm and long-term toxicity: the antibiotics are usually only effective for new-formation biofilm. Once the mature biofilm has formed, both the minimum inhibitory concentration and the minimum bactericidal concentration (MBC) of sessile bacteria within biofilm increased dramatically by 1-3 order of magnitude comparing with planktonic ones.^[11] To treat the biofilm-related chronic infections, a long-term

high-dosage antibiotics are required, causing high toxicity for liver and kidney;^[12](d) low cost performance for development: currently, the creation of new antibiotics remains an unappealing investment option for major pharmaceutical companies, which can be attributed to the fact that antibiotics have highly uncertain lifecycles and they might become obsolete at any moment with the increasing crisis of drug-resistance.^[13]

1.1.3. Nanomaterials as a new strategy against MDR bacterial infection

To avoid the limitations of antibiotics-based therapies and the dilemma of no effective antibacterial medicine in the near future, it is of vital importance to develop new strategies against MDR bacterial and biofilm infections. Up to now, many antibiotic-free approaches have been reported such as bacteriophage therapy,^[14] photothermal/photodynamic/sonodynamic therapies,^[15-17] immunotherapy,^[18-19] antibacterial peptides,^[20] and multimodal synergistic therapy.^[21-22] Although promising progress has been achieved, some drawbacks of those approaches are remain to be solved. For instance, the hyperthermia and reactive oxygen species (ROS) respectively generated from photothermal and photodynamic therapies show non-specific toxicity towards both bacteria and cells, which compromise the therapeutic effect.^[23] Also, the bacteria are able to rapidly gain resistance against bacteriophage within several hours of coculture.^[24] It is anticipated that the bactericidal efficacy of phage-therapy can be further strengthened. Therefore, it is of high importance to develop a novel platform, which can not only diversely infuse multi-model therapeutic mechanism, but also overcome the remaining problems.

Thanks to the rapid progress of nanotechnology, scientists have developed various essential concepts for fabricating bacterial/biofilm-killing nanoplatforms, which can be categorized as: (1) antimicrobial polymers;^[25-26] (2) nanostructures that possess intrinsic bactericidal properties by causing toxicity to bacterial components like metal ions or nanoparticles;^[27-32] (3) nanocomposites that are able to produce hyperthermia upon near-infrared light (NIR);^[33-34] (4) nanostructures showing reactive oxygen

species (ROS) generation with auxiliaries or extra energy input;^[35-36] and (5) synergistic treatments that combine several above-mentioned antibacterial mechanisms to achieve satisfactory therapeutic efficacies.^[37] Although many of them have shown satisfactory disinfection results, they still encounter challenges such as only affecting specific bacterial components, non-specific toxicity, and poor stability. For instance, Ag nanocomposites have been extensively studied and shown to have a broad spectrum of bacteria or biofilm inactivation. However, their high and non-specific toxicity poses high risks towards healthy cells, thereby severely restricting their application in *in-vivo* therapies.^[38] Additionally, the ion-release bactericidal mechanism is challenging to maintain stable bactericidal activity in long-term. As such, there is an urgent need to develop more effective and safer approaches to overcome the challenges associated with traditional nanomaterial-based antibacterial strategies.

Taking lesson from the human immune system, ROS generated from enzymatic catalysis can effectively inactivate pathogens or regulate cell apoptosis. For example, the peroxidase found in both lysosomes and neutrophils shows the ability to catalyze the conversion of hydrogen peroxide (H₂O₂) to hydroxyl radicals (•OH), which led to severe oxidative damage to pathogens.^[39] However, direct application of natural enzymes as antimicrobials is not a feasible option due to their inherent drawbacks such as high manufacturing expenses, complex purification processes, and limited stability in varying pH levels, solvents, and temperature conditions. Therefore, to create an economical catalytic nanoplatform for antibacterial purposes, researchers have recently focused on developing nanocatalytic materials (NCMs) based on metals, carbon, or polymers.^[40-43] These NCMs have demonstrated multiple benefits, including adjustable composition and catalytic activity, low toxicity when used in relevant doses, exceptional stability, and distinctive energy-conversion capabilities, making them an ideal option for bacterial disinfection treatments. With these exceptional physicochemical properties, NCMs have emerged as a critical and highly attractive area with unparalleled potential for future bacterial disinfection therapies.

1.2. Antibacterial nanocatalytic materials (NCMs)

Based on the bactericidal or biofilm-killing mechanisms, the NCMs can be cataloged as following and also overviewed in Figure 3:

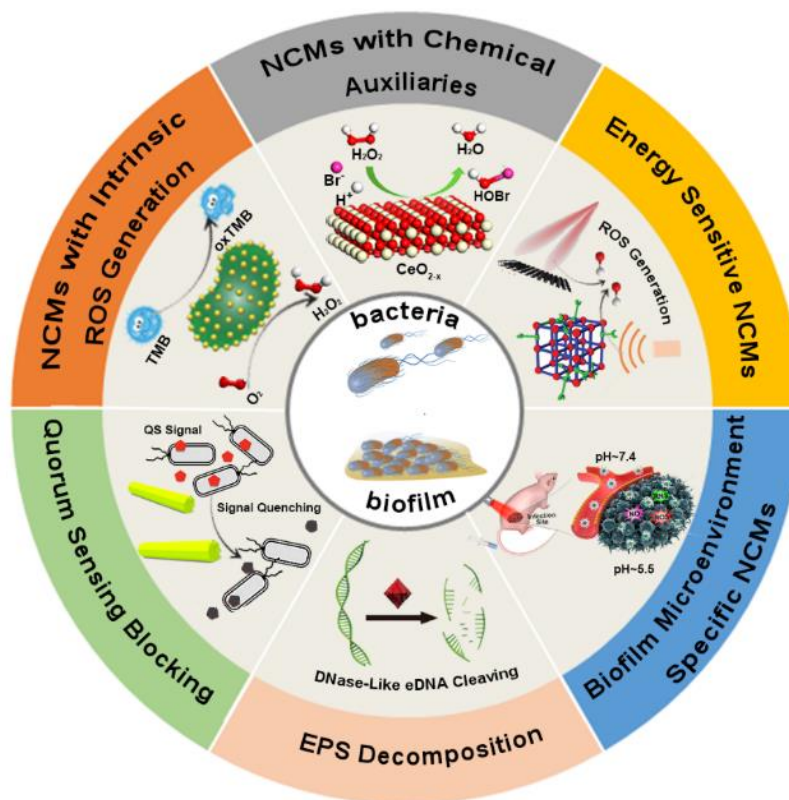


Figure 3. Types and bactericidal mechanisms of NCMs. Reprinted with permission from Ref.^[44] Copyright 2021, WILEY-VCH Verlag GmbH & Co. KGaA, Weinheim, Germany.

1.2.1. Intrinsically reactive-oxygen-species-producing NCMs

Redox NCMs exhibit an innate capacity to generate ROS. For instance, nanocatalysts that mimic oxidases can facilitate the production of $\bullet\text{O}_2^-$ in the presence of oxygen, leading to the non-selective damage of bacteria by disrupting their membrane structures, enzymes, or DNA. This approach makes it challenging for bacteria to develop resistance as it can result in toxicity in both genetic and structural levels. Tao et.al. developed silica-supported gold nanoparticles (Figure 4A, B), which were able to inherently convert oxygen to different kinds of ROS.^[45] With this powerful property,

silica-supported gold nanoparticles could effectively kill both *E. coli* and *S. aureus* (Figure 4C). Very recently, with both oxidase (OXD)- and POD-mimetic properties were synthesized, exhibiting the extraordinary bactericidal efficacy via a OXD-to-POD cascade catalysis, where oxygen could be *in situ* convert to $\bullet\text{OH}$ (Figure 4D).^[46] As a result, 2 $\mu\text{g/mL}$ of CWS could reduce both *E. coli* and *S. aureus* by 5 orders of magnitude, which is comparable to traditional antibiotics.

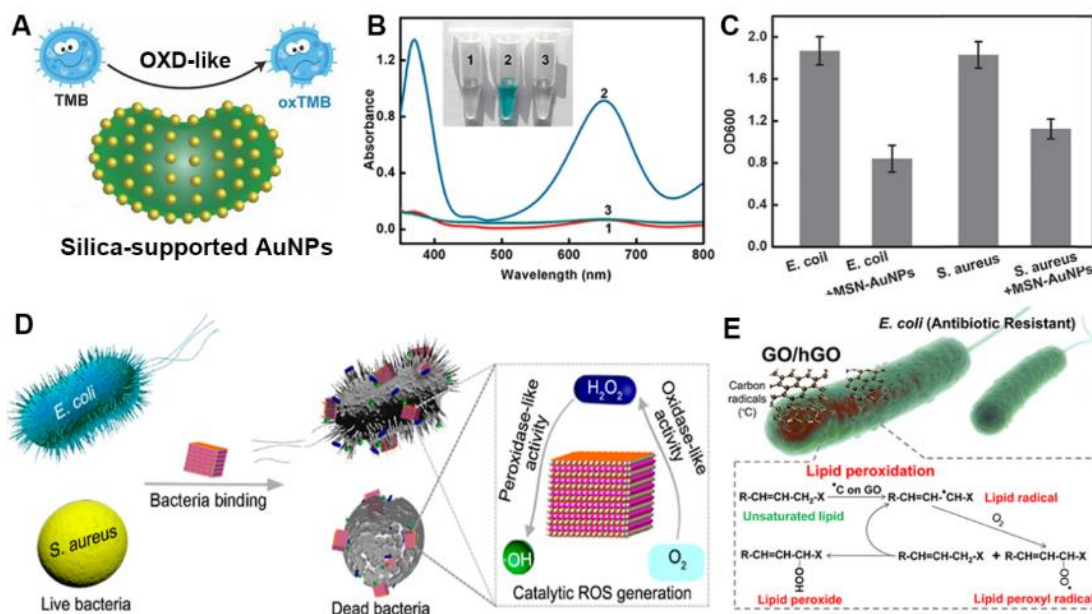


Figure 4. (A) Scheme that shows the silica-supported gold nanoparticles (AuNPs) with intrinsic OXD-like catalytic performance. (B) UV-vis spectra for characterizing OXD-like catalysis induced by silica-supported AuNPs in the presence of substrate 3,3',5,5'-tetramethylbenzidine (TMB). No.1-3 in inset and curves referred to TMB only, TMB + silica-supported AuNPs and TMB + silica, respectively. (C) The bacterial reduction after treatment by silica-supported AuNPs that quantified by measuring the optical density at 600 nm. (D) Schematic illustration of CWS' bacterial killing ability by initiating a cascade OXD-POD-like catalysis. (E) Scheme of bacterial lipid peroxidation induced by hydrated graphene oxides. Reprinted and adapted with permission from Ref.^[44] Copyright 2021, WILEY-VCH Verlag GmbH & Co. KGaA, Weinheim, Germany.

Moreover, hydrated graphene oxides (hGOs) were reported to show strong antibacterial effect against drug-resistant *E. coli* via inducing a lipid peroxidation. Specifically, the carbon radicals within hGOs can react with bacterial lipid to form lipid radicals, leading to the lipid peroxidation and membrane damage (Figure 4E).^[47]

1.2.2. Chemical-responsive NCMs

Some NCMs can produce ROS by incorporating chemical auxiliaries. For instance, while H₂O₂ is a commonly used disinfectant, a high treatment concentration (up to 3%) is normally required in wound treatment to achieve satisfactory antibacterial effects, which can also harm healthy neighboring tissues.^[48] To address this problem, peroxidase (POD)-mimic NCMs were developed, which can convert H₂O₂ to high-efficient bactericidal •OH, thus reducing the administration dosage of H₂O₂. Liu et.al. synthesized a zeolite-imidazole-framework (ZIF)-8-derived NCM that containing zinc single-atom sites, which can mimic both the structure and property of natural POD (Figure 5A and B).^[49] Confirming by electron spin resonance (ESR), the ZIF-8-derived NCM could catalyze the generation of •OH in the presence of H₂O₂ (Figure 5C). As illustrated by DFT calculations, the zinc single-atom can first bind a H₂O₂ molecule, which is then followed by a homolytic dissociation resulting in the formation of two OH* intermediates. Then, one of the intermediates was released as •OH, serving as the main bactericidal product (Figure 5D). As a result, the ZIF-8-derived NCM achieved robust *in-vitro* *P. aeruginosa* killing efficacy with a bacterial reduction of 99.9%. Also, in an *in-vivo* wound infection model, the ZIF-8-based NCM was proved to promote the wound healing with limited toxicity towards tissue and organs.

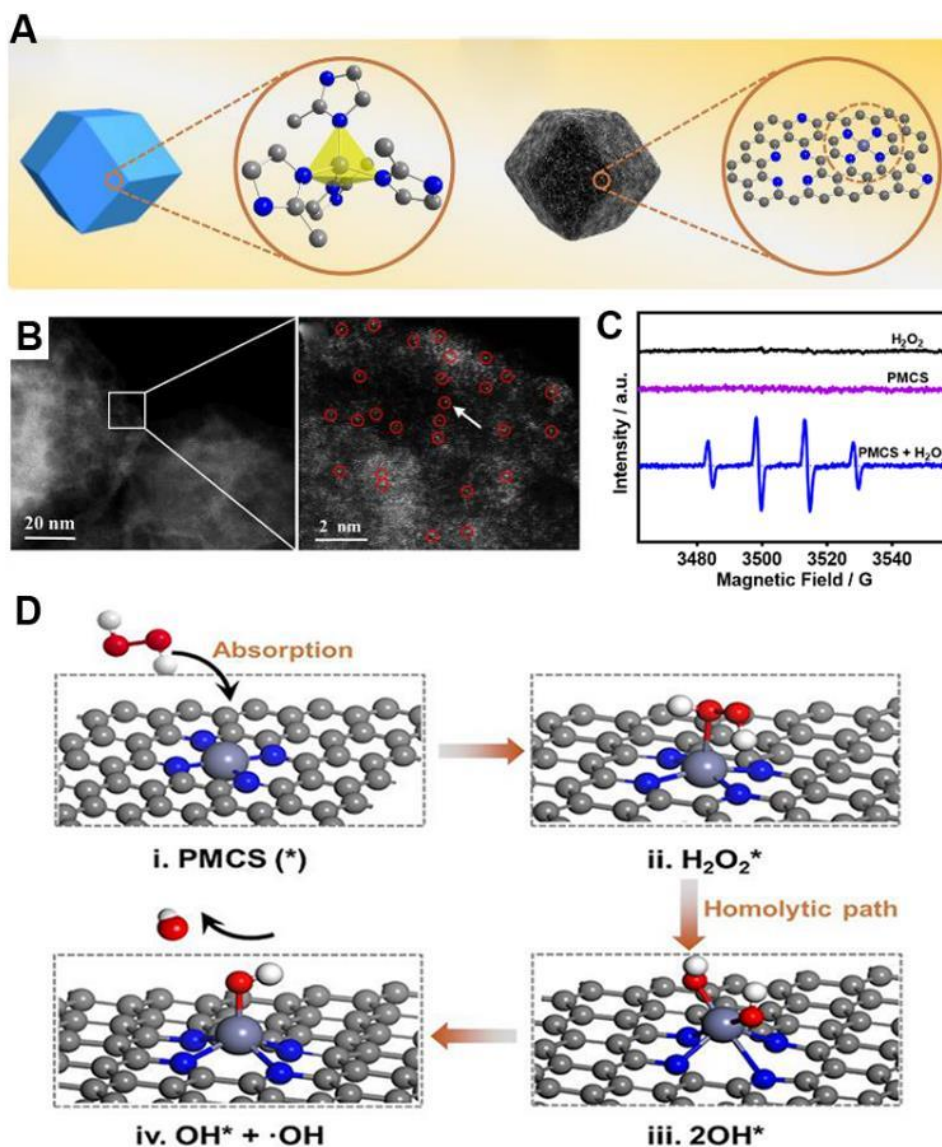


Figure 5. (A) Scheme showing the synthesis of a ZIF-8-derived zinc single-atom catalysts (PMCS). (B) High resolution TEM images that showed the zinc single-atom sites anchored on the carbon matrix. (C) ESR spectra for characterizing the generation of $\bullet\text{OH}$ in the presence of PMCS and H_2O_2 . Reprinted and adapted with permission from Ref.^[49] Copyright 2019, WILEY-VCH Verlag GmbH & Co. KGaA, Weinheim, Germany.

Additionally, NCMs with haloperoxidase (HPO)-mimetic properties have the ability to simultaneously produce various types of ROS like hypohalous acid and $^1\text{O}_2$ when the H_2O_2 and halogen ions are present, thus leading to effective eradication of bacteria and

biofilms.^[50] As shown in Figure 6A, the HPO-mimetic vanadium pentoxides (V_2O_5) have ability to catalyze the bromide ions and H_2O_2 to form bactericidal hypobromous acid and singlet oxygen via the bromination process. As a result, V_2O_5 NCM showed strong antibacterial performance with a reduction ratio of 96% against *S. aureus* and 78% against *E. coli* (Figure 6B). Different from the Fenton mechanism which only takes place in acidic condition, the HPO-mimetic catalysis can happen in mild basic condition, which make it possible to be applied as antibacterial ship coating or seawater disinfection.^[51] Similarly, it was demonstrated that the cerium oxides NCMs with HPO-mimetic properties could significantly reduce bacterial viability after only 5s of coculture.^[52]

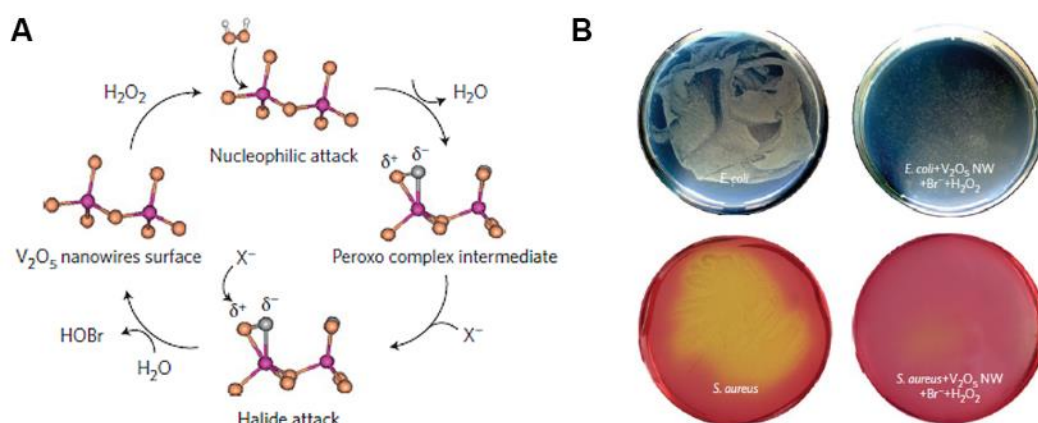


Figure 6. (A) Mechanism of V_2O_5 nanowires catalyzing the production of $HOBr$ in the presence of H_2O_2 and halide ions. (B) The *E. coli* and *S. aureus* colonies before-and-after treatment of $V_2O_5 + Br^- + H_2O_2$. Reprinted with the permission of Ref.^[51] Copyright 2012, Springer Nature.

1.2.3. Energy-responsive NCMs

For the energy-responsive NCMs, the ROS production ability can be activated or further enhanced by the extra energy input. The exogenous energy-activated NCMs usually possess higher efficiency and provides better controllability in eradicating bacteria as compared to chemo-responsive NCMs. Additionally, by cooperating energy-responsive NCMs with other inherent bactericidal chemicals like metals and positively charged polymers, a multi-modal bactericidal platform can be easily obtained.

For instance, Mao et al. developed a chitosan-BP composite by doping BP nanosheets into chitosan hydrogels, which achieved efficient visible light-activated bacterial photodynamic therapy (PDT) against bacterial infection, promoting the wound healing.^[53]

Owing to the deep penetration, low tissue damage, and ability for initiating PDT and photothermal therapy (PTT), the near-infrared (NIR) laser is recently becoming attractive.^[54-57] The synergetic effect of NIR-induced PDT and PTT can lead to physical and chemical bacterial damage in the same time, which not only improve the bactericidal efficacy, but also minimize the possibility of inducing bacterial resistance. Recently, the red phosphorus-based-NCMs and a NIR-photosensitizer IR780 were used as surface coating above titanium, which achieved bacterial disinfection through the PDT-enhanced PTT effect (Figure 7A).^[58] Under NIR laser irradiation, the surface could reach above 50 °C within 250 seconds and produce singlet oxygen in the same time. With this PDT-PTT synergistic effect, the surface reached a significant bacterial reduction with a ratio of 89.3%, whereas much weaker bactericidal efficacies were noticed induced by single PDT or single PTT modality. Importantly, when being used as an *in-vivo* bone implant, the PDT-PTT synergistic effect of coated titanium could also be activated by NIR, leading to a thorough biofilm eradication (Figure 7B, C).

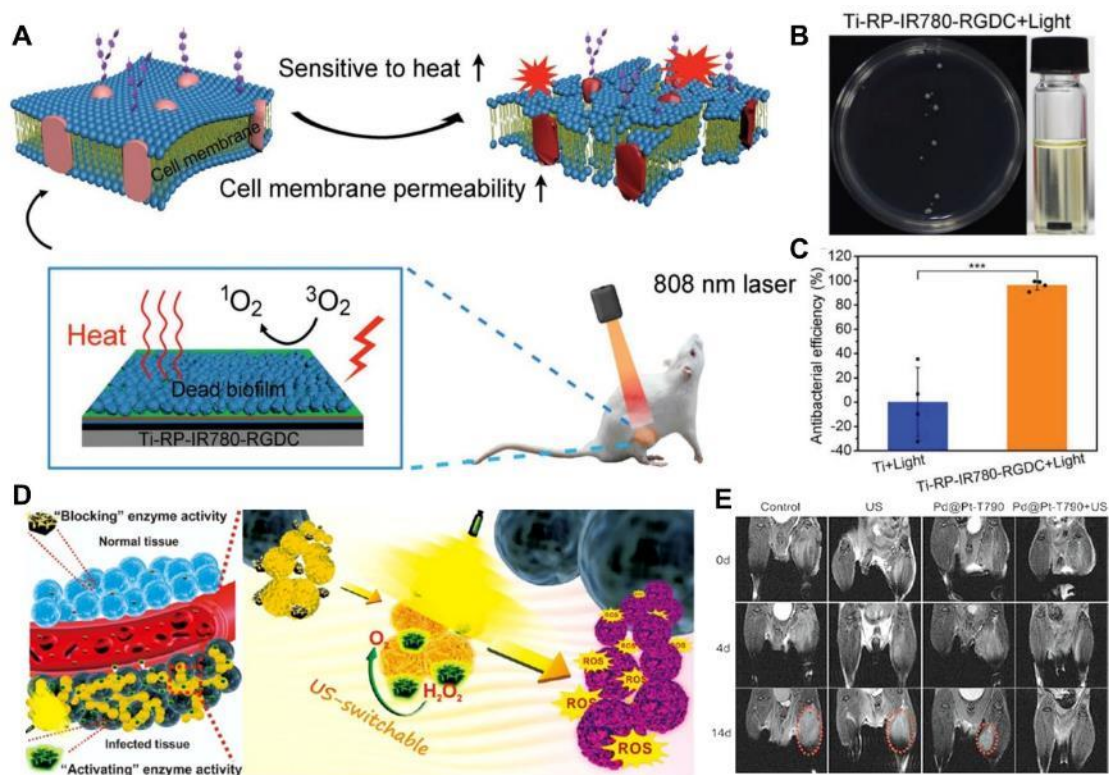


Figure 7. (A) Scheme that shows the surfaces modified by red phosphorus and photosensitizer can generate heat and ROS to kill the formed biofilm upon NIR laser irradiation. (B) The agar plates showing the low bacterial colonies in biofilm-contaminated *in-vivo* implant. (C) The relative antibacterial efficiency of modified surface and pristine surface under NIR laser. (D) Scheme showing the ultrasound-responsive NCM, Pd@Pt-T790 was able to increase the oxygen and ROS level for combating deep bacterial infections with the assistance of ultrasound. (E) Magnetic resonance images monitoring the bacterial myositis recovering under different treatments. (A-C) Reprinted with permission from Ref.^[58] Copyright 2018, WILEY-VCH Verlag GmbH & Co. KGaA, Weinheim, Germany. (D, E) Reprinted with permission from Ref.^[59] Copyright 2020, American Chemical Society.

With the development of sonocatalytic therapy (SCT), ultrasound (US) has recently become a new energy source for eliminating the deep bacterial infections.^[60-63] Pang et.al. created a SCT nanosystem for targeting multidrug-resistant bacteria by combining the sonosensitizer purpurin 18 (P18) and maltohexaose-modified cholesterol in DSPG-

based nanoliposomes.^[64] The maltohexaose guides the nanoliposomes to bacterial sites, where they are broken down by bacterial phospholipase to release P18. Upon stimulation by US, P18 could then generate ROS to kill the bacteria. Similarly, Zheng et al. developed a sono-sensitive NCM called Pd@Pt-T790 for treating MRSA-induced myositis.^[59] A sonosensitizer, mesotetra(4-carboxyphenyl)porphine (T790) was added to inhibit the catalase-mimetic property of Pd@Pt, while the catalytic behavior could be restored under US and ROS generation was accelerated (Figure 7D). As thus, by this highly controllable and disease-loci-specific NCM, the MRSA-induced myositis was eradicated (Figure 7E).

1.2.4. Quorum-sensing-blocking NCMs

The biofilm formation highly relies on bacterial quorum sensing (QS) process, in which the bacteria sense each other by secreting QS signal molecules and coordinate gene expressions. Typically, the cerium-based and vanadium-based NCMs were effectively for inactivation QS signal molecules and interfering the bacterial QS system, respectively, thus preventing the biofilm formation. A model QS signal molecule, N-acyl homoserine lactones (AHLs) can be quenched by hypohalous acid which generated by HPO-mimetic cerium oxides (Figure 8A, B).^[65] By applying the cerium oxides as coating, the biofilm formation on the surfaces was significantly suppressed (Figure 8C). Similarly, HPO-mimetic V₂O₅-based NCM was able to generate HOBr and singlet oxygen, thus inactivating the bacterial QS system and inhibiting bacterial adhesion (Figure 8D).^[51] The samples with V₂O₅-based NCM coating prevented the biofilm contamination after being immersed in seawater for 60 days (Figure 8E).

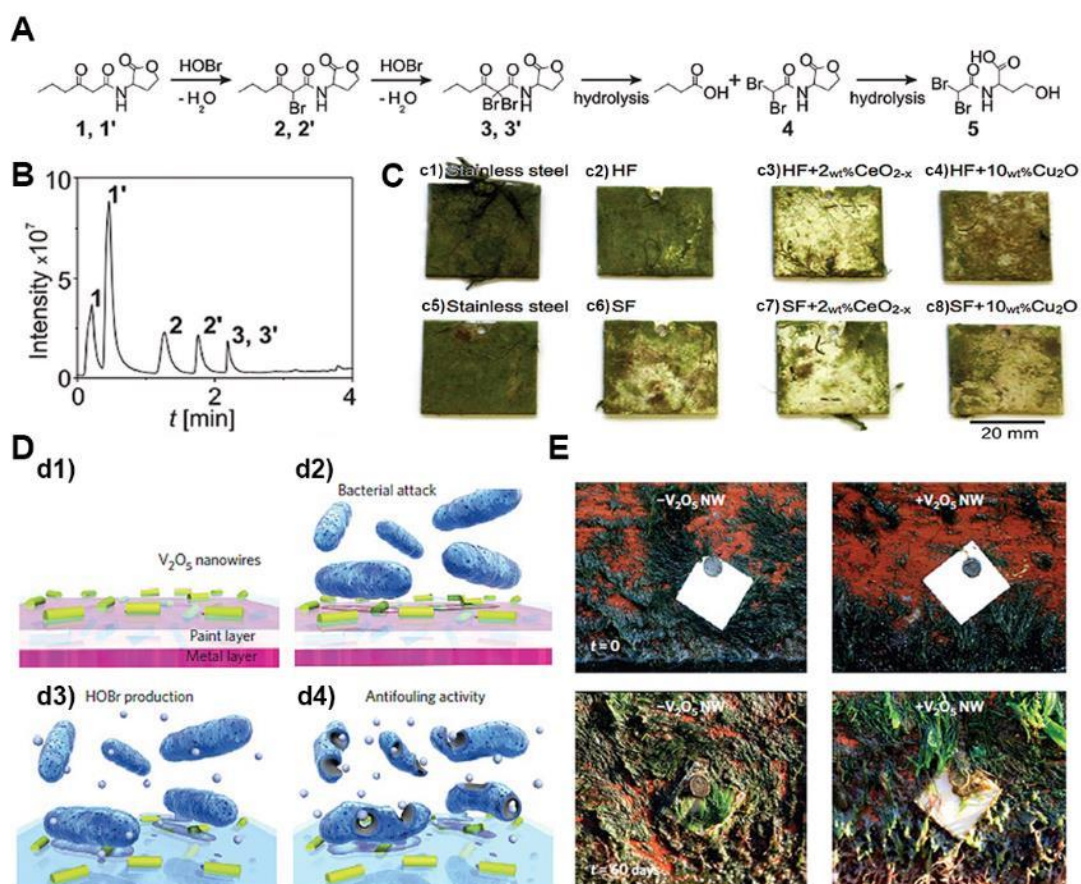


Figure 8. (A) AHL's bromination and hydrolysis reactions catalyzed by CeO_{2-x} . (B) Ion chromatography for detecting the products during catalysis. (C) Photos of surfaces with different coatings after being soaked in seawater for 52 days. c1 and c5 are pristine stainless steel; c2, c4 and c6 are commercial hard coating (HF), HF with CeO_{2-x} , and HF with Cu_2O , respectively; c6, c7 and c8 are commercial soft coating (SF), SF with CeO_{2-x} , and SF with Cu_2O , respectively. (D) Scheme showing the antibacterial effect of V_2O_5 nanowires via catalyzing HOB_r production. (E) Photos of surfaces with and without V_2O_5 coatings after being soaked in seawater for 60 days. Reprinted and reedited with permission from Ref.^[44] Copyright 2021, WILEY-VCH Verlag GmbH & Co. KGaA, Weinheim, Germany.

1.2.5. Extracellular-DNA-cleaving NCMs

In a mature biofilm, the extracellular DNA (eDNA) plays a crucial role in keeping the biofilm structural integrity. For one thing, the eDNA can promote the bacterial adhesion

so that strengthen the biofilm structure. For another, the negatively charged eDNA shows the ability to chelates and inactivates the positively charged antimicrobials.^[66-67] Therefore, deoxyribonuclease (DNase)-mimic NCMs have been developed, by which eDNA can be cleaved and the biofilm can then be eradicated.^[68] Recently, Ce(IV)-based NCMs that possess outstanding biocompatibility and exhibit high catalytic activities have recently been discovered to mimic DNase in the hydrolysis of DNA or RNA. Xu and colleagues conducted a comprehensive investigation into the DNase-mimic properties of CeO₂ and put forward a mechanism.^[69] According to their findings, the Ce centers in the nanoparticles initially chelated the non-bridging oxygen atoms within phosphate group, and subsequently, a hydroxide ion on CeO₂ attacked phosphorus atom, leading to the cleavage of DNA (Figure 9A). Moreover, by attaching cerium complexes onto AuNPs that are integrated onto Fe₃O₄/SiO₂ nanoparticles, NCMs possessing DNase activity have been synthesized. Results from anti-biofilm experiments confirmed the noteworthy bacterial colonization inhibition of this NCM, reaching up to 90% inhibition ratio. Significantly, the NCM also demonstrated strong DNase-mimetic activity, effectively disintegrating even 120-hour-aged mature biofilms.^[70] Based on this work, Qu et.al. have recently combined two types of enzyme mimics to create a NCM that can eradicate mature biofilms comprehensively and prevent biofilm recurrence effectively.^[71] Firstly, an Au-doping iron-based metal organic framework (MOF) was synthesized, followed by the assembly of cerium-based ligand on the MOF, providing the NCM with DNase-mimetic properties. The resulting NCM, MOF-Au-Ce, could eradicate biofilms via both ROS production and DNA cleavage mechanisms (Figure 9B and C). The DNA cleavage process of the cerium center in this work was similar to their previous research (Figure 9D and E). By using agarose gel electrophoresis, it was demonstrated that MOF-Au-Ce could degrade small single-strand DNA and genomic DNA of *S. aureus* at a low concentration (Figure 9F and G). The antibacterial treatment confirmed that MOF-Au-Ce was capable of eliminating most of the biofilms in the presence of H₂O₂ (Figure 9H).

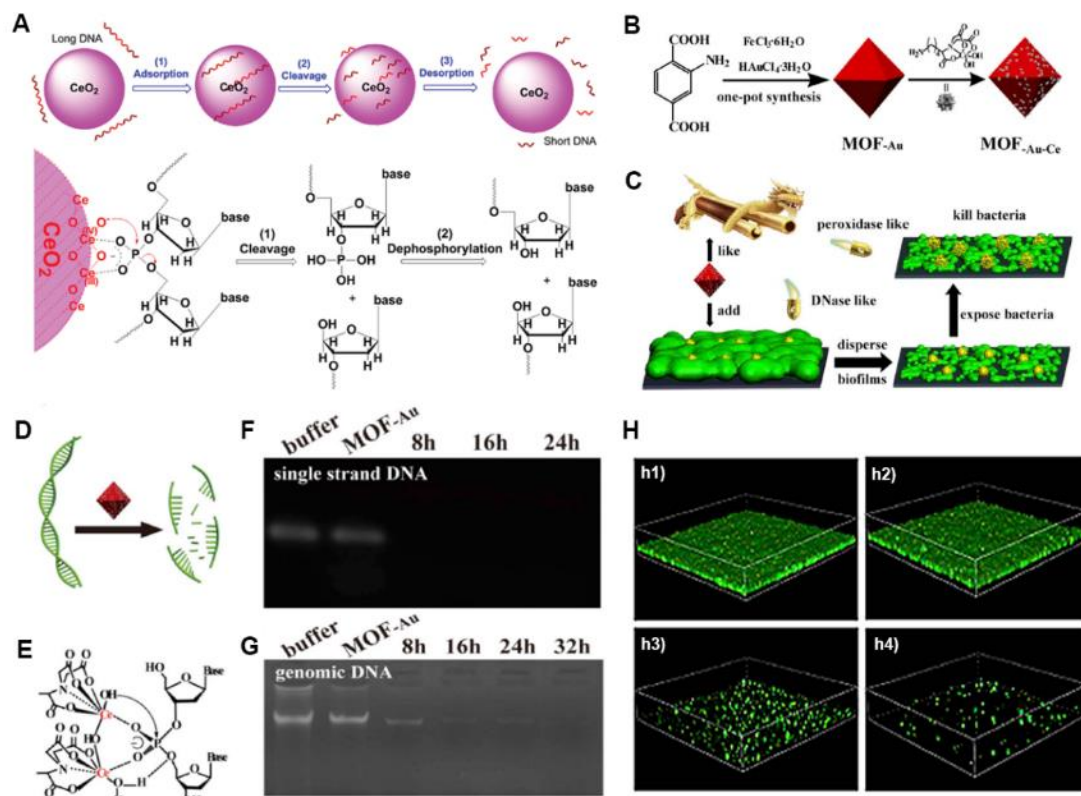


Figure 9. (A) The scheme and mechanism of CeO₂'s DNase-mimetic property. (B) The synthesis of DNase-mimetic MOF-Au-Ce NCM. (C) Scheme showing the MOF-Au-Ce NCM can kill bacteria and biofilm via POD-like and DNase-like properties. (D) Scheme and (E) mechanism of DNA cleavage induced by MOF-Au-Ce. Agarose gel electrophoresis of (F) single strand DNA and (G) genomic DNA which were incubated with MOF-Au-Ce for different times. Reprinted with permission from Ref.^[44] Copyright 2021, WILEY-VCH Verlag GmbH & Co. KGaA, Weinheim, Germany.

1.2.6. Biofilm-microenvironment (BME)-responsive NCMs

The biofilm microenvironment (BME) usually tends to have low pH and high reducibility.^[42-43, 72] Taking advantage of these characteristics, some pH- or reductant-responsive NCMs were synthesized, which only produced bactericidal agents under BME, allowing a highly localized and efficient biofilm eradication. Iron oxide displayed excellent POD-mimetic property in mildly acidic conditions similar to those found in BME.^[73] Taking advantage of this pH-sensitive catalytic performance, Koo et

al. utilized dextran-coated ferrous NCM for eradicating oral biofilms. Kinetic analysis confirmed that the catalytic activity of the NCMs was significantly higher at a pH of 4.5 than that at a pH of 6.5, which makes this NCM highly toxic in BME but safe for a healthy oral cavity.^[74] In another study, V. Rotello et.al. developed a pH-responsive NCM for biorthogonal biofilm-labelling (Figure 10A).^[75] By the virtue of charge-switchable zwitterion ligands, the NCM carried positive charges under BME while was electroneutrality in physiological pH (~7.2). Then, the loaded Ru-based catalysts could catalyze a non-fluorescent substrate (alloc-rho) to generate a fluorescent product, labeling the biofilm area. Meanwhile, due to the low penetration ability of electroneutral NCM under physiological pH, the NCM did not retain in healthy tissue and mislabel the healthy cells.

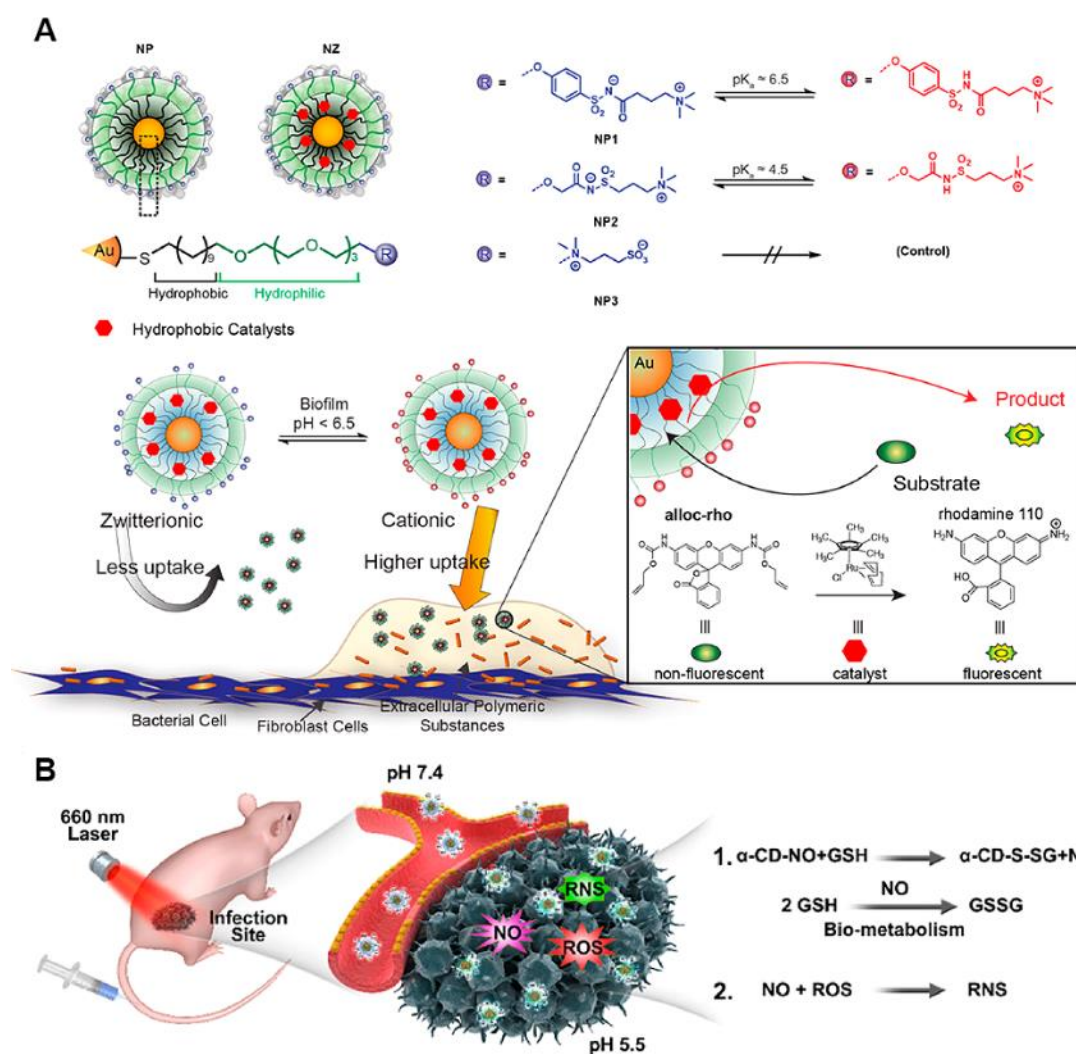


Figure 10. (A) Scheme showing that the zwitterionic NCM becomes positively charged under BME, facilitating its biofilm penetration ability. Then, the NCMs within biofilm can catalyze a non-fluorescent substrate alloc-rho to produce a fluorescent product rhodamine 110 via a bio-orthogonal reaction, thus labelling the biofilm. (B) Scheme showing the a BME-responsive NCM is able to release NO and reactive nitrogen species for killing biofilm. Reprinted with permission from Ref.^[44] Copyright 2021, WILEY-VCH Verlag GmbH & Co. KGaA, Weinheim, Germany.

The abundance of reductive GSH in biofilms is a significant factor that hampers the effectiveness of NCMs. This is because GSH can counteract the ROS produced by NCMs, preserving the viability of bacteria within biofilm. To address this issue, Ji et.al. proposed the use of a GSH depletor in combination with laser-triggered antibiofilm PDT. To achieve this, they synthesized a supramolecular NCM by anchoring the chlorin e6- and nitric oxide-functionalized α -cyclodextrins to pH-sensitive PEG-based copolymer via host-guest interactions.^[42] The NCMs had a negative surface charge under physiological pH (7.4), which ensured stability in blood. Under acidic conditions of BME (pH~5.5), the NCMs became positively charged, which facilitates the biofilm penetration. Then, the NCMs were able to serve as GSH depletory and release NO. As GSH was consumed, the ROS within biofilm were accumulated, thereby reinforcing the PDT effects. Additionally, GSH-triggered NO reacted with the ROS, leading to the formation of RNS and further strengthen the antibiofilm effect (Figure 10B).

1.2.7. Challenges

Although the current NCMs-based therapies have achieved significant progress, they are still facing two main challenges which should be preferentially improved in the near future. Firstly, some NCMs kinetically showed lower activity as compared to natural enzymes.^[76] Restricting by the limited catalytic efficiency, a relatively large dosage (milligram to gram scale) is therefore required, which may increase the potential

toxicity and the risk for side effects. Secondly, the NCMs should be designed to be more specific to bacteria, thus localizing the ROS killing effects in infectious sites without doing harm to the surrounding cells and tissues. As mentioned above, the NCMs that can only generate toxic agents under BME condition, have been successfully developed. Afterwards, more antibacterial NCMs with bacterial-enzyme responsiveness, pH responsiveness and ROS responsiveness aiming at better bacterial specificities were developed.^[77-80] However, considering the possible bacterial infection sites can be very different with a wide range from highly acidic stomach environment, mild acidic skin or oral environment, to mild basic blood or tissue environment, surrounding by numerous ions, sugars and proteins,^[81] the existing NCMs still have a high off-target possibility. Therefore, it is expected to develop more advanced NCMs with inherent bacterial affinity and bacteria-targeted ability.

1.3. Further functionalization of antibacterial NCMs

1.3.1. Structure and reaction path innovation

To further enhance the catalytic performance of NCMs, the structure and catalytic reaction path require innovation. Generally, doping metals can effectively adjust the catalytic sites' crystal facet or d-band center, thus improving the reaction path. For example, by doping trace amount of palladium into platinum nanodendrite (Figure 11A and B), a NCM with much higher catalytic efficacy than palladium nanocubes was obtained, suggesting that metal doping facilitates the formation of high-index facet platinum which improves the POD-mimetic reaction path (Figure 11C).^[82] Owing to the superior catalytic performance, this NCM was able to achieve high antibacterial effect with a ratio of 71.9% in the presence of only 10 μM of H_2O_2 . Also, a satisfactory *in-vivo* wound disinfection results of the NCM were witnessed, demonstrating a reliable potential for being used as an antibacterial nanomedicine. Recently, to synthesize single-atom NCMs are considering a revolutionary strategy for further improving the catalytic performance. Sharing the structural similarity with natural enzyme (Figure

11D), the single-atom NCMs were reported to have similarly advanced reaction path and highly comparable catalytic kinetics as natural enzymes. [83]

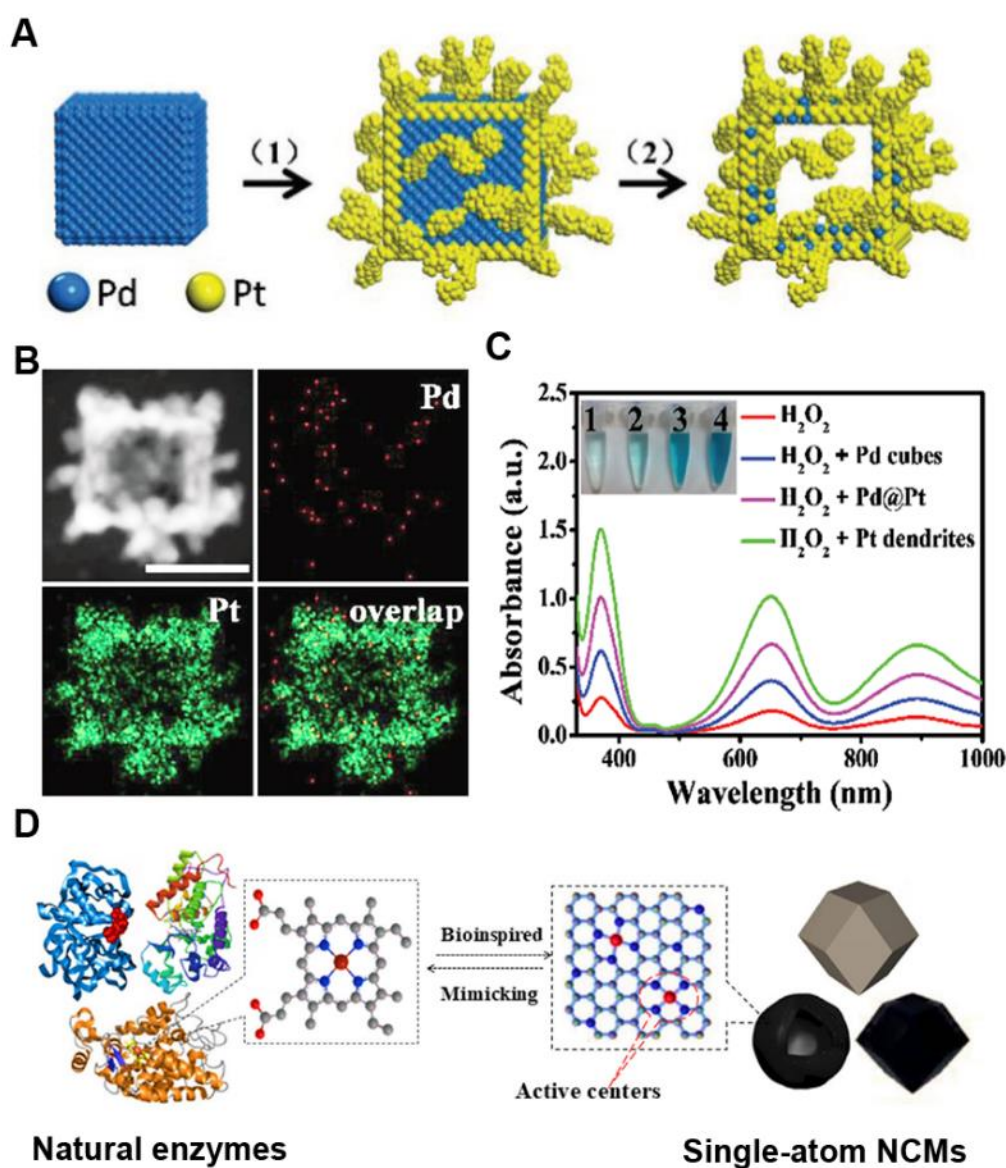


Figure 11. (A) The synthesis scheme and (B) the TEM EDX mapping of Pd-containing Pt nanodendrite. (C) UV-vis spectra for catalyzing the POD-mimetic performance of samples. (D) Structural similarity of natural enzymes and single-atom NCMs. (A-C) Reprinted with permission from Ref.^[82] Copyright 2018, WILEY-VCH Verlag GmbH & Co. KGaA, Weinheim, Germany. (D) Reprinted with permission from Ref.^[83] Copyright 2020, Elsevier.

Besides, the catalytic substrates can be further diversified. As mentioned above, substrates like H_2O_2 for initiating POD catalysis, has inherent toxicity towards cells and tissues, which limit the addition amount of exogenous H_2O_2 over the antibacterial treatment. As a result, the H_2O_2 can be rapidly consumed, resulting in a limited bactericidal performance. Therefore, some efforts and progress have been made recently to get rid of adding toxic substrate. For example, by combining glucose oxidase (GOx) with POD-mimetic NCMs, a cascade catalysis that *in situ* converts glucose to hydroxyl radicals is initiated.^[84-86] Because of nontoxicity, high dosage of glucose can be introduced, and under the catalysis of a low concentration of GOx, it can continuously and stably supply H_2O_2 over the treatment, leading to long-term and mild antibacterial effect. Recently, a GOx-loading POD-mimetic NCM was synthesized, which catalyzed the production of hydroxyl radicals via cascade catalysis of GOx and Fenton reaction (Figure 12A).^[85] A dramatic decrease of bacterial colonies was observed after a treatment (Figure 12B). Similarly, Liu et.al. anchored GOx on 2D MOF to obtain a self-activated cascade catalytic nanosystem. The system first catalyzed the oxidation of glucose to form H_2O_2 and gluconic acid. Then, with the pH decreasing, the second step of catalyzing H_2O_2 to $\bullet\text{OH}$ could be promoted (Figure 12C).^[84] Considering the drawbacks of natural enzymes like low stability in physiological conditions and high cost, the gold nanoparticles, were recently applied as GOx-alternatives to initiate the cascade catalysis. The success has been demonstrated by antitumor, antibacterial and diagnosis studies.^[45, 87-90]

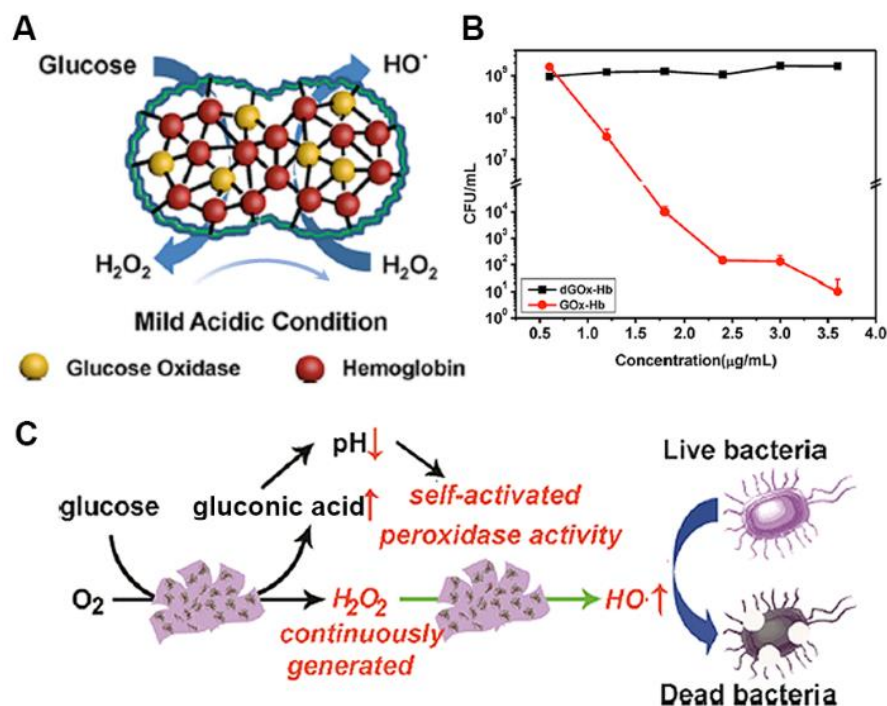


Figure 12. (A) Scheme illustration of a cascade catalysis induced by a GOx-loading POD-mimetic NCM. (B) Bacterial colonies of after treatments with different concentrations of NCM with denatured GOx (dGOx-Hb) and active GOx (GOx-Hb). Reprinted with permission from Ref.^[44] Copyright 2021, WILEY-VCH Verlag GmbH & Co. KGaA, Weinheim, Germany.

1.3.2. Enhancing bacterial binding

In order for NCMs-based therapies to be both safe and bacteria-targeted, it is highly necessary to endow NCMs with inherent bacterial binding abilities. Physically, by rational designing the materials' surficial topography, the non-specific interaction between surfaces and bacteria can be significantly strengthened. Typically, the materials with spiky or rough surfaces tended to bind on the bacterial outer membranes rather than randomly distribute over the treatments, thus shortening the diffusion distance of bactericidal agents from the material and localizing the toxicity in limited area.^[50, 91-92] For example, Yu et.al. synthesized a pollen-like nanostructures, which were able to inherently bind bacteria via the nanospikes topography, leading to localized lysozyme release and bacterial killing.^[93] Qu et.al. synthesized a 3D MoS₂-

based hydrogel scaffold with high surficial roughness, by which the interaction .^[91] Both *in-vitro* and *in-vivo* antibacterial experiments proved that the scaffold could effectively capture the bacteria and impose enhanced bactericidal effect against bacteria via the *in-situ* ROS release. Also, take advantage of the strong interaction between scaffold and bacteria, the dead bacteria can be easily removed from the wound sites after treatment, accelerating the wound healing process.

Chemically, targeted bacterial binding can be realized by grafting certain ligands that showing specific ligand-receptor interaction with bacteria to the material surface. Especially, the carbohydrate-protein interactions were widely used to fabricate the targeted bacterial binding and killing platform. Recently, Zhang et.al. developed a NCM with biofilm binding, imaging and killing all-in-one ability by cooperation of galactoside and spiropyran within copolymer.^[94] Specifically, galactoside showed targeted binding with lectin A in *P. aeruginosa*'s cell wall, and then, the spiropyran could be released and generate fluorescence under acidic BME, thus labelling the biofilm. Similarly, Xu et.al. synthesized MoS₂ with mannoside, glucoside and galactoside for enhancing bacterial targeting ability via carbohydrate-protein interactions.^[95] In this work, the mannose-modified MoS₂ was found to exhibit *E. coli*-targeted binding and agglutination ability. Upon NIR irradiation, a high bacteria-targeted PTT killing with a reduction ratio of more than 99.9% was noticed.

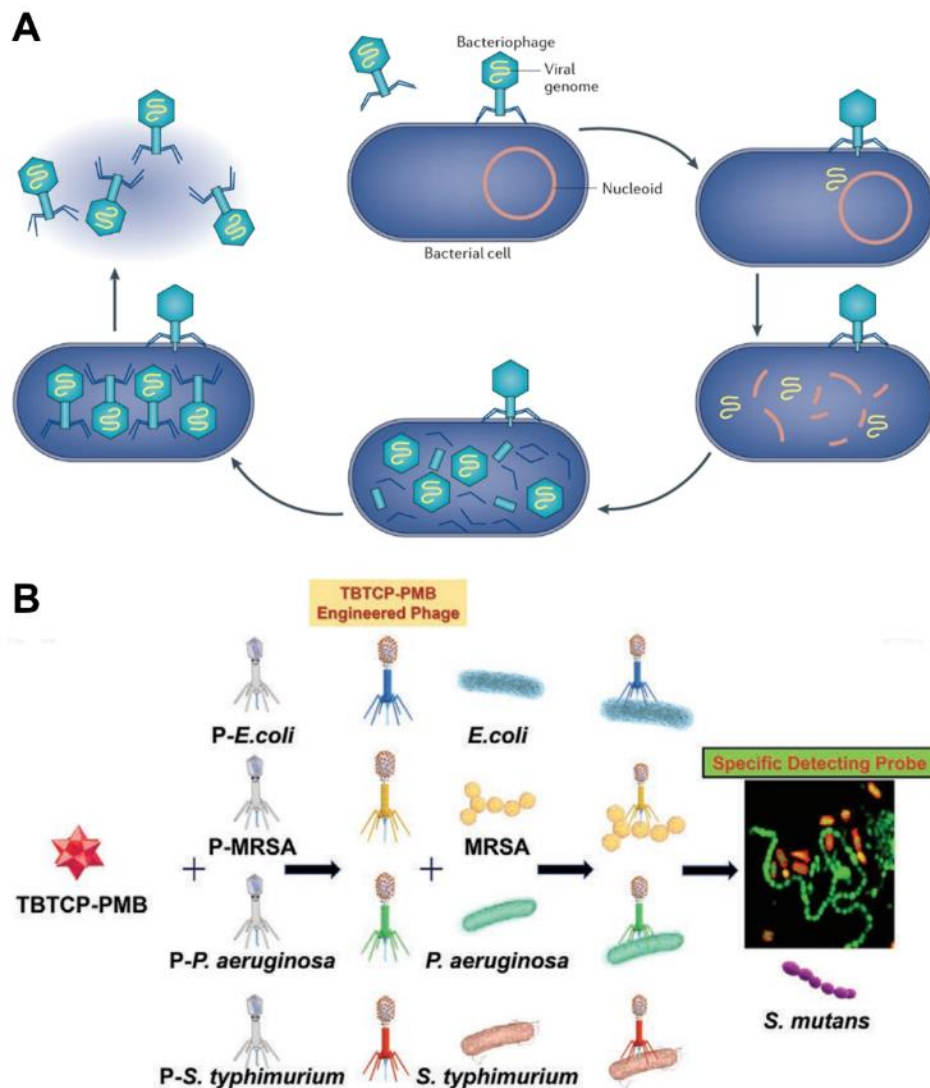


Figure 13. (A) Lytic cycle of bacteriophage. (B) Scheme showing the AIE-modified bacteriophages are able to target and label their host bacteria. (A) Reprinted with permission from Ref.^[96] Copyright 2015, Springer Nature. (B) Reprinted with permission from Ref.^[97] Copyright 2023, WILEY-VCH Verlag GmbH & Co. KGaA, Weinheim, Germany.

Biologically, bacteriophage (or phage), a natural bacterial predator, is considered to be a promising candidate for targeted bacterial disinfection. The bacteriophage's tail protein can specifically bind certain receptors of host bacteria like lipid polysaccharide, proteins and flagellum.^[24, 98] After the binding happens, the bacteriophage can inject

their genetic materials into bacteria, and hijack them for producing their progenies. Once the progenies are ready, they can lyse the bacteria via producing lysozyme and further infect surrounding bacteria (Figure 13A). Tang et.al. designed a bacteriophage-based NCM for bacterial targeting imaging and killing.^[99] In the system, the bacteriophage can first guide NCM to the bacterial infection sites, then the aggregation-induced fluorescence-emission (AIE) photosensitizer was able to image the bacteria. Under white light exposure, the AIE photosensitizer produced $^1\text{O}_2$, which synergistically assisted the bacteriophage with the bacterial killing. In the follow-up work, different types bacteriophages were equipped with AIE photosensitizer, were found to be highly targeted and bactericidal against their host bacteria in blood (Figure 13B).^[97] These works suggest bacteriophage can serve as a wonderful bacterial targeting component in developing narrow-spectrum bactericidal NCMs.

2. Scientific goals

Up to now, the strategies for combating MDR bacterial infection are still limited. As overviewed above, the novel NCMs are becoming a promising candidate against MDR bacterial infection since they catalyze the ROS production, showing the prominent toxicity against bacterial without leading to the resistance. However, present NCMs also suffer from some challenges like non-specific toxicity, limited catalytic efficiency, and requirement of adding toxic chemical auxiliaries during a treatment, which compromised the *in vivo* therapeutic effects. Thus, we believe there is still an urgent need for advanced *in vivo* antibacterial NCMs. The overall scientific goal of this PhD study is to develop highly efficient and biosafe *in vivo* anti-MDR-bacterial NCMs. To achieve this goal, three projects are proposed:

(1) A BME-responsive NCM with inherent bacterial binding ability

There are three scientific goals in this work: first, the NCM should have high-class catalytic performance for ROS production; second, the NCM should possess inherent bacterial affinity, which shortens the diffusion distance of ROS and enhances bactericidal efficiency. A ROS-based antibacterial modal alone might show limited effect for biofilm eradication. Therefore, third, by combining with other bactericidal mechanism like PTT, the antibiofilm effect could be further strengthened. To achieve the goals mentioned above, herein, a nickel-cobalt dual-metal doping nanocarbons will be synthesized. Owing to the acidic-preferential POD-like property of transition-metal, the NCM will only catalyze the generation of $\bullet\text{OH}$ under BME. By adding dicyandiamide during carbonization, the ammonia and hydrocarbon gas are generated, under which the surficial cobalt particles of NCM serve as catalyst for *in-situ* synthesis of nanohook-like carbon nanotubes (CNTs). With this unique nanohook-like CNTs, it is envisioned that the NCM will show inherent bacterial binding ability. Also, as a carbon-based material, the NCM with photothermal effect can initiate PTT, leading to a robust synergistic bactericidal effect with ROS.

(2) A bacteriophage-based NCM with highly bacterial-targeted ability

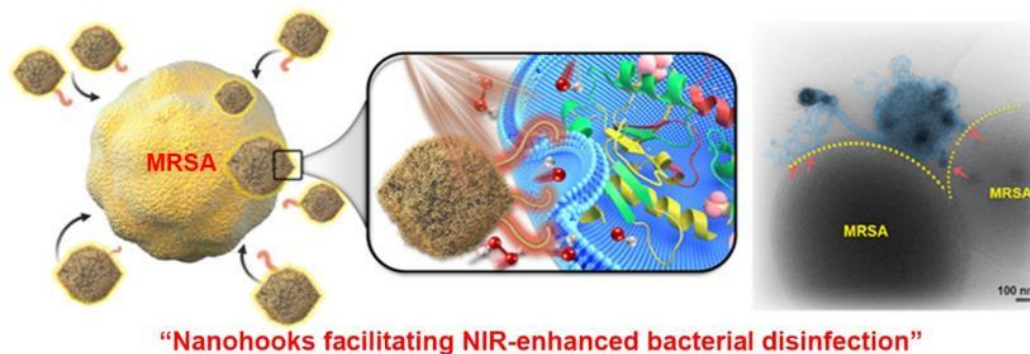
The aim of this work is to design a NCM with superior bacterial strain specificity, bactericidal efficacy, and biosafety. As a natural bacterial predator, the bacteriophage is considered to be a wonderful candidate for construction of highly bacterial-targeted system since it can selectively bind and hijack bacteria, ending up with a bacterial lysis.^[96] However, bacteria were also proved to gain resistance against bacteriophage's actions.^[24] Therefore, it is of vital importance to equip the bacteriophage with other bactericidal modality, facilitating the bacterial eradication in a short time. Herein, by anchoring photocatalytic cadmium-based quantum dots (QDs) onto the bacteriophage via avidin-biotin bioconjugation, a bacteriophage-based NCM can be synthesized. Inheriting from the bacteriophage's nature, it is anticipated the NCM is able to specifically bind bacteria. Upon the light irradiation, the photocatalytic QDs are expected to *in situ* catalyze oxygen to generate ROS,^[100] which synergistically kill bacteria with phage.

(3) A cascade NCM for treating bacterial diabetic ulcers

As mentioned in 1.1, by adjusting the compositions and catalytic pathway, the NCM can catalyze different substrates, as thus fulfilling different clinic requirements. Therefore, in the third project, we anticipate to customize a NCM for overcoming a long-term medical challenge: MDR bacterial-related diabetic ulcers. A bacterial diabetic ulcer is hard-to-cure due to the overabundance of the glucose in affected area, which hinders the actions of immune system but promotes the bacterial growth. Targeting to this feature, we will design a NCM that can catalyze glucose to bactericidal ROS, thus controlling the bacteria and glucose in ulcers in the same time. Herein, a copper-based nanosheets anchored with gold nanoparticles will be synthesized as a cascade NCM, in which gold nanoparticles first catalyzes the glucose to H₂O₂, followed by the production of •OH via the POD-mimetic catalysis from copper. To maximize the utilization of copper and minimize the potential toxicity of copper ions leaching, it is preferential to reduce the copper size to atomic level. It is envisioned that this NCM has great potential in treating MDR bacterial diabetic ulcers.

3. Publications

- 3.1. A Nanohook-equipped bionanocatalyst for localized near-infrared-enhanced catalytic bacterial disinfection



Xin Fan, Xizheng Wu, Fan Yang, Lei Wang, Kai Ludwig, Lang Ma, Andrej Trampuz*, Chong Cheng*, and Rainer Haag*.

Angew. Chem. Int. Ed. 2022, 61, e202113833

DOI: <https://doi.org/10.1002/ange.202113833>

This is an open access article under the terms of the [Creative Commons Attribution Non-Commercial License](#).

Author contributions:

Xin Fan performed the main experiments, and wrote the manuscript. Xizheng Wu conducted the animal experiments and assisted the data analysis. Fan Yang conducted the XAS measurements and assisted the data analysis. Lei Wang conducted partial antibacterial experiments. Kai Ludwig performed cryo-EM measurement. Lang Ma provided lab and animals for *in-vivo* studies. Andrej Trampuz provided the lab and drug-resistant bacterial strains for supporting the *in-vitro* antibacterial studies. Andrej Trampuz, Chong Cheng, and Rainer Haag conceived and supervised the project.



Catalytic Therapy Hot Paper

Zitierweise: *Angew. Chem. Int. Ed.* **2022**, *61*, e202113833

Internationale Ausgabe: doi.org/10.1002/anie.202113833

Deutsche Ausgabe: doi.org/10.1002/ange.202113833

A Nanohook-Equipped Bionanocatalyst for Localized Near-Infrared-Enhanced Catalytic Bacterial Disinfection

Xin Fan, Xizheng Wu, Fan Yang, Lei Wang, Kai Ludwig, Lang Ma, Andrej Trampuz,*
Chong Cheng,* and Rainer Haag*

Abstract: Novel bionanocatalysts have opened a new era in fighting multidrug-resistant (MDR) bacteria. They can kill bacteria by elevating the level of reactive oxygen species (ROS) in the presence of chemicals like H_2O_2 . However, ROSs' ultrashort diffusion distance limit their bactericidal activity. We present a nanohook-equipped bionanocatalyst (Ni@Co-NC) with bacterial binding ability that shows robust ROS-generating capacity under physiological H_2O_2 levels. The Ni@Co-NC's pH-dependent performance confines its effects to the biofilm microenvironment, leaving healthy tissue unaffected. Furthermore, it can generate heat upon NIR laser irradiation, enhancing its catalytic performance while achieving heat ablation against bacteria. With the Ni@Co-NC's synergistic effects, bacterial populations fall by >99.99%. More surprisingly, the mature biofilm shows no recurrence after treatment with the Ni@Co-NC, demonstrating its tremendous potential for treating MDR bacterial related infections.

Introduction

Infections by multidrug-resistant (MDR) pathogenic bacteria have afflicted millions of people, and worldwide they cause almost one million deaths every year.^[1,2] To address this serious threat to global health, numerous chemically engineered functional nanomaterials with potent antibacte-

rial therapeutic effects have emerged as potential substitutes for traditional antibiotics. This new class of nanomaterials, with mechanisms as diverse as reactive oxygen species (ROS) generation, selective ion leaching, and heat ablation effects, represents a new era in nanomedicine.^[3-9] In particular, nanomaterials that can mimic oxidoreductases like peroxidase (POD), oxidase (OXD), and catalase (CAT) have sparked increasing interest because they can be used to fine-tune local ROS levels for satisfactory bactericidal outcomes.^[10-15] But these oxidoreductase-mimicking nanomaterials, also known as bionanocatalysts, can show undesirable off-target activity during in vivo biofilm treatment, leading to unpredictable toxicity.^[16,17] Therefore, the ideal bionanocatalyst will not only deliver strong catalytic-reaction-based therapeutic effects to biofilm-infected sites, but will limit its action to these sites while leaving healthy tissues unaffected. The pursuit of this combination of traits stands as a significant challenge in developing antibacterial bionanocatalysts.

Under the encapsulation of extracellular polymeric substances, the biofilm microenvironment (BME) usually lacks oxygen, resulting in anaerobic glycolysis, ion channel turbulence, and lower pH (≈ 5.5).^[18] To address these highly complex BME conditions, transition metals (iron, cobalt, nickel, manganese, etc.) that exhibit POD-like catalytic reactions are expected to be promising bionanocatalyst

[*] X. Fan, Prof. Dr. R. Haag
Institute for Chemistry and Biochemistry, Freie Universität Berlin,
Takustraße 3, 14195 Berlin (Germany)
E-mail: haag@zedat.fu-berlin.de

X. Fan, Dr. L. Wang, Prof. Dr. A. Trampuz
BIH Center for Regenerative Therapies (BCRT)
Charité-Universitätsmedizin Berlin
Corporate Member of Freie-Universität Berlin
Humboldt-Universität zu Berlin
and Berlin Institute of Health (BIH)
Berlin (Germany)
E-mail: andrej.trampuz@charite.de

X. Wu, Prof. Dr. C. Cheng
College of Polymer Science and Engineering
State Key Laboratory of Polymer Materials Engineering, Sichuan
University, Chengdu 610064 (China)
E-mail: chong.cheng@scu.edu.cn

F. Yang
Department of Physics, Freie Universität Berlin, Arnimallee 14,
14195 Berlin (Germany)

Dr. L. Wang, Prof. Dr. A. Trampuz
Center for Musculoskeletal Surgery
Charité—Universitätsmedizin Berlin
Corporate Member of Freie Universität Berlin
Humboldt-Universität zu Berlin
and Berlin Institute of Health
Berlin (Germany)

Dr. K. Ludwig
Research Center for Electron Microscopy and Core Facility
BioSupraMol
Institute for Chemistry and Biochemistry
Freie Universität Berlin
Fabeckstrasse 36a, 14195 Berlin (Germany)

Prof. Dr. L. Ma
Department of Ultrasound, West China Hospital, Sichuan Univer-
sity, Chengdu 610065 (China)

© 2021 The Authors. Angewandte Chemie published by Wiley-VCH GmbH. This is an open access article under the terms of the Creative Commons Attribution Non-Commercial License, which permits use, distribution and reproduction in any medium, provided the original work is properly cited and is not used for commercial purposes.

candidates because they show ROS generation capabilities that are well-matched to BME pH conditions. With their intrinsic POD-like properties, these transition-metal-based bionanocatalysts can produce ROS in a pH-dependent manner without requiring the additional input of oxygen or energy.^[19] Despite significant progress in the design and investigation of POD-like bionanocatalysts, many challenges remain in developing bionanocatalysts for in vivo MDR bacteria biofilm eradication. For instance, at physiological H₂O₂ concentrations (50–100 μM), these transition-metals-based bionanocatalysts can hardly generate levels of hydroxyl radicals (\bullet OH, a kind of ROS) that are sufficient for combating biofilm.^[18] Moreover, the ultra-short lifetimes (<200 ns) of \bullet OH radicals produced at the active sites of bionanocatalysts mean that they are likely to be quenched immediately, limiting both diffusion distance and bactericidal efficacy.^[20] Therefore, to further enhance bionanocatalysts' abilities to destroy MDR bacterial biofilm, we must improve their H₂O₂-catalytic activity in BME conditions and shorten the distance between bionanocatalysts and bacteria. To date, no research has simultaneously overcome these two challenges.

Here we present a nanohook-equipped bionanocatalyst with a nickel-cobalt bimetal doping nanostructure (Ni@Co-NC) for localized, near-infrared laser (NIR)-enhanced catalytic bacterial biofilm disinfection. Two properties of this bionanocatalyst enhance its specificity in targeting bacterial biofilm. First, its unique nanohook-equipped structure enables this Ni@Co-NC bionanocatalyst to spontaneously hook onto bacteria and their biofilm, an effect that localizes its catalytic bactericidal effects to the infected area. Meanwhile, its pH-dependent POD-like catalytic performance limits the biocatalytic effects of Ni@Co-NC to the BME; in other words, Ni@Co-NC catalyzes H₂O₂ to toxic \bullet OH in BME pH conditions while showing no such POD-like \bullet OH generation under physiological neutral pH. Notably, Ni@Co-NC generates heat upon NIR laser irradiation, simultaneously enhancing its catalytic performance and achieving heat ablation against bacteria. As a result of these synergistic effects, bacteria are reduced by over 99.99% in the presence of Ni@Co-NC. More surprisingly, mature biofilm, whether established in vitro or in vivo, shows no recurrence after treatment with Ni@Co-NC. We propose this new bionanocatalyst forward as a potential candidate for the next generation of antibiotic-free antibacterial strategies to counter MDR bacteria.

Results and Discussion

We began by preparing the nanohook-equipped bionanocatalyst, Ni@Co-NC, via the pyrolysis of a Ni-doped zeolitic imidazolate framework-67 (ZIF67), termed as Ni@ZIF67 and illustrated in Figure 1a. For comparison in the further structural and catalytic study, we also produced its cousin material Co-NC by the same protocol, except without the addition of nickel. We then systematically studied the chemical and physical structures of Ni@Co-NC by scanning electron microscopy (SEM), transmission electron micro-

scopy (TEM), X-ray diffraction (XRD), X-ray photoelectron spectroscopy (XPS), and X-ray absorption energy near-edge structure (XANES). Both TEM images (Figure 1b and Figure 1c) and SEM images (Figure S1) confirmed that the carbon nanotubes (CNTs) could be generated by adding an extra amount of dicyandiamide (DCD) during the carbonization process of Ni@Co-NC. The DCD decomposed and generated ammonia gas and acted as carbon and nitrogen sources for the generation of CNTs; the morphologies of Ni@Co-NC synthesized with the different amounts of DCD are shown in Figure S2 (detailed mechanism was discussed in the synthesis part in the Supporting Information). These carbon nanotubes can function as nanohooks to interact with bacteria and biofilm, as we will demonstrate below after a brief material characterization of Ni@Co-NC. The XRD pattern of Ni@Co-NC (Figure S3) shows five peaks located at 26.0°, 36.8°, 44.3°, 51.5°, and 76.0°, corresponding respectively to the (002) facet of the graphite layer, the (311) facet of cobalt oxide, while the (111), (200), and (220) facets of face-centered cubic (FCC) Co and Co–Ni alloy metals. The selected area electron diffraction (SAED) (Figure 1d) indicated the major diffraction rings of the Ni@Co-NC, which matches well with the XRD data. Energy-dispersive spectroscopy (EDS) mapping (Figure 1e) also revealed that C, N, Co, and Ni elements were homogeneously distributed throughout the Ni@Co-NC.

To further verify and quantify the atomic Co and Ni distribution in the CNTs' structures, we conducted STEM-based line scanning across the nanocrystal (Figure 1f). Site I, at a distance of around 5 nm, showed a high C signal but low and uniform Co, Ni, and N signals, reflecting the carbon layer with Co–N_x and Ni–N_x sites; while site II, at a distance of around 14 nm, displayed an element ratio, for C:N:Co:Ni, of 10.54:1:36.18:1.06, suggesting the coexistence of Ni–N_x sites and Co nanoparticles. High-resolution TEM images of the end of the nanohook (Figure 1g) showed the lattice fringes of both carbon layers and nanocrystalline Co and Co–Ni alloys, wherein 0.325 nm reflects the typical interlayer d-spacing of C (002) and 0.198 nm is the d-spacing of the Co and Co–Ni alloys' (111) planes. We used XPS to analyze the chemical composition, binding states, and atomic ratio of Ni@Co-NC (Figure S4). Taken together, these results demonstrate the unique structure of Ni@Co-NC, whose surface is equipped with nanohooks consisting of abundant Co–N_x, Ni–N_x, and cobalt nanoparticles sites.

To understand the influence of Ni incorporation on the local structure of Co sites within Ni@Co-NC, we performed XANES spectroscopy. As a reference, we also plotted Co foil, CoO, Co₃O₄, and Co-NC. Co K-edge XANES data (Figure 1h) revealed Ni@Co-NC and Co-NC showed similar position and intensity of Co pre-edge, indicating that Ni ions homogeneously replace Co sites of ZIF67 without changing the coordination geometry.^[21]

According to previous studies, the oxidation states of catalytic centers can greatly affect their structures and properties, such as spin state and work function. Thus, by regulating the oxidation states, the catalytic performance of the catalytic center can be improved.^[22] The absorption energies of both Ni@Co-NC and Co-NC fall between those

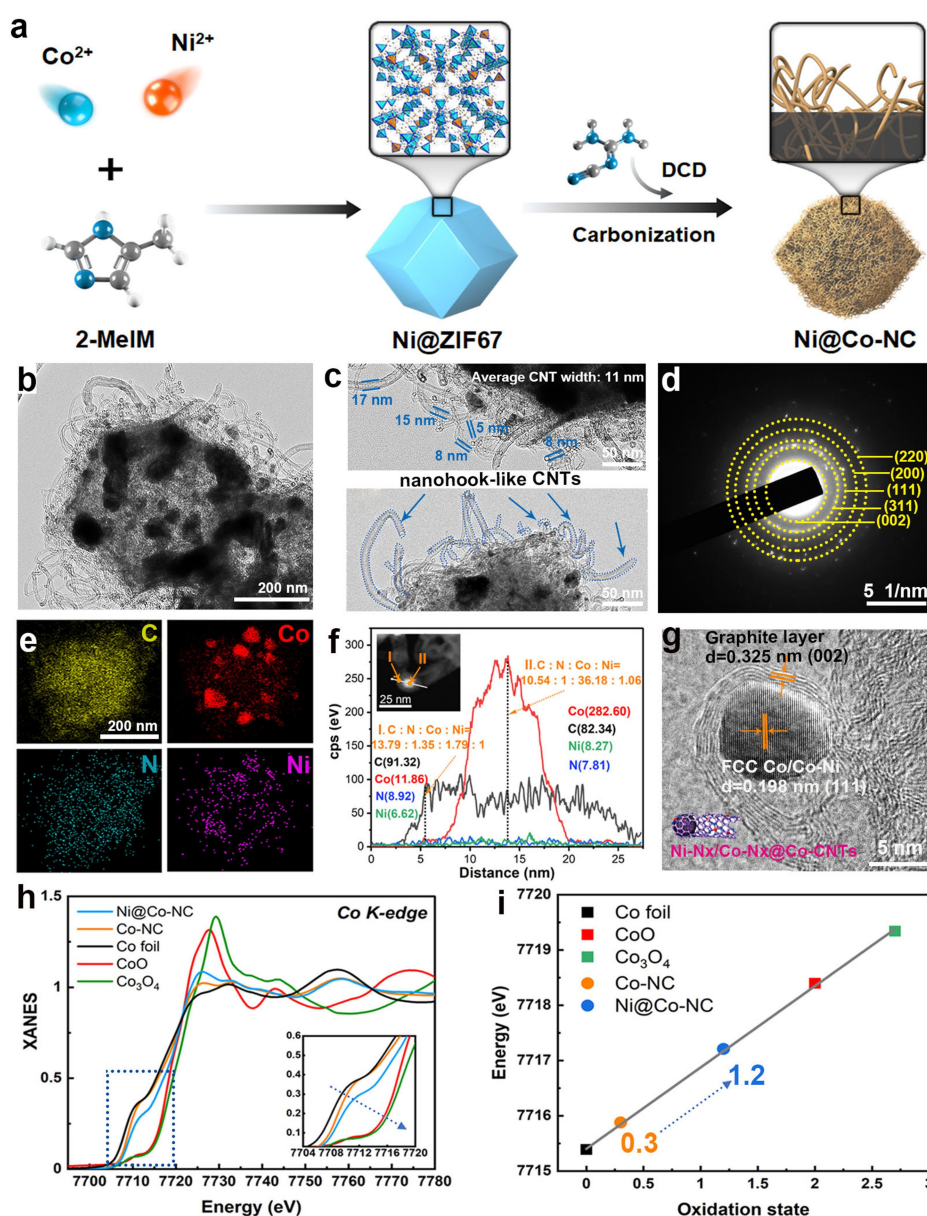


Figure 1. Fabrication of Ni@Co-NC, and its morphological and structural characterizations. a) Scheme of synthesis of Ni@Co-NC. b, c) TEM images reveal the unique nanohook-equipped structure of Ni@Co-NC. d) Selected area electron diffraction (SAED) pattern and e) EDS mapping of Ni@Co-NC. f) STEM images and corresponding elemental line scan of Ni@Co-NC, showing nanohook with Co nanoparticles and Co-N_x and Ni-N_x sites. g) High-resolution TEM image, h) XANES, and i) oxidation state analysis of Ni@Co-NC.

of Co foil and CoO, indicating that their cobalt sites show oxidation states between 0 and 2. In light of the standard curve fitted by reference compounds with known oxidation states,^[23] we were surprised to find that after introducing a trace amount of Ni species at a Ni:Co doping molar ratio of 1:40, the average oxidation state of cobalt increased significantly from 0.3 to 1.2 (Figure 1i), indicating that the interaction between Co and Ni within Ni@Co-NC may have caused an electron transfer from Co to Ni, thus increasing the oxidation state of Co.^[24]

Transition metal doping is a good strategy for modulating the d-band center of catalytic sites, thus optimizing the catalytic process.^[25–27] Based on this knowledge, combined

with the ability of oxidation state regulation to improve catalytic function, we anticipated that the oxidation state enhancement of the catalytic center, caused by doping with trace amounts of nickel, would further affect the POD-like catalytic performance of the cobalt center.

Therefore, to understand whether nickel doping promoted the POD-like performance of Co-NC, we examined hydroxyl radicals $\cdot\text{OH}$, the representative bactericidal product of the POD-like reaction, in the presence of H_2O_2 . At a BME pH of ≈ 5.5 , Ni@Co-NC generated a significantly larger amount of $\cdot\text{OH}$ than Co-NC, implying that the nickel doping promoted the POD-like catalytic performance (Figure 2a). Also, we noticed that Ni@Co-NC showed the best

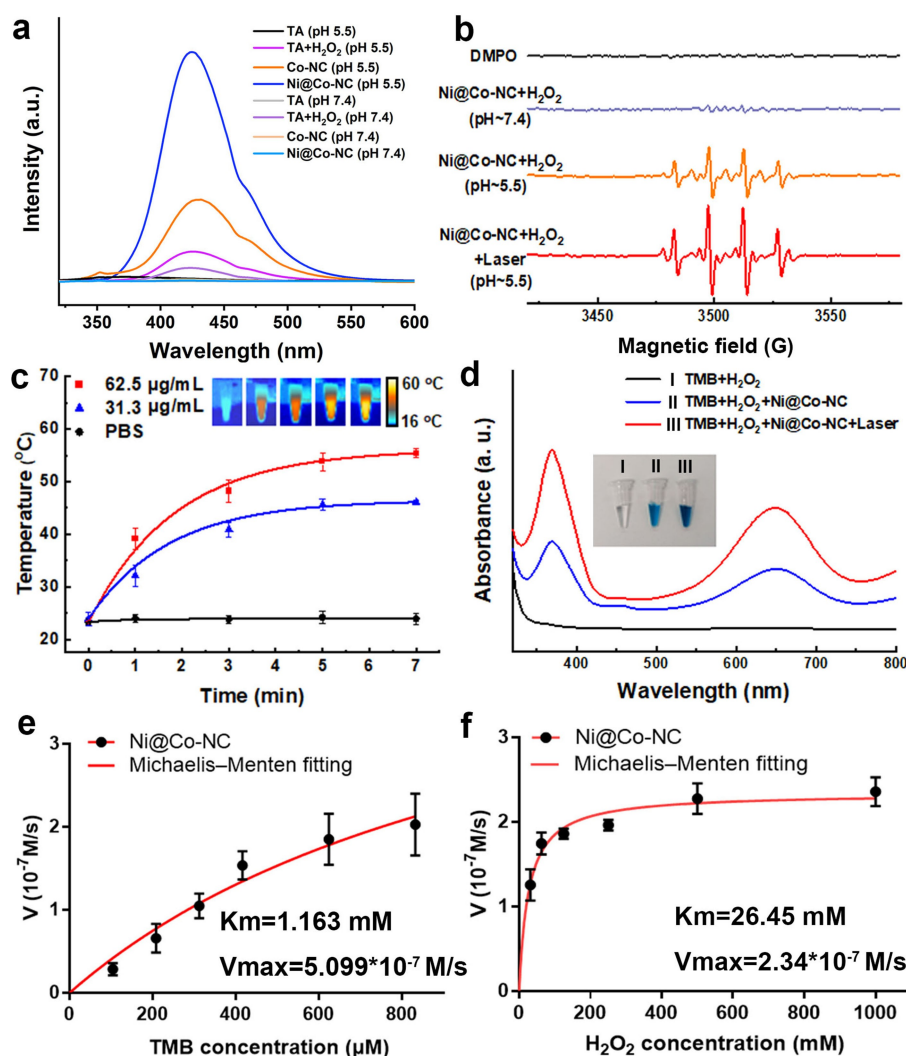


Figure 2. pH-dependent NIR-enhanced catalytic performance of Ni@Co-NC. a) Ni@Co-NC's $\cdot\text{OH}$ generation ability at biofilm microenvironment pH (5.5) and physiological pH (7.4) in the presence of H_2O_2 . Both Co-NC and Ni@Co-NC groups contained 3 mM of terephthalic acid and 100 μM of H_2O_2 . b) ESR data reveal the NIR-enhanced $\cdot\text{OH}$ generation. c) Photothermal heating profile of Ni@Co-NC exposed to NIR laser at a power density of 1 W cm^{-2} . Inset: infrared photos of Ni@Co-NC solution ($62.5 \mu\text{g mL}^{-1}$) exposed to laser for 0, 1, 3, 5, and 7 min. d) NIR-enhanced POD-like activity of Ni@Co-NC. Steady-state kinetic assay of Ni@Co-NC for TMB (e) and H_2O_2 (f).

$\cdot\text{OH}$ generation ability compared to its related nanomaterials synthesized with different pyrolysis temperatures (Figure S5), while we saw nearly no $\cdot\text{OH}$ generation at a physiological pH of ≈ 7.4 , suggesting that pH can serve as a switch for the POD-like ROS generation behavior of Ni@Co-NC. Interestingly, we noticed that the POD-like ROS generation was further enhanced by exposing Ni@Co-NC to NIR laser radiation, a result that was confirmed by electronic spin resonance (ESR). Characteristic ESR signals of 5,5-dimethyl-1-pyrroline N-oxide (DMPO)-OH with an amplitude ratio of 1:2:2:1 were clearly observed in an acidic environment and were intensified upon introducing NIR radiation, elucidating the bionanocatalyst's NIR-enhanced POD-like potential (Figure 2b). According to the Arrhenius equation,^[28,29] the chemical reaction can be significantly accelerated by increasing temperature; therefore, by comparing the POD-like activity of Ni@Co-NC under four

different conditions, we found the NIR-enhanced POD-like activity can be attributed to the temperature rising owing to photothermal conversion property of Ni@Co-NC (Figure S6a). We further monitored the NIR-induced heating profile of Ni@Co-NC. The Ni@Co-NC showed a concentration-dependent temperature increase after exposure to NIR laser (Figure 2c). We observed that the temperature rose to 55.4°C within 7 minutes at a concentration of $62.5 \mu\text{g mL}^{-1}$, while we observed no significant temperature variation for the PBS, confirming the robust photothermal conversion ability of Ni@Co-NC. Interestingly, we found that this unique nanohooks-equipped structure promote the photothermal properties (Figures S6b, S7a, and S7c, detailed discussion is presented in the Supporting Information). Moreover, the dispersity of the Ni@Co-NC with different concentrations under biological media was examined (Figure S8).

We then selected the most common and sensitive POD substrate, 3,3',5,5'-Tetramethylbenzidine (TMB), to test the POD-like activity and steady-state kinetic parameters of Ni@Co-NC. After a 5-min incubation, the TMB + H₂O₂ + Ni@Co-NC group exhibited blue products with remarkable absorption peaks reflecting oxidized TMB at both 370 nm and 652 nm, revealing robust POD-like activity (Figure 2d). Meanwhile, this POD-like activity was also strengthened upon NIR laser activation. We noticed the production of dark blue products with intensified absorption peaks for the laser-exposed group, resulting from the promotion of TMB oxidation by NIR-enhanced •OH generation. The dose-dependent POD-like activity of Ni@Co-NC was exhibited in Figure S6c. Moreover, we calculated the Michaelis–Menten constant (K_m) and the maximum initial velocity (V_{max}) to assess the catalytic performance of Ni@Co-NC (Figures 2e,f and Table S1). The K_m value of the Ni@Co-NC was 26.45 mM for H₂O₂ substrate and 1.163 mM for TMB substrate, indicating the comparable affinity of Ni@Co-NC for H₂O₂ and TMB substrates with that of natural horseradish peroxidase (HRP) (3.70 mM for H₂O₂ substrate and 0.434 mM for TMB substrate). Meanwhile, by comparing the K_m values of Ni@Co-NC (26.45 mM) and Co-NC (41.64 mM) (Figure S9), we noticed that the affinity between the bionanocatalyst and H₂O₂ substrate was significantly enhanced after nickel doping.^[30] Importantly, the V_{max} values of Ni@Co-NC for H₂O₂ and TMB showed respective ≈ 1.2 -fold and ≈ 2 -fold increases relative to Co-NC, suggesting that the nickel doping accelerated the POD-like catalytic process. Furthermore, by comparing with the nanohook-free sample, Ni@ZIF67-C, we found that the anchoring of nanohooks could also enhance the POD-like activity of the materials by enriching the superficial N-doped carbons and metal-N_x sites, which have also been observed by previous studies (Figures S6d,e, S7b,d, detailed discussion is presented in the Supporting Information).^[31,32] The above experimental results confirm that both Ni doping and anchoring of nanohook can promote the POD-like activity; meanwhile, the Ni@Co-NC offers NIR-enhanced and pH-selective POD-like performance, thus giving it tremendous potential for achieving on-demand BME-targeted catalytic disinfection.

Next, to study the possible in vitro planktonic MRSA killing actions of Ni@Co-NC, we used confocal laser scanning microscopy (CLSM), cryogenic electron microscopy (cryo-EM), and SEM to observe the interactions between Ni@Co-NC and MRSA. First, we used CLSM to investigate MRSA (stained by fluorescein isothiocyanate, or FITC) and treated with Ni@Co-NC (non-covalently labeled by rhodamine B) for different incubation times (Figure S10). We noticed that Ni@Co-NC gradually bound with the bacteria cells as the incubation time increased, and we detected a higher intensity of bacteria cells with fluorescence; meanwhile, from colocalization analysis, after 30 min of incubation, the Pearson's correlation coefficient reached 0.5183, revealing the high colocalization relation between Ni@Co-NC and MRSA and thus indicating that Ni@Co-NC had bonded to the MRSA cell surface. SEM images showed that the amount of Ni@Co-NC bonded to

the MRSA cell surface was remarkably higher than the nanohook-free sample, Ni@ZIF67-C, thus demonstrating that the nanohooks did facilitate the bacterial binding ability of bionanocatalysts (Figure S11). Meanwhile, SEM and TEM images offered a close-up depiction of the binding between Ni@Co-NC and MRSA via nanohooks (Figure S12).

We further carried out cryo-EM measurements to monitor the actions of Ni@Co-NC against MRSA. For untreated MRSA, cryo-EM images confirm its intact dual-membrane morphology (Figure 3b). However, after treating the MRSA with Ni@Co-NC, we observed Ni@Co-NC hooking onto the MRSA surface (Figure 3c, orange arrows), facilitated by its nanohook-equipped structure. To prove direct hooking of the Ni@Co-NC to the bacterium, which is difficult to determine from individual projection images alone, we also recorded side-by-side stereograms (stereo pairs of cryo-EM at 8° view angle) (Figure S13). The introduction of laser and H₂O₂ activated the bactericidal potential of Ni@Co-NC. We observed that the deformed MRSA cells suffered from severe membrane disruption or that the bacteria retained only part of their transparent outer membrane structure and underwent significant cytoplasm leakage. These results indicate the violent bactericidal actions of localized ROS and photothermal ablation caused by Ni@Co-NC (Figures 3d and S14). The protein leakage profile (Figure 3e) also provides strong evidence of disrupted MRSA membrane structure and cytoplasm leakage. As a result, MRSA treated with activated Ni@Co-NC (a term we use to refer to Ni@Co-NC activated by both laser and H₂O₂ unless otherwise stated) showed remarkably higher protein leakage amount than other groups treated under different conditions. This higher leakage suggests that the NIR-enhanced ROS generation and ablation effects promoted the protein leakage, an effect that we ascribe to the unmatched severity of bacterial membrane structural damage that we observed under treatment with activated Ni@Co-NC.

To investigate the bactericidal efficacy of Ni@Co-NC in mildly acidic environments, we calculated the bactericidal ratio by agar plate counting (Figures 3f and S15). We observed a bactericidal ratio of over 99.99% at a concentration of 62.5 $\mu\text{g mL}^{-1}$ of activated Ni@Co-NC, whereas we witnessed a much weaker bactericidal efficacy for the nanohook-free sample (Ni@ZIF67-C) at the same condition, indicating that the nanohooks can induce both binding ability and promote the bactericidal efficacy (Figure S16a). At this concentration, we also found significant bacterial viability reduction for the H₂O₂-activated Ni@Co-NC treatment group, with a bactericidal ratio of 89.95%. In contrast, we saw poor bactericidal effects for Ni@Co-NC + laser and bare Ni@Co-NC groups, with respective bactericidal ratios of 36.16% and 10.21%. Therefore, the H₂O₂ activation should be regarded as a major contributor to the bactericidal performance, and the laser activation function as a coadjutor that further promotes bactericidal outcomes via ablation and acceleration of ROS generation. Also, this bactericidal action was effective towards gram-negative drug-resistant bacteria (Figure S17). It is worth mentioning that negligible

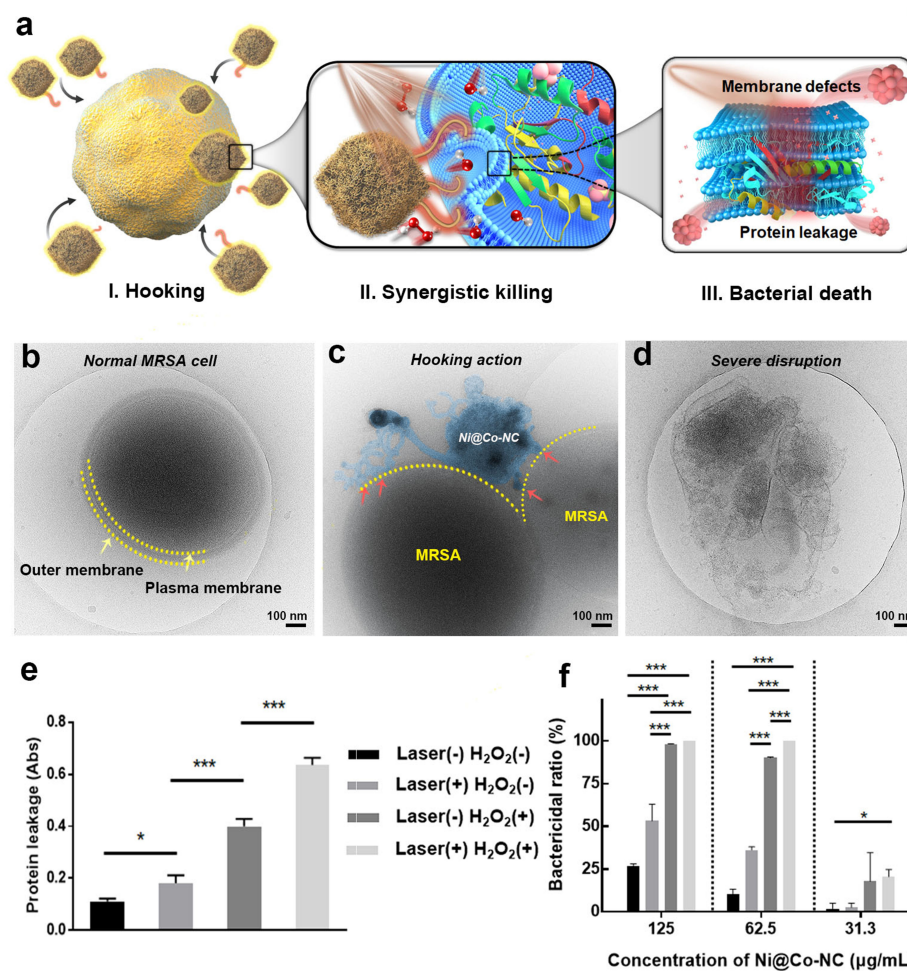


Figure 3. In vitro planktonic MRSA killing profile of Ni@Co-NC. a) This schematic image shows that Ni@Co-NC can hook onto bacterial surfaces and kill them through localized NIR-enhanced ROS generation and heat ablation, resulting in severe membrane disruption and intracellular substance leakage. Cryo-EM images of b) normal MRSA cell, c) MRSA cells incubated with Ni@Co-NC for 30 min, and d) disrupted MRSA cell treated with NIR-activated Ni@Co-NC and H₂O₂. e) Bacterial protein leakage profile and f) bactericidal ratio of Ni@Co-NC under different activation conditions. All experimental data are displayed as the average values (mean ± SD, $n = 3$). Asterisks indicate significant differences (* $P < 0.1$, ** $P < 0.01$, *** $P < 0.001$).

bactericidal activity was found for activated Ni@Co-NC ($62.5 \mu\text{g mL}^{-1}$) in the neutral environment, implying moderate behavior by Ni@Co-NC in physiological conditions (Figure S16b). Together these results show that Ni@Co-NC can first bind to the bacterial surface through hooking action and then synergistically kill bacteria through localized NIR-enhanced ROS generation and heat ablation, resulting in severe membrane disruption and intracellular substance leakage (Figure 3a).

Encouraged by the bionanocatalyst's robust planktonic MRSA killing performance, we then tested Ni@Co-NC for mature biofilm eradication. We first investigated the biofilm binding ability of Ni@Co-NC with CLSM. Due to the strong bionanocatalyst–bacteria interaction that we demonstrated above, the dye-labeled Ni@Co-NC could also bind accurately to the biofilm area after a 30-min incubation, providing strong support for subsequent biofilm eradication (Figure S18). Next, the biofilms treated with Ni@Co-NC under different activation conditions were stained with a

live/dead BacLight bacterial viability kit and observed using 3D CLSM (Figures 4a and 4b). Compared with untreated MRSA biofilm, the biofilms' viability under Ni@Co-NC or Ni@Co-NC + laser treatments showed a very slight decrease, indicating biofilms' powerful barrier effects against heat and foreign substances. Notably, for biofilms treated with Ni@Co-NC + H₂O₂, live (green) signals become very weak and sparse, with a viability of 32.26%. This result suggests that a great deal of biofilm can be killed via the localized ROS generation catalyzed by Ni@Co-NC. Strikingly, the biofilms treated with Ni@Co-NC + laser + H₂O₂ showed conspicuous red fluorescence, while green fluorescence was nearly non-detectable due to the strong synergistic actions of NIR-enhanced ROS generation and heat ablation. Furthermore, to study whether biofilm would recur after treatment, we used an isothermal microcalorimetry instrument that can non-destructively monitor the heat flow related to microbial metabolism to detect the growth of biofilm for another 48 h after treatment (Figure 4c). Com-

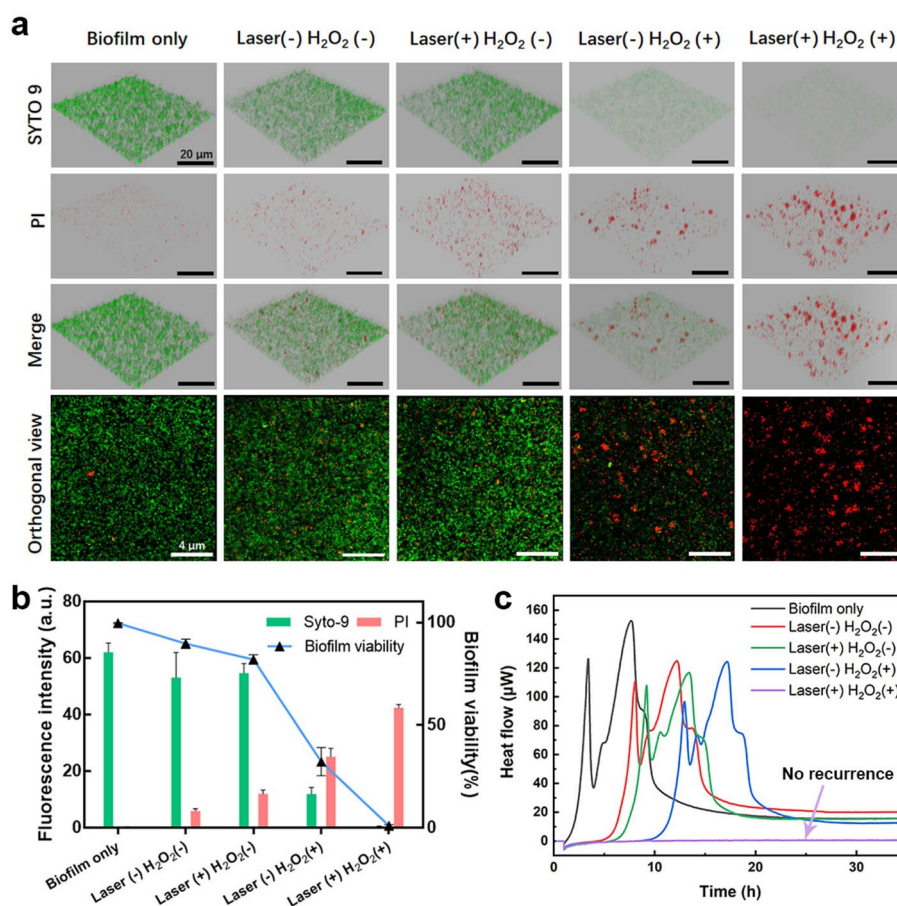


Figure 4. Antibiofilm profile of Ni@Co-NC. a) CLSM images of MRSA biofilm after incubation with PBS and Ni@Co-NC under different activation conditions (green fluorescence: live MRSA biofilm stained with SYTO 9; red fluorescence: dead MRSA biofilm stained with propidium iodide (PI)). Black scale bar is 20 μm ; white scale bar is 4 μm . b) Semiquantitative statistics of biofilm viability from analysis of fluorescence intensity percent of SYTO 9 over total fluorescence intensity of SYTO 9 and PI. c) Microcalorimetry analysis of MRSA biofilm after different treatments. Each curve shows the heat produced by viable bacteria within biofilm after treatment under different conditions.

pared to untreated biofilm, we saw different levels of heat flow production delays in biofilms treated with Ni@Co-NC, Ni@Co-NC+laser, and Ni@Co-NC+H₂O₂, indicating that these treatments can somewhat reduce the number of viable cells within the biofilm and delay biofilm recurrence, while still struggling to achieve complete biofilm eradication. By contrast, no heat flow production was seen in the Ni@Co-NC+laser+H₂O₂ treated group, demonstrating that the activated Ni@Co-NC could inflict irreversible damage on biofilms and thoroughly eradicate them. In this way, we showed that activated Ni@Co-NC could easily bind with bacteria and biofilm and achieve striking bactericidal activity via localized NIR-enhanced ROS generation and heat ablation.

Before performing animal experiments, we investigated the cytotoxicity of Ni@Co-NC using human skin keratinocytes (Figure S19). The results confirmed a very low toxicity of Ni@Co-NC under effective bactericidal concentration (90.7% cell viability under 62.5 $\mu\text{g mL}^{-1}$). We performed a wound disinfection experiment to further verify the feasibility of Ni@Co-NC as an *in vivo* biofilm treatment. We first established the biofilm infected wounds on rabbits' epider-

mis by removing an area of skin 1 cm in diameter and introducing MRSA (dosage: 100 μL ; concentration: 1×10^8 CFU mL⁻¹). One day after introducing bacteria, we observed a heavily infected wound with abscess, and then we applied the activated Ni@Co-NC for short-term treatment. After treatment, the pyogenic wound recovered quickly with epidermal tissue regeneration (Figure 5a).

In these animal experiments, to evaluate the *in vivo* antibiofilm efficacy of activated Ni@Co-NC, we used H₂O₂, Ni@Co-NC+laser, and Ni@Co-NC+H₂O₂ as comparisons. We also tested vancomycin in view of its role as the typical clinical strategy against MRSA. We used a digital camera to record the entire process of wound healing (Figures 5b and S20). The image made clear that after being infected with MRSA for 1 day, the wounds formed abscesses full of sanies, demonstrating MRSA colonization and biofilm formation. On day 2 we performed different treatments and used a thermal imaging camera to monitor the *in vivo* NIR-triggered heating profile of Ni@Co-NC. Due to the robust photothermal conversion ability of Ni@Co-NC, the temperature rose rapidly to 55 °C after a 2-minute irradiation (2.5 W cm⁻²), the time is sufficient for the acceleration of

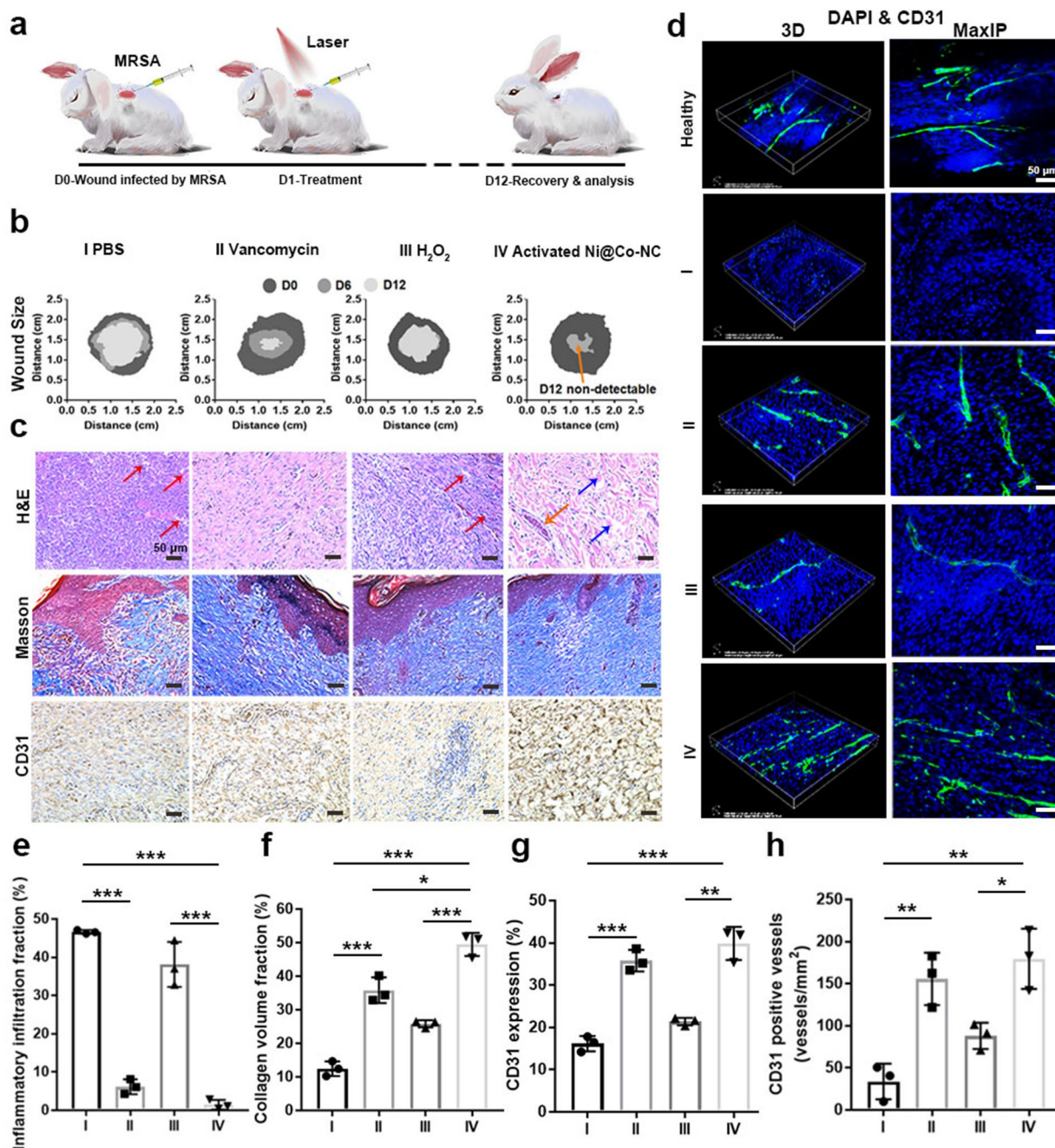


Figure 5. In vivo antibiofilm performance of Ni@Co-NC. a) Schematic illustration of the treatment schedule for in vivo antibiofilm experiment. b) Traces of wound closure over 12 days for groups treated with (I) PBS, (II) vancomycin, (III) H₂O₂, and (IV) Ni@Co-NC + laser + H₂O₂. c) Histologic analysis of the wounds treated by (I)–(IV) after 12 days of therapy. Black scale bar is 50 μm. In this experiment, we used H&E, Masson, and CD31 staining, respectively, to study inflammation response, collagen deposition, and revascularization in the wound area. d) CD31 and DAPI staining images of 3D reconstruction and corresponding maximum intensity projection (MaxIP) for healthy tissue and wounds treated by (I)–(IV). White scale bar is 50 μm. e) Inflammatory infiltration fraction, f) collagen volume fraction, g) CD31 expression, and h) CD31 positive vessels number of wounds treated by (I)–(IV) after 12 days of therapy. Asterisks indicate significant differences (**P* < 0.1, ***P* < 0.01, ****P* < 0.001). All data were acquired from the rabbits' wound tissues in different groups 12 days after treatment. All values are expressed as mean ± SD, *n* = 3.

catalytic procedure as well as bacterial ablation, and will not lead to skin burns (detailed discussion is presented in the Supporting Information). Whereas very limited temperature change was detected for the PBS group (Figure S21). After treatment, we collected bacteria from the wound area and

monitored them through agar plate counting (Figure S22). We found no viable bacterial colonies for wounds treated with vancomycin or with activated Ni@Co-NC. These comparable results show that our activated bionanocatalyst achieves highly efficient bactericidal activity on par with

antibiotics. In contrast, numerous viable bacteria remained after the other three treatment groups, suggesting that they offer limited disinfection capabilities. As shown in wound stack diagrams and wound photos (Figures 5b and S20), wounds treated with PBS, H₂O₂, and Ni@Co-NC+laser remained swollen with very limited closure until day 6. By contrast, for wounds treated with either vancomycin or activated Ni@Co-NC, the sanies vanished and we observed apparent area reductions. Notably, by day 12, the activated Ni@Co-NC-treated wound made a full recovery. In the vancomycin-treated group, only very small wounds remained at this time. On the contrary, we saw much slower closures for the groups treated with PBS, H₂O₂, Ni@Co-NC+laser, and Ni@Co-NC+H₂O₂, with large wounds encompassing different levels of the swollen epidermis, indicating an ongoing inflammatory response. To further investigate the infection state of wounds, we also performed the pathological analysis of histological sections via hematoxylin and eosin (H&E) staining. Compared to healthy tissues, we observed large areas of neutrophil infiltration and necrotic cells (indicated by red arrows) for PBS, H₂O₂, Ni@Co-NC+laser, and Ni@Co-NC+H₂O₂ groups (Figures 5c and S23), suggesting unrecovered inflammation responses induced by MRSA; meanwhile, the collagen fibrils in the intercellular substance also showed disordered texture, signifying severe damage during infection. We observed that the wounds treated with PBS and H₂O₂ showed very high respective inflammatory infiltration fractions (IIFs) of 46.63 % and 38.13 %. The Ni@Co-NC+laser and Ni@Co-NC+H₂O₂ groups also showed inflammatory response; however, after treatment with vancomycin and activated Ni@Co-NC, their respective IIF values decreased significantly to 6.17 % and 1.47 %, respectively (Figure 5e). Meanwhile, we noted nascent fibroblasts (indicated by blue arrows) and vessels (orange arrows), which confirmed the highly efficient and effective wound disinfection capability of activated Ni@Co-NC. Moreover, we uncovered no apparent rejection reaction or accumulation of Ni@Co-NC in the regenerated epidermis. And more importantly, the wounds treated with activated Ni@Co-NC show similar pathological characteristics to those treated with vancomycin, showing the remarkable potential of the activated Ni@Co-NC system as an antibiotic alternative. Furthermore, we carefully investigated the biosafety of activated Ni@Co-NC via H&E staining of the major organs (Figure S24). The lack of observable lesions confirms the safety of Ni@Co-NC-based NIR-enhanced catalytic therapy. We also performed Masson's trichrome staining to investigate collagen recovery in the wound healing process (Figures 5c, f, and S23). Here the group treated with activated Ni@Co-NC showed extensive and well-organized collagen deposition, with the highest collagen volume fraction of any group (49.48 %).

Neovascularization typically accompanies the wound healing process.^[33] With the help of CD31 staining, endothelial cells can be labeled to show newly formed vessels during the recovery of the wound area. As shown in Figures 5c and 5g, small CD31-positive areas were found in the PBS and H₂O₂ groups, with expressions of 16.18 % and 21.39 %. The Ni@Co-NC+laser and Ni@Co-NC+H₂O₂ groups showed

increased CD31 expressions (Figure S23), but the groups treated with activated Ni@Co-NC and vancomycin showed even further increased CD31 expressions of 35.81 % and 39.88 %, respectively, thus demonstrating better wound healing outcomes. Furthermore, we used CLSM imagery and immunofluorescence staining of CD31 to create a 3D reconstruction of the revascularization (Figures 5d, h and S25). This reconstruction revealed that the groups treated with activated Ni@Co-NC (179.53 vesselsmm⁻²) and vancomycin (155.82 vesselsmm⁻²) showed the highest number of new capillaries, indicating accelerated wound healing compared to the other groups. Taken together, these results confirm that activated Ni@Co-NC can effectively eradicate bacteria in vivo and achieve accelerated regenerative wound healing.

Conclusion

We have developed a nanohook-equipped bionanocatalyst, Ni@Co-NC, for localized NIR-enhanced catalytic bacterial and biofilm disinfection. With its unique nanohook-equipped structure, this bionanocatalyst can spontaneously hook onto bacteria and biofilms, thus localizing its catalytic bactericidal effect to the site of infection. And because of its pH-dependent catalytic performance, Ni@Co-NC can confine its catalytic activities to biofilm-infected sites while remaining safe to healthy tissue at neutral pH. Notably, upon NIR laser irradiation, Ni@Co-NC can generate heat, which simultaneously enhances its catalytic performance and enables heat ablation against bacteria. As a result of these synergistic effects, bacterial populations are significantly reduced (by >99.99 %) in the presence of Ni@Co-NC. More surprisingly, no recurrence is seen for mature biofilm established either in vitro or in vivo after treatment with Ni@Co-NC. It is believed that this bionanocatalyst will not only be a promising candidate in the next generation of antibiotic-free disinfectant against topical or subcutaneous biofilm-related infection but also provide new perspective for the design of bionanocatalytic antimicrobials. Besides, the bionanocatalysts also face some challenges, for example, due to its size and unknown accumulative toxicity in bloodstream and organs, it is yet difficult to be given intravenously and cure unknown bacterial infected lesions as traditional antibiotics do, but we optimistically believe those issues will be solved in the near future, and bionanocatalysts-based antibacterial therapy will achieve unparalleled success.

Acknowledgements

This work was financially supported by the National Key R&D Program of China (2019YFA0110600, 2019YFA0110601), and the Deutsche Forschungsgemeinschaft (DFG) of Germany through grants from Collaborative Research Centers (SFB) 765 and 1449. We also acknowledge the assistance of the Core Facility BioSupraMol supported by the DFG. X. Fan, F. Yang, and L. Wang

acknowledge the support of the China Scholarship Council (CSC). Prof. C. Cheng and Dr. L. Ma are grateful for support from the National Natural Science Foundation of China (Nos. 52173133, 82102064, 82102065, 82071938, 82001824, and 82001829), the Science and Technology Project of Sichuan Province (Nos. 2021YFH0087, 2021YFH0135, 2021YFS0050, 2021YJ0434, 21YYJC2714, 21ZDYF3763, 2021YFH0180, 2020YFH0087, and 2020YJ0055), the 1·3·5 Project for Disciplines of Excellence, West China Hospital, Sichuan University (No. ZYJC21047), the State Key Laboratory of Polymer Materials Engineering (Grant No. sklpm2021-4-02). The authors are grateful for the support of Benjamin Allen in polishing the language of the manuscript. Open Access funding enabled and organized by Projekt DEAL.

Conflict of Interest

The authors declare no conflict of interest.

Keywords: Antibacterial · Biofilm Microenvironment · Bionanocatalysts · Catalytic Therapy · Regenerative Wound Healing

- [1] W. Kim, W. Zhu, G. L. Hendricks, D. Van Tyne, A. D. Steele, C. E. Keohane, N. Fricke, A. L. Conery, S. Shen, W. Pan, K. Lee, R. Rajamuthiah, B. B. Fuchs, P. M. Vlahovska, W. M. Wuest, M. S. Gilmore, H. Gao, F. M. Ausubel, E. Mylonakis, *Nature* **2018**, *556*, 103–107.
- [2] J. M. A. Blair, M. A. Webber, A. J. Baylay, D. O. Ogbolu, L. J. V. Piddock, *Nat. Rev. Microbiol.* **2015**, *13*, 42–51.
- [3] S. Cheeseman, A. J. Christofferson, R. Kariuki, D. Cozzolino, T. Daeneke, R. J. Crawford, V. K. Truong, J. Chapman, A. Elbourne, *Adv. Sci.* **2020**, *7*, 1902913.
- [4] M. Liang, F. Wang, M. Liu, J. Yu, Y. Si, B. Ding, *Adv. Fiber Mater.* **2019**, *1*, 126–136.
- [5] X. Fan, F. Yang, J. Huang, Y. Yang, C. Nie, W. Zhao, L. Ma, C. Cheng, C. Zhao, R. Haag, *Nano Lett.* **2019**, *19*, 5885–5896.
- [6] Y. Wang, Y. Yang, Y. Shi, H. Song, C. Yu, *Adv. Mater.* **2020**, *32*, 1904106.
- [7] M. Zhang, W. Wang, F. Wu, K. Graveran, J. Zhang, C. Wu, *Chem. Eur. J.* **2018**, *24*, 12890–12901.
- [8] T. Shi, X. Hou, S. Guo, L. Zhang, C. Wei, T. Peng, X. Hu, *Nat. Commun.* **2021**, *12*, 493.
- [9] M. Zhang, F. Wu, W. Wang, J. Shen, N. Zhou, C. Wu, *Chem. Mater.* **2019**, *31*, 1847–1859.
- [10] X. Fan, F. Yang, C. Nie, L. Ma, C. Cheng, R. Haag, *Adv. Mater.* **2021**, *33*, 2100637.
- [11] B. Yang, Y. Chen, J. Shi, *Chem. Rev.* **2019**, *119*, 4881–4985.
- [12] Z. Wei, Y. Zhang, L. Wang, Z. Wang, S. Chen, J. Bao, Y. Xie, B. Su, C. Zhao, *ACS Appl. Mater. Interfaces* **2021**, *13*, 32316–32331.
- [13] Y. Yang, X. Wu, L. Ma, C. He, S. Cao, Y. Long, J. Huang, R. D. Rodriguez, C. Cheng, C. Zhao, *Adv. Mater.* **2021**, *33*, 2005477.
- [14] L. Ma, F. Jiang, X. Fan, L. Wang, C. He, M. Zhou, S. Li, H. Luo, C. Cheng, L. Qiu, *Adv. Mater.* **2020**, *32*, 2003065.
- [15] L. Li, L. Cao, X. Xiang, X. Wu, M. Lang, F. Chen, S. Cao, C. Cheng, D. Deng, L. Qiu, *Adv. Funct. Mater.* **2021**, *31*, 2107530.
- [16] Y. Zhang, P. Sun, L. Zhang, Z. Wang, F. Wang, K. Dong, Z. Liu, J. Ren, X. Qu, *Adv. Funct. Mater.* **2019**, *29*, 1808594.
- [17] Z. Yuan, C. Lin, Y. He, B. Tao, M. Chen, J. Zhang, P. Liu, K. Cai, *ACS Nano* **2020**, *14*, 3546–3562.
- [18] G. Guo, H. Zhang, H. Shen, C. Zhu, R. He, J. Tang, Y. Wang, X. Jiang, J. Wang, W. Bu, *ACS Nano* **2020**, *14*, 13391–13405.
- [19] Z. Chen, Z. Wang, J. Ren, X. Qu, *Acc. Chem. Res.* **2018**, *51*, 789–799.
- [20] Y. Sang, W. Li, H. Liu, L. Zhang, H. Wang, Z. Liu, J. Ren, X. Qu, *Adv. Funct. Mater.* **2019**, *29*, 1900518.
- [21] S. Peng, X. Han, L. Li, S. Chou, D. Ji, H. Huang, Y. Du, J. Liu, S. Ramakrishna, *Adv. Energy Mater.* **2018**, *8*, 1800612.
- [22] Z.-Z. Wu, F.-Y. Gao, M.-R. Gao, *Energy Environ. Sci.* **2021**, *14*, 1121.
- [23] M. Risch, F. Ringleb, M. Kohlhoff, P. Bogdanoff, P. Chernev, I. Zaharieva, H. Dau, *Energy Environ. Sci.* **2015**, *8*, 661–674.
- [24] Q. Zhang, N. M. Bedford, J. Pan, X. Lu, R. Amal, *Adv. Energy Mater.* **2019**, *9*, 1901312.
- [25] Z. Wang, Z. Lin, J. Deng, S. Shen, F. Meng, J. Zhang, Q. Zhang, W. Zhong, L. Gu, *Adv. Energy Mater.* **2021**, *11*, 2003023.
- [26] Z. Chen, Y. Song, J. Cai, X. Zheng, D. Han, Y. Wu, Y. Zang, S. Niu, Y. Liu, J. Zhu, *Angew. Chem. Int. Ed.* **2018**, *57*, 5076–5080; *Angew. Chem.* **2018**, *130*, 5170–5174.
- [27] Z. Chen, Y. Liu, C. Liu, J. Zhang, Y. Chen, W. Hu, Y. Deng, *Small* **2020**, *16*, 1904964.
- [28] J. Shan, K. Yang, W. Xiu, Q. Qiu, S. Dai, L. Yuwen, L. Weng, Z. Teng, L. Wang, *Small* **2020**, *16*, 2001099.
- [29] S. Li, L. Shang, B. Xu, S. Wang, K. Gu, Q. Wu, Y. Sun, Q. Zhang, H. Yang, F. Zhang, *Angew. Chem. Int. Ed.* **2019**, *58*, 12624–12631; *Angew. Chem.* **2019**, *131*, 12754–12761.
- [30] L. Gao, J. Zhuang, L. Nie, J. Zhang, Y. Zhang, N. Gu, T. Wang, J. Feng, D. Yang, S. Perrett, *Nat. Nanotechnol.* **2007**, *2*, 577–583.
- [31] Y. Hu, X. Gao, Y. Zhu, F. Muhammad, S. Tan, W. Cao, S. Lin, Z. Jin, X. Gao, H. Wei, *Chem. Mater.* **2018**, *30*, 6431–6439.
- [32] W. Shao, C. He, M. Zhou, C. Yang, Y. Gao, S. Li, L. Ma, L. Qiu, C. Cheng, C. Zhao, *J. Mater. Chem. A* **2020**, *8*, 3168–3179.
- [33] S. Saraswati, S. M. Marrow, L. A. Watch, P. P. Young, *Nat. Commun.* **2019**, *10*, 3027.

Manuscript received: October 12, 2021

Accepted manuscript online: November 26, 2021

Version of record online: January 3, 2022

Supporting Information

A Nanohook-Equipped Bionanocatalyst for Localized Near-Infrared-Enhanced Catalytic Bacterial Disinfection

X. Fan, X. Wu, F. Yang, L. Wang, K. Ludwig, L. Ma, A. Trampuz, C. Cheng*, R. Haag**

Supporting Information

Materials. All chemicals and solvents are reagent or HPLC grade, used as received, and purchased from Sigma-Aldrich (Steinheim, Germany) unless stated otherwise. The deionized water used is purified using a Millipore water purification system with minimum resistivity of 18.0 M Ω ·cm.

Synthesis of Ni@ZIF67. Typically, 2.910 g of Co(NO₃)₂·6H₂O and 0.073 g of Ni(NO₃)₂·6H₂O were firstly dissolved in 250 mL methanol to form solution A. 6.560 g of 2-methyl imidazole was dissolved in 250 mL methanol to form solution B. Then, quickly pour solution A into solution B, shake it vigorously and leave it to stand overnight. The purple precipitates were centrifuged at 11000 rpm, washed with ethanol, and dried in a vacuum at 338 K overnight.

Synthesis of Ni@Co-NC. Following a typical procedure, the dicyandiamide (100 mg) and Ni@ZIF67 (100 mg) were separately placed on a corundum boat. The corundum boat was firstly heated in a tube furnace under argon environment to 450 °C (at 2 °C /min) for 8 h, then was further heated to 800 °C (at 5 °C/min) for 2 h. The yielded Ni@Co-NC were collected after cooling. Similarly, Co-NC was synthesized using the ZIF67 as a precursor by the same protocol without adding Ni(NO₃)₂·6H₂O. As a comparison, cousin materials without nanohooks, Ni@ZIF67-C, were prepared by the same protocol without adding dicyandiamide (DCD) during pyrolysis. The underlying mechanism can be attributed to the *in-situ* thermal chemical vapor deposition (T-CVD) process. Briefly, the excess carbon produced by the pyrolysis of the precursor can be catalyzed by the transition metals (Co, Ni, Fe) in a reducing atmosphere (like H₂, CO, and NH₃) to form carbon nanotubes (CNTs). Excess carbon will precipitate on the surface of catalysts, and then diffuses into the catalyst, and ultimately nucleates to form the CNT at the edges of the catalyst. In this article, DCD provides the reductive NH₃ and is also one of the sources of nitrogen and carbon. During the carbonization, the in-situ generated Ni/Co nanocrystals catalyzed the excess carbon species to form nanohook-like CNTs under the NH₃ atmosphere.

Material characterizations. A Discover D8 (Bruker) was used to measure powder X-ray diffraction patterns. High-resolution transmission electron microscopy (HRTEM) and EDS were performed using an FEI Tecnai G2 F20 S-TWIN (200KV). SEM testing was carried out using a Hitachi SU8030. XPS

was performed using a K-alpha X-ray photoelectron spectrometer system (Thermo Scientific) with a Hemispheric 180° dual-focus analyzer with a 128-channel detector. XAS spectra at the cobalt K-edge were collected at the BESSY synchrotron (Berlin, Germany) at beamlines KMC-3.

Photothermal conversion of Ni@Co-NC. To investigate the photothermal conversion performances of the Ni@Co-NC, the temperatures of Ni@Co-NC under suspensions with different concentrations (62.5 and 31.3 $\mu\text{g/mL}$) were measured by a thermal imaging camera (NEC Avio Thermo Tracer TH9100). The samples were dispersed in PBS (0.2 mL). Then, a laser beam (FC-D-808, CNI Optoelectronics Technology Co. Ltd., Changchun, China) focused on the suspension at a power density of 1 W/cm^2 for 7 min in a uniform distance of 5 cm. At the same time, the infrared thermal images were taken under certain time intervals. PBS was used as a control. The experiments were repeated at least three times to get an average value.

Peroxidase-like activity of Ni@Co-NC. To monitor the peroxidase-like property of the Ni@Co-NC, the 3,3',5,5'-tetramethylbenzidine (TMB) molecular probe was utilized, and reactions were carried out in 0.1 mL acetate buffer solution (0.1 M, pH = 4.0), and the final concentrations of TMB, H_2O_2 , and Ni@Co-NC were 1 mM, 10 mM, and 33 $\mu\text{g/mL}$, respectively. After 5 min reaction time with/without laser irradiation (1 W/cm^2), photos were taken, and the UV-vis absorption spectra were determined with a plate reader Tecan (Infinite M200 Pro).

The steady-state kinetic assay was performed at room temperature. For kinetic parameters, the experiments were carried out in 100 μL NaAc buffer containing 62.5 $\mu\text{g/mL}$ Ni@Co-NC, 832 μM TMB, and a series of concentrations of H_2O_2 ranging from 0 to 1000 mM, or containing 62.5 $\mu\text{g/mL}$ Ni@Co-NC, 100 mM H_2O_2 , and a series of concentrations of TMB ranging from 0 to 832 μM . The absorbances of all reactions were monitored in a time-scan mode at 652 nm through a plate reader Tecan (Infinite M200 Pro), and the Michaelis–Menten constant was calculated according to the Michaelis–Menten saturation curve by GraphPad Prism 7.0 (GraphPad Software).

•OH generation activity of Ni@Co-NC. Terephthalic acid (TA) was used as a fluorescent probe that easily reacts with •OH to form a highly fluorescent product, 2-hydroxy terephthalic acid (HA). In a typical procedure, 30 μg of Ni@Co-NC was dispersed in 1.5 mL of PBS (pH~7.4) or NaAc-HAc

(pH~5.5) buffer. Then, the Ni@Co-NC-buffer dispersions were mixed with 1.5 mL of 6 mM TA solution containing 100 μ M H₂O₂ for 12 h in the dark, and finally, the changes in the 435 nm fluorescence emission peak were recorded using a Fluorescence Spectrometer Jasco FP-6500.

Besides, electron spinning resonance (ESR) measurements were also conducted using a Bruker ESR EMX Plus to test \bullet OH generation activity of Ni@Co-NC under different pH conditions with/without laser irradiation. 5,5-Dimethyl-1-pyrroline-N-oxide (DMPO) spin-trapping adduct was used to detect \bullet OH generation. Specifically, 20 μ L of 10 mM H₂O₂, 20 μ L of DMPO, and 200 μ L of Ni@Co-NC-buffer solution with a 1 mg/mL concentration were mixed. The ESR spectra were recorded 5 min after the reaction. For the NIR groups, 808 nm laser irradiation (1.0 W/cm², 5 min) was employed.

Culture and harvest MRSA biofilm. MRSA (ATCC 43300) was used in this research. Regarding MRSA biofilm culturing, a MRSA suspension (100 μ L, 10⁸ CFU/mL) and a lysogeny broth medium (LB, 100 μ L) were placed in ibidi 8-well slides, and then they were cultured at 37 °C. Twenty-four hours later, the medium was removed, and the unattached bacteria were gently washed away with sterile PBS three times, and the resulting biofilm on ibidi 8-well slides was harvested. The *in vitro* experiment's pH was adjusted by adding PBS solution (pH 5.5, 10 mM) when required.

***In vitro* bacteria/biofilm binding tests.** Octadecyl rhodamine B chloride (R18) was used as labeling dye for Ni@Co-NC, and fluorescein isothiocyanate (FITC) was used as labeling dye for bacteria. For bionanocatalysts labeling, typically, 5 μ L of 0.1 mM -ethanol solution was mixed with 95 μ L of 1 mg/mL Ni@Co-NC-PBS dispersion. After incubation in the dark for 45 minutes, the R18-labeled bionanocatalysts were washed by PBS 3 times to remove the excess dye. Typically, for bacteria labeling, 0.5 mg of FITC was dissolved in 1 mL of PBS (pH~8) as a labeling buffer. Afterward, a certain amount of labeling buffer was introduced into glutaraldehyde-fixed bacteria/biofilm, and the staining procedure lasted for 45 minutes in the dark. Then, the FITC-labeled bacteria/biofilm were washed by PBS 3 times to remove the excess dye.

For the *in vitro* planktonic bacteria binding tests, FITC-labeled MRSA solution (~10⁸ CFU/mL) was introduced into the lysine pre-treated ibidi 8-well slides for 1 min and was pipetted out to leave a thin layer of MRSA on the well surface. Then, R18-labeled Ni@Co-NC was introduced into the well

and a SP8 confocal microscope (Leica, Germany) was used for in-situ monitoring the interaction between bacterial and bionanocatalysts as increasing incubation time (5-30 min). While for biofilm binding test, a biofilm (24 h aged) was grown in ibidi 8-well slide and labelled by FITC. After incubation with bionanocatalysts for 30 minutes, a PBS washing step was performed to remove uncoupled bionanocatalysts. Then the fluorescent and bright-field images were acquired on a SP8 confocal microscope (Leica, Germany). For SEM sample preparation, the bionanocatalysts-bacteria solution was first centrifuged at 3000 rpm 3 times to remove the uncoupled bionanocatalysts. Subsequently, the pellet was fixed by 2.5% glutaraldehyde overnight at 4 °C and subjected to gradient dehydration using ethanol series (30%, 50%, 70%, 90%, and 100%, 10 min of each). Then dropped it onto aluminum foil and dried it at room temperature.

***In vitro* planktonic bacterial killing tests.** Typically, the samples Ni@Co-NC were firstly dispersed in LB media (pH~5.5). Then, 100 μ L of sample dispersions with a series of dilution times and H₂O₂ with the final concentration of 100 μ M were introduced into 100 μ L of $\sim 10^6$ CFU/mL bacterial suspensions. After incubation for 30 minutes under mild shaking, the bacteria/bionanocatalysts' suspensions were irradiated by an 808 nm laser (1 W/cm²) for 5 min. After near-infrared irradiation, the suspensions were incubated at 37 °C for 6 h. Experimental groups without laser irradiation and H₂O₂ were carried out as the control. At last, the bactericidal ratio for the samples under different conditions was studied via agar plate counting. The bacterial suspensions were diluted and cultured on agar plates for 12 h to count the bacterial colonies. We calculated all bactericidal ratios by comparing the treatment groups with control groups in the same intervention condition. For example, groups treated by Ni@Co-NC with H₂O₂ were compared to control with H₂O₂ to obtain the bactericidal ratio. Moreover, both SEM and cryo-TEM (Talos Arctica, Thermofisher, USA) were utilized to observe the bactericidal actions of Ni@Co-NC. The protein leakage amounts of bacteria after treatment were measured using PierceTM BCA Protein Assay Kit.

***In vitro* anti-biofilm tests.** Typically, for 3D confocal observation, 200 μ L of Ni@Co-NC-PBS dispersion (125 μ g/mL, pH~5.5) was introduced into 24-hour-aged biofilm in ibidi 8-well slides. After incubation for 30 minutes, H₂O₂ with a final concentration of 100 μ M was introduced to each well, and 5-min laser irradiation was conducted. Experimental groups without laser irradiation and H₂O₂

were carried out as the control. After incubation at 37 °C for 12 h, the biofilms were gently washed by PBS three times and then stained by LIVE/DEAD® BacLight Bacterial Viability Kits. The 3D Z-stack fluorescent and orthogonal-stack images were acquired on the SP8 lighting confocal laser scanning microscope (Leica, Germany). The fluorescent intensities are analyzed by ImageJ pro. The biofilm viability is quantified by comparing the live bacterial intensity with the total intensity of live and dead bacterial intensity.

Furthermore, an isothermal microcalorimetry instrument (IMC, Thermal Activity Monitor, Model 3,102 TAM III, TA Instruments, New Castle, DE, USA) was utilized to monitor the recurrence of biofilm after treatment. IMC is a non-destructive method that allows for the monitoring in the microwatt range of any exothermic or endothermic reaction related to the physical, chemical, and biological process in the tested sample. IMC enables precise real-time monitoring of the heat flow related to microbial metabolism.^[1] As long as the bacteria proliferate, their metabolism heat flow can be precisely recorded by IMC; therefore, in this study, we think IMC is a good method to test whether biofilm recurrence will happen after treatment. Briefly, the treated biofilms grown in 96-well plates were detached and transferred into ampoules containing 3 mL of LB media. Afterward, airtight sealed ampoules were sequentially introduced into the microcalorimetry channels and lowered to an equilibrium position for 15 min to reach a temperature of 37 °C. The heat generated in real-time by recovering bacteria within biofilm after treatment was continuously measured. Heat flow (μW) was measured at 120 s-intervals are recorded for 24 h.

Cytotoxicity. Human skin keratinocyte cell line HaCaT was chosen as model cell line to investigate the cells toxicity of the bionanocatalysts. HaCaT cells were grown in Eagle's minimal essential medium (DMEM) supplemented with 10% fetal bovine serum, 4.5 g/L glucose, 2 mM L-glutamine, 100 mg/ml streptomycin, and 100 units/ml penicillin) in a 96-well plate at 37 °C and 5% CO₂. The cytotoxicity was then measured via CCK-8 assay according to the manufacturer's instruction. Briefly, after being exposed to the bionanocatalysts for 24 h, the cells were washed twice with medium, and then 10 μL of CCK-8 solution was introduced to each well. After 3 h of incubation, the optical density at 450 nm of each well was measured by a microplate reader, and the viability was calculated by dividing the treated group's absorbance by the control group's absorbance.

***In vivo* biofilm eradication.** All animal experiments were performed humanely in compliance with guidelines reviewed by the animal ethics committee of West China Hospital (approval number:

2021024A). For *in vivo* experiments, healthy adult New Zealand white rabbits (2.5-3.0 Kg, male, Chengdu Dossy Biological Technology Co. Ltd. (China)) were used. After anesthetized with 2% sodium pentobarbital, a small wound (about 10 mm in diameter) was created on the rabbit epidermis, then 0.5 mL MRSA bacterial suspension (1×10^8 CFU/mL) was dropped onto the wound. After cultured for 1 day, activated Ni@Co-NC treatment was conducted. In brief, Ni@Co-NC suspension (1 mg/mL) was dropped onto the infected wound. Then, the wound was irradiated by a laser (2.5 W/cm^2) for 2 min to achieve antibacterial disinfection. After the near-infrared treatment, the wound was washed by saline 3 times. During the antibacterial process, photothermal images were taken by a thermal imaging camera (NEC Avio Thermo Tracer TH9100). For comparison, groups of vancomycin (16 $\mu\text{g/mL}$), H_2O_2 (100 μM), Ni@Co-NC+laser, and Ni@Co-NC+ H_2O_2 are also conducted to evaluate the *in vivo* biofilm eradication efficacy of activated Ni@Co-NC.

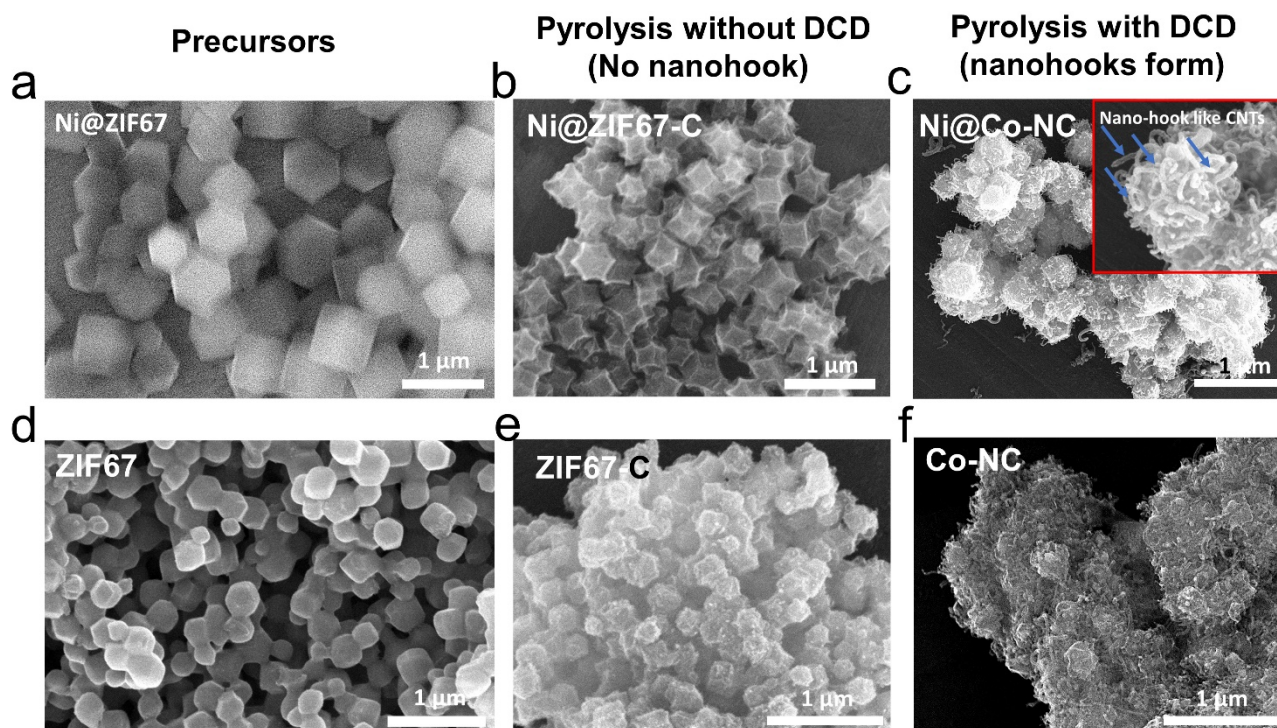


Figure S1. SEM images of precursors (a, d) and corresponding bionanocatalysts without adding DCD during pyrolysis (b, e) and with adding DCD (c, f).

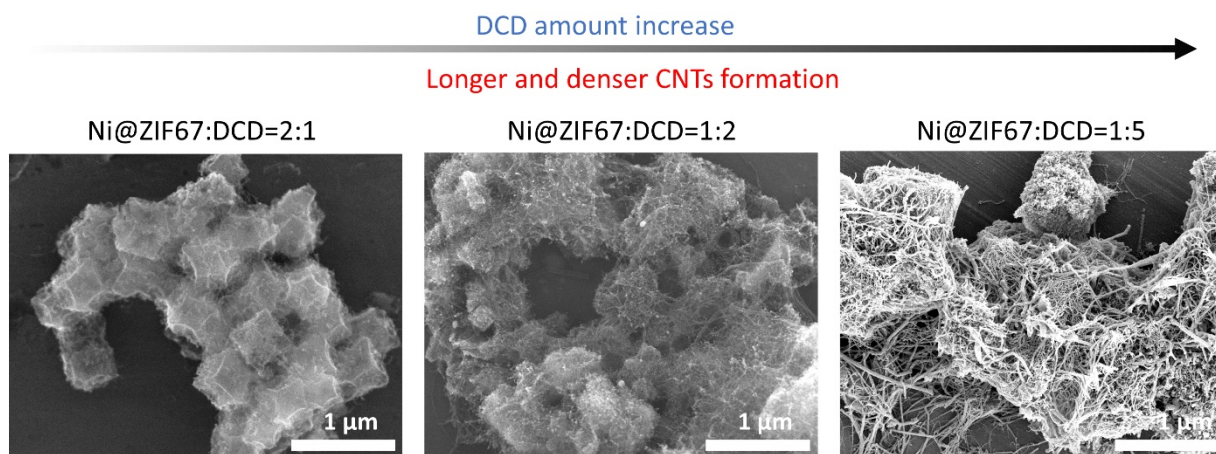


Figure S2. Morphology of Ni@Co-NC bionanocatalysts with different mass ratios of Ni@ZIF67 and DCD.

As shown in Figure S2, the nanohooks became denser with the increasing amount of DCD. It is noticed that adding too much DCD may cause the self-entanglement of bionanocatalysts; and when the DCD amount is insufficient, for example Ni@ZIF67 : DCD=2 : 1, the number of CNTs on the surface is very limited. By tuning the mass ratio of Ni@ZIF67 : DCD, it is found that the 1 : 1 mass ratio can yield the optimal nanohook structure (Figure S1c).

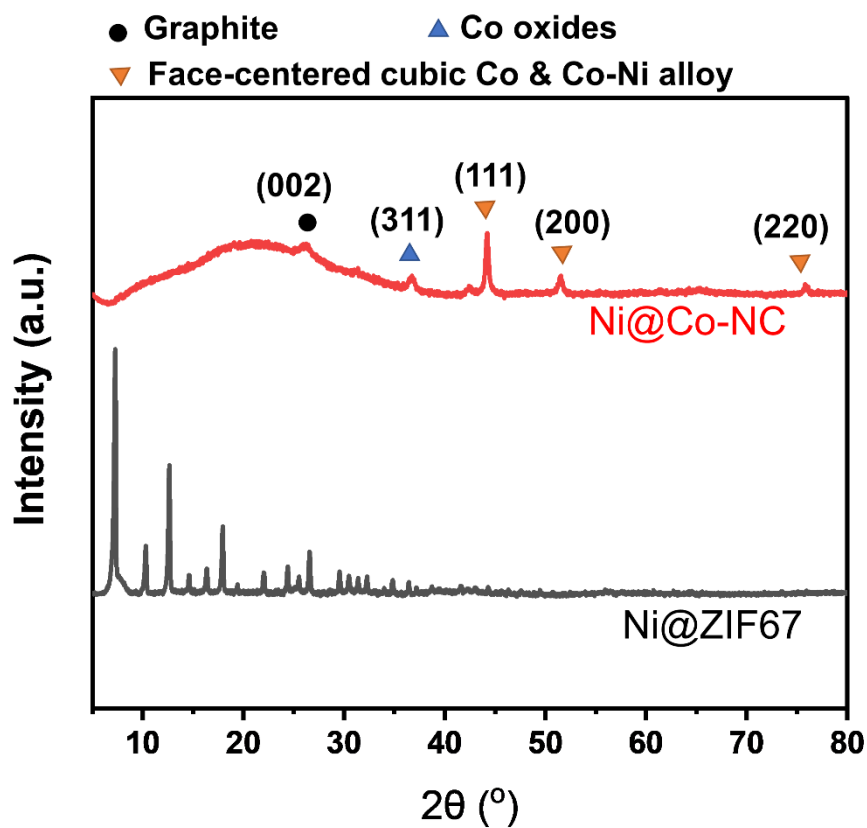


Figure S3. XRD patterns of Ni@Co-NC and its precursor (Ni@ZIF67).

Ni@ZIF67 showed the same XRD pattern as the ZIF67(CCDC code GITTOT), indicating trace amount of nickel doping did not change the crystal structure of ZIF67.

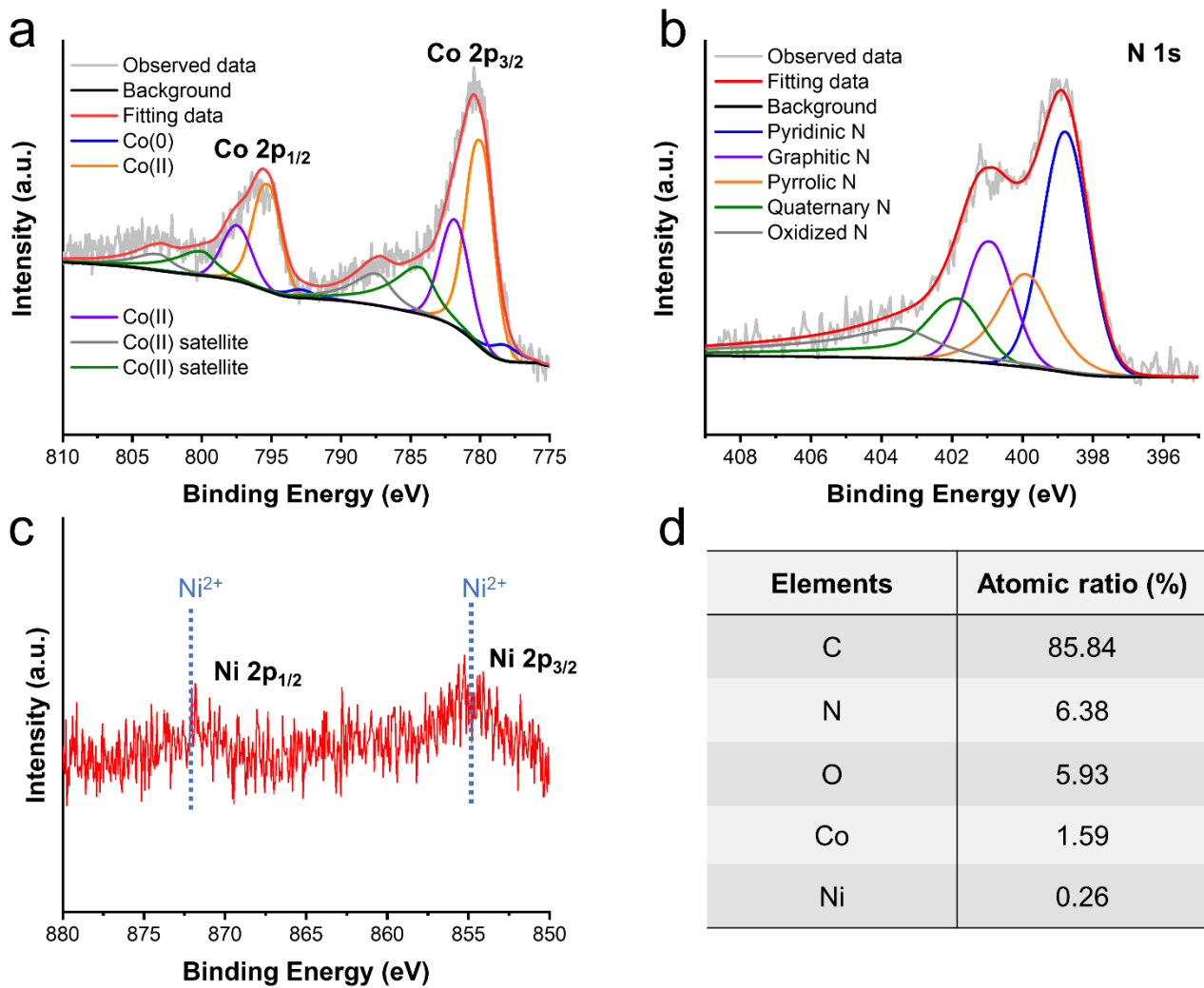


Figure S4. XPS data of Ni@Co-NC. High-resolution XPS spectra of (a) Co 2p, (b) N 1s and (c) Ni 2p. (d) The atomic ratios of C, N, O, Co, and Ni were calculated from XPS data.

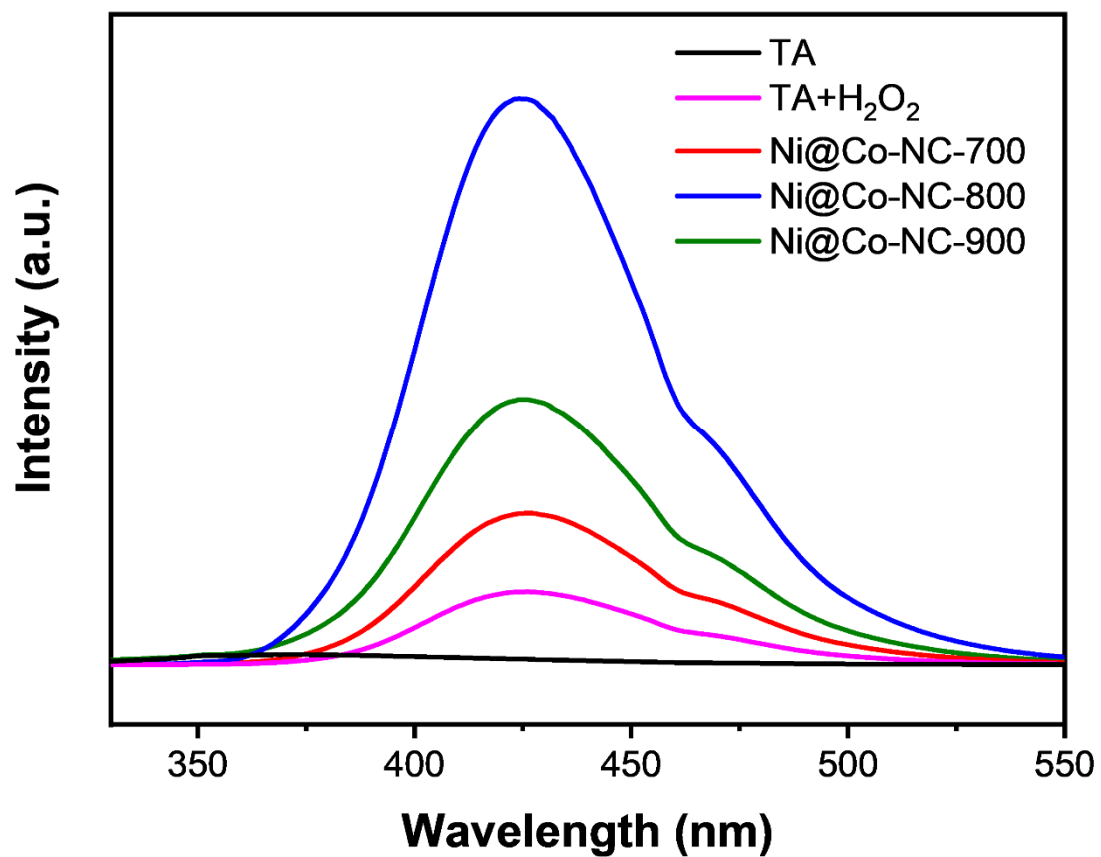


Figure S5. Catalytic $\bullet\text{OH}$ generation activities of Ni@Co-NC when pyrolyzed at 700 °C, 800 °C, and 900 °C, respectively. Unless otherwise noted, Ni@Co-NC in this article refers to Ni@Co-NC-800.

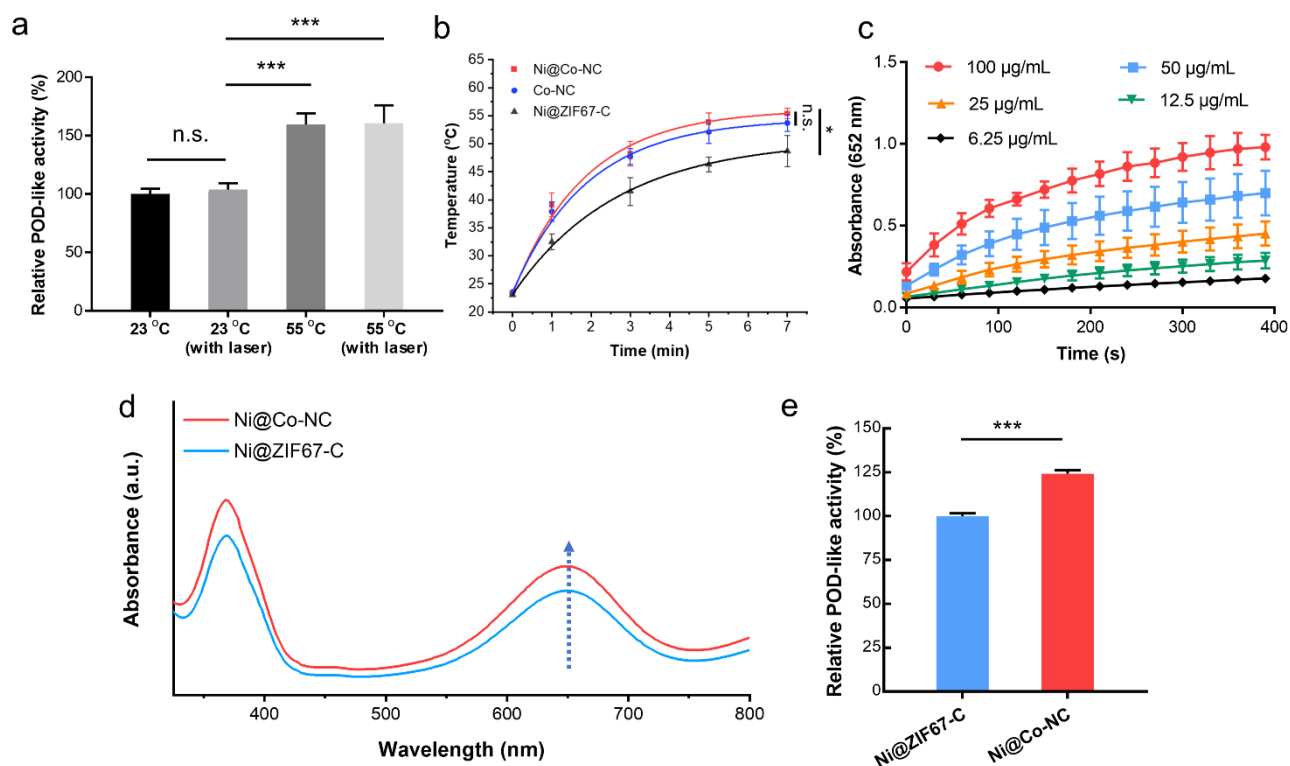


Figure S6. (a) The relative POD-like activity of Ni@Co-NC under four different conditions, from left to right: 1. room temperature (23 °C); 2. exposed to laser but in 23 °C thermostatic water bath, which allowed temperature maintained at around 23 °C over the measurement; 3. in 55 °C thermostatic water bath; and 4. heated up to 55 °C by laser. The relative POD-like activity was calculated by the absorbance at 652 nm using TMB as substrate. (b) Photothermal heating profiles of Ni@Co-NC, Co-NC, and Ni@ZIF67-C exposed to NIR laser at a power density of 1 W/cm². (c) Dose-dependent POD-like activity of Ni@Co-NC. (d) POD-like activity and (e) relative POD-like activity calculated from UV-vis spectra at the absorbance of 652 nm of Ni@Co-NC and Ni@ZIF67-C. All experimental data are displayed as the average values (mean ± SD, n = 3). Asterisks indicate significant differences (*P < 0.1, **P < 0.01, ***P < 0.001), and n.s. indicates a non-significant difference.

Discussion of photothermal ability: the photothermal property of Ni@Co-NC originates from its abundant sp²-carbon structures. Just like sp²-carbons in CNTs and graphene, such structures can absorb and convert the near-infrared (NIR) light to heat, also named as photothermal agents.^[3-6] Therefore, we have calculated the surface sp²-carbon contents of Ni@Co-NC, Co-NC, and Ni@ZIF67-C from the XPS C1s data. Due to the covering of sp²-carbon-riched CNT nanohooks, both the Ni@Co-NC and Co-NC showed higher sp²-carbon contents than Ni@ZIF67-C (Figures S7a and S7c). From the

photothermal heating curves, we found that Co-NC exhibited comparable photothermal conversion ability with Ni@Co-NC, whereas the Ni@ZIF67-C showed relatively weak heating ability (Figure S6b). Therefore, by introducing more sp^2 -carbons on the surface, these nanohooks enhanced the photothermal ability of bionanocatalysts.

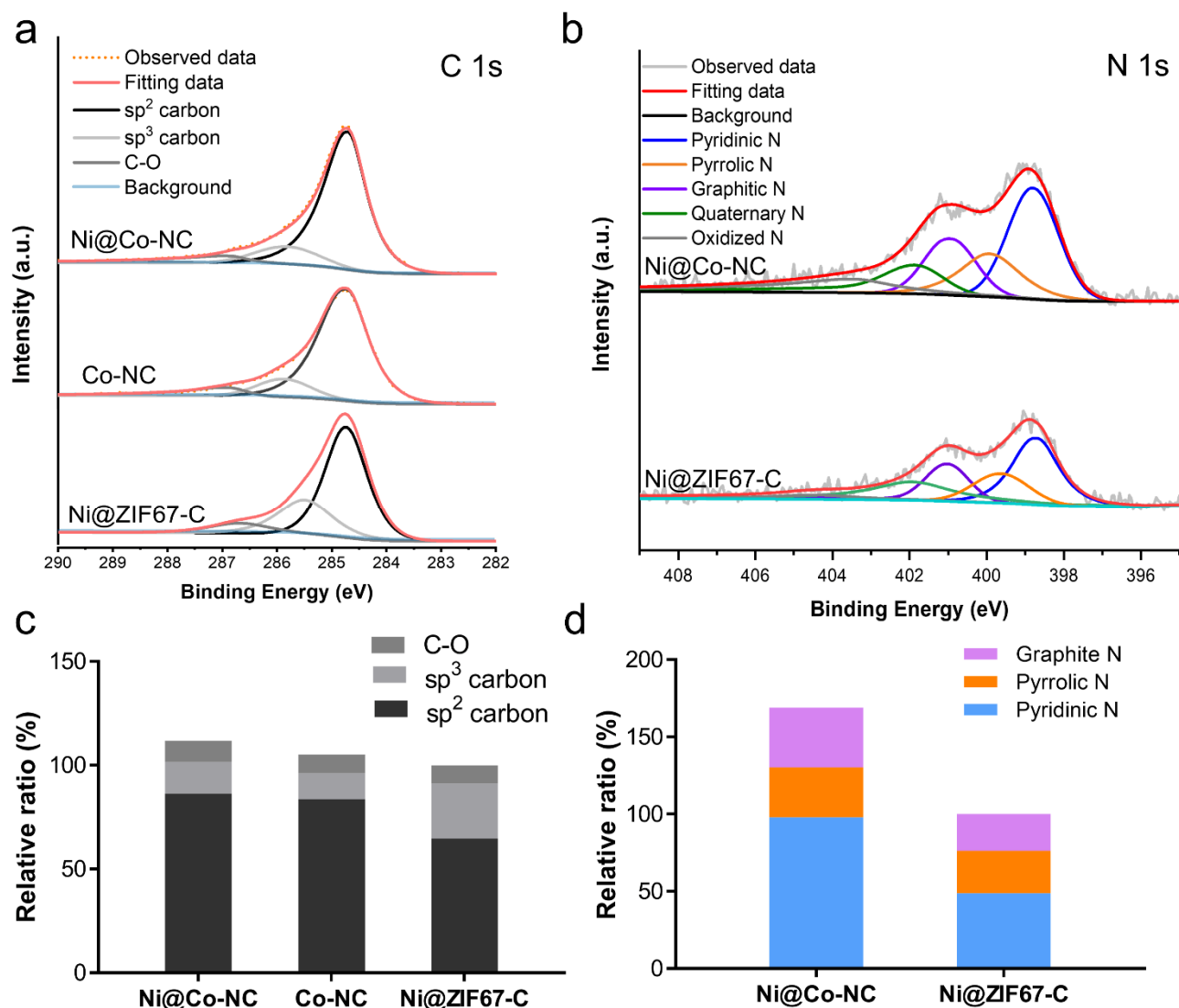


Figure S7. High-resolution XPS (a) C1s and (b) N1s data and corresponding (c) carbon contents and (d) nitrogen contents in Ni@Co-NC and the comparison samples.

Discussion of catalytic ability: we found that after anchoring with nanohooks, the relative peroxidase-like activity of bionanocatalysts slightly increased for about 25% (Figures S6d and S6e). Furthermore, the total superficial nitrogen amount increased significantly after anchoring nanohooks from XPS high-resolution N1s data. Especially, the pyridinic N contents of Ni@Co-NC increased to around twice that of Ni@ZIF67-C (Figures S7b and S7d), indicating the nanohooks enriched metal- N_x and N-doped carbon sites of bionanocatalysts, which can also be demonstrated from STEM-based elemental line scanning (Figure 1f). Previous studies have revealed that the N-doped carbons and metal- N_x sites had good POD-like activity,^[7-8] therefore, we speculate that the nanohooks structures can enhance POD-like catalytic activity by enriching the superficial N-doped carbons and metal- N_x sites of bionanocatalysts.

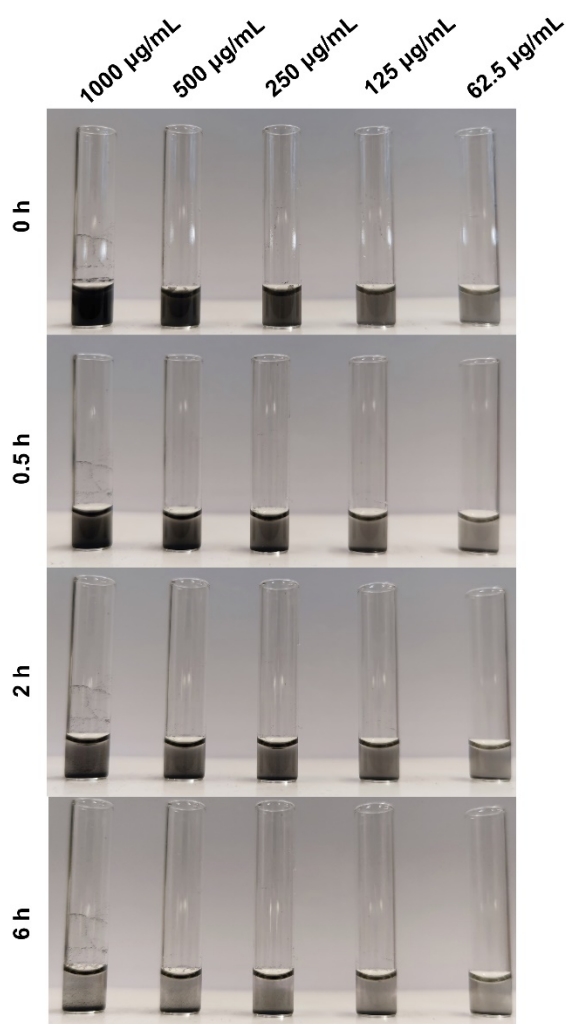


Figure S8. Photographs of Ni@Co-NC with different concentrations and precipitation times in PBS.

We found that 62.5 µg/mL of Ni@Co-NC showed good stability over 6 h, and it can still be stable for 2 h at a concentration of 125 µg/mL. While when the concentration increased to more than 250 µg/mL, the Ni@Co-NC precipitated much faster.

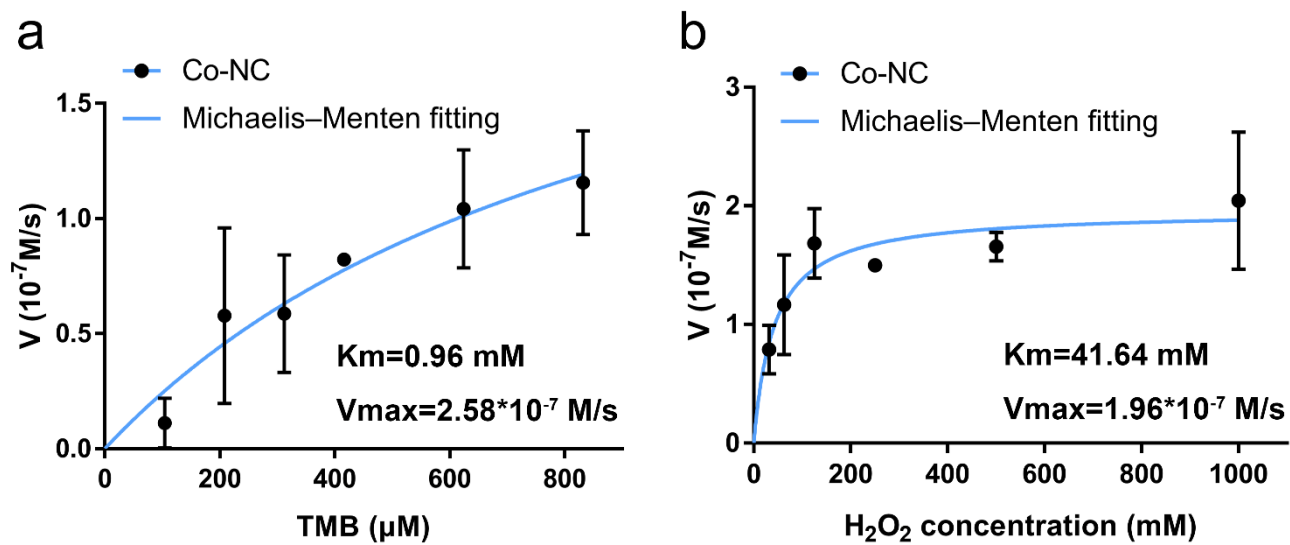


Figure S9. Steady-state kinetic assay of Co-NC for g) TMB and h) H_2O_2 .

Table S1. Comparison of the kinetic parameters of Ni@Co-NC, Co-NC, and HRP.

Catalysts	Substrates	K_m/mM	$V_{\text{max}}/(\text{M/s})$
Ni@Co-NC	H ₂ O ₂	26.45	2.34×10^{-7}
	TMB	1.163	5.10×10^{-7}
Co-NC	H ₂ O ₂	41.64	1.96×10^{-7}
	TMB	0.96	2.58×10^{-7}
HRP	H ₂ O ₂	3.7	8.71×10^{-8}
	TMB	0.434	1.00×10^{-7}

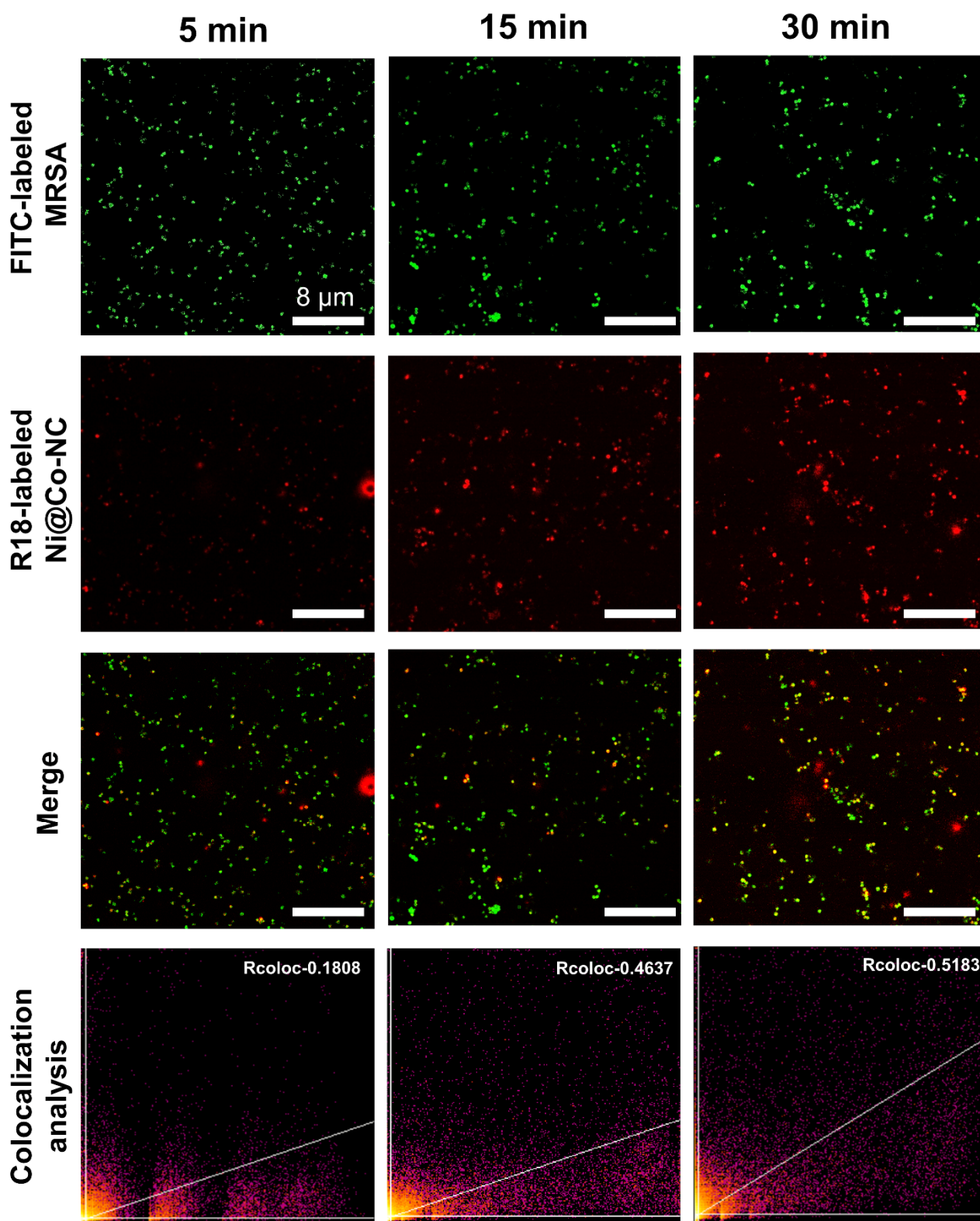


Figure S10. CLSM images and corresponding colocalization analysis of FITC-labeled MRSA were in-situ recorded after 5, 15, and 30 min of incubation with R18-labeled Ni@Co-NC.

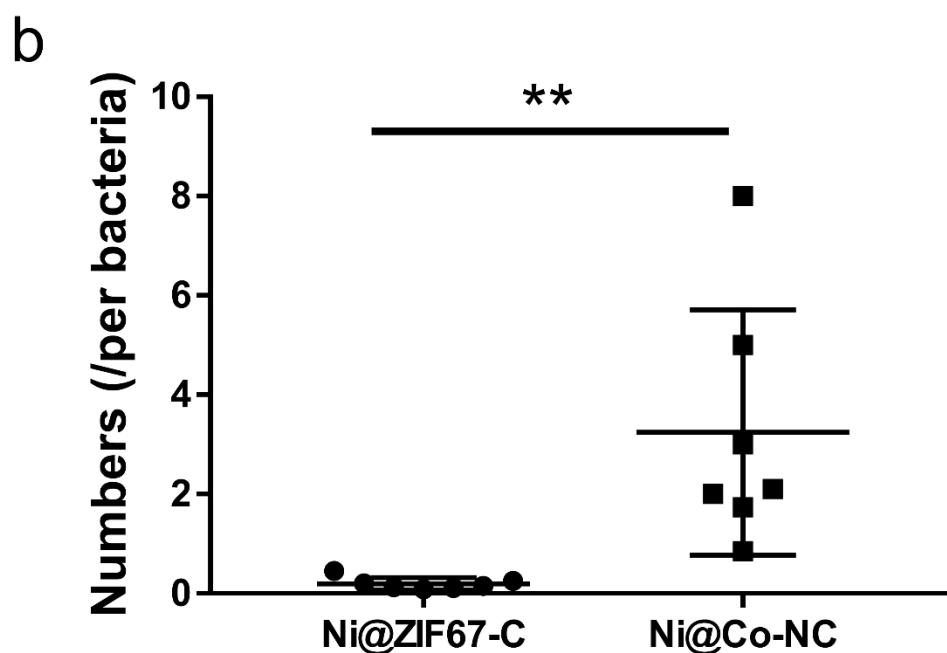
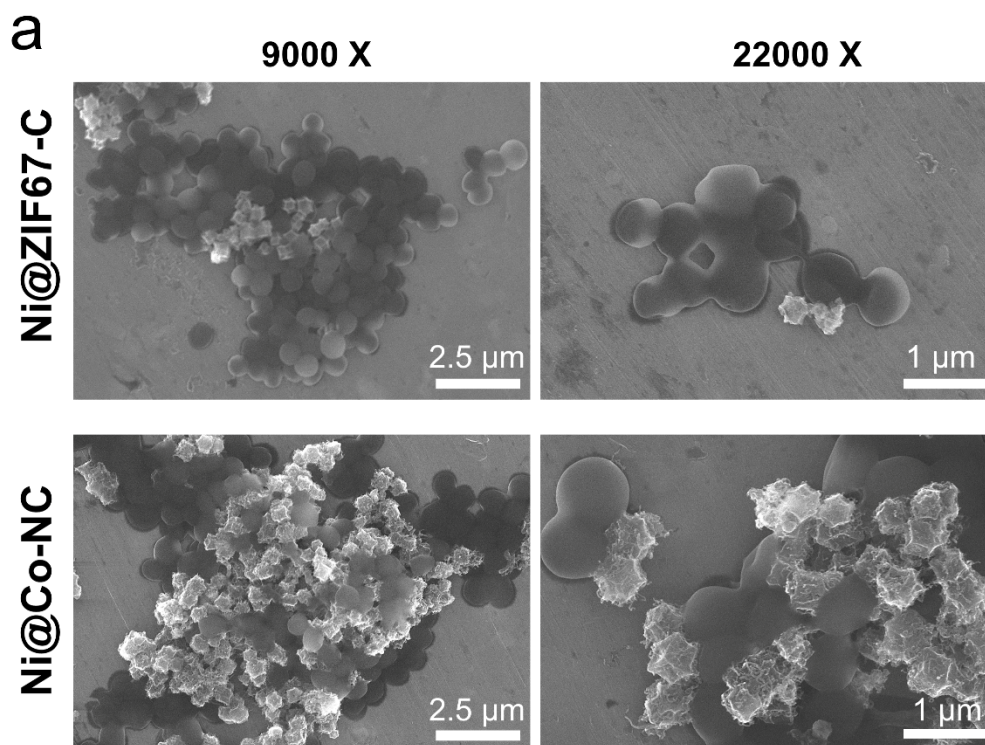


Figure S11. (a) SEM images of MRSA after treatment with an identical concentration of Ni@ZIF67-C and Ni@Co-NC for 30 min. The uncoupled bionanocatalysts were removed by centrifugation at 3000 rpm three times. (b) Numbers of bionanocatalysts that bind with bacteria, which were estimated from 7 SEM images. All experimental data are displayed as the average values (mean \pm SD, $n = 7$). Asterisks indicate significant differences (* $P < 0.1$, ** $P < 0.01$, *** $P < 0.001$).

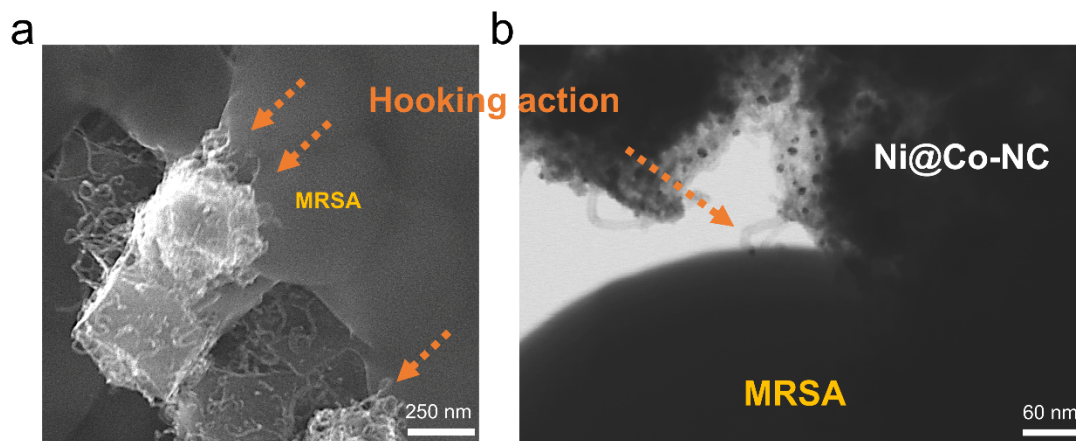


Figure S12. Close-up (a) SEM and (b) TEM images that reveal the hooking action imposed by Ni@Co-NC.

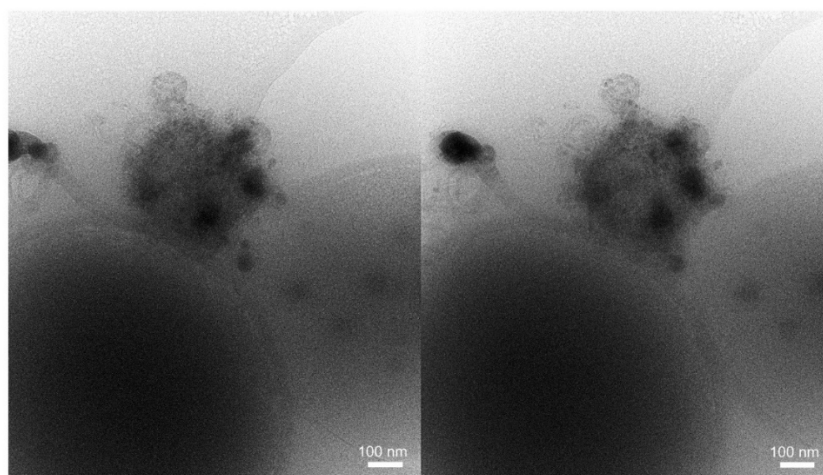


Figure S13. Cryo-TEM image of MRSA after incubated with Ni@Co-NC for 30 min.

In order to prove the direct binding of the Ni@Co-NC to the bacteria, which is difficult to determine from individual projection images alone, side-by-side stereograms (stereo pairs of cryo-TEM at 8° view angle) were recorded. Scale bar: 100 nm.

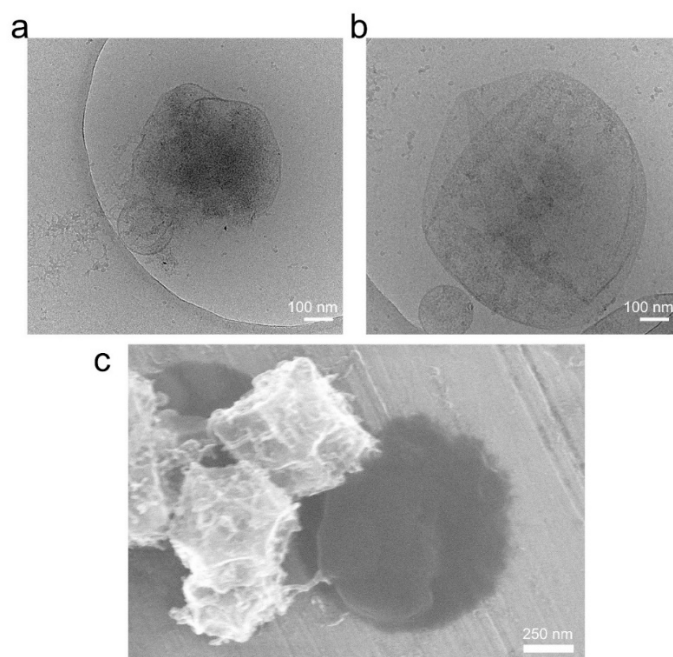


Figure S14. Cryo-TEM images of the Ni@Co-NC-treated MRSA with (a) severe membrane disruption and (b) significant cytoplasm leakage. Scale bar: 100 nm. (c) SEM images of MRSA-treated by Ni@Co-NC. Scale bar: 250 nm.

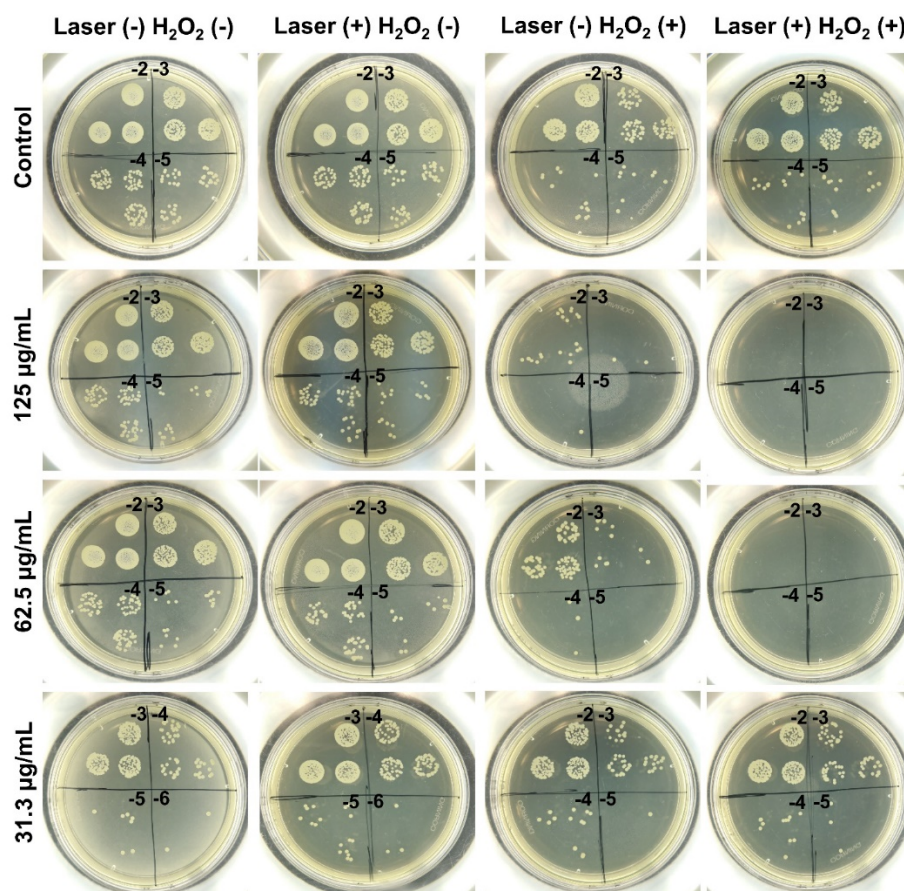


Figure S15. Typical agar plate photos of MRSA after treatment with Ni@Co-NC at pH 5.5 under different concentrations and activation conditions. -2, -3, -4, -5, and -6 represent 100, 1000, 10000, 100000, and 1000000 times, respectively, of dilution for bionanocatalysts-bacterial solution before performing plate count method.

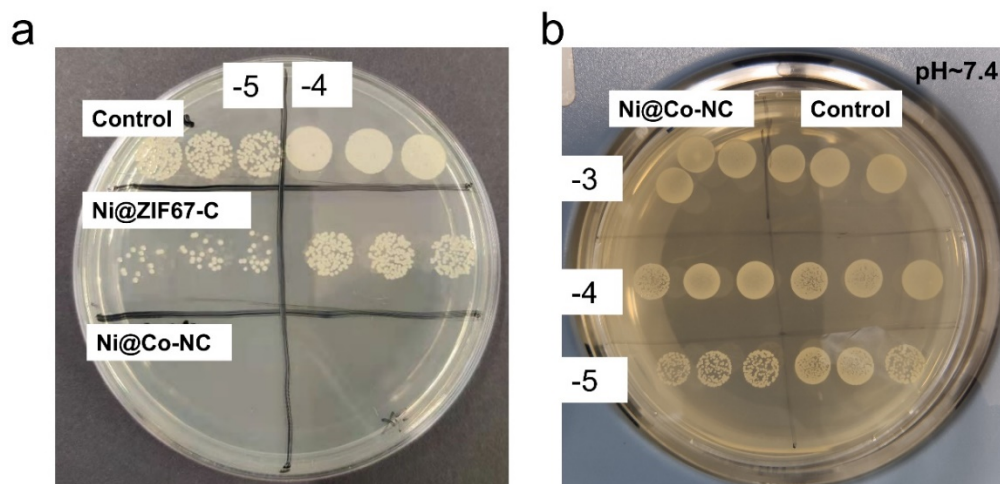
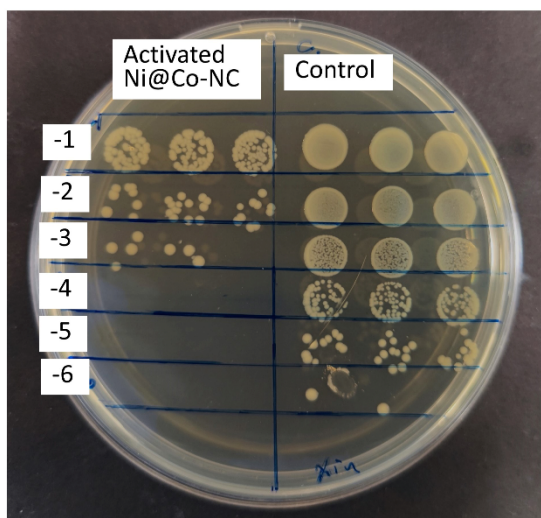


Figure S16. Typical agar plate photo of MRSA before-and-after treatment of (a) Ni@ZIF67-C and Ni@Co-NC at pH 5.5 and (b) Ni@Co-NC at pH 7.4. -3, -4, and -5 represent 1000, 10000, 100000 times, respectively, of dilution for the bionanocatalysts-bacterial solution before performing the plate count method.

a



b

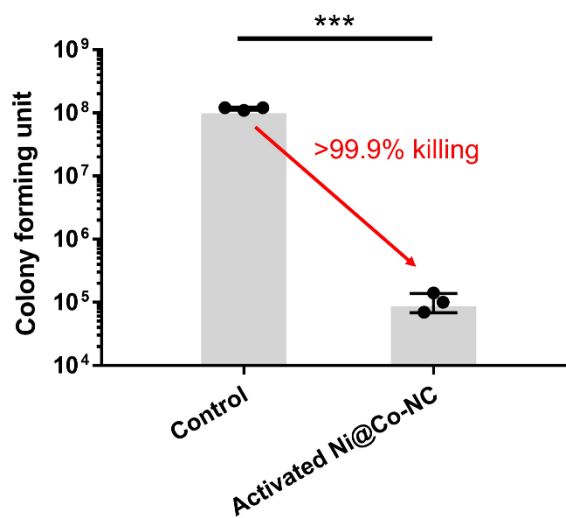


Figure S17. Colony-forming unit of extended-spectrum β -lactamase-producing *Escherichia coli* before-and-after treatment with activated Ni@Co-NC.

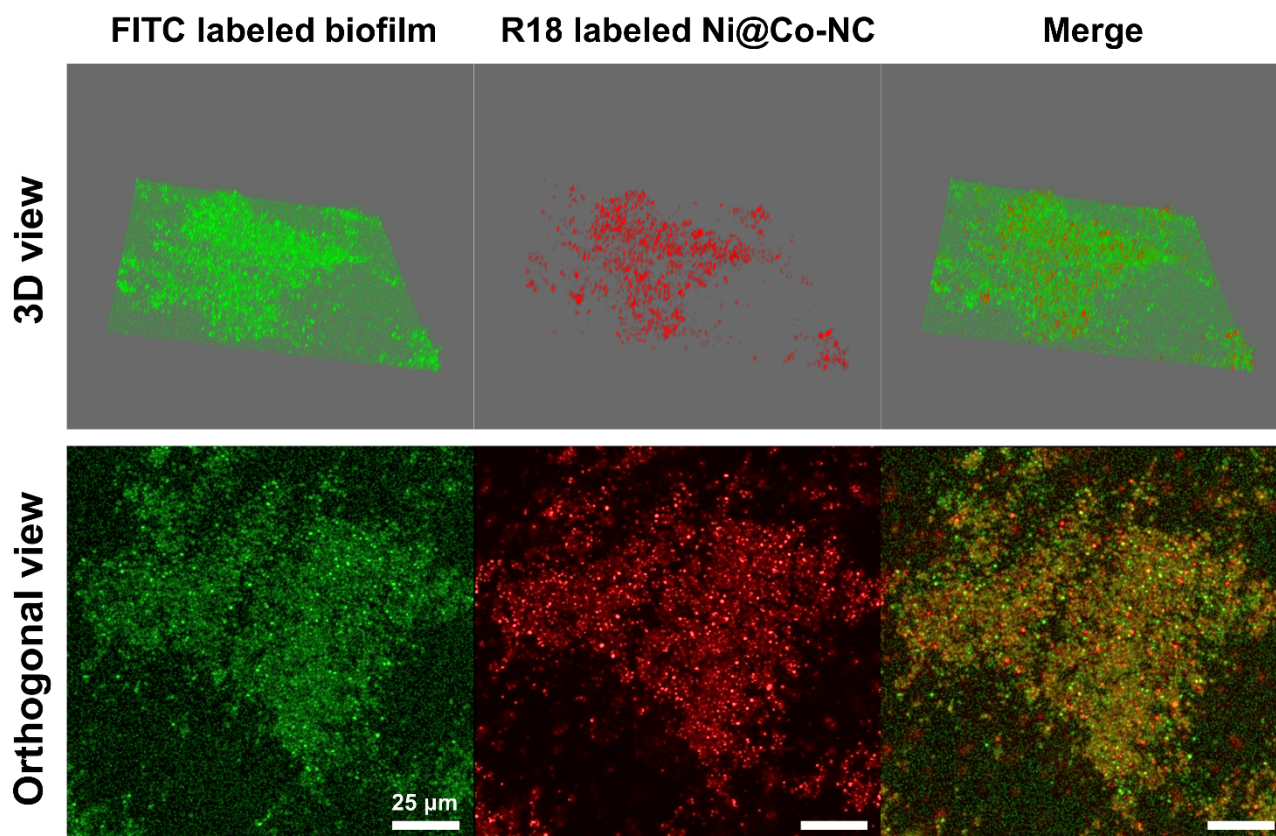


Figure S18. 3D confocal images and corresponding orthogonal views of FITC-labeled MRSA biofilm after treatment with R18-labeled Ni@Co-NC for 30 min.

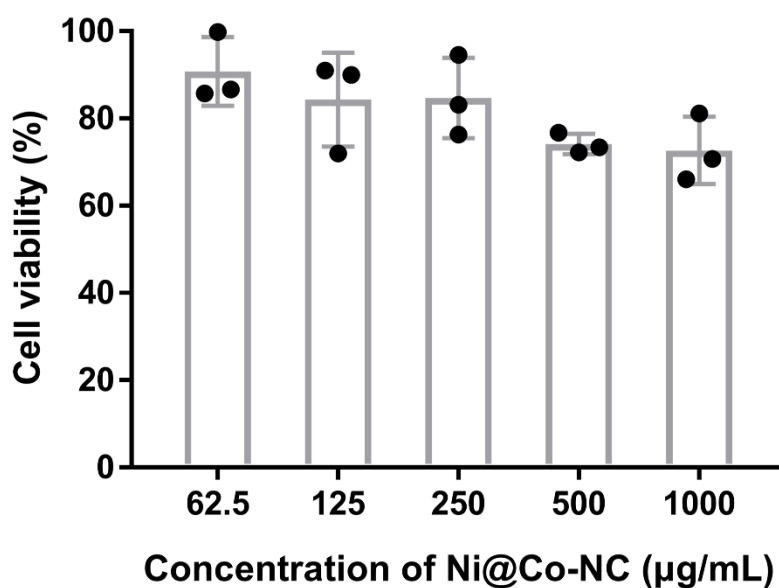


Figure S19. CCK-8 assay for HaCaT cells incubated with different concentrations of Ni@Co-NC.

The potential reason for causing slight cytotoxicity: the nanohook-equipped bionanocatalysts might cause slight cytotoxicity because the nanohooks structure can also bind to cells by hydrophobic interaction, thus resulting in slight physical damage towards cells. While it is worth mentioning that this toxicity was not permanent as demonstrated in animal experiments, and the cells will soon regrow after disinfection. Therefore, we think this slight cytotoxicity was acceptable in the practical wound infection treatment.

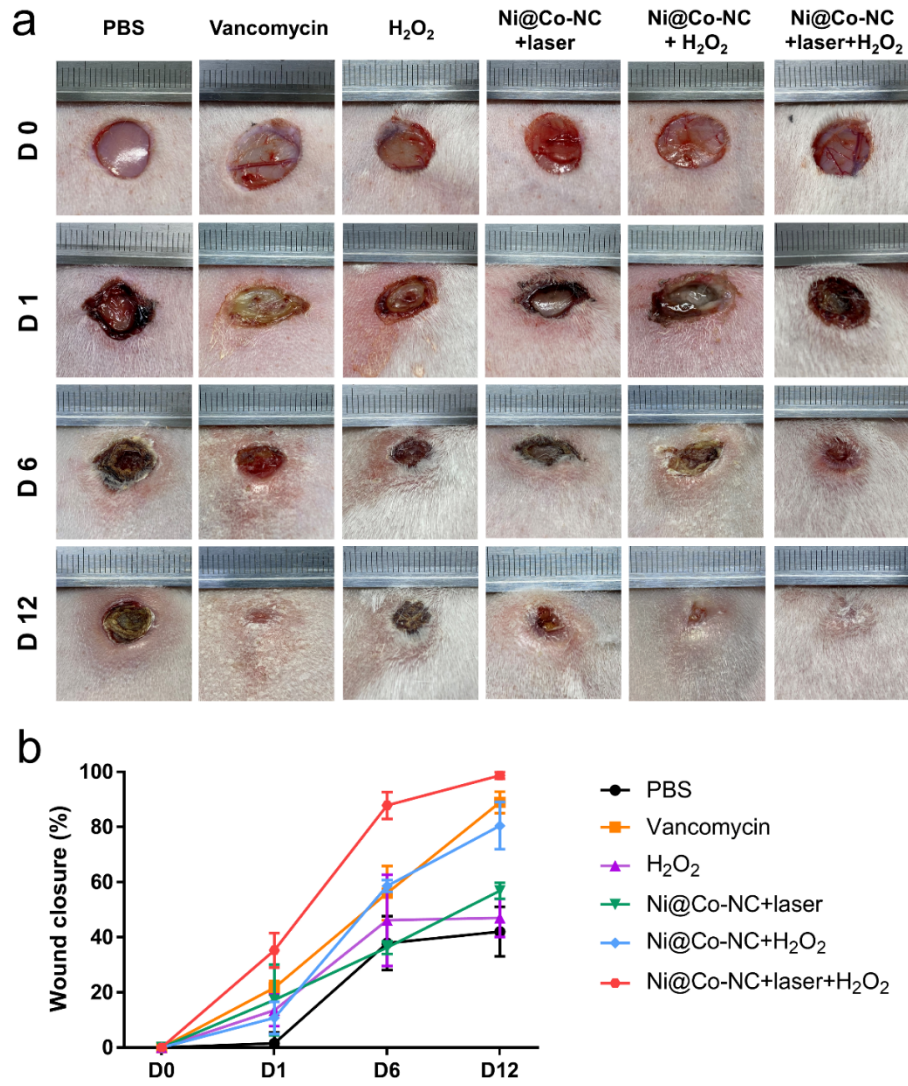


Figure S20. (a) Representative photos of wounds after different treatments at day 0, day 1, day 6, and day 12. (b) Wound closure after different treatments.

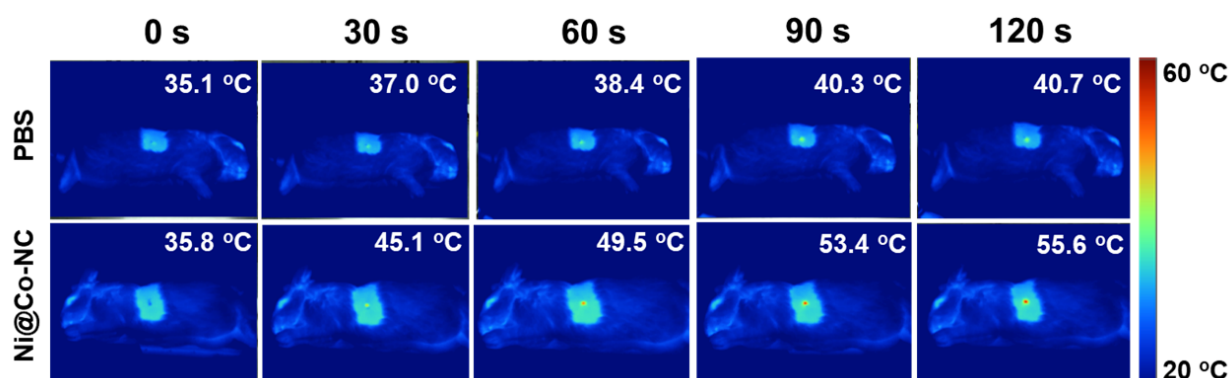


Figure S21. *In vivo* NIR-triggered heating images of wounds treated by Ni@Co-NC and PBS.

The photothermal treatment condition for in vivo experiments: according to the previous study, human skin burns partially at 55 °C when exposure time up to 70 seconds, but below this range, might only feel discomfort.^[2] From previous animal studies with photothermal treatment (around or even above 55 °C) as well as our animal study presented in this article, no lesion of the burn was noticed from histological analysis after treatment, indicating this 55 °C local heat will not lead to irreversible damage towards skin tissues.^[3-5]

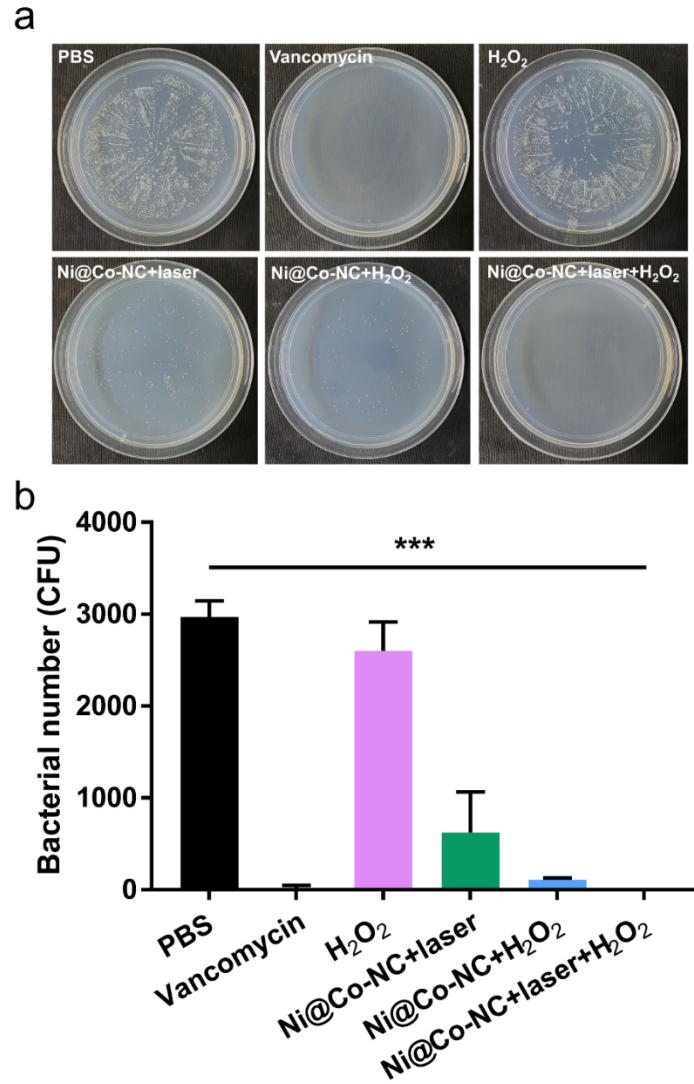


Figure S22. (a) Agar plates of MRSA that taken in the wound after different treatments on day 1. (b) Corresponding MRSA colony counted from the agar plates. The asterisks indicate significant differences (P values: *P < 0.05, **P < 0.01, ***P < 0.001). Values are expressed as mean \pm SD, n = 3.

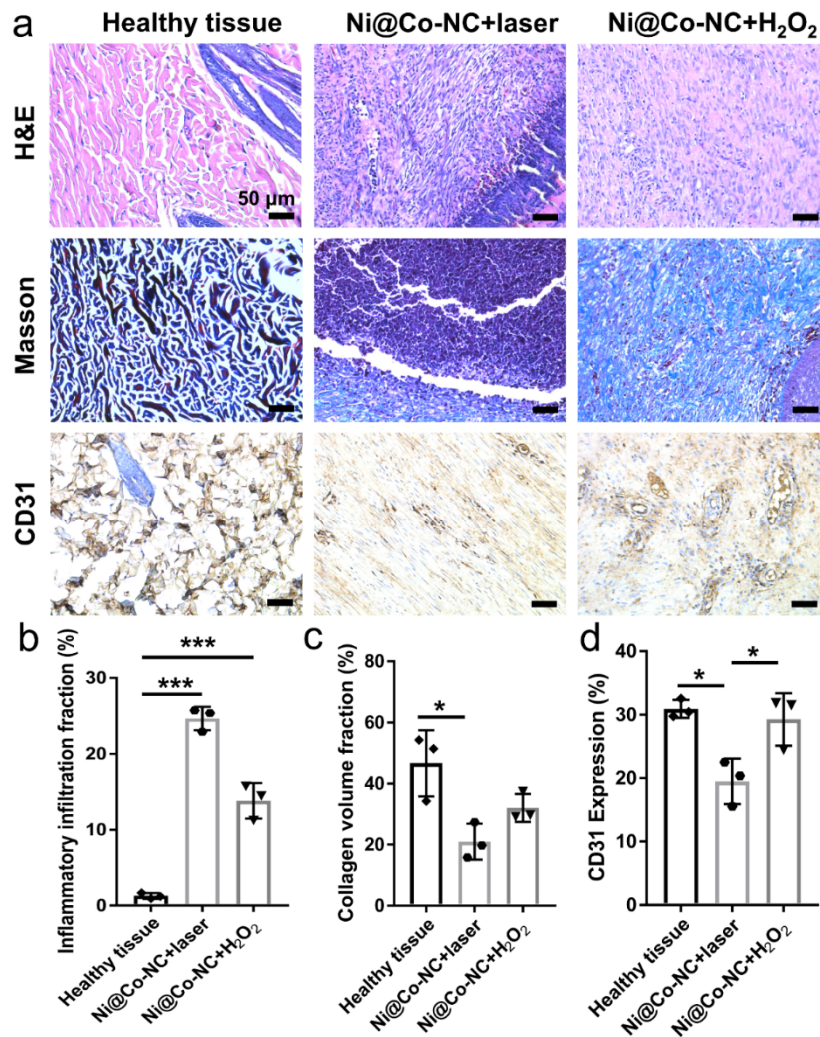


Figure S23. (a) Histologic analysis of the healthy tissues and wounds treated by Ni@Co-NC+laser and Ni@Co-NC+H₂O₂. In this experiment, H&E, Masson, and CD31 staining were used to study inflammation response, collagen deposition, and revascularization in the wound area, respectively. (b) Inflammatory infiltration fraction, (f) collagen volume fraction, and (g) CD31 expression of healthy tissue and wounds treated by Ni@Co-NC+laser and Ni@Co-NC+H₂O₂. Asterisks indicate significant differences (*P<0.1, **P < 0.01, ***P < 0.001). All data are acquired from the rabbits' wound tissues in different groups after 12 days' post-treatment. All values are expressed as mean ± SD, n = 3.

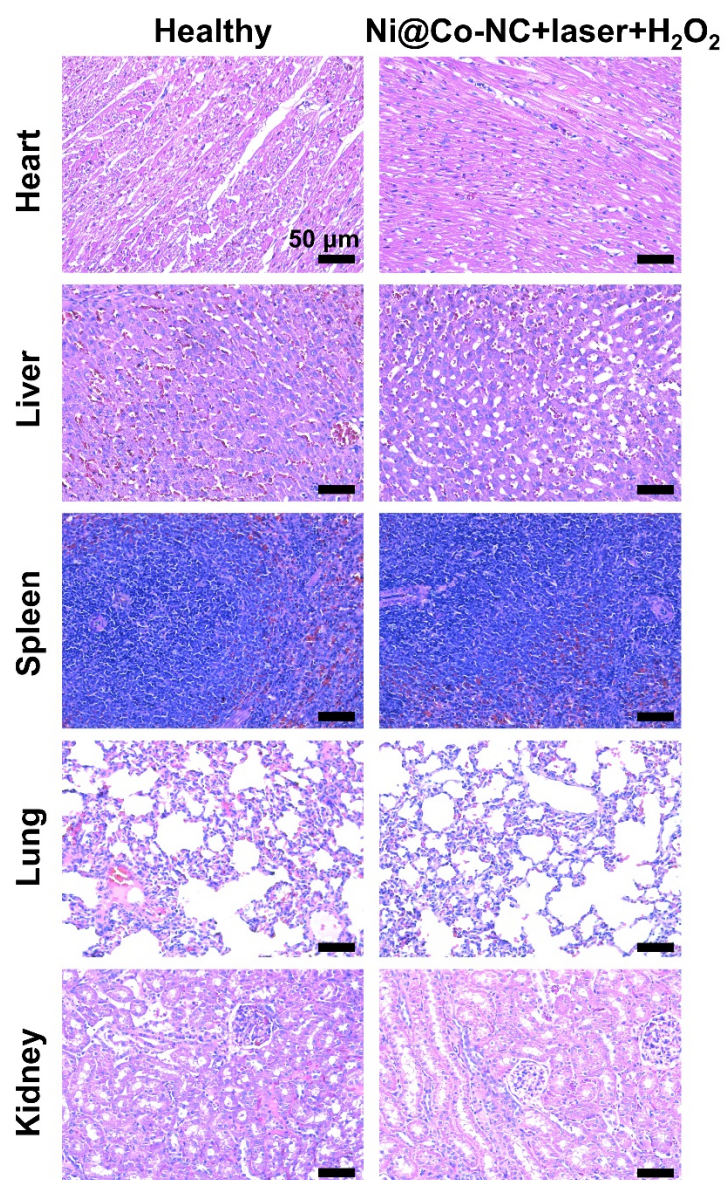


Figure S24. H&E staining of the major organs includes the heart, liver, spleen, lung, and kidney of healthy rabbits and rabbits after treatment of activated Ni@Co-NC.

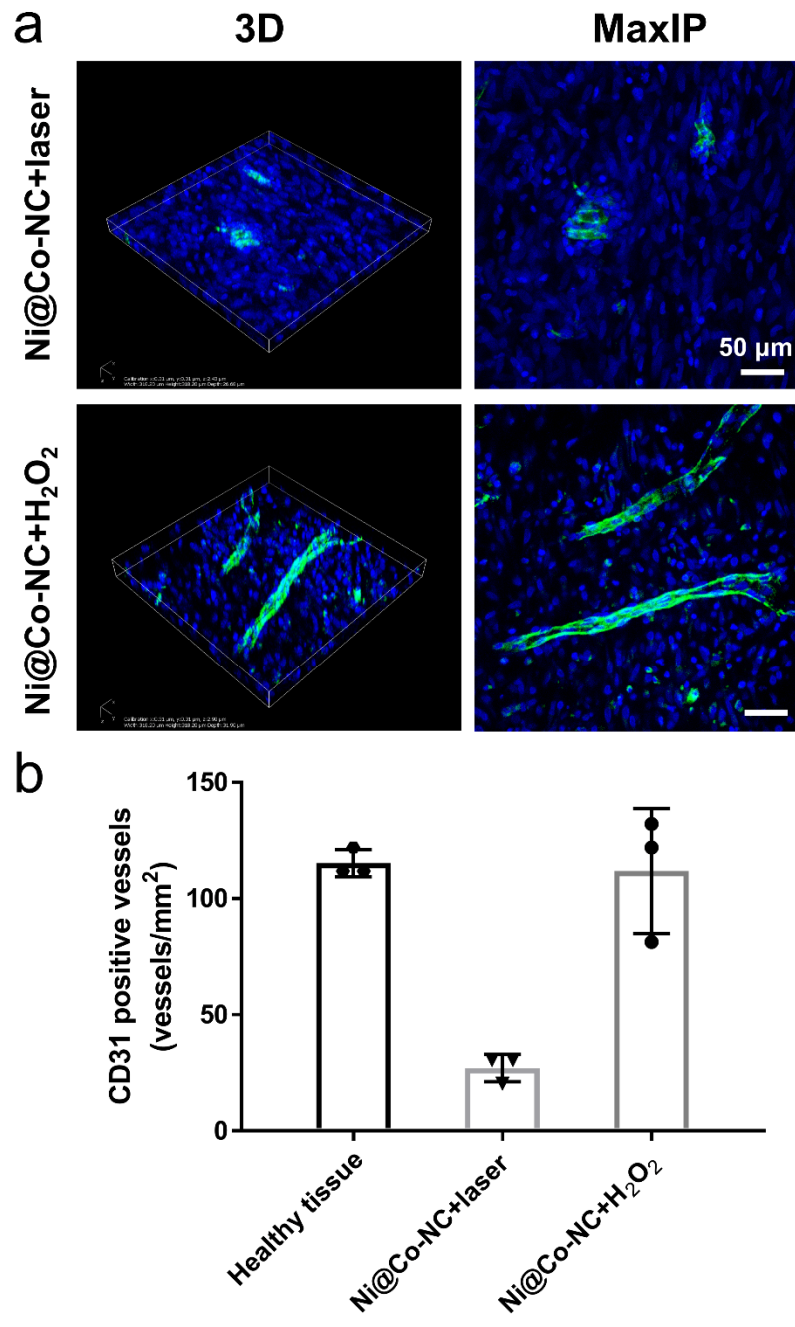
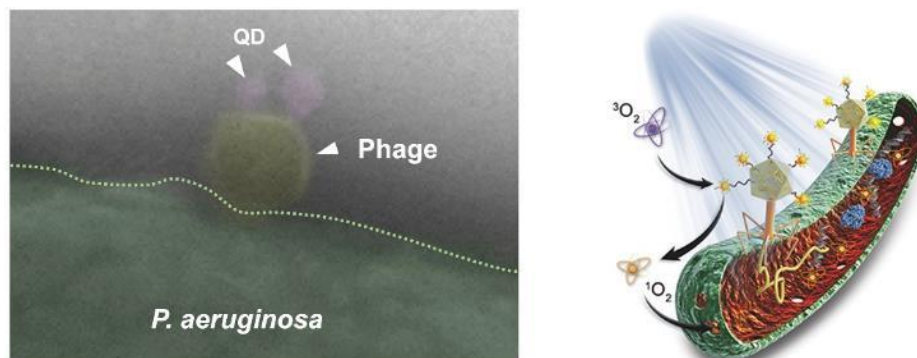


Figure S25. (a) CD31/DAPI staining images of 3D reconstruction and corresponding maximum intensity projection (MaxIP) for wounds treated by Ni@Co-NC + laser and Ni@Co-NC+H₂O₂. (b) CD31 positive vessels number of healthy tissue, Ni@Co-NC + laser and Ni@Co-NC + H₂O₂ treated wounds.

References

- [1] M. Clauss, A. Trampuz, O. Borens, M. Bohner, T. Ilchmann, *Acta biomaterialia* **2010**, *6*, 3791-3797.
- [2] J. Lawrence, J. Bull, *Engineering in medicine* **1976**, *5*, 61-63.
- [3] J. Ouyang, X. Ji, X. Zhang, C. Feng, Z. Tang, N. Kong, A. Xie, J. Wang, X. Sui, L. Deng, *Proceedings of the National Academy of Sciences* **2020**, *117*, 28667-28677.
- [4] Z. Tu, H. Qiao, Y. Yan, G. Guday, W. Chen, M. Adeli, R. Haag, *Angewandte Chemie* **2018**, *130*, 11368-11372.
- [5] M. Huo, L. Wang, Y. Wang, Y. Chen, J. Shi, *ACS nano* **2019**, *13*, 2643-2653.

3.2. Photocatalytic quantum dot-armed bacteriophage for combating drug-resistant bacterial infection



Lei Wang¹, **Xin Fan**^{1*}, Mercedes Gonzalez Moreno, Tamta Tkhilaishvili, Weijie Du, Xianlong Zhang, Chuanxiong Nie, Andrej Trampuz*, and Rainer Haag*.

¹These authors contributed equally to the work.

Adv. Sci. 2022, 9, 2105668

DOI: <https://doi.org/10.1002/advs.202105668>

This is an open access article under the terms of the [Creative Commons Attribution License](#).

Author contributions:

Lei Wang and **Xin Fan** performed the main experiments, and wrote the manuscript. Mercedes Gonzalez Moreno revised and edited the manuscript. Tamta Tkhilaishvili provided the bacteriophages and protocol of bacteriophage proliferation and purification. Weijie Du conducted the cytotoxicity experiments. Xianlong Zhang provided the lab and mice for animal experiments. Chuanxiong Nie, Xin Fan and Rainer Haag conceived the project. Andrej Trampuz provided the lab and drug-resistant bacterial strains for supporting the *in-vitro* antibacterial studies. Xin Fan, Andrej Trampuz and Rainer Haag supervised the project.

Photocatalytic Quantum Dot-Armed Bacteriophage for Combating Drug-Resistant Bacterial Infection

Lei Wang, Xin Fan,* Mercedes Gonzalez Moreno, Tamta Tkhilaishvili, Weijie Du, Xianlong Zhang, Chuanxiong Nie, Andrej Trampuz,* and Rainer Haag*

Multidrug-resistant (MDR) bacterial infection is one of the greatest challenges to public health, a crisis demanding the next generation of highly effective antibacterial agents to specifically target MDR bacteria. Herein, a novel photocatalytic quantum dot (QD)-armed bacteriophage (QD@Phage) is reported for combating green fluorescent protein-expressing *Pseudomonas aeruginosa* (GFP-*P. aeruginosa*) infection. The proposed QD@Phage nanosystem not only specifically binds to the host GFP-*P. aeruginosa* while preserving the infectivity of the phage itself, but also shows a superior capacity for synergistic bacterial killing by phage and by the photocatalytic localized reactive oxygen species (ROS) generated from anchored QD components. Notably, this highly targeted QD@Phage nanosystem achieves robust in vitro antibacterial elimination for both planktonic (over 99.9%) and biofilm (over 99%) modes of growth. In a mouse wound infection model, this system also shows remarkable activity in eliminating the wound infection and promoting its recovery. These results demonstrate that the novel QD@Phage nanosystem can diversify the existing pool of antibacterial agents and inspire the development of promising therapeutic strategies against MDR bacterial infection.

infections will kill over 10 million people annually by 2050 due to the shortage of active antibiotics.^[2] MDR *Pseudomonas aeruginosa* (*P. aeruginosa*) infections are of particular concern because they often result in chronic wounds and are the leading causes of hospitalizations, disabilities, and deaths worldwide. This growing health crisis is mainly caused by the frequent misuse and overuse of antibiotics, especially broad-spectrum antibiotics, which lack specific bacterial targeting ability. On top of that, the formation of biofilm, which is complex clusters of bacteria, merged by extracellular polymeric substances (EPS), results in a further increase in bacterial tolerance to antibiotics by three orders of magnitude.^[3] In contrast, the development of new drugs is rather slow, with only a few new antibiotics approved to treat “superbugs” in the past several decades.^[4] Therefore, it is of critical necessity to develop alternative antibacterial therapeutic approaches to control MDR bacterial infections.

1. Introduction

The rapid emergence of multidrug-resistant (MDR) bacteria, also known as “superbugs,” is endangering the efficacy of antibiotic therapy,^[1] and it is predicted that MDR bacterial

As a natural predator of bacteria, bacteriophages (phages), offer hope as a promising alternative treatment for MDR bacteria since they show a different bactericidal mechanism than antibiotics.^[5] Upon infecting host bacteria, the phages hijack the bacterial machinery to produce their progenies,^[6] which

L. Wang, M. Gonzalez Moreno, T. Tkhilaishvili, A. Trampuz
Centre for Musculoskeletal Surgery
Charité – Universitätsmedizin Berlin
Corporate Member of Freie Universität Berlin
Humboldt-Universität zu Berlin
and Berlin Institute of Health
Berlin 10117, Germany
E-mail: andrej.trampuz@charite.de

L. Wang, X. Fan, M. Gonzalez Moreno, W. Du, C. Nie, A. Trampuz
BIH Center for Regenerative Therapies (BCRT)
Berlin Institute of Health (BIH)
Berlin 13353, Germany
E-mail: xinf94@zedat.fu-berlin.de

X. Fan, R. Haag
Department of Chemistry and Biochemistry
Freie Universität Berlin
Takustraße 3, Berlin 14195, Germany
E-mail: haag@zedat.fu-berlin.de

T. Tkhilaishvili
Department of Tropical Medicine and Infectious Diseases
University of Rostock
Rostock 18057, Germany

X. Zhang
Department of Orthopedics
Shanghai Sixth People's Hospital
Shanghai Jiao Tong University
Shanghai 200233, China

 The ORCID identification number(s) for the author(s) of this article can be found under <https://doi.org/10.1002/advs.202105668>

© 2022 The Authors. Advanced Science published by Wiley-VCH GmbH. This is an open access article under the terms of the Creative Commons Attribution License, which permits use, distribution and reproduction in any medium, provided the original work is properly cited.

DOI: 10.1002/advs.202105668

eventually induce bacterial lysis and infect adjacent bacteria. In the biofilm, some phages encoding EPS-degrading enzymes might be particularly useful against biofilms. A diverse group of phage-encoded enzymes, called depolymerases, capable of degrading EPS involved in the biofilm matrix in order to promote phage diffusion through the biofilm has been described,^[7] ultimately causing great damage to the biofilm. Furthermore, thanks to their high host specificity, phages do not affect the skin microflora.^[8] However, due to their high mutative tendency, host bacteria can develop resistance against phages, subverting their bactericidal action.^[9] Therefore, it is difficult for mono-phage therapy to achieve bacterial eradication.^[10] Different strategies have been studied to improve successful treatments, especially against biofilm infections, such as combination with antibiotics.^[7] Nowadays, new concepts are emerging in the design of phage-based treatments to maximize the therapeutic efficacy of phage, where phage functionalization might have a great potential.

Nanomaterials have been developed as alternatives to antibiotics in fighting bacterial infections. A range of nanomaterials has attracted interest as photosensitizers that can offer antimicrobial behavior for photocatalytic therapy (PCT).^[11] Especially, quantum dots (QDs) have received extensive attention as a photosensitizer for PCT,^[12] owing to their advantages of ultra-small size (5–25 nm) for loading into multifunctional systems, high photocatalytic efficiency for bacterial elimination,^[13] and inherent fluorescence emission for acting as imaging probes to detect bacteria.^[14] Upon light irradiation, these QDs can generate reactive oxygen species (ROS) that contribute to highly oxidative damage of cellular substances such as cell membranes and nucleic acids.^[15] Yet, the ultrashort lifetime and diffusion distance of ROS remain significant challenges, resulting in greatly compromised antibacterial efficacy due to quantum dots' inability to recognize bacteria. Meanwhile, nonspecific ROS production over the course of treatment can cause great damage to healthy tissues near the infection site.^[16] Clearly, targeting photosensitizer to the MDR bacteria is crucial to overcoming the shortcomings of today's QD-based PCT and promoting its further application. To the best of our knowledge, no studies to date have reported a strategy of synergistic phage-assisted PCT (PA-PCT).

Herein, we report a novel QD@Phage hybrid nanosystem that combines the advantages of phage-based therapies and PCT. Using avidin-biotin bioconjugation, a Cd-based QD is successfully conjugated to a phage that targets green fluorescent protein-expressing *P.aeruginosa* (GFP-*P. aeruginosa*).^[17] By virtue of the phage component, the phage first assists the QD in locating on the surface of bacteria, and then, upon light irradiation, the generation of singlet oxygen (¹O₂), a kind of ROS, destroys the host GFP-*P. aeruginosa* via PA-PCT (Figure 1a). In a mouse wound model, as a result of PA-PCT, the QD@Phage functioned as a "precision-guided killer", which significantly reduced the bacterial colonization and accelerated the wound healing process without leading to inflammation. We anticipate the novel nanosystem with highly specific targeting, rapid photocatalytic antibacterial efficacy, and good biosafety has a great promise as a candidate for next-generation antimicrobial therapies.

2. Results and Discussion

2.1. Synthesis and Characterization of QD@Phage Nanosystem

The QD@Phage nanosystem was prepared by avidin-biotin conjugation (Figure 1a). Briefly, the phage, whose genome is shown in Figure S1 (Supporting Information), was first biotinylated (Phage-biotin) using *N*-hydroxysuccinimidobiotin (Biotin-NHS), then streptavidin-coated Cd-based QD (QD) was anchored onto the biotinylated phages via bioconjugation reaction. Figure 1b shows that the phages maintained high infectivity with a negligible titer decrease after biotinylation. However, when the Biotin-NHS linker amount was beyond 9.78 μM, a sharp decrease in phage titer was witnessed, because the overdoses linkers may also anchor the phage tail fibers, which play crucial roles in host bacterial recognition, and eventually impair phage infectivity. Therefore, 9.78 μM was chosen as the optimized biotinylation condition (Figure S2, Supporting Information). Next, the fluorescence emission profile of the QD@Phage (Figure 1c,d) was investigated to verify whether the QD had been successfully anchored onto the phages. The QD@Phage exhibited a fluorescence emission peak at 590 nm when excited at 360 nm; the spectra were identical to pristine QD, implying that the QD had been successfully anchored upon the surface of the phages. Moreover, QD@Phage displayed a wide excitation range, but with a stable emission wavelength at 590 nm, demonstrating that it is an excellent imaging agent. Collectively, the fluorescence emission properties of QD@Phage convince us of its potential for targeting and imaging bacteria. By transmission electron microscope (TEM), the unique structure of QD@Phage was also observed (Figure 1e). Meantime, the pristine phage without functionalization is shown in Figure S3, Supporting Information. Besides, the QD@Phage nanosystem presented in our study is in principle phage-independent and could be adapted to other types of phages, as the vast majority of phages exhibit an outermost protein layer composed of proteins which are in turn composed of long chains of amino acid subunits, which display primary amine (–NH₂) groups on their N-terminus, necessary to conjugate the Biotin-NHS linker.

Then, to validate the photocatalytic performance of QD@Phage, 1,3-diphenylisobenzofuran (DPBF) was used as a probe to detect the ¹O₂ generation of QD@Phage.^[18] Both groups showed typical absorbance of DPBF at 510 nm at 0 min (Figures 1f,g, and S4, Supporting Information), presenting apparent blue fluorescence in the cuvettes (Figure 1i). The absorbance of the DPBF solution with QD@Phage at 510 nm decreased by 85% after 16 min light irradiation (Figure 1h). The solution also turned from blue to colorless during this process, indicating the depletion of ¹O₂ by DPBF. Without light excitation, both QD@Phage and the control group exhibited a negligible change in absorbance over a 16-min incubation (Figure S4, Supporting Information), suggesting a lack of ¹O₂ generation. These results reveal that the QD@Phage possesses robust photocatalytic ¹O₂ production ability. We assume the combined capability of the QD@Phage, including inherent bacterial recognition by phage and robust photocatalytic performance by QD, highlights the potential of this nanosystem as an antibacterial agent via PA-PCT.

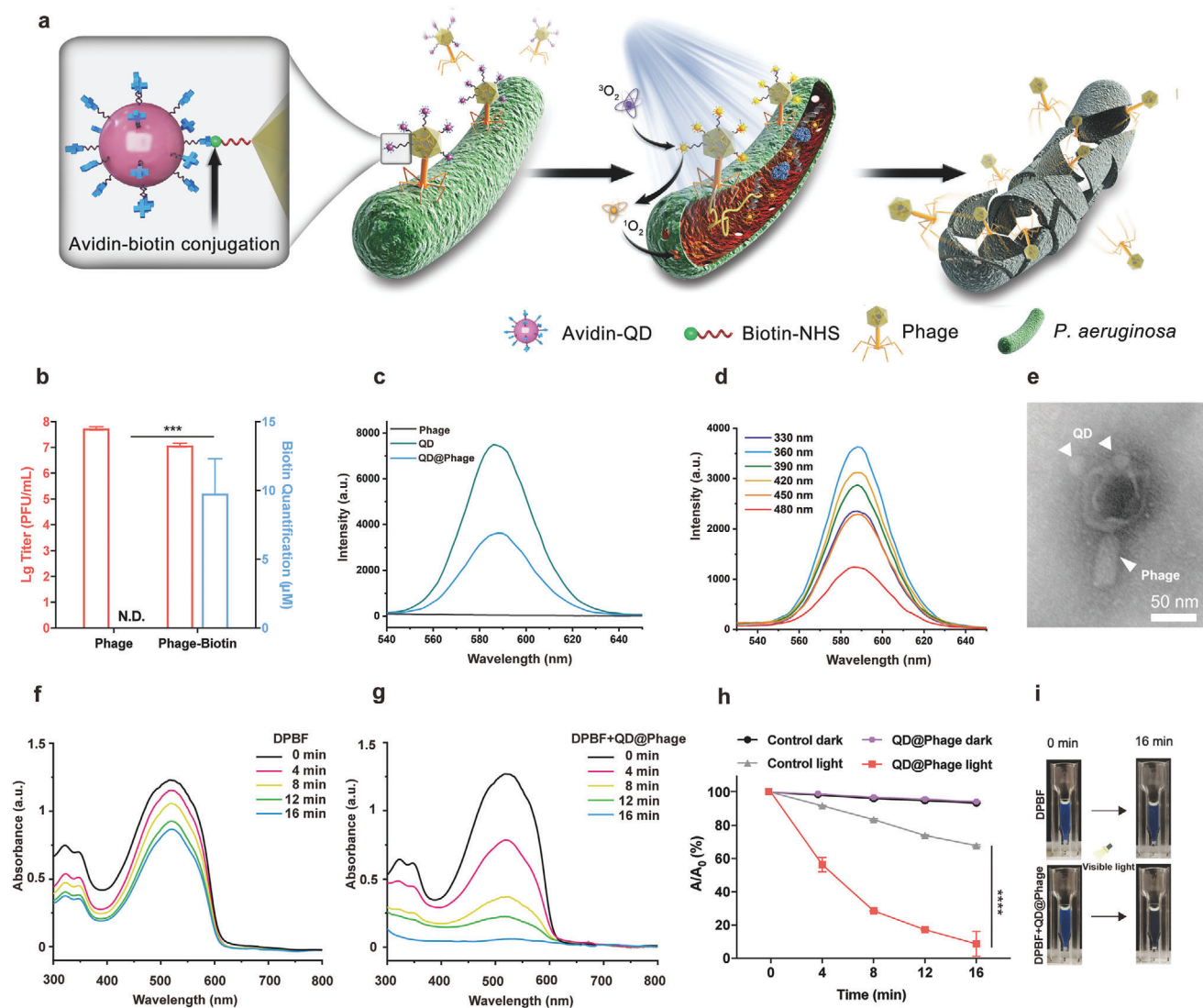


Figure 1. Synthesis and photocatalytic performance of QD@Phage. a) Schematic illustration of phage-assisted photocatalytic therapy against GFP-*P. aeruginosa*. b) Phage titer and biotin quantification after optimal dropping dose of Biotin-NHS. N.D. represents no detection. The data are presented as mean \pm standard deviation (SD), $n = 3$. c) Fluorescence spectra of phage, QD, and QD@Phage at excitation wavelength 360 nm. d) Fluorescence spectra of QD@Phage with the excitation wavelength from 330 to 480 nm. e) A representative transmission electron microscope (TEM) image of the QD@Phage. Scale bar: 50 nm. UV-vis absorption spectra of f) 1,3-diphenylisobenzofuran (DPBF) and g) DPBF + QD@Phage with visible light irradiation, respectively. h) Time-dependent bleaching of DPBF by QD@Phage with or without exposure to visible light. A_0 is the initial absorbance of DPBF, and A indicates the residual absorbance in solution at time t . The PBS treatment served as control group. i) Photographs of DPBF, in the absence and presence of QD@Phage, under 16 min of visible light irradiation. The data are presented as mean \pm SD, $n = 3$. *** $p < 0.001$ and **** $p < 0.0001$ by t -test for data in (b) and (h).

2.2. In Vitro Antibacterial Activity of QD@Phage Nanosystem

For the antibacterial activity study, we first used TEM to monitor the PA-PCT process. As shown by the phage adsorption rate in Figure S5 (Supporting Information), after 30 min of incubation, the majority of QD@Phage had targeted and aggregated to the host cells. Therefore, we decided to apply light irradiation after 30 min of incubation in the following tests. As evidenced also by TEM (Figure 2a), after a 30 min incubation, QD@Phage was successfully located on the surface of the GFP-*P. aeruginosa*. Once

light irradiation was applied, after another 30 min of incubation, we observed a cluster of progeny phages that were going to release from the lysed bacteria (Figure 2b). Finally, as a result of PA-PCT, we found a large number of lysed bacteria after incubating for 90 min (Figure 2c), which could be attributed to the synergistic bactericidal effect of phage and QD-generated 1O_2 against GFP-*P. aeruginosa*.

We then used confocal scanning microscopy (CLSM) to test the host bacterial recognition and imaging ability of QD@Phage. As shown in Figure 2d, the GFP-*P. aeruginosa*, with inherent

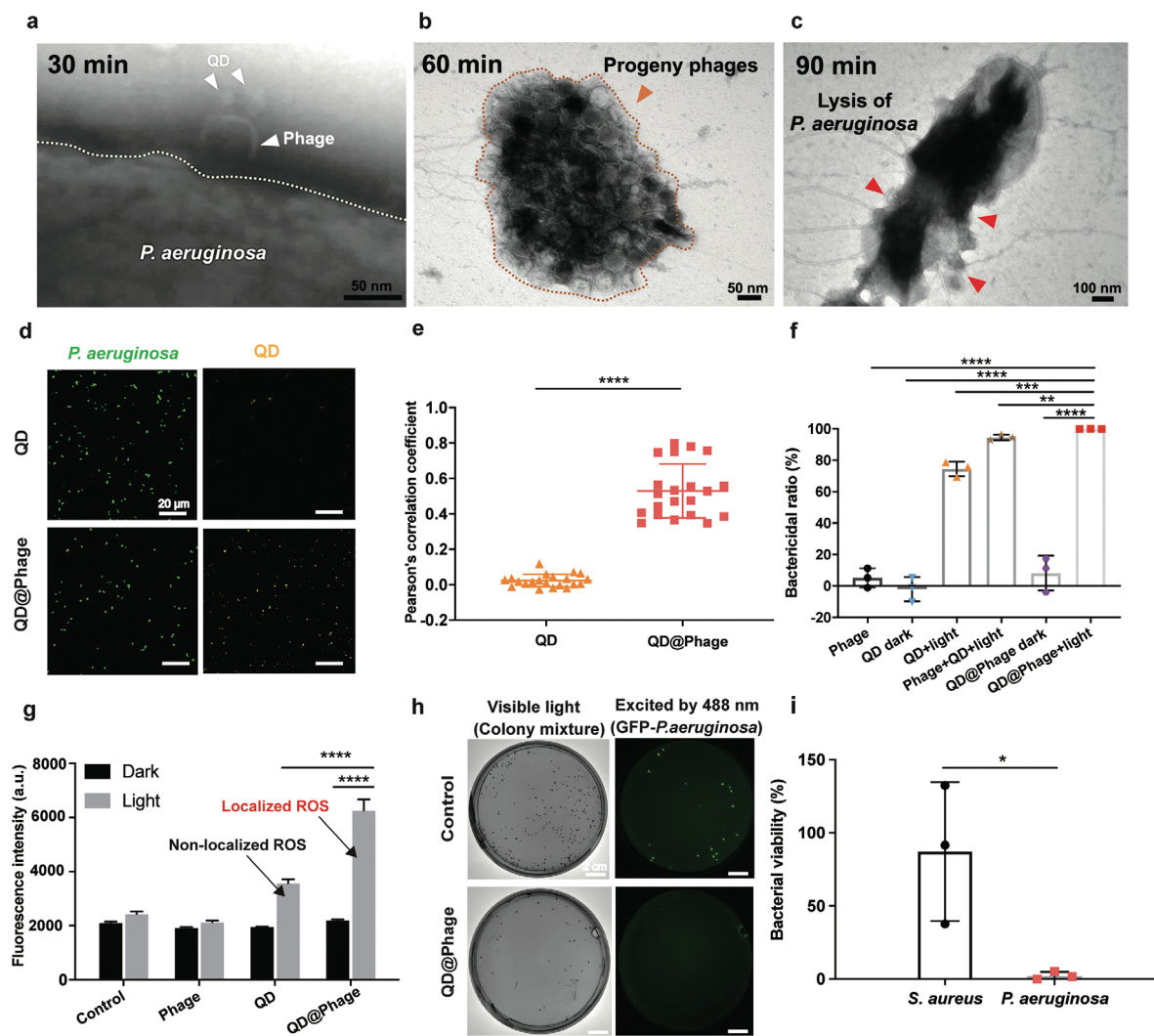


Figure 2. In vitro antibacterial profile of QD@Phage. TEM images revealing PA-PCT processes of QD@Phage: a) host bacteria binding, b) progeny phages releasing, and c) lysis of a bacterium. Scale bar: 50 nm in (a) and (b); 100 nm in (c). d) Confocal scanning microscopy (CLSM) images of QD and QD@Phage treated GFP-*P. aeruginosa*. GFP-*P. aeruginosa* (green fluorescence); QD (yellow fluorescence). Scale bar: 20 μm . e) Colocalization analysis as determined by the Pearson's correlation coefficient statistically analyzed from CLSM images. The data are presented as mean \pm SD, $n = 20$. f) Bactericidal ratios for phage, QD, phage+QD, and QD@Phage against GFP-*P. aeruginosa* under different conditions after 90 min of incubation. The data are presented as mean \pm SD, $n = 3$. g) Intracellular ROS level of GFP-*P. aeruginosa* after co-incubation with phage, QD, and QD@Phage, with or without light irradiation, for 90 min using 2',7'-dichlorodihydrofluorescein diacetate (DCF-DA) assay kit. The data are presented as mean \pm SD, $n = 3$. h) Specific antibacterial test of QD@Phage by imaging of GFP-*P. aeruginosa* and MRSA, with visible light representing a mixture of bacteria, and the green fluorescence excited by 488 nm irradiation representing the GFP-*P. aeruginosa*. Scale bar: 2 cm. i) Bacterial viability of GFP-*P. aeruginosa* and MRSA after the QD@Phage light treatment. The PBS treatment served as the control group in all experiments. The data are presented as mean \pm SD, $n = 3$. $^{**}p < 0.01$; $^{***}p < 0.001$; $^{****}p < 0.0001$ by one-way ANOVA followed by Dunnett's post hoc test for data in (e–g), $^{*}p < 0.05$ by *t*-test for data in (i).

green fluorescence, was labeled in yellow by QD@Phage after a 30 min incubation, whereas only a weak yellow signal was detected in the QD-treated group. By investigating Pearson's correlation coefficient between the green and yellow channels, we found that the QD@Phage-treated group showed a remarkably higher colocalization correlation as compared to the QD-treated group. This finding demonstrates that QD@Phage possesses robust host bacterial recognition and imaging abilities (Figure 2e).^[19]

We further investigated the bactericidal activity of QD@Phage against GFP-*P. aeruginosa* by plate-counting (Figure 2f and

Figure S6, Supporting Information). In this experiment, phage, QD, mixture of phage, and QD treated groups were compared with QD@Phage. QD@Phage and QD with visible light irradiation, each exerted a significantly higher bactericidal effect as compared to their application under the dark condition and to the action of the phage alone; this is due to the photocatalytic $^1\text{O}_2$ production ability of QD.^[20] Notably, by imposing PA-PCT on bacteria, QD@Phage displays robust bacteria-killing properties (over 99.9%) after a 30 min incubation and a 60 min visible light irradiation. Moreover, we evaluated the antibacterial efficiency of QD@Phage by a time-killing assay, as shown in Figure S7

(Supporting Information). Meanwhile, a mixture of phage and QD under light irradiation demonstrated lower antibacterial activity (94.54%) than QD@Phage under light irradiation, which suggests that localizing ROS on the surface of bacteria played a critical role in achieving high bactericidal efficacy. Overall, both the QD dark group and the phage group showed relatively weak destructive effects.^[21] Also, in comparing QD@Phage with gentamicin, we found that QD@Phage showed a comparable bactericidal effect and a significantly higher bactericidal efficiency at an earlier incubation time (Figure S8, Supporting Information).

We also semiquantitatively measured the bacterial intracellular ROS level when treated with phage, QD, and QD@Phage by using a 2',7'-dichlorodihydrofluorescein diacetate (DCF-DA) assay kit. The analysis revealed a significantly higher ROS level within the bacterial cells after treatment by QD@Phage light (Figure 2g) as compared to the QD light group, suggesting that the localized ROS generated by QD@Phage caused greater oxidative stress than the non-localized ROS generated by the QD light group.

To investigate whether the nanosystem can selectively target the host bacteria, we applied QD@Phage in a polymicrobial condition with GFP-*P. aeruginosa* (G-) and MRSA (G+) to investigate its bacterial killing activity by observing the colonies in bright-field and fluorescent images after 90 min coinubation (Figures 2h,i). Nearly all of the GFP-*P. aeruginosa* were successfully killed, with no colony observed when excited by 488 nm irradiation, whereas a great number of MRSA colonies were still witnessed, indicating the high selective capacity of the QD@Phage system towards the targeted bacteria (GFP-*P. aeruginosa*). Besides, QD@Phage showed infectivity stability comparable to phage (Figure S9, Supporting Information), which guarantees its long-term application.

2.3. In Vitro Antibiofilm Activity of QD@Phage Nanosystem

The formation of biofilm is the major cause of bacterial chronic disease, since it endows bacteria with additional resistance to antimicrobials.^[22] We therefore evaluated the antibiofilm efficacy of QD@Phage against mature GFP-*P. aeruginosa* biofilm by determination of GFP-*P. aeruginosa* biofilm colony counts and biofilm biomass. As shown in Figure 3a and Figure S10 (Supporting Information), the QD@Phage light group showed significantly enhanced antibiofilm properties as compared to other groups, with a bactericidal rate of 99.24%. Meantime, we evaluated the anti-biofilm efficiency of QD@Phage by the time-killing assay, as shown in Figure S11 (Supporting Information). Additionally, under crystal violet staining, this group showed the lowest amount of biofilm biomass in the well (Figure 3b, top-view), demonstrating that the PA-PCT using QD@Phage caused great damage to the biofilm structure, whereas all other groups showed relatively low antibiofilm activity. Moreover, the biofilm bactericidal ratio of phage, QD light, and QD@Phage light under different dosages was also measured (Figure S12, Supporting Information), suggesting a dose-dependent efficacy in the tested groups.

Meanwhile, we used CLSM to observe the 3D biofilm structure and dead bacteria in different treatment groups. The alive bacteria in all groups showed a similar intensity of GFP fluorescence (Figure S13, Supporting Information), whereas the dead

cells specifically labeled in red by propidium iodide (PI) displayed a significantly different intensity (Figure 3c). Upon treatment with QD@Phage light, representative images and statistical analysis (Figure 3d) revealed that the majority of bacterial cells within the biofilm exhibited apparent red fluorescence compared to other tested groups, implying that QD@Phage can also significantly and effectively kill sessile cells. Taken together, these findings indicate that QD@Phage shows robust antibacterial and antibiofilm activity in vitro; we therefore envision that it may also serve in vivo as an antibacterial agent for the treatment of bacterial infections.

2.4. In Vivo Assessment of Wound Sterilization and Healing

Before carrying out the in vivo antibacterial study, cytotoxicity assays showed that QD@Phage had good cytocompatibility in human A549 and human keratinocyte (HaCat) cell lines (Figure S14, Supporting Information). We then developed a mouse wound infection model using GFP-*P. aeruginosa* to evaluate the efficiency of QD@Phage light on in vivo anti-infective therapy. The QD@Phage with light treatment procedure is illustrated in Figure 4a. In brief, a small round incision (1cm in diameter) on the dorsal epidermis of mice was first infected for 24 h with 100 μ L of GFP-*P. aeruginosa* (1×10^8 CFU mL⁻¹) to establish the in vivo wound infection model. Afterwards, 100 μ L of QD@Phage (10^6 PFU mL⁻¹, only one dosage over the entire treatment) was directly applied to the infected wounds. 30 min later, visible light irradiation was introduced to begin PA-PCT for wound disinfection. Eventually, granulation tissue was regenerated and deposited from the dorsal dermis tissue, and the wound tissue formed scabs and exfoliated.

We used digital photography to record the wound healing process at different timepoints (Figure S15, Supporting Information). On day 1, we observed that the infected wounds were all surrounded by inflamed epidermis with sanies, demonstrating successful infection with GFP-*P. aeruginosa*. Representative traces of wound areas over 9 days are shown in Figure 4b; the corresponding therapeutic effect was analyzed using the wound closure rate (Figure S16, Supporting Information). On Day 9, QD@Phage with visible light irradiation showed a closure ratio of 91.2% of the original wound area, demonstrating that treatment by QD@Phage with visible light irradiation can effectively eliminate GFP-*P. aeruginosa* infection and accelerate wound healing. The phage and QD light groups with suppuration presented much lower closure ratios than QD@Phage light (59.8% and 76.3%, respectively), suggesting delayed wound healing.

In vivo fluorescence imaging of the infected wounds revealed bacterial intensity during treatment (Figure 4c).^[23] We noticed very large areas of high fluorescence intensity on day 1, which again indicated the successful in vivo establishment of GFP-*P. aeruginosa* wound infection. For the QD@Phage light-treated group, both the area and intensity of fluorescence decreased dramatically over time, and by day 7 no intensity was detected, suggesting that the bacteria had been successfully killed in the wound sites.^[24] On the contrary, the other groups still showed fluorescence after 7 days of treatment, indicating the continued existence of GFP-*P. aeruginosa* infection, fostering a prolonged

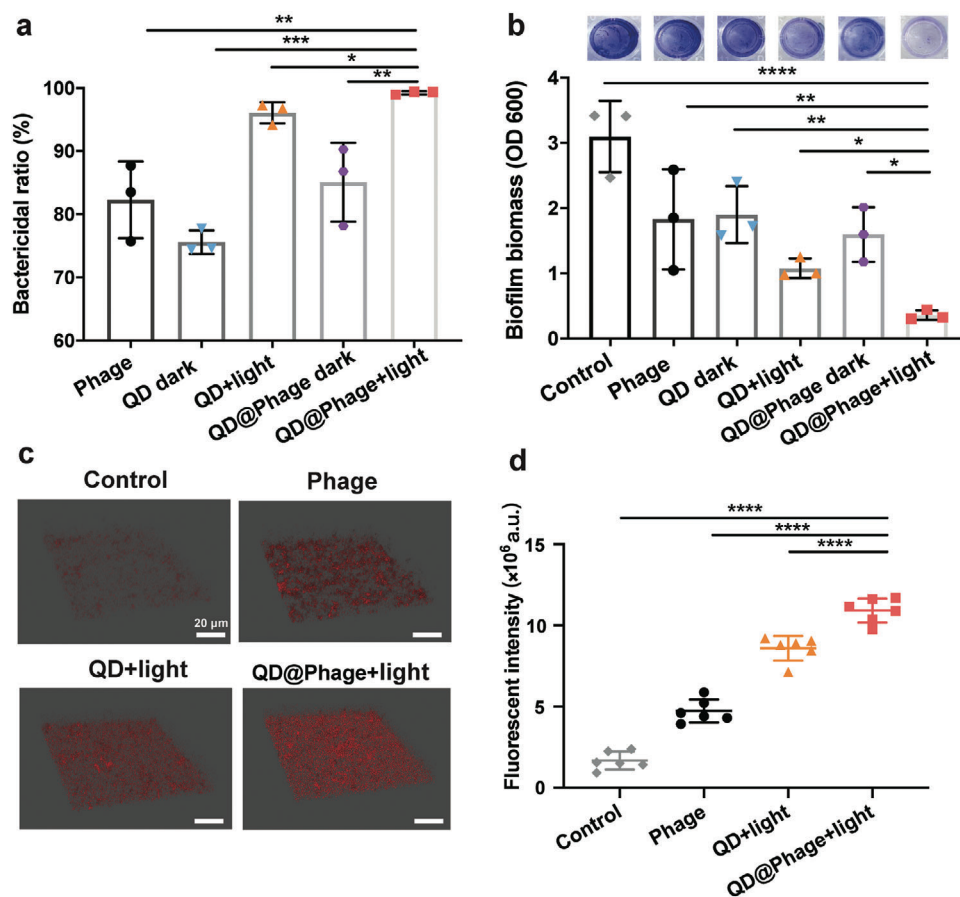


Figure 3. In vitro antibiofilm activity of QD@Phage. a) The biofilm bactericidal ratio of phage, QD, and QD@Phage under different conditions after 24 h of incubation. The data are presented as mean \pm SD, $n = 3$. b) Biofilm biomass quantification using crystal violet staining after various treatments. The data are presented as mean \pm SD, $n = 3$. c) Confocal microscopy images of dead cells in the biofilm structure after treatments by phage, QD, and QD@Phage under different conditions. Dead cells are labeled in red with propidium iodide (PI). Scale bar: 20 μ m. d) Semiquantitative statistics of dead cells' fluorescence intensity in the biofilm structure in (c). The PBS treatment served as a control group in all experiments. The data are presented as mean \pm SD, $n = 6$. * $p < 0.05$; ** $p < 0.01$; *** $p < 0.001$; **** $p < 0.0001$ by one-way ANOVA followed by Dunnett's post hoc test for data in (a), (b), and (d).

inflammation state of the wound, which could be the reason for a slower healing process.

To explore the inflammation and healing status of the wound, we further investigated the wound areas using H&E and Masson staining (Figure 4d); the corresponding semiquantitative analyses are shown in Figures 4e,f. No significant infiltration of neutrophils was observed after QD@Phage light treatment, which was comparable to healthy skin tissue (Figure S17, Supporting Information). Apparent lobulated neutrophil infiltration (indicated by red arrows in Figure 4d) was seen in other groups, demonstrating an apparent sign of continued bacterial infection. The collagen fibrils were analyzed by Masson staining (Figure 4f), and the wounds of the QD@Phage light group exhibited well-established collagen fibers and dermal layers after 9 days of treatment. Furthermore, an abundance of dead cellular debris and areolar connective tissues with disordered texture were noticed in the rest groups, indicating a delayed tissue regeneration process. The above results add excellent antibacterial properties to PA-PCT's roster of advantages, confirming that one dose of QD@Phage with visible light irradiation offers great promise for

treating MDR bacterial skin infections. For one thing, a single dose of the QD@Phage demonstrates significant bacterial reduction when exposed to visible light as we discussed before, for another thing, the progeny phage from QD@Phage can keep killing the bacteria in the remaining days to promote wound healing.

3. Conclusion

In summary, we have successfully synthesized a QD@Phage nanosystem for combating bacterial infections. In a unique type of phage-assisted photocatalytic therapy, termed PA-PCT, QD@Phage can target host bacteria via the inherent infectivity of phages, and upon visible light irradiation, the QD can locally generate massive ROS to further enhance bactericidal activity. In vitro experiments showed that QD@Phage efficiently eliminated planktonic bacteria (by over 99.9%) with good cytocompatibility. More surprisingly, it showed highly efficient antibiofilm activity (over 99%) and can achieve safe and robust skin wound healing. The data above demonstrate the proposed QD@Phage nanosystem's promising therapeutic effects: robust bacterial disinfection

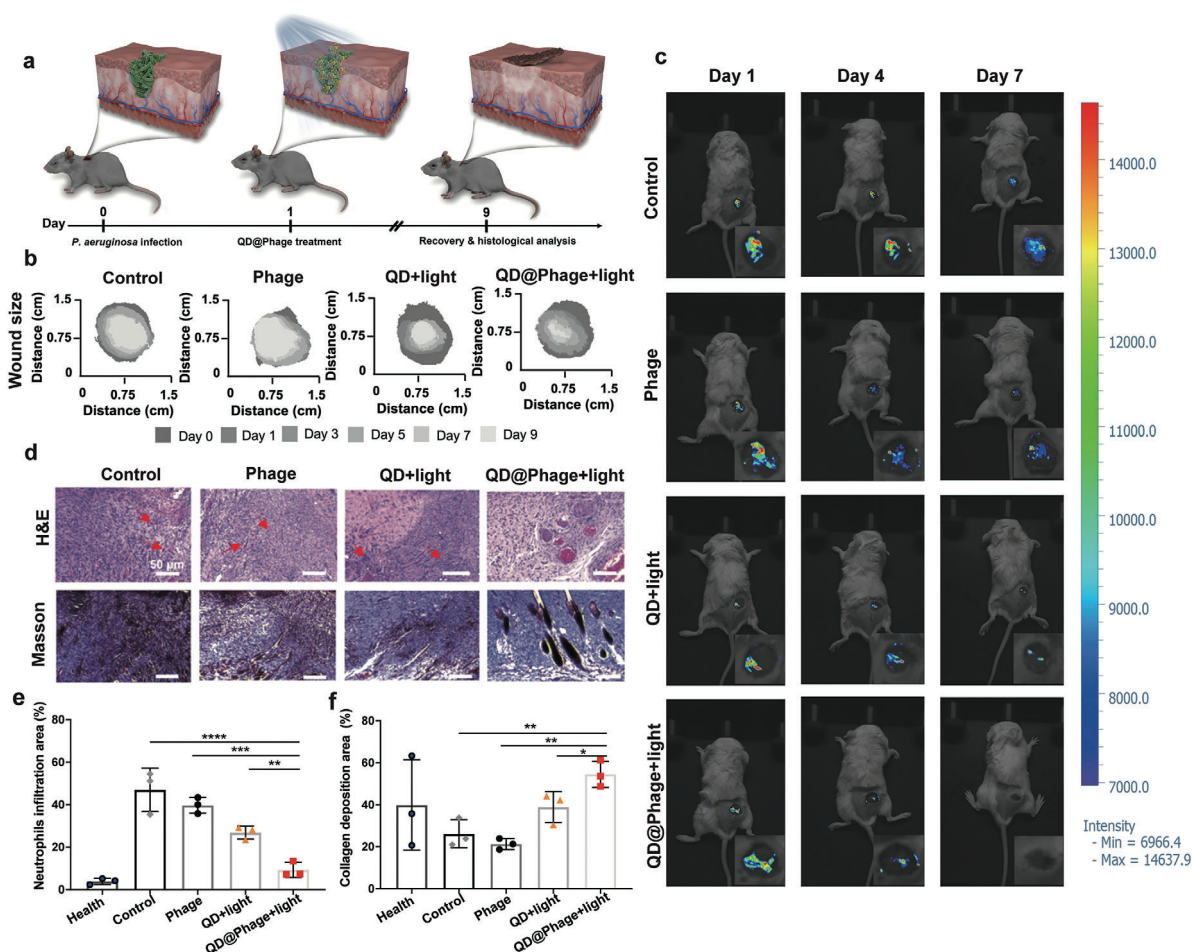


Figure 4. In vivo antibacterial profile of QD@Phage. a) Schematic illustration of mouse wound infection model and the process of treatment with QD@Phage. b) Traces of wound area after 9 days of various treatments. c) Representative fluorescence imaging signals for GFP-*P. aeruginosa* in the wound during treatment. d) Representative histological photomicrographs of epidermal sections of GFP-*P. aeruginosa*-infected wound after various treatments, with Hematoxylin and Eosin (H&E) and Masson staining. Red arrows highlight typical neutrophils. Scale bar: 50 μm . Percentage of e) neutrophil infiltration area and f) collagen deposition area after various treatments, based on corresponding images of H&E staining and Masson trichrome staining. The PBS treatment served as control group. The data are presented as mean \pm SD, $n = 3$. * $p < 0.05$; ** $p < 0.01$; *** $p < 0.001$; **** $p < 0.0001$ by one-way ANOVA followed by Dunnett's post hoc test for data in (e) and (f).

capability for targeting and eradicating MDR bacterial infections. Our findings also provide a new perspective for the development of novel catalytic antibacterial nanoplatfoms with high specificity. Notably, limited from the short tissue penetration depth of visible light, the QD@Phage is still facing challenges in treating deep bacterial infections, but it is expected that by using our proposed synthetic method, phages conjugated with near-infrared laser- or sono-sensitizers can also be successfully fabricated and applied for treating deep tissue bacterial related infections in the near future.

4. Experimental Section

Synthesis of QD@Phage: The synthesis of QD@Phage includes two main steps: phage biotinylation and bioconjugation between biotinylated phage (Phage-biotin) and streptavidin-coated quantum dot (QD). For phage biotinylation, typically, 300 μg of Biotin-NHS was dissolved in 40 μL

of Dimethyl sulfoxide (DMSO) to prepare a biotinylation solution, then the biotinylation solution was introduced to 1 mL of purified phages solution (10^7 PFU mL^{-1} in PBS, $\text{pH} \approx 8$), and the whole biotinylation process lasted overnight under room temperature with mild stirring. After removing the excess Biotin-NHS by dialysis for 24 h two times at 4 $^{\circ}\text{C}$, Phage-biotin was collected for subsequent use. For bioconjugation, typically, 10 μL of QD aqueous (1 μM) was mixed with Phage-biotin for overnight under room temperature with mild stirring, the residual QD was removed by centrifugation using an Ultrafree-MC Centrifugal Filter (Merck), finally, the QD@Phage was collected for further use.

Supporting Information

Supporting Information is available from the Wiley Online Library or from the author.

Acknowledgements

This work was financially supported by the Deutsche Forschungsgemeinschaft (DFG) of Germany through grants from Collaborative Research

Centers (SFB) 765 and 1449. The authors were grateful for the support of Benjamin Allen in polishing the language of the manuscript, and the authors appreciate Yongjun Guan's grateful help for the support of animal study. This work was funded by the PRO-IMPLANT Foundation (<https://www.pro-implant-foundation.org>), a non-profit organization supporting research, education, global networking, and care of patients with bone-, joint-, or implant-associated infection. L. Wang and X. Fan acknowledge the support of the China Scholarship Council (CSC). The authors thank Sara Timm from the Core Facility for Electron Microscopy at Charité- Universitätsmedizin Berlin, for her help in the collection of the phage pictures under the transmission electron microscope. The authors thank Dr. Jeroen Wagemans from the Laboratory of Gene Technology at KU Leuven for his support and guidance on the phage genome extraction, sequencing, and annotation. All animal experiments were performed in compliance with guidelines reviewed by the animal ethics committee of Shanghai Sixth People's Hospital (approval number: 2021-0288).

Open Access funding enabled and organized by Projekt DEAL.

Conflict of Interest

The authors declare no conflict of interest.

Author Contributions

L.W. and X.F. contributed equally to this work. C. N., X. F., L. W., A. T., and R. H. conceived the idea for this project. X. F., L. W., and C. N. assisted with the figure layout and scheme design. X. F., L. W., C. N., M. G. M., T. T., and X. L. Z discussed the manuscript structure and modified figures. L. W. and X. F. synthesized the QD@Phage. L. W., M. G. M., and T. T. performed bacterial/biofilm binding study and in vitro and in vivo antibacterial/antibiofilm tests. X. F. measured the catalytic performance of the QD@Phage and performed CLSM observation. W. J. D. performed cytocompatibility experiment and analyzed the data. The manuscript was written through the contributions of all the authors. All authors have approved the final version of the manuscript.

Data Availability Statement

The data that support the findings of this study are available from the corresponding author upon reasonable request.

Keywords

bacteriophage therapy, biofilm-associated infection, functional antibacterial nanosystem, photocatalytic therapy, reactive oxygen species (ROS)

Received: December 7, 2021

Revised: March 11, 2022

Published online: April 18, 2022

- [1] J. M. Blair, M. A. Webber, A. J. Baylay, D. O. Ogbolu, L. J. Piddock, *Nat. Rev. Microbiol.* **2015**, *13*, 42.
[2] J.-P. Pirnay, T. Ferry, G. Resch, *FEMS Microbiol. Rev.* <https://doi.org/10.1093/femsre/ufab040>.

- [3] a) L. Dieltjens, K. Appermans, M. Lissens, B. Lories, W. Kim, E. V. Van der Eycken, K. R. Foster, H. P. Steenackers, *Nat. Commun.* **2020**, *11*, 107; b) C. R. Arciola, D. Campoccia, L. Montanaro, *Nat. Rev. Microbiol.* **2018**, *16*, 397.
[4] C. L. Ventola, *P T.* **2015**, *40*, 277.
[5] a) C. Schmidt, *Nat. Biotechnol.* **2019**, *37*, 581; b) S. Reardon, *Nature* **2014**, *510*, 15; c) S. Aslam, A. M. Courtwright, C. Koval, S. M. Lehman, S. Morales, C. L. L. Furr, F. Rosas, M. J. Brownstein, J. R. Fackler, B. M. Sisson, *Am. J. Transplant.* **2019**, *19*, 2631; d) R. M. Dedrick, C. A. Guerrero-Bustamante, R. A. Garlena, D. A. Russell, K. Ford, K. Harris, K. C. Gilmour, J. Soothill, D. Jacobs-Sera, R. T. Schooley, *Nat. Med.* **2019**, *25*, 730; e) E. J. Cano, K. M. Cafisch, P. L. Bollyky, J. D. Van Belleghem, R. Patel, J. Fackler, M. J. Brownstein, B. A. Horne, B. Biswas, M. Henry, *Clin. Infect. Dis.* **2021**, *73*, e144.
[6] P. P. Kalelkar, M. Riddick, A. J. García, *Nat. Rev. Mater.* <https://doi.org/10.1038/s41578-021-00362-4>.
[7] a) T. Tkhalishvili, L. Lombardi, A.-B. Klatt, A. Trampuz, M. Di Luca, *Int. J. Antimicrob. Agents* **2018**, *52*, 842; b) L. Wang, T. Tkhalishvili, A. Trampuz, M. G. Moreno, *Front. Microbiol.* **2020**, *11*.
[8] I. Cho, M. J. Blaser, *Nat. Rev. Genet.* **2012**, *13*, 260.
[9] S. J. Labrie, J. E. Samson, S. Moineau, *Nat. Rev. Microbiol.* **2010**, *8*, 317.
[10] H. G. Hampton, B. N. Watson, P. C. Fineran, *Nature* **2020**, *577*, 327.
[11] M. Zhang, F. Wu, W. Wang, J. Shen, N. Zhou, C. Wu, *Chem. Mat.* **2018**, *31*, 1847.
[12] L. Wang, X. Zhang, X. Yu, F. Gao, Z. Shen, X. Zhang, S. Ge, J. Liu, Z. Gu, C. Chen, *Adv. Mater.* **2019**, *31*, 1901965.
[13] a) X. Dou, Q. Zhang, S. N. A. Shah, M. Khan, K. Uchiyama, J.-M. Lin, *Chem. Sci.* **2019**, *10*, 497; b) X. Tian, Y. Sun, S. Fan, M. D. Boudreau, C. Chen, C. Ge, J.-J. Yin, *ACS Appl. Mater. Interfaces* **2019**, *11*, 4858.
[14] a) J.-H. Jung, M. Kotal, M.-H. Jang, J. Lee, Y.-H. Cho, W.-J. Kim, I.-K. Oh, *RSC Adv.* **2016**, *6*, 73939; b) X. Tang, X. Zeng, H. Liu, Y. Yang, H. Zhou, H. Cai, *Microchim. Acta* **2019**, *186*, 163.
[15] a) D. L. Sai, J. Lee, D. L. Nguyen, Y.-P. Kim, *Exp. Mol. Med.* **2021**, *53*, 495; b) F. Gao, T. Shao, Y. Yu, Y. Xiong, L. Yang, *Nat. Commun.* **2021**, *12*, 745; c) X. Fan, F. Yang, C. Nie, L. Ma, C. Cheng, R. Haag, *Adv. Mater.* **2021**, *33*, 2100637; d) B. Yang, Y. Chen, J. Shi, *Adv. Mater.* **2019**, *31*, 1901778.
[16] a) Y. Deng, F. Jia, S. Chen, Z. Shen, Q. Jin, G. Fu, J. Ji, *Biomaterials* **2018**, *187*, 55; b) C. M. Courtney, S. M. Goodman, J. A. McDaniel, N. E. Madinger, A. Chatterjee, P. Nagpal, *Nat. Mater.* **2016**, *15*, 529.
[17] J.-f. Pan, N.-h. Liu, L.-y. Shu, H. Sun, *J. Nanobiotechnol.* **2015**, *13*, 37.
[18] H. Dong, S. Tang, Y. Hao, H. Yu, W. Dai, G. Zhao, Y. Cao, H. Lu, X. Zhang, H. Ju, *ACS Appl. Mater. Interfaces* **2016**, *8*, 3107.
[19] X. Xue, S. Jin, Z. Li, C. Zhang, W. Guo, L. Hu, P. C. Wang, J. Zhang, X. J. Liang, *Adv. Sci.* **2017**, *4*, 1700229.
[20] D. Li, X. Li, T. Zhao, H. Liu, S. Jiang, Q. Zhang, H. Ågren, G. Chen, *ACS Nano* **2020**, *14*, 12596.
[21] A. V. Holguín, G. Rangel, V. Clavijo, C. Prada, M. Mantilla, M. C. Gomez, E. Kutter, C. Taylor, P. C. Fineran, A. F. G. Barrios, *Viruses* **2015**, *7*, 4602.
[22] a) S. Amin Yavari, S. M. Castenmiller, J. A. van Strijp, M. Croes, *Adv. Mater.* **2020**, *32*, 2002962; b) M. Magana, C. Sereti, A. Ioannidis, C. A. Mitchell, A. R. Ball, E. Magiorkinis, S. Chatzipanagiotou, M. R. Hamblin, M. Hadjifrangiskou, G. P. Tegos, *Clin. Microbiol. Rev.* **2018**, *31*, e00084.
[23] H. Wang, T. Ding, J. Guan, X. Liu, J. Wang, P. Jin, S. Hou, W. Lu, J. Qian, W. Wang, *ACS Nano* **2020**, *14*, 14779.
[24] P. Avci, M. Karimi, M. Sadasivam, W. C. Antunes-Melo, E. Carrasco, M. R. Hamblin, *Virulence* **2018**, *9*, 28.

Supporting Information

for *Adv. Sci.*, DOI 10.1002/adv.202105668

Photocatalytic Quantum Dot-Armed Bacteriophage for Combating Drug-Resistant Bacterial Infection

Lei Wang, Xin Fan, Mercedes Gonzalez Moreno, Tamta Tkhilaishvili, Weijie Du, Xianlong Zhang, Chuanxiong Nie, Andrej Trampuz* and Rainer Haag**

Supporting Information

©Wiley-VCH 2022

69451 Weinheim, Germany

Photocatalytic Quantum Dot-Armed Bacteriophage for Combating Drug-Resistant Bacterial Infection

Lei Wang^{[1][3]†}, Xin Fan^{[2][3]†*}, Mercedes Gonzalez Moreno^{[1][3]}, Tamta Tkhilaishvili^{[1][4]}, Weijie Du^[3], Xianlong Zhang^[5], Chuanxiong Nie^[2], Andrej Trampuz^{[1][3]*}, Rainer Haag^{[2]*}

^[1] Centre for Musculoskeletal Surgery, Charité – Universitätsmedizin Berlin, Corporate Member of Freie Universität Berlin, Humboldt-Universität zu Berlin, and Berlin Institute of Health, Berlin, Germany

^[2] Department of Chemistry and Biochemistry, Freie Universität Berlin, Takustraße 3, 14195 Berlin, Germany

^[3] BIH Center for Regenerative Therapies (BCRT), Berlin Institute of Health (BIH), Berlin, Germany.

^[4] Department of Tropical Medicine and Infectious Diseases, University of Rostock, Rostock, Germany

^[5] Department of Orthopedics, Shanghai Sixth People's Hospital, Shanghai Jiao Tong University, 200233 Shanghai, China

†These authors contributed equally to this work.

* Corresponding authors: xinf94@zedat.fu-berlin.de; andrej.trampuz@charite.de; haag@zedat.fu-berlin.de

Supporting Information

Materials

The GFP-expressing *Pseudomonas aeruginosa* (ATCC® 10145™), MRSA (ATCC® 43300™), human A549 and human keratinocyte (HaCat) cell lines were obtained from the American Type Culture Collection (ATCC); A novel lytic bacteriophage infecting GFP-*P. aeruginosa* was isolated from hospital sewage. Cd-based Core/Shell Quantum Dots with Streptavidin (OCNQSS525) and Biotin-NHS (203112), dimethyl sulfoxide (DMSO, 99.7%), Crystal violet (1092180500), 1,3-diphenylisobenzofuran (DPBF, 105481) and Masson kit (HT1) were purchased from Sigma-Aldrich; Ultrafree-MC Centrifugal Filter was purchased from Merck; Cell Counting Kit-8 (ab228554) and H&E Staining Kit (ab245880) were purchased from Abcam. EZ-Link® Biotin-NHS Reagents (20217), Pierce™ Biotin Quantitation Kit (28005) propidiumiodid (P1304MP) and 2',7'-dichlorodihydrofluorescein diacetate assay kit (DCF-DA) were purchased from Thermo Scientific.

Material characterizations

The morphological characterization of QD@Phage and phage was performed using a transmission electron microscope (TEM, Leo TEM 906, ZEISS). Ultraviolet-Visible spectra was measured on UV/vis Spectrometer Agilent Cary 8454 and fluorescent spectra was measured on plate reader (Tecan, Infinite M200 Pro). A 1-cm path length quartz cuvette was used for singlet oxygen detection at room temperature. Fluorescence images *in-vivo* were measured by a VISQUE InVivo Smart-LF (Vieworks, Anyang, South Korea).

Annotation and bioinformatic analysis of phage genomes

Sequencing was performed on an Illumina MiSeq instrument equipped with a nanoFlowcell (Illumina MiSeq Reagent Nano Kit v2, Brussels, Belgium, paired-end 2*250 bp reads). The phage genome was assembled using the SPAdes-based PATRIC genome assembly v3.6.1261. The closest similar phage was retrieved using BLASTn v2.13.063. Genome alignment to these identified phages was performed using MEGA11. Resulting aligned phage genomes were functionally annotated through the RASTtk pipeline and manually curated using the BLASTp program v2.13.0. Genbank files were finalized using Artemis v18.1.0. To visualise and illustrate phage genome, a circular representation was created using

Proksee (<https://proksee.ca/>). The databases of CARD, Resfinder, PlasmidFinder, and VFDB were used to exclude the undesirable genes.

Biotinylation of phage

Typically, phage solution (10^7 PFU/mL, 1 mL in pH~8 PBS) was incubated with Biotin-NHS (feeding dose: 878.79 μ M, 40 μ L in DMSO) overnight. Afterwards, the unreacted Biotin-NHS was removed via dialysis and the Phage-biotin was ready for further use. Also, Phage-biotin 1 and phage-biotin 2 were synthesized with different feeding doses of 87.87 μ M and 1757.6 μ M of Biotin-NHS, respectively, which were used as comparisons. The biotin amount of Phage-biotin (10^6 PFU/mL, 1 mL) was further quantified by Pierce™ Biotin Quantitation Kit according to manufacturer's instructions. Meanwhile, the double layer agar plaque assay is employed for enumeration of phage titer.

Transmission electron microscopy

For transmission electron microscopy observation, 10 μ L of QD@Phage solution (10^6 PFU/mL) was loaded on a copper grid with carbon support layer 45 s, and the excess solution was removed using a filter paper. Afterwards, the grid was negatively stained with 2% uranyl acetate for 45 s and washed three times with distilled water. Finally, the grid was air-dried and ready for morphology observation. Moreover, to monitor the bacterial killing process upon PA-PCT treatment, the solution of QD@Phage incubated with host bacteria under different protocols (30 min with dark; 30 min with dark + 30 min with light; 30 min with dark + 60 min with light) were dripped on copper grids. Afterwards, all grids were stained, washed and observed with the same protocol.

Singlet Oxygen Detection

First, 5 μ L of the QD@Phage solution (10^6 PFU/mL in SM buffer) was added to 500 μ L of DPBF solution (30 μ M, dissolved in DMF) in cuvette, and DPBF+PBS solution was served as a control. The mixture was irradiated under visible light (5W) in 16 min while recording the UV-vis spectra using UV-vis spectrometer every 4 mins. In parallel, they were also measured under dark condition.

Adsorption rate

The adsorption curve assay was performed to determine the phage adsorption rate. Briefly, GFP-*P. aeruginosa* was grown in 10 mL Luria-Bertani (LB) broth at 37 °C under shaking conditions (160 rpm/min) to reach an OD600 of 0.4 (corresponding to approx. 10^8 CFU/mL). Then QD@Phage (10^6

PFU/mL) was mixed with the bacterial suspension at MOI = 0.1 and incubated at 37°C. Aliquots of 100 µL were taken at 5 min intervals during 25 min and diluted in 4.4 mL LB broth containing 0.5 mL of chloroform. The number of non-adsorbed phage particles at each incubation time was determined by the double agar overlay method.

Intracellular ROS assay

The 2',7'-dichlorodihydrofluorescein diacetate (DCF-DA) Assay Kit was performed to detect the intracellular ROS level of the bacteria induced by QD@Phage. Briefly, GFP-*P. aeruginosa* cells were treated with phage, QD, and QD@Phage under dark and light conditions for 90 min at 37 °C. After washing with PBS, the treated samples were co-incubated with 10 µM DCF-DA probe for 30 min in the dark, followed by detecting fluorescence intensity using plate reader (Ex/Em = 492/517 nm).

Specific antibacterial test

GFP-*P. aeruginosa* and MRSA bacterial mixture suspensions ($\sim 10^6$ CFU/mL) in LB were used for the specific antibacterial tests. The 100 µL of mixture bacterial suspension was firstly mixed with 900 µL of $\sim 10^5$ PFU/mL QD@Phage in centrifuge tubes and incubated for 30 min under dark at 37 °C, and then they were incubated under light for another 60 min. 100 µL of mixture bacterial suspensions were then serially diluted and added onto the LB agar plates. After incubation at 37 °C for 24 h, the mixture bacterial colonies were distinguished and recorded by Gel Documentation System Bio-Rad (Chemidoc MP).

Binding and imaging ability

GFP-*P. aeruginosa* suspensions (10^8 CFU/mL) were treated with QD and QD@Phage (almost equivalent QD contents (determined by fluorescence intensity using plate reader)) for 30 mins at 37 °C under dark condition. Samples were then washed three times to remove the unbound QD using Ultrafree-MC Centrifugal Filter (Merck) via centrifugation. Then, the mixture was resuspended in PBS for obtaining fluorescent images on confocal laser scanning microscope (CLSM, TCS SP8, Leica, Germany).

Antibacterial test

Typically, 10 µL of QD@Phage solution (10^6 PFU/mL) was introduced into 90 µL of $\sim 10^5$ CFU/mL bacterial suspensions. After incubation under dark at 37 °C for 30 minutes, the bacterial suspensions were incubated at 37 °C for another 60 min under darkness conditions or with visible light irradiation

by a 5 W LED lamp with a power density of 0.1 W/cm². Experimental groups including phage (10⁶ PFU/mL), QD, QD@Phage and gentamicin (8 µg/mL, minimum bactericidal concentration) with different conditions carried out as comparison. At last, the bactericidal ratio for all groups were evaluated via agar plate counting. The bacterial suspensions were diluted and cultured on agar plates for quantification of bacterial counts after overnight incubation at 37 °C. The bactericidal ratio of the examined samples was calculated by the following equation: $R=(100-I_s/I_c) \times 100\%$, where R represents the bactericidal ratio, I_c represents average amount of control group, and I_s represents the average amount of bacteria treated with different groups. The antibacterial activity of QD@Phage was evaluated against planktonic of GFP-*P. aeruginosa* by the time-killing assay. Briefly, the planktonic cells (10⁵ CFU/mL) were incubated with QD@Phage at 37 °C for 0, 30, 60 and 90 min. Subsequently, ten-fold serial dilutions of cells were plated onto LB agar and incubated for 18-24 h at 37°C for cell counting.

Biofilm eradication test.

GFP-*P. aeruginosa* biofilm was cultured by adding 200 µL GFP-*P. aeruginosa* suspension (10⁵ CFU/mL in LB medium) was placed in 8-well slides, then they were cultured at 37 °C. Twenty-four hours later, the medium was removed, thereby, the unattached bacteria was gently washed away with sterile PBS three times, and the mature biofilm on 8-well slides was harvested. Next, the prepared biofilm was treated with QD@Phage for 30 min under dark at 37 °C, and then it was irradiated by visible light overnight at 37 °C. Finally, the sessile cells were diluted and cultured on agar plates for overnight to count the bacterial colonies. The anti-biofilm activity of QD@Phage was evaluated against GFP-*P. aeruginosa* biofilm by the time-killing assay. 24 h-old biofilm was incubated with QD@Phage at 37 °C for 0, 6, 12 and 24 h, subsequently, ten-fold serial dilutions of the biofilm-embedded cells were plated onto LB agar and after 18-24 h incubation at 37°C for cell-counting.

To calculate the antibiofilm efficiency, the following formula was used: $C=(100-B/A) \times 100\%$, where C indicates antibiofilm efficiency, A is the number of colony forming units (CFUs) in the control group (PBS), and B is the number of CFUs in experimental groups. Furthermore, crystal violet staining assay was used to investigate the biofilm biomass. Briefly, the treated biofilms were stained with crystal violet (0.1%, 10 min), then they were washed with PBS three times. Thereafter, the crystal violet was dissolved into 200 µL of ethanol. The biomass of the biofilm was evaluated by measuring

the absorbance at 595 nm. Experimental groups including phage (10^6 PFU/mL), QD, and QD@Phage with different conditions were carried out as comparison.

In addition, 200 μ L of QD@Phage (10^6 PFU/mL) was introduced into the mature biofilm in 8-well slides for 3D confocal observation. After incubation at 37 °C for 30 min, the visible light irradiation was conducted for overnight. Subsequently, the biofilms were gently washed by PBS three times and co-stained with propidium iodide (PI) according to the protocol (DEAD BacLight Bacterial Viability Kit, L7012, Molecular Probes). After sample fixation with 4% paraformaldehyde (fresh prepared in PBS, pH 7.2) at room temperature for 20 min, the 3D Z-stack fluorescent and orthogonal-stack images were acquired on the SP8 lighting confocal laser scanning microscope (Leica, Germany). The fluorescent intensities were analyzed by ImageJ pro.

Cytotoxicity

Human A549 and HaCat cell lines were chosen as models to investigate the cells toxicity. 1×10^5 cells were grown in Eagle's minimal essential medium (DMEM) supplemented with 10% FCS and 1% Pen/Strep (100 U/mL penicillin; 100 μ g/mL streptomycin) in a 96-well plate at 37 °C and 5% CO₂. After that, 10 μ L of QD@Phage and PBS were mixed with the resuspended cells (100 μ L) to investigate cell toxicity. For the QD@Phage-treated cells, they were exposed to visible light irradiation for overnight. For the control group (PBS), cells were kept in darkness for overnight. Cell viability was then analyzed by CCK-8 method. Detailly, 100 μ L of different treated cells containing 10 μ L CCK-8 solution were added into each well and incubated at 37 °C for 2 h, the absorbance at 450 nm was recorded using a Plate Reader Tecan (Multiscan GO, Thermo Scientific).

***In-vivo* antibacterial activity evaluation**

All animal experiments were performed humanely in compliance with guidelines reviewed by the animal ethics committee of Shanghai Sixth People's Hospital (approval number: 2021-0288). For *in-vivo* experiments, healthy adult BALB/c mice (500 g, male, Chengdu Dossy Biological Technology Co. Ltd. (China)) were used, and they were randomly divided into four groups: (1) control group (PBS); (2) phage group; (3) QD light group; (4) QD@Phage light group (n= 3 per group). After anesthetized with 2% sodium pentobarbital, a small round incision (1cm in diameter) on the dorsal epidermis of mice was firstly infected by 100 μ L of GFP- *P. aeruginosa* (1×10^8 CFU/mL) for 24 h to establish *in-vivo* biofilm. After cultured for 1 day, QD@Phage (200 μ L, 10^6

PFU/mL, only one dosage over the whole treatment) was dropped onto the infected wound. Then, the wound was irradiated by a xenon lamp (60 W, 1 m high, 2 h) with the power density of 0.1 W/cm² to achieve antibacterial disinfection. During the antibacterial process, fluorescence images were measured by a VISQUE In Vivo Smart-LF (Vieworks, Anyang, South Korea) under inhalation anesthesia every two days with an excitation of 488 nm and an emission of 509 nm. For comparison with activated QD@Phage, groups of phage, pristine QD light and PBS were also conducted to evaluate the *in-vivo* biofilm eradication efficacy. The mice in these different groups were photographed and the size of infected wounds were dynamically monitored through measurements to evaluate the healing efficacy. The wound was photographed with reference ruler and the size was processed by Image J. After treatment for 9 days, all mice were sacrificed, and the tissues of infected wound area were harvested for pathological histology analysis.

Hematoxylin–Eosin and Masson staining

The extracted tissues were fixed in 4% paraformaldehyde, paraffin embedded, and sectioned for H&E and Masson staining using standard protocols. The conventional paraffin sections were soaked in xylene for 30 min, dehydrated with 100, 95, 85, and 75% ethanol solutions for 5 min, followed by water washing, hematoxylin staining for 10 min, soaking in 1% hydrochloric acid, and rinsing with distilled water. Eosin staining (Dakwei, Beijing, China) for 3 min, 75, 85, 95, and 100% ethanol solution for 2 min, xylene transparent treatment, drop neutral resin cover glass, and placed under an inverted microscope (Leica, DM300) to observe the results. Masson staining was used to observe collagen deposition in the wound tissue. Paraffin sections of the wound tissue were dewaxed and hydrated. Ponceau acid fuchsin solution was used for staining for 5–10 min. After washing with distilled water, 1% phosphomolybdic acid solution was used for staining for 5 min. After removing the dye solution, the sections were stained with aniline blue for 5 min, washed with distilled water, and treated with 1% glacial acetic acid for 1 min. The samples were dehydrated with 95% ethanol and anhydrous ethanol, transparent with xylene, and sealed.

Statistical Analysis

All experimental data were expressed as the mean \pm standard deviation. Statistical analyses were conducted using GraphPad Prism 9 software (GraphPad Software, Inc., San Diego, CA, USA). The mean values of two groups were compared using t test and one-way ANOVA followed by Dunnett's post-hoc test. A probability (*P*) value of ≤ 0.05 was considered statistically significant.

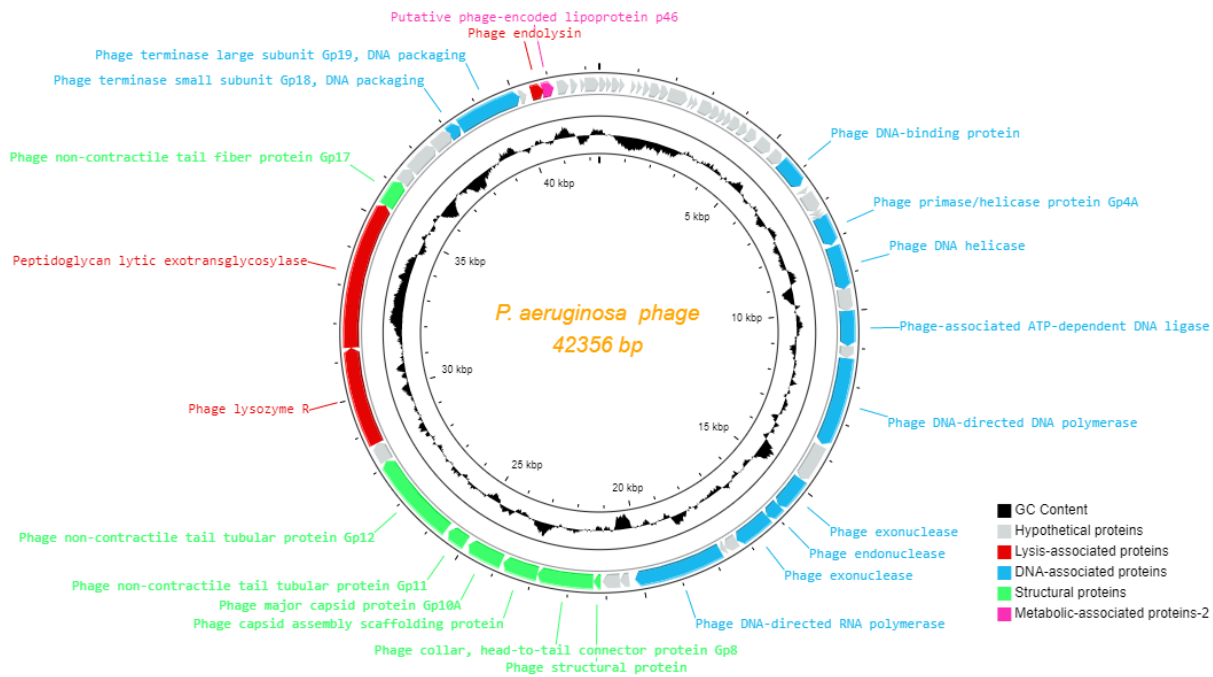


Figure S1. Circular representation of the genome of the *P. aeruginosa* phage. The outer circle indicates the gene coding region. The colour of each gene coding region refers to the functional category: hypothetical proteins (grey), lysis-associated proteins (red), DNA-associated proteins (blue), structural proteins (green) and metabolic-associated proteins (pink). The black inner circle indicates the GC content, and the most inner ring shows genome location (kbp). Genome size: 42,356 bp with a GC content of 62.3%. BLASTn identified most similarity to *P. aeruginosa* phage phiNFS (Genbank accession number NC_047852; 99% query cover; 96.84% sequence identity), therefore being classified as a new phage member within the *Phikmvirus* genus. The undesirable genes did not detect from the described database.

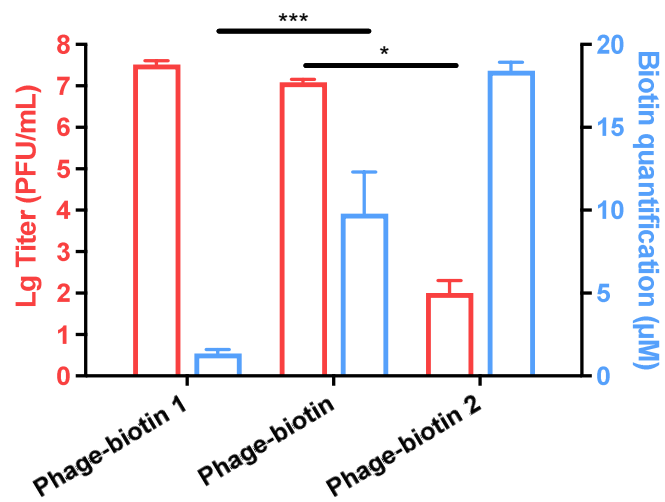


Figure S2. Biotin quantifications and corresponding titers for different series of Phage-biotin. Phage-biotin 1, phage-biotin and phage-biotin 2 synthesized with different feeding doses of 87.87 μM , 878.7 μM and 1757.6 μM of Biotin-NHS, respectively. The data are presented as mean \pm standard deviation (SD), $n=3$. $*P < 0.05$, $***P < 0.001$ by one-way ANOVA followed by Dunnett's post-hoc test.

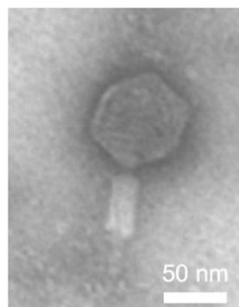


Figure S3. A representative transmission electron microscope (TEM) image of Phage. Scale bar: 50 nm.

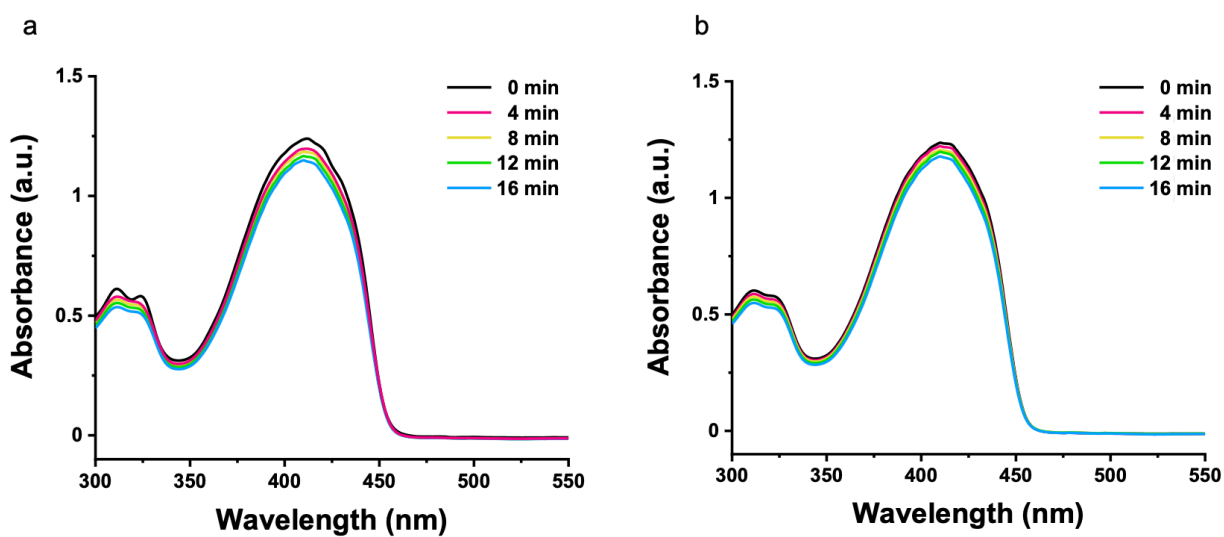


Figure S4. UV-vis absorption spectra of (a) DPBF and (b) DPBF + QD@Phage under dark incubation, respectively.

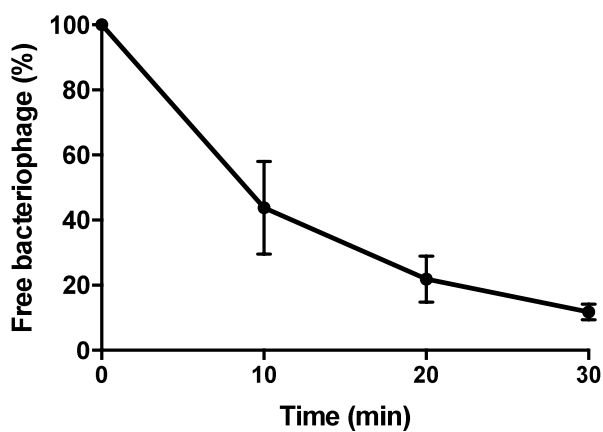


Figure S5. Adsorption curve of QD@Phage assessed on GFP- *P. aeruginosa*. Data are expressed as the mean \pm standard deviation (SD), $n=3$. The free QD@Phage decrease 88.7% from the supernatant with prolongation of the incubation time from 0 to 30 min when used the characteristic of phage adsorption rate.

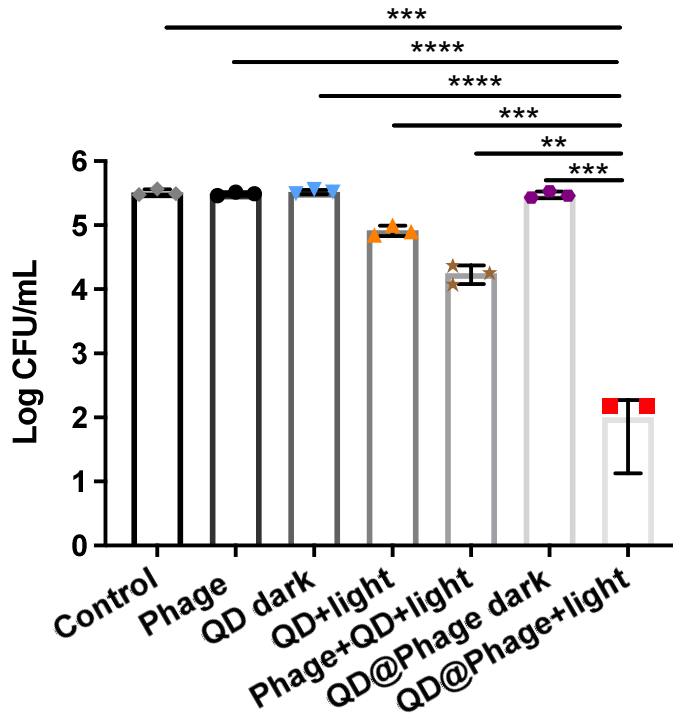


Figure S6. The cell count of phage, QD dark, QD+light, Phage+QD+light, QD@Phage dark and QD@Phage+light against planktonic of GFP-*P. aeruginosa*, respectively. The PBS treatment served as the control group. The data are presented as mean \pm SD, $n=3$. ** $P < 0.01$, *** $P < 0.001$, **** $P < 0.0001$ by one-way ANOVA followed by Dunnett's post-hoc test. In QD@Phage+light group, one group showed no colony after treatment, therefore, the data is not present.

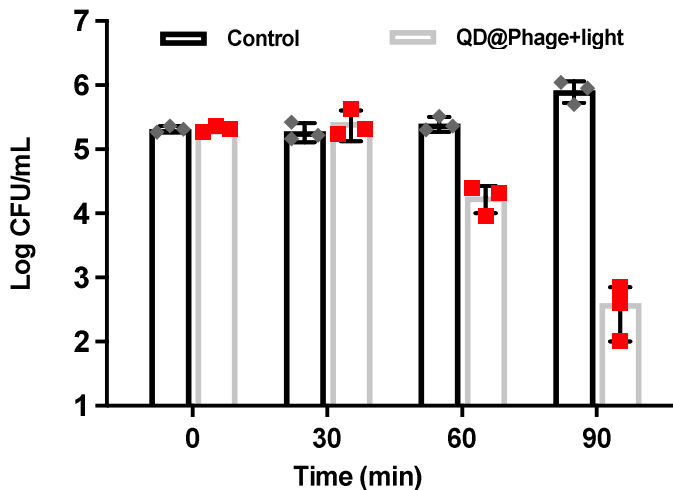


Figure S7. Bacterial cell count of planktonic GFP-*P. aeruginosa* treated with QD@Phage (10^6 PFU/mL) and untreated monitored at 30 min intervals during 90 min by the time-killing assay. The PBS treatment served as the control group. Data are expressed as mean \pm SD, $n=3$.

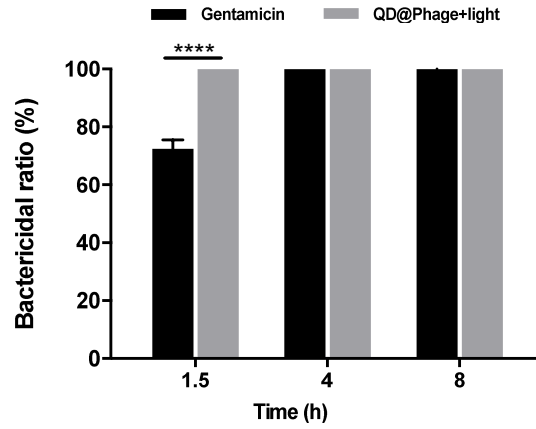


Figure S8. Bactericidal ratio of gentamicin and QD@Phage with visible light irradiation at different incubation time. The data are presented as mean \pm SD, n=3. **** $P < 0.0001$ by t test.

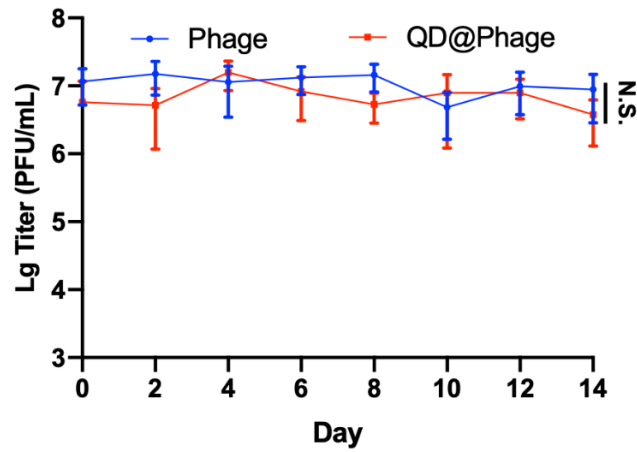


Figure S9. The infectivity stability of phage and QD@Phage. The data are presented as mean \pm SD, n=3. N.S. represents no significance, $P > 0.05$ by t test.

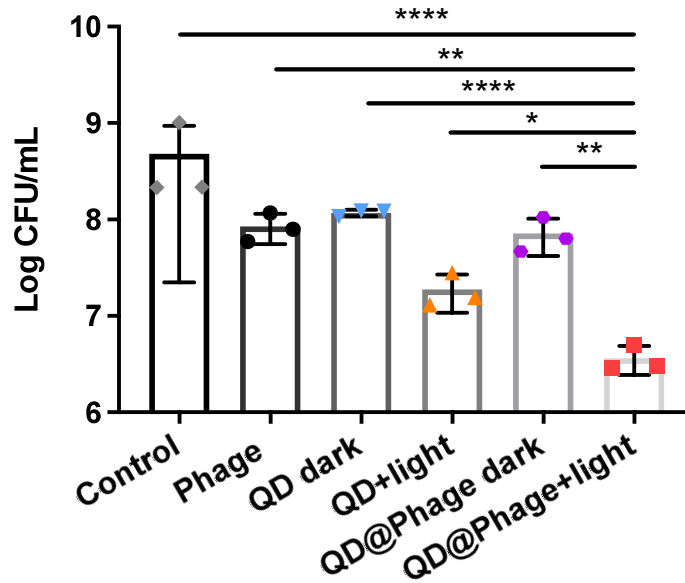


Figure S10. The cell count of phage, QD dark, QD+light, QD@Phage dark and QD@Phage+light against biofilm of GFP-*P. aeruginosa*, respectively. The PBS treatment served as the control group. The data are presented as mean \pm SD, n=3. * $P < 0.05$, ** $P < 0.01$, **** $P < 0.0001$ by one-way ANOVA followed by Dunnett's post-hoc test.

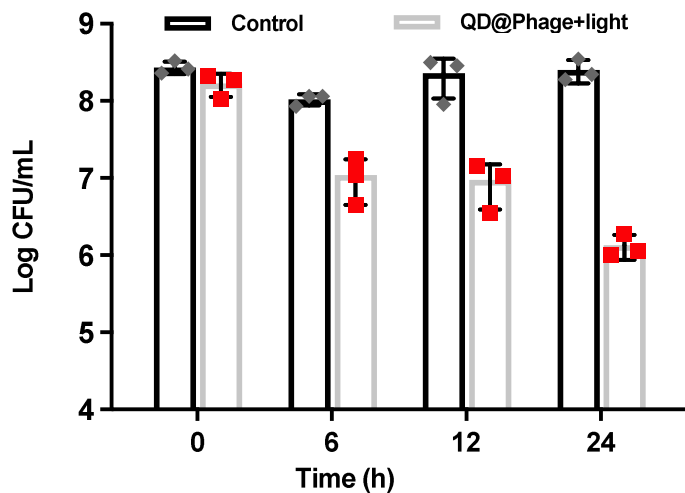


Figure S11. Bacterial cell count of GFP-*P. aeruginosa* biofilms treated with QD@Phage (10^6 PFU/mL) and untreated monitored at different time during 24 h. The PBS treatment served as the control group. Data are expressed as mean \pm SD, n=3.

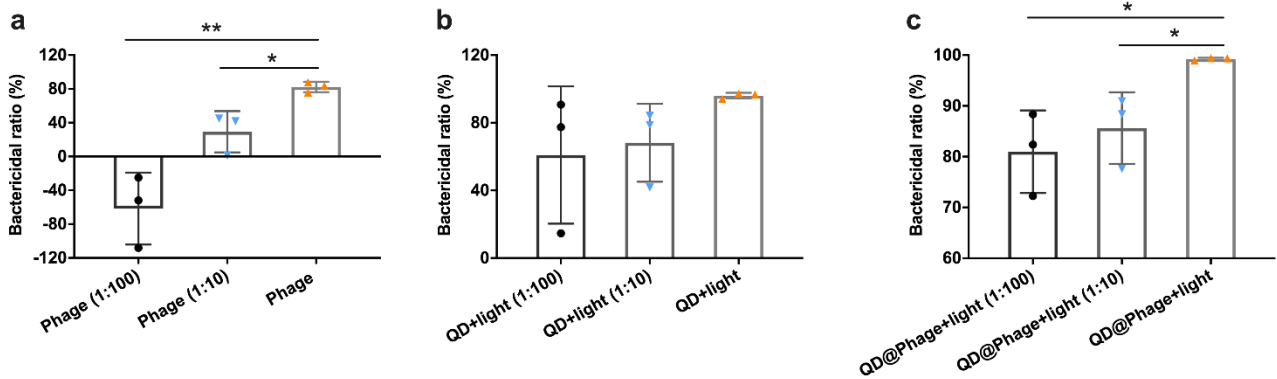


Figure S12. The biofilm bactericidal ratio of different concentrations of (a) phage, (b) QD light, and (c) QD@Phage light against GFP-*P. aeruginosa*, respectively. 1:10 and 1:100 referred to 10 and 100 times dilution of samples, respectively. The data are presented as mean \pm SD, $n=3$. * $P < 0.05$, ** $P < 0.01$ by one-way ANOVA followed by Dunnett's post-hoc test for data in (a) and (c).

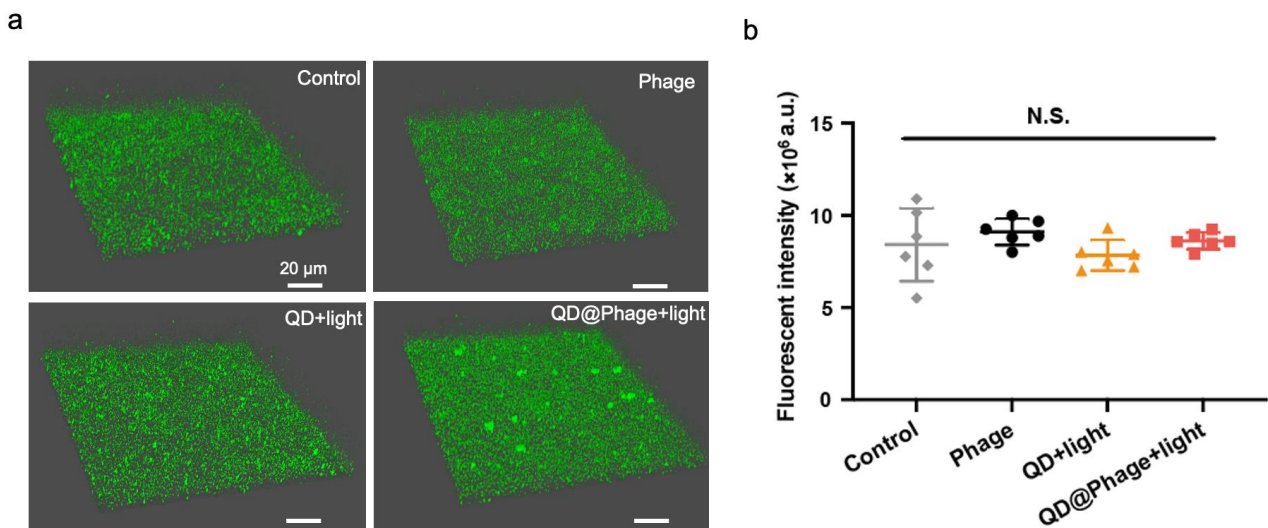


Figure S13. (a) The confocal microscopy images of GFP-*P. aeruginosa* in the biofilm structure after treatments of PBS, phage, QD and QD@Phage under different conditions excited by 488 nm and (b) corresponding semiquantitative statistics of fluorescent intensity of alive cells in the biofilm structure. The data are presented as mean \pm SD, $n=6$. N.S. represents no significance, $P > 0.05$ by one-way ANOVA followed by Dunnett's post-hoc test for data in (b). Scale bar: 20 μm . The PBS treatment served as the control group. We noticed no significant difference among groups, which might be attributed to the GFPs still presented in *P. aeruginosa* cell after treatment.

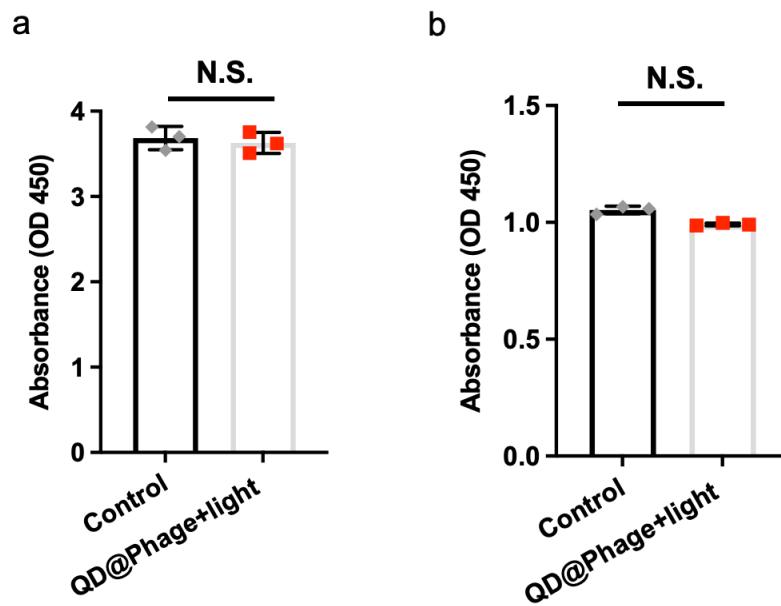


Figure S14. Cell Counting kit-8 (CCK-8) analysis of (a) human A549 cell and (b) human keratinocyte cell. The PBS treatment served as the control group. The data are presented as mean \pm SD, n=3. N.S. represents no significance, $P > 0.05$ by t test.

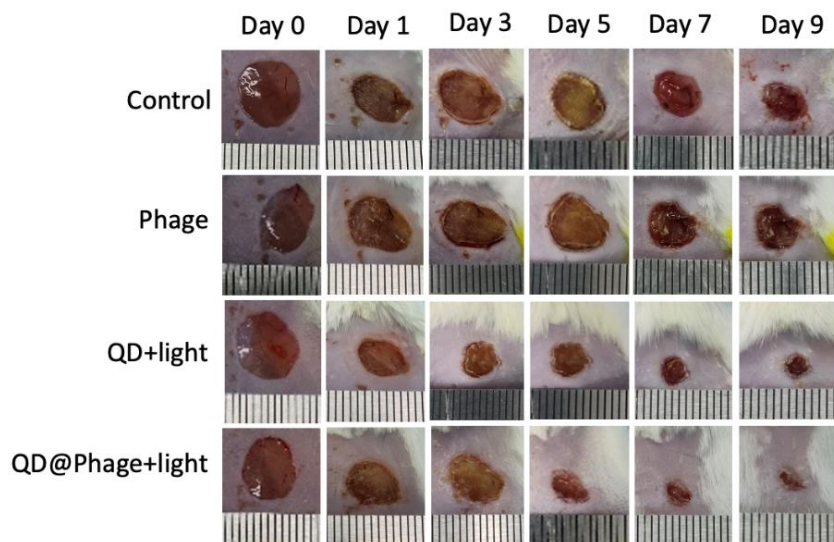


Figure S15. Typical wound photos during healing of groups treated with phage, QD and QD@Phage. The PBS treatment served as the control group.

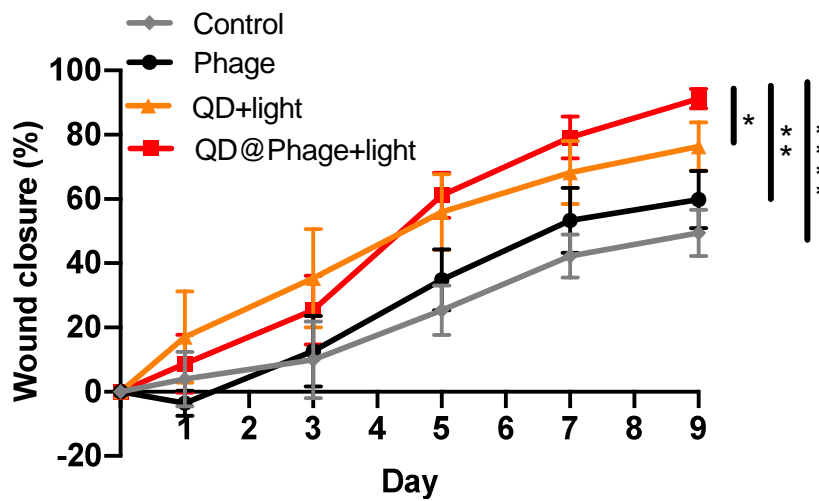


Figure S16. The wound-closure rate after the treatments of phage, QD and QD@Phage under different conditions. The data were recorded via a digital camera and analyzed by ImageJ. The PBS treatment served as the control group. The data are presented as mean \pm SD, $n=3$. * $P < 0.05$, ** $P < 0.01$, **** $P < 0.0001$ by one-way ANOVA followed by Dunnett's post-hoc test.

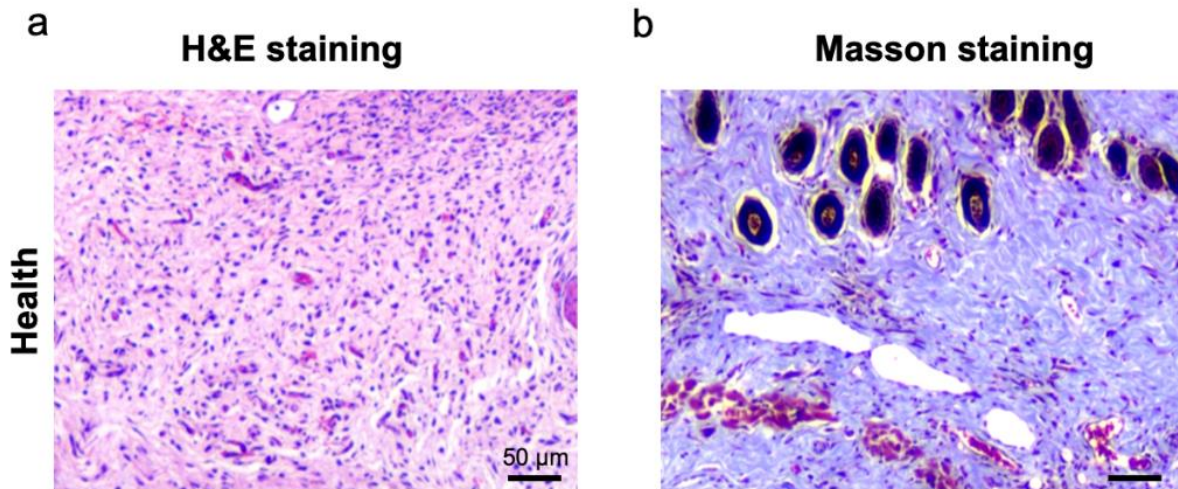


Figure S17. Histological photomicrographs of the healthy epidermal histological sections after (a) H&E and (b) Masson staining. Scale bar: 50 μm .

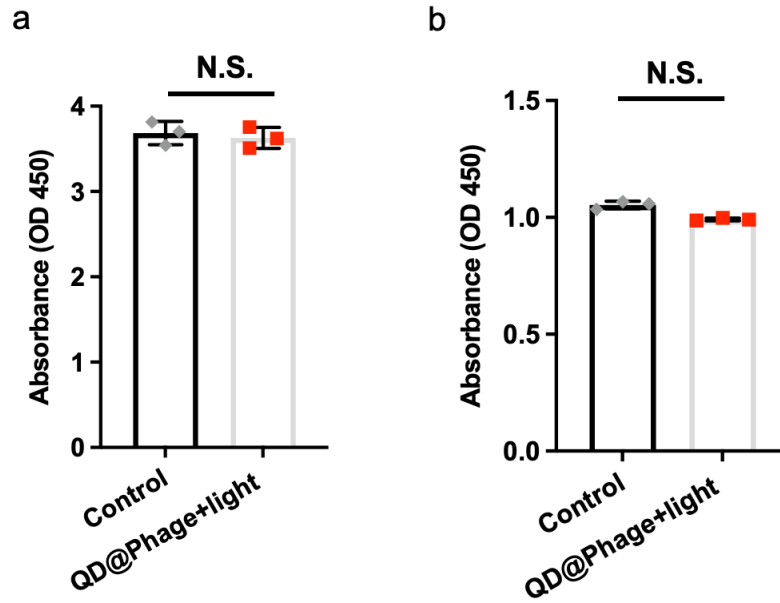


Figure S14. Cell Counting kit-8 (CCK-8) analysis of (a) human A549 cell and (b) human keratinocyte cell. The PBS treatment served as the control group. The data are presented as mean \pm SD, $n=3$. N.S. represents no significance, $P > 0.05$ by t test.

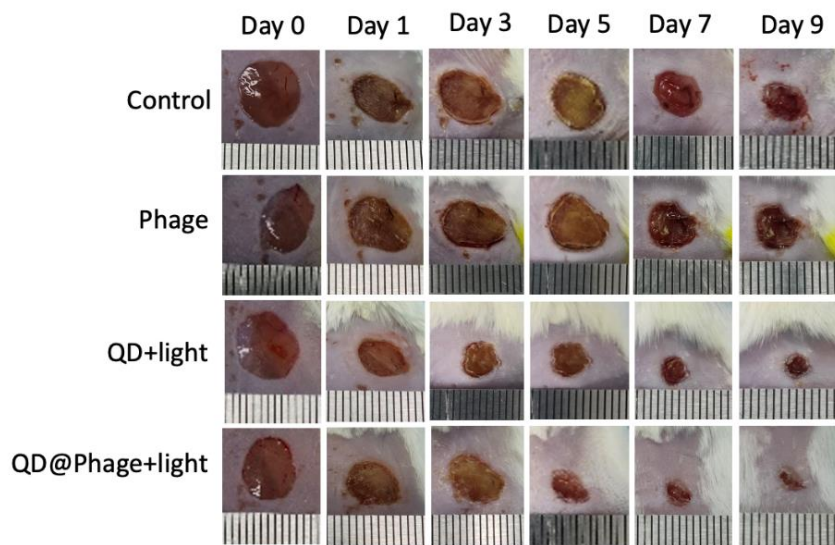


Figure S15. Typical wound photos during healing of groups treated with phage, QD and QD@Phage. The PBS treatment served as the control group.

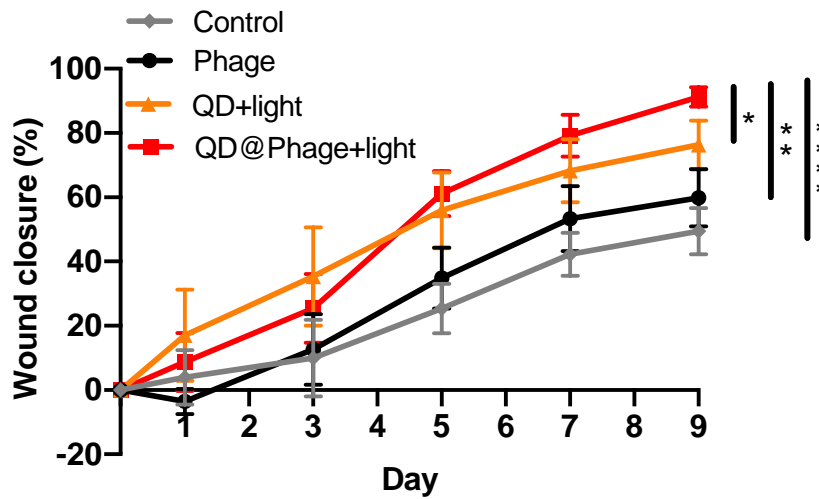


Figure S16. The wound-closure rate after the treatments of phage, QD and QD@Phage under different conditions. The data were recorded via a digital camera and analyzed by ImageJ. The PBS treatment served as the control group. The data are presented as mean \pm SD, $n=3$. * $P < 0.05$, ** $P < 0.01$, **** $P < 0.0001$ by one-way ANOVA followed by Dunnett's post-hoc test.

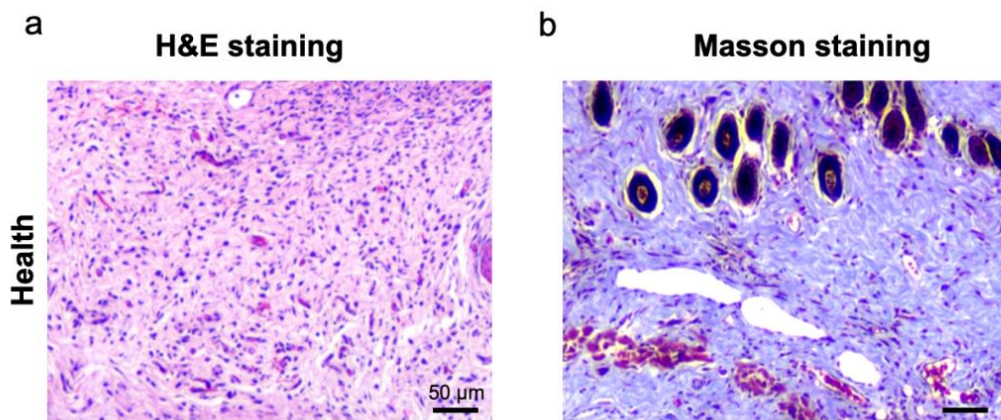
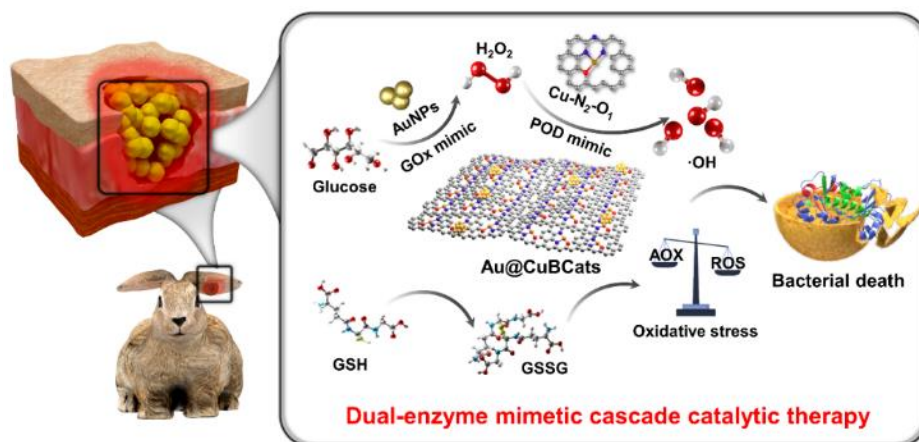


Figure S17. Histological photomicrographs of the healthy epidermal histological sections after (a) H&E and (b) Masson staining. Scale bar: 50 μm .

3.3. A copper single-atom cascade bionanocatalyst for treating multidrug-resistant bacterial diabetic ulcer



Xin Fan¹, Yang Gao¹, Fan Yang, Jian Liang Low, Lei Wang, Beate Paulus, Yi Wang, Andrej Trampuz*, Chong Cheng*, and Rainer Haag*.

¹These authors contributed equally to the work.

Adv. Funct. Mater. 2023, 2301986.

DOI: <https://doi.org/10.1002/adfm.202301986>

This is an open access article under the terms of the [Creative Commons Attribution Non-Commercial License](#).

Author contributions:

Xin Fan performed the main experiments, and wrote the manuscript. Yang Gao performed animal experiments. Fan Yang conducted the XAS measurements and assisted the data analysis. Jian Liang Low and Beate Paulus conducted the DFT studies and modelled the structures. Lei Wang assisted the *in-vitro* antibacterial experiments. Yi Wang performed the high-resolution TEM measurements. Andrej Trampuz provided the lab and drug-resistant bacterial strains for supporting the *in-vitro* antibacterial studies. Andrej Trampuz, Chong Cheng, and Rainer Haag conceived and supervised the project.

A Copper Single-Atom Cascade Bionanocatalyst for Treating Multidrug-Resistant Bacterial Diabetic Ulcer

Xin Fan, Yang Gao, Fan Yang, Jian Liang Low, Lei Wang, Beate Paulus, Yi Wang, Andrej Trampuz,* Chong Cheng,* and Rainer Haag*

Diabetic ulcers induced by multidrug-resistant (MDR) bacteria have severely endangered diabetic populations. These ulcers are very challenging to treat because the local high glucose concentration can both promote bacterial growth and limit the immune system's bactericidal action. Herein, a glucose oxidase-peroxidase (GOx-POD) dual-enzyme mimetic (DEM) bionanocatalyst, Au@CuBCats is synthesized to simultaneously control glucose concentration and bacteria in diabetic ulcers. Specifically, the AuNPs can serve as GOx mimics and catalyze the oxidation of glucose for the formation of H₂O₂; the H₂O₂ can then be further catalytically converted into OH via the POD-mimetic copper single atoms. Notably, the unique copper single atoms coordinated by one oxygen and two nitrogen atoms (CuN₂O₁) exhibit better POD catalytic performance than natural peroxidase. Further DFT calculations are conducted to study the catalytic mechanism and reveal the advantage of this CuN₂O₁ structure as compared to other copper single-atom sites. Both in vitro and in vivo experiments confirm the outstanding antibacterial therapeutic efficacy of the DEM bionanocatalyst. This new bionanocatalyst will provide essential insights for the next generation of antibiotic-free strategies for combating MDR bacterial diabetic ulcers, and also offer inspiration for designing bionanocatalytic cascading medicines.

1. Introduction

Diabetes and its complications have emerged as one of the major threats to human health, causing a large number of deaths annually.^[1,2] Especially, a diabetic ulcer is one of the most serious chronic complications, featured with slow-healing wounds that are very sensitive to bacterial infections.^[3] An important factor responsible for this complication is the overabundance of glucose in the wound area, which promotes the proliferation of bacteria and prevents the immune system from killing them, resulting in long-term bacterial colonization and an extremely hard-to-cure lesion.^[4] To make matters worse, the emergence of multidrug-resistant (MDR) bacteria, which vitiate antibiotics' bactericidal effects, has now aggravated the situation, further endangering diabetic ulcer patients. It is therefore important to develop new strategies not only for combating MDR

X. Fan, R. Haag
Institute of Chemistry and Biochemistry
Freie Universität Berlin
Takustraße 3, 14195 Berlin, Germany
E-mail: haag@chemie.fu-berlin.de

X. Fan, L. Wang, A. Trampuz
Charité – Universitätsmedizin Berlin
Freie Universität Berlin
Humboldt-Universität zu Berlin, and Berlin Institute of Health
14195 Berlin, Germany
E-mail: andrej.trampuz@charite.de

Y. Gao
Department of Ultrasound
West China Hospital
Sichuan University
610041 Chengdu, China

F. Yang
Department of Physics
Freie Universität Berlin
Arnimallee 14, 14195 Berlin, Germany

J. L. Low, B. Paulus
Institute of Chemistry and Biochemistry
Freie Universität Berlin
Arnimallee 22, 14195 Berlin, Germany

Y. Wang
College of Materials Science and Engineering
Nanjing University of Aeronautics and Astronautics
210016 Nanjing, China

C. Cheng
College of Polymer Science and Engineering, State Key Laboratory of
Polymer Materials Engineering
Sichuan University
610065 Chengdu, China
E-mail: chong.cheng@scu.edu.cn

 The ORCID identification number(s) for the author(s) of this article can be found under <https://doi.org/10.1002/adfm.202301986>

© 2023 The Authors. Advanced Functional Materials published by Wiley-VCH GmbH. This is an open access article under the terms of the Creative Commons Attribution-NonCommercial License, which permits use, distribution and reproduction in any medium, provided the original work is properly cited and is not used for commercial purposes.

DOI: 10.1002/adfm.202301986

bacterial infections but also for controlling the glucose levels in diabetic ulcers.

Glucose oxidase (GOx) is a natural enzyme originally generated by fungi and insects.^[5] Recently, it has been explored as a good candidate for treating bacterial diabetic ulcers, since it shows the ability to catalyze the glucose oxidation to generate hydrogen peroxide (H_2O_2), which is toxic to bacteria. Moreover, since glucose is one of the major nutrition sources for bacterial growth, its consumption can also lead to bacterial starvation.^[6] Until now, GOx has been encapsulated in diverse matrices like hydrogel,^[7–8] metal-organic frameworks,^[9–11] covalent organic frameworks,^[12–13] and porous silica^[14] to fabricate therapeutic platforms. However, to achieve effective antibacterial efficacy, the dosage or concentration of H_2O_2 must be very high, which causes inevitable toxicity and inflammation. Recent studies have innovatively combined GOx and peroxidase (POD) in a single system in which the generated H_2O_2 can be further catalyzed into more efficient bactericidal hydroxyl radicals ($\bullet OH$), thus achieving a better therapeutic effect with higher biosafety.^[15–16] Nevertheless, these natural-enzyme-based therapies still face challenges due to their high synthesis cost, poor stability, and limited mass production.

Inspired by the natural POD with multiple transition metallic active sites coordinated by nitrogen and oxygen, transition-metal-based composites have been constructed and applied for diverse scenarios that require the mass generation of OH. For example, $[FeIII(OH)(tpena)]^+$ complex was synthesized and proven to activate H_2O_2 with the formation of OH under pH 8,^[17] Co_3O_4 nanoplates were synthesized as POD mimics for detecting glucose in the presence of GOx,^[18] and copper-based nanozymes were designed for phenol degradation.^[19] These results confirm that the transition metallic sites serve as high-performance POD mimics. However, their bioapplications are still very limited because of the potential toxicity from ion leaching. This limitation prompted us to develop bionanocatalytic medicines with single metallic atom catalytic centers; here we can not only take maximum advantage of metal, but also minimize the danger of ion leaching, since the overall dosage of metal is significantly reduced and these metallic atoms are fixed by heteroatoms in the matrix. In addition, recent studies have revealed that small gold nanoparticles (AuNPs, approved by the US Food and Drug Administration)^[20] of ≈ 5 nm in diameter can oxidize glucose to generate gluconic acid and H_2O_2 , just as GOx does.^[21] Due to their high biosafety and easy synthesis, we consider AuNPs an excellent building block for constructing abiotic GOx-POD mimetic cascade catalytic platforms. To the best of our knowledge, such a rational design of dual-enzyme mimetic AuNPs/single metallic atomic bionanocatalysts for treating multidrug-resistant bacterial diabetic ulcer has not been reported until now.

In this work, we synthesized an AuNP-anchored copper single atomic bionanocatalyst (Au@CuBCats) as a novel GOx-POD dual enzyme mimetic treatment platform for bacterial diabetic ulcers. Specifically, the AuNPs can serve as GOx mimics and catalyze the oxidation of glucose for the formation of H_2O_2 ; the H_2O_2 can then be further catalytically converted into OH via POD-mimetic copper single atoms without extra energy input. Thus, upon the treatment with Au@CuBCats, both glucose concentration and bacterial infection in diabetic ulcers can be effectively controlled. Notably, the unique copper single atoms coordinated by one oxygen and two nitrogen atoms (CuN_2O_1) exhibit better

POD catalytic performance than natural horseradish peroxidase (HRP). Further density functional theory (DFT) calculations were conducted to facilitate a fundamental understanding of the catalytic activity and reveal the advantage of the CuN_2O_1 structure compared to other copper single-atom sites. In vitro antibacterial results demonstrate that bionanocatalysts can induce a significant bacteria-killing effect against both gram-positive and gram-negative strains. In vivo study of bacterial diabetic ulcers in a rabbit ear model confirms the outstanding therapeutic efficacy and biosafety of the bionanocatalyst. Therefore, we believe that this novel bionanocatalyst will provide essential perspectives to the next generation of antibiotic-free strategies for combating MDR bacterial infection of diabetic ulcers, and that it will also yield inspiration for designing bionanocatalytic cascading medicines.

2. Results and Discussion

The synthesis of the Au@CuBCats started with the coordination reaction of copper ions and chloranilic acid (CA), and the obtained precursors were termed as CuCA. Then, CuCA was subjected to a dicyandiamide (DCD)-assisted pyrolysis step followed by an acid etching step, producing the bionanocatalysts with abundant single-atomic copper, termed as CuBCats. Finally, the gold nanoparticles were reduced in situ on CuBCats' surface to obtain the final product, Au@CuBCats, as illustrated in **Figure 1a**. We then systematically studied the chemical and physical structures of Au@CuBCats by scanning electron microscopy (SEM), scanning transmission electron microscopy (STEM), X-ray powder diffraction (XRD), X-ray photoelectron spectroscopy (XPS) and X-ray absorption spectroscopy (XAS). Both STEM images (**Figure 1b**; **Figure S1**, Supporting Information) and SEM images (**Figure S2**, Supporting Information) confirmed that the bionanocatalysts had 2D structures before-and-after AuNPs loading. Meanwhile, we observed from the aberration-corrected high-angle annular dark-field scanning transmission electron microscopy images with atomic resolution (**Figure 1c**; **Figure S3a**, Supporting Information) that the isolated copper atoms were well-dispersed on the carbon matrix, where no apparent copper particle or cluster was found. Energy dispersive spectroscopy (EDS) mapping (**Figure 1d**; **Figure S3b**, Supporting Information) suggested that various elements were uniformly distributed in the bionanocatalysts. Also, the XRD pattern (**Figure S4**, Supporting Information) showed no copper crystal peaks; instead, the typical peaks for the (111), (200), (220), and (311) facets of AuNPs appeared, confirming the successful synthesis of Au@CuBCats.

The XPS survey scanning of CuCA-C (CuCA-C is the CuBCats without acid etching), CuBCats, and Au@CuBCats shows a clear N peak, whereas no apparent N signal was noticed for CuCA precursors, suggesting that the DCD-assisted pyrolysis facilitates N-doping (**Figure S5**, Supporting Information). Meanwhile, the atomic ratio of each sample has been summarized based on XPS results in **Table S1** (Supporting Information). Based on the atomic ratio, the AuNPs loading rate was calculated to be 21 wt%. To understand the nitrogen atoms' bonding environment, the high-resolution XPS N1s spectra were fitted (**Figure S6**, Supporting Information). Here we found the highest percentage of pyridinic-N (36.17%), which plays an important role in anchoring atomic metals according to previous studies,^[22–24] suggesting the formation of $Cu-N_x$ sites. To further study the oxidation state

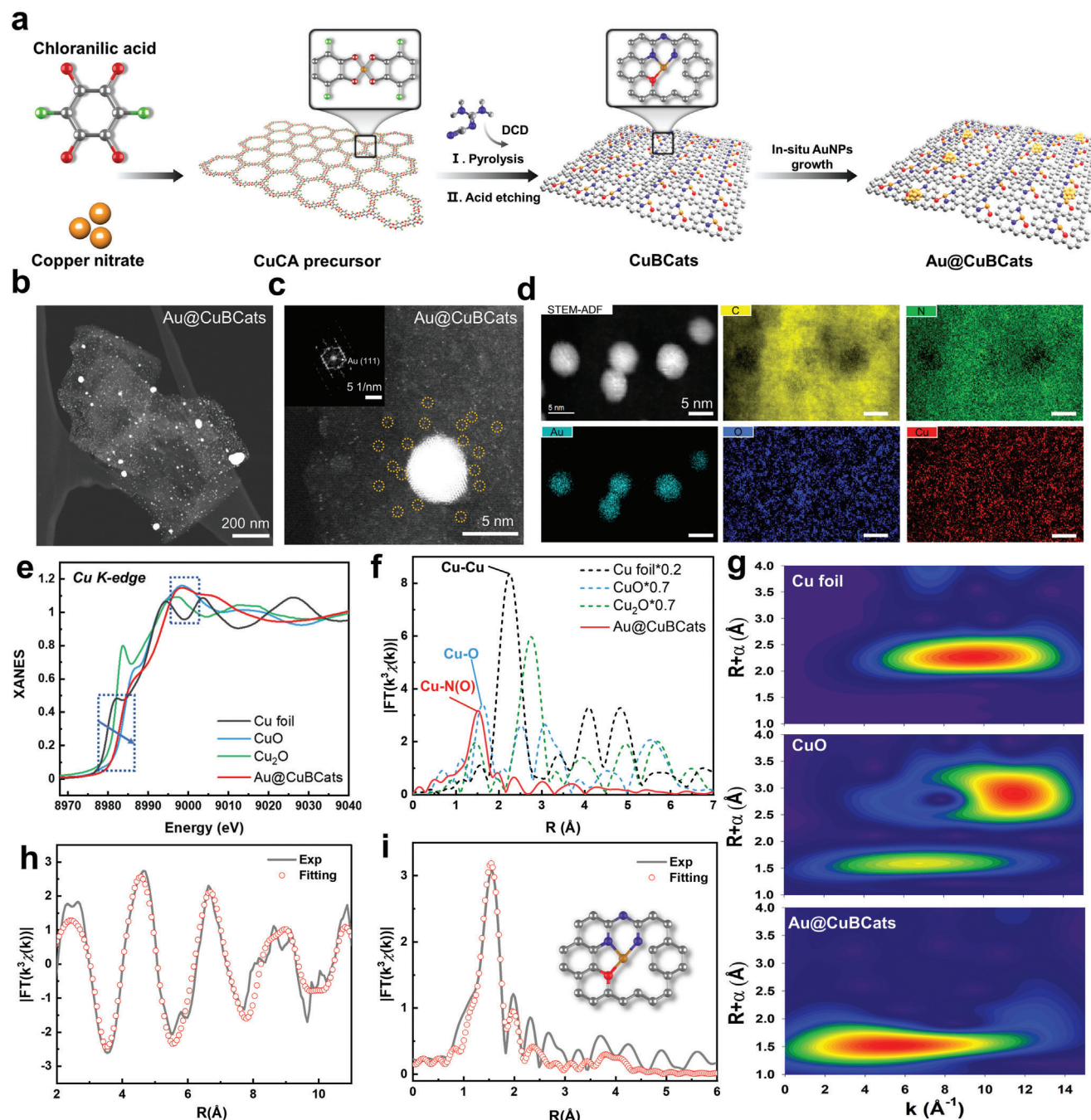


Figure 1. Synthesis and structural characterizations of Au@CuBCats. a) Schematic illustration of the synthesis of Au@CuBCats. b,c) STEM images of Au@CuBCats, on which the copper single-atoms are highlighted by yellow circles. Insert: Fast Fourier transform (FFT) pattern of gold nanoparticle. d) EDS mapping of Au@CuBCats. e,f) XANES and EXAFS spectra at Cu K-edge of Au@CuBCats. g) Wavelet transform of Cu foil, CuO, and Au@CuBCats. h,i) EXAFS fitting result of Au@CuBCats at k and R space, respectively.

of the Cu single atoms in Au@CuBCats, we measured X-ray absorption energy near-edge structure (XANES) of Cu foil, Cu₂O, CuO, and Au@CuBCats (Figure 1e). The results confirmed that the XANES of Au@CuBCats were located between those of Cu₂O and CuO, suggesting the valency of copper single-atoms was between +1 and +2. Subsequently, the extended X-ray absorption fine structure (EXAFS) was investigated to analyze the coordina-

tion configurations of the Cu sites. As shown in Figure 1f, the first coordination shell is located at 1.5 Å, suggesting Cu–N or/and Cu–O coordination. Meanwhile, no obvious Cu–Cu scattering at 2.2 Å was noticed in Au@CuBCats. Moreover, wavelet transform based on the EXAFS results was conducted to distinguish the backscattering atoms (Figure 1g). We observed the maximum intensity of Cu foil and CuO at 9.7 and 11.5 Å⁻¹, respectively, which

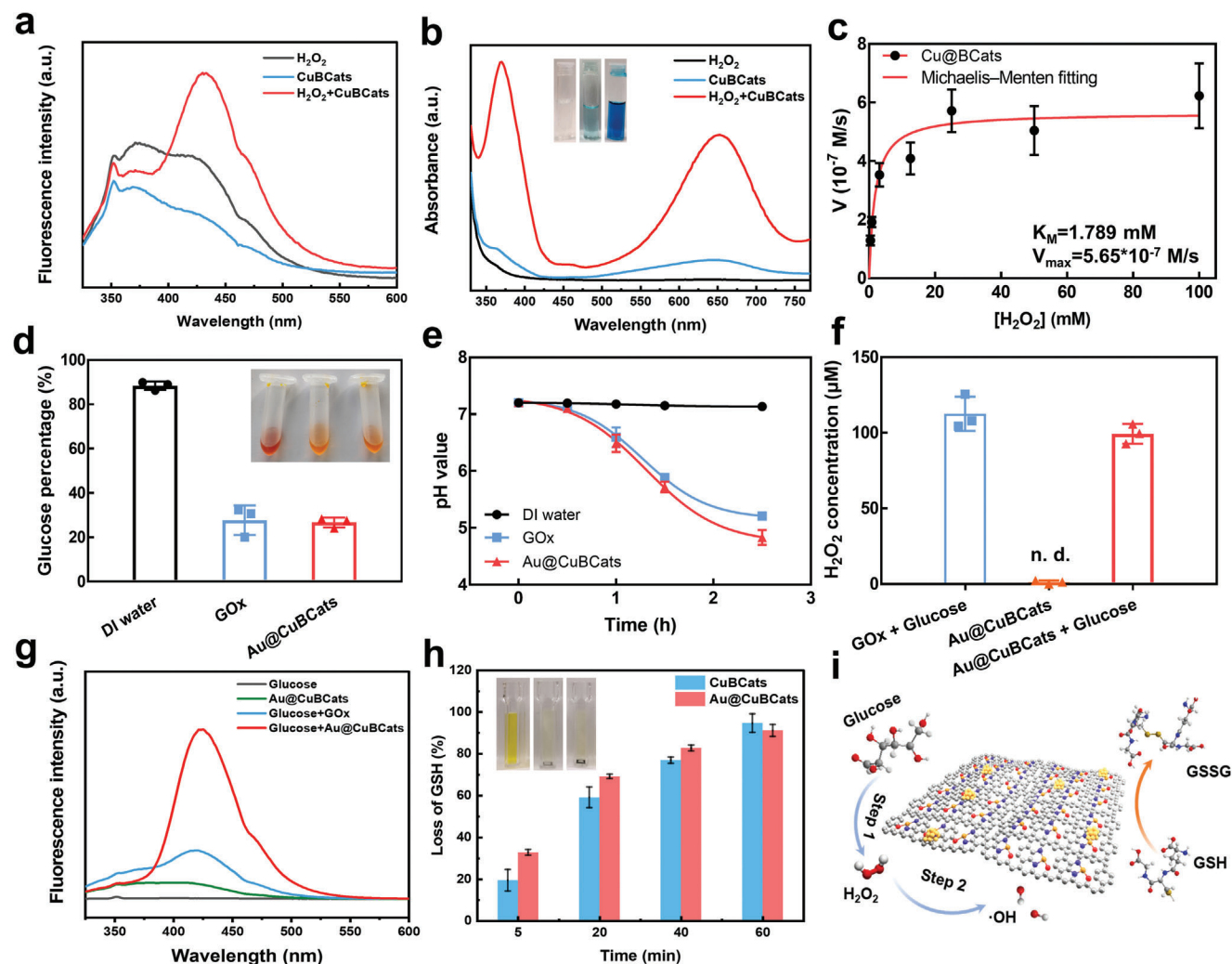


Figure 2. Catalytic performance of Au@CuBCats and CuBCats. a) Fluorescence spectroscopy in the presence of TA for measuring the OH generation property of CuBCats in the presence of H₂O₂, b) UV-Vis spectroscopy in the presence of TMB for characterizing peroxidase-like property, and c) Michaelis–Menten fitting curve of initial oxi-TMB generation velocities against H₂O₂ concentrations. d) Glucose percentage after 2 h incubation. e) The change of pH value with the increasing incubation time. f) H₂O₂ generation after 2 h incubation. n.d. represents non-detectable. g) OH generation property of Au@CuBCats in the presence of glucose. h) GSH consumption caused by Au@CuBCats and CuBCats. i) Schematic illustration of Au@CuBCats as a dual-enzyme-mimetic platform for initiating cascade catalysis and GSH depletion.

can be assigned to the Cu–Cu configuration. In comparison, the Au@CuBCats showed the maximum intensity at 5.2 Å⁻¹, which is assigned to Cu–N or/and Cu–O configuration. Although the copper was pre-anchored by oxygen in CuCA precursors, the coordinated O species also reacted with carbon and escaped under high temperatures.^[25] Meanwhile, the N species generated from dicyandiamide would take over the vacancies during pyrolysis, thus assisting with anchoring the atomic Cu. Based on the synthesis procedures mentioned above, we speculate that both Cu–N and Cu–O exist in this structure. From the fitting result, we determined the coordination number (CN) of Cu–N(O) to be very close to three. Nevertheless, further unveiling the respective coordination number of N and O could be challenging due to the similar bond lengths of Cu–N and Cu–O. Therefore, in accordance with a previous study,^[24] the back-scattering paths of N and O were simultaneously applied to obtain the best-fitting result; the fittings

with fixed CN of N and O were also compared (Table S2 and Table S3, Supporting Information). Upon fitting the EXAFS spectra to various structural models optimized with DFT, we confirmed that the best fit was obtained when the Cu center coordinated with one O atom and two N atoms (Figure 1 h,e). Therefore, the atomic Cu structure model of Au@CuBCats can be deduced; it is shown in the inset of Figure 1i.

Next, to study the OH generation property of bionanocatalysts, terephthalic acid (TA) was used as a probe since it can be oxidized by OH to generate the fluorescent compound TAOH, which can be easily detected by fluorescence spectroscopy under excitation at 315 nm. The significant TAOH signal at 430 nm confirms that CuBCats can catalyze H₂O₂ to generate abundant OH (Figure 2a). This OH generation can be attributed to the intrinsic POD-like activity of the atomic metal center.^[26,27] Thus, a POD substrate, 3,3',5,5'-tetramethylbenzidine (TMB) was used

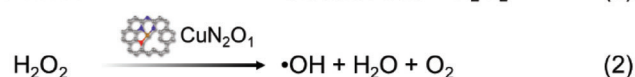
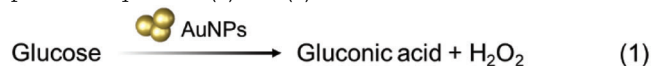
to study the POD-like property and steady-state catalytic kinetics. After 5 min of incubation, the TMB + H₂O₂ + CuBCats group became blue, with remarkable absorption peaks reflecting oxidized TMB at both 370 and 652 nm (Figure 2b). Then, we calculated the Michaelis–Menten constant (K_M) and the maximum initial velocity (V_{max}) to assess the catalytic efficacy of CuBCats (Figure 2c). The K_M value of the CuBCats was 1.789 mM for H₂O₂ substrate, indicating the higher affinity of CuBCats for H₂O₂ than that of HRP (3.70 mM for the H₂O₂ substrate).^[28] Meanwhile, the V_{max} value of CuBCats showed around a 10-fold increase compared to HRP (V_{max} of HRP against H₂O₂ substrate is $8.71 \times 10^{-8} \text{ m s}^{-1}$), suggesting the advanced POD-like performance of atomic copper sites.

After anchoring the AuNPs on CuBCats' surface, glucose was used to initiate the GOx-POD cascade catalytic process of Au@CuBCats. As shown in Figure 2d, a large amount of glucose consumption was noticed after a 2 h incubation with Au@CuBCats, almost equivalent to that of GOx, revealing the comparable glucose oxidative activity of Au@CuBCats ($50 \mu\text{g mL}^{-1}$) and GOx (2 U mL^{-1}). The downstream products—gluconic acid, H₂O₂, and OH were also examined by real-time pH meter, H₂O₂ assay kit, and TA measurement, respectively. We noticed a significant decrease in pH value over the incubation period (Figure 2e), revealing the generation of gluconic acid. Subsequently, we confirmed the generation of H₂O₂ in the Au@CuBCats + glucose group by H₂O₂ assay kit (Figure 2f). In agreement with TA measurements of CuBCats, we further demonstrated that Au@CuBCats can not only continuously catalyze the in situ-generated H₂O₂ to OH (Figure 2g), but also lead to the oxidation of TMB in the presence of glucose (Figure S7, Supporting Information). We did not notice a significant difference of DEM catalytic property of Au@CuBCats after exposing to air at room temperature over one month (Figure S8, Supporting Information). Moreover, glutathione (GSH), a common reducing agent in bacteria, was used as a model compound to test the intrinsic oxidative property of the catalysts. It was observed that the depletion rates of GSH were up to 94.66% and 91.11% at 60 min for CuBCats and Au@CuBCats, respectively, suggesting that these catalysts with single atomic copper sites have great power in weakening the bacterial antioxidant system and inducing oxidative stress. All of the above data confirm that the Au@CuBCats can catalyze the decomposition of glucose to OH via a dual-enzyme-mimetic cascade catalysis, and also further improve ROS treatment efficacy by depleting bacterial alternative oxidase (AOX).

The mechanism of how AuNPs catalyzes the oxidation of glucose to H₂O₂ has been studied both experimentally and theoretically.^[21,29] For the further mechanistic understanding of the entire reaction, we performed DFT studies on the subsequent generation of OH from H₂O₂. Based on geometric fitting to our XAS data, we built a model of CuN₂O₁ embedded in graphene, as shown in Figure 1i. Upon characterizing the first-shell coordination geometry around Cu, we further considered that the N-containing precursor DCD exhibits the N–C–N–C–N connectivity (Figure S9, Supporting Information), prompting us to include an additional nitrogen dopant two atoms away from the coordination N. In fact, among the three possible arrangements of the CuN₂O₁ motifs, the motif shown is most stable only with the ad-

ditional nitrogen dopant (Figure S10, Supporting Information). It is thus likely that this particular CuN₂O₁ arrangement, which fits best to the EXAFS data, is a result of bidentate coordination of DCD onto Cu during pyrolysis, while the remaining O originates from the initial coordination to CA. In addition to CuN₂O₁, other kinds of atomic copper sites were also calculated for comparison.

A proposed scheme of the reaction is shown in Figure 3a. The reaction starts from the adsorption of an H₂O₂ molecule. In the absence of solvent molecules, the geometry optimization of the H₂O₂-adsorbed led to the dissociation of H₂O₂ to form 2OH bound to CuN₂O₁. Although this already highlights the high catalytic activity of the Cu center, it cannot explain how OH radicals could be generated, since OH bound to Cu is unlikely to dissociate as radicals. Nevertheless, this contradiction is resolved by adding a single H₂O molecule to the calculations, upon which dissociation still occurs but the OH can be stabilized by H₂O in the ^{*}OH–H₂O–OH intermediate. With the assistance of H₂O, the OH is able to diffuse away from the reaction center instead of binding to Cu. For comparison of the dissociation kinetics, we further obtained the transition state for the dissociative step. In this mechanism, the OH that remains bound to the CuN₂O₁ site is unlikely to spontaneously desorb on its own as OH because of its strong binding (Figure S11, Supporting Information). Instead, the catalyst can be regenerated via protonation-reduction of ^{*}OH to form H₂O that finally desorbs. Since the evolution of O₂ was generated during the reaction (Figure S12, Supporting Information), we assumed the electrons originate from other H₂O₂ molecules and simulated the final reductive step at the standard reduction potential $U = E^0(\text{O}_2/\text{H}_2\text{O}_2) = 0.70 \text{ V}$. Based on both experimental and theoretical results we mentioned above, the possible reaction mechanism of the cascading catalysis of was proposed as Equations (1) and (2):



A combined free energy diagram, shown in Figure 3b, confirms that the reaction on the CuN₂O₁ site has a significantly lower energy barrier (0.44 eV) than that of CuN₄ (Figure 3b) and is thus more suitable for the H₂O₂ decomposition. In contrast, the dissociation of H₂O₂ on CuN₃ could be considered barrier-free, as the dissociation already occurs upon geometry optimization of the H₂O₂(H₂O) intermediate. However, the instability of CuN₃ is reflected in the final reductive step, where the release of ^{*}OH would be inhibited. Therefore, in contrast to the other two motifs, CuN₂O₁ exhibits the ideal reactivity, one that is favorable for both the dissociation and desorption steps. Bader charge analysis showed the CuN₂O₁ center to be positively charged at +0.72 e, a value between those of CuN₄ (+1.11 e) and CuN₃ (+0.68 e). Generally, a more positively charged center implies a higher oxidation state of Cu and a lower tendency for releasing ^{*}OH,^[22] consistent with the result for the OH-releasing step in the free energy diagram: the free energy for releasing ^{*}OH: CuN₄ > CuN₂O₁ > CuN₃. From the above results, we can conclude that the POD-like reaction pathway of atomic copper centers can be much improved by adjusting the copper coordination microenvironment.

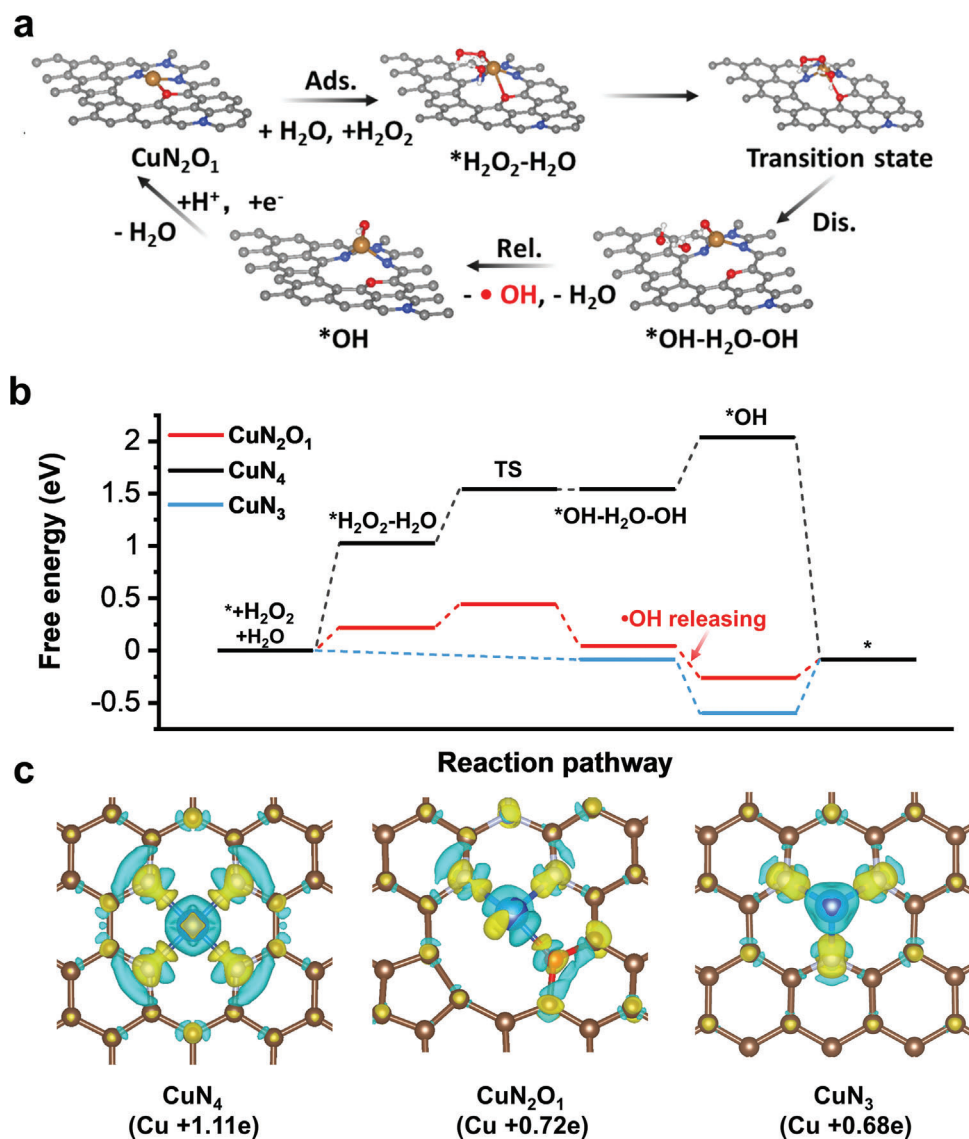


Figure 3. Mechanism of POD-like activity on CuN₂O₁ site. a) Scheme of the proposed reaction mechanism on CuN₂O₁ site. b) Free energy diagram for the reaction process on CuN₂O₁, CuN₄, and CuN₃ sites. c) Charge density difference plot and Bader charge of Cu in CuN₂O₁, CuN₄, and CuN₃ sites.

Encouraged by the above experimental and theoretical studies, we expect that the Au@CuBCats can serve as an ideal bactericidal agent in the presence of glucose via DEM cascade catalysis. To prove this concept, methicillin-resistant *Staphylococcus aureus* (MRSA, Gram-positive multidrug-resistant strain) and clinically isolated extended-spectrum β -lactamases producing *E. coli* (ESLP *E. coli*, a gram-negative MDR strain) were selected as representative bacteria for the in vitro antibacterial study. As shown in **Figure 4a**, the bacterial colonies of both strains after treatment with Au@CuBCats were significantly smaller than those treated by PBS, glucose, glucose+GOx and glucose+CuBCats. Importantly, we noticed a significant difference ($P < 0.0001$) between glucose+GOx and glucose+Au@CuBCats groups (**Figure 4c**), attributable to the OH, generated by the cascade catalysis, further improving bactericidal performance.

Furthermore, we used SEM and confocal laser scanning microscope (CLSM) to investigate the antibacterial mechanism of Au@CuBCats from morphology and intracellular ROS level aspects, respectively. From SEM images (**Figure 4b**), we observed that the MRSA and ESLP *E. coli* exposed to the PBS, glucose and glucose+CuBCats maintained their original plump structures with intact outer membranes. After being treated with glucose+GOx, we noticed some distorted bacterial structures owing to the oxidative damage from H₂O₂. By contrast, in the group treated with glucose+Au@CuBCats, most of the bacteria suffered significant morphological deformations like collapse, distortion and breakage (highlighted by red arrows), indicating the highest bactericidal efficacy. Apart from the planktonic bacterial model, we also tested the antibiofilm performance. As shown in **Figure S13** (Supporting Information), significant

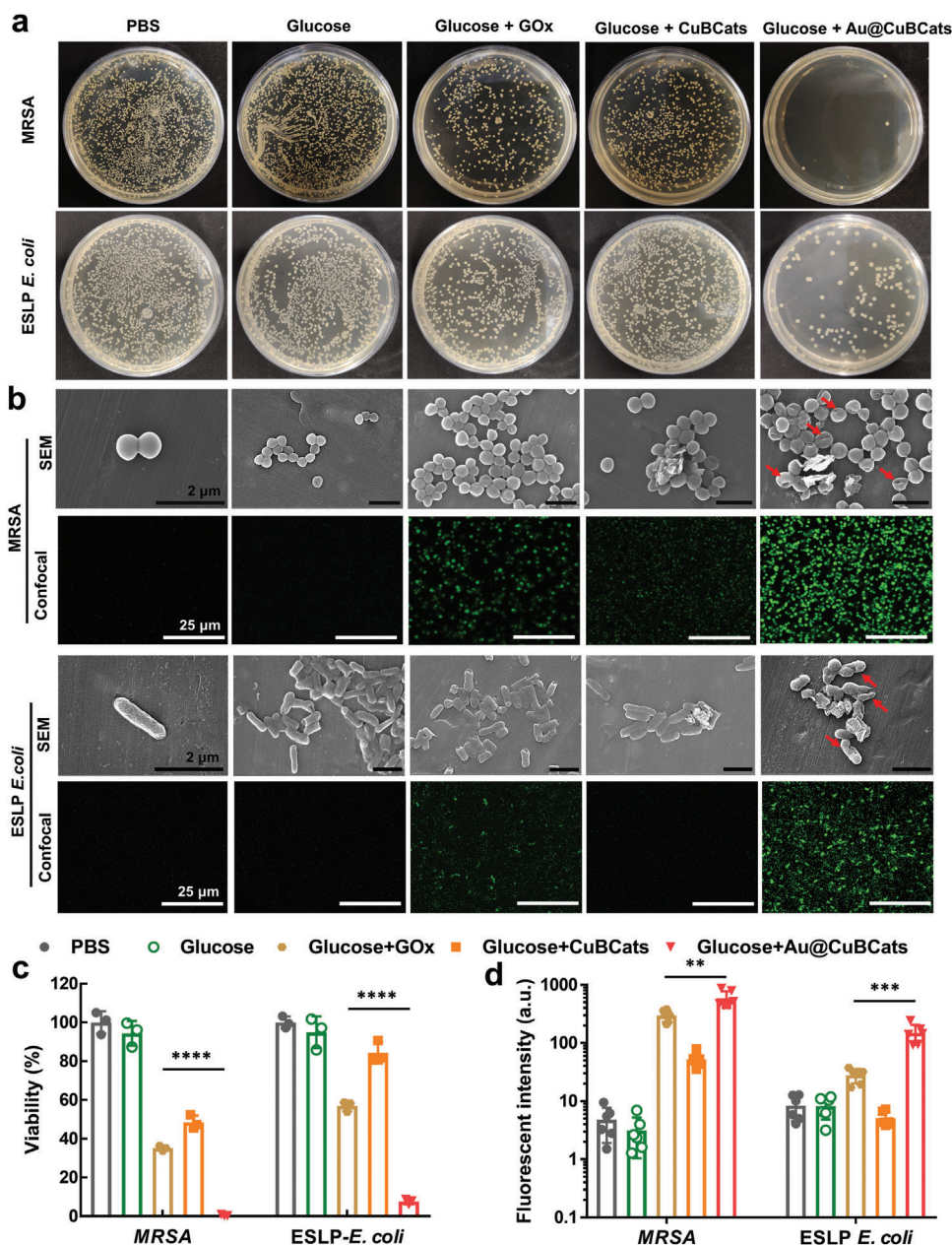


Figure 4. In vitro bacterial killing profile of Au@CuBCats. a) Bacterial colonies after different treatments. b) SEM and CLSM images for bacterial cells after different treatments. Before confocal observation, the bacteria were dye-labelled by 2',7'-dichlorodihydrofluorescein diacetate (DCF-DA) assay kit, which revealed the intracellular ROS level of bacteria. White scale bar: 25 μm . Black scale bar: 2 μm . c) Bacterial viability calculated from agar plates. The data are normalized to the PBS-treated group as 100% and presented as mean \pm SD, $n = 3$. d) Semiquantitative statistics of intercellular ROS level of bacteria. The data are estimated from six fluorescent images by ImageJ. * $p < 0.05$; ** $p < 0.01$; *** $p < 0.001$; **** $p < 0.0001$ by multiple t -tests for data in (c) and (d).

biofilm biomass reduction can be noticed for all Au@CuBCats treated groups. When the concentration was 800 $\mu\text{g mL}^{-1}$, Au@CuBCats were able to reduce 84.6% of biofilm, suggesting the robust antibiofilm effect. We then applied a fluorescent probe, namely DCF-DA, to further determine the intracellular ROS level of bacteria. Consistently, we found the highest intracellular ROS level for both strains in the glucose+Au@CuBCats treatment group (Figure 4b,d), suggesting that the highest oxidative stress was induced by OH. Interestingly, we also noticed that

the Au@CuBCats were able to effectively reduce the intracellular GSH level of MRSA (Figure S14, Supporting Information), leading to the oxidative stress.

Before conducting animal experiments, we first evaluated the biosafety of Au@CuBCats in both cellular and blood level. From CCK-8 results, we noticed the cell viability could fully recover to $\approx 100\%$ at day 3 after treatment by Au@CuBCats below 200 $\mu\text{g mL}^{-1}$ (Figure S15, Supporting Information). Also, the Au@CuBCats exhibited no hemolytic effect even under high

concentration of $800 \mu\text{g mL}^{-1}$ (Figure S16, Supporting Information). Therefore, we are confident to further investigate the Au@CuBCats' ability for healing infected diabetic ulcers (Figure 5a). Wounds (6 mm in diameter) were inflicted on the ear of the diabetic rabbits and subsequently infected by *MRSA* to become ulcers. The formed diabetic ulcers were then randomly divided into four groups ($n = 6$ for each group) based on the following treatments: i) PBS; ii) CuBCats; iii) Vancomycin; iv) Au@CuBCats. To monitor the ulcer healing process, we photographed the ulcers every 4 days and the ulcer area was calculated from these images. As shown in Figure 5b and Figure S17 (Supporting Information), the vancomycin and Au@CuBCats groups recovered significantly faster and achieved 100% ulcer closure at day 11, when swollen ulcers were still observed in the PBS and CuBCats groups. Also, we found no viable *MRSA* colony for the vancomycin and Au@CuBCats groups (Figure 5c; Figure S18, Supporting Information). Consistent with these results, the bacterial number (BN) in the epidermis was calculated from the Giemsa staining (Figure 5d,e). Almost no bacterial cells were found in the epidermis for the vancomycin and Au@CuBCats groups, revealing that Au@CuBCats' bactericidal efficacy is as robust as that of vancomycin.

To further investigate the epidermis recovery and potential toxicity of Au@CuBCats at the tissue level after treatment, we collected the ulcer area and conducted systematic histological studies (Figure 5d,e). In order to determine inflammation levels in the ulcers after the different treatments, we applied hematoxylin and eosin (H&E) staining and immunofluorescence staining of proinflammatory cytokines including interleukin-1 beta (IL-1 β) and tumor necrosis factor-alpha (TNF- α).^[30] From H&E staining, we analyzed the inflammatory infiltration area (IIA) in ulcer tissues. Notably, the tissues of the Au@CuBCats and vancomycin groups exhibited well-ordered collagen structures and no apparent inflammation, properties similar to healthy tissues (Figure S19, Supporting Information). The absence of visible lesions demonstrates the good biosafety of Au@CuBCats treatment. By contrast, a great number of neutrophils and large IIA were observed for the tissues in the PBS and CuBCats groups, suggesting severe tissue inflammation originating from the surviving bacterial colonies. Compared to the PBS group, the vancomycin and Au@CuBCats groups showed very limited IL-1 β expressions of 14.31% and 10.12%, respectively. In addition, significantly less TNF- α was found in the vancomycin (5.95%) and Au@CuBCats (6.59%) groups than in the PBS group. Besides, we did not find any lesion in major organs' H&E staining images (Figure S20, Supporting Information). These data confirmed the highly efficient therapeutic effect and good biosafety of the Au@CuBCats treatment.

The rebirth of collagen and vessels is an important indicator of tissue recovery.^[31,32] Therefore, we used Masson's trichrome staining and cluster of differentiation 31 (CD31) immunofluorescence staining, respectively, to study the ulcer healing status via collagen deposition and neovascularization. The group treated with Au@CuBCats showed the highest collagen deposition area (CDA), suggesting the best collagen recovery. The CD31 expressions in the PBS and CuBCats groups were apparently limited as compared to the Au@CuBCats and vancomycin groups, with tissues still unrecovered from bacterial infection. Meanwhile, the Au@CuBCats and vancomycin groups had more than

twice as many new vessels as the PBS group, confirming accelerated tissue healing. Taken together, these results demonstrate that Au@CuBCats can effectively cure bacterial diabetic ulcers in vivo and achieve accelerated regenerative ulcer healing. Also, as a ROS-based antibacterial therapy, the proposed Au@CuBCats have advantages like less possibility to arouse bacterial resistance, higher stability, and wider antibacterial spectrum as comparing to vancomycin. Therefore, we believe the Au@CuBCats show the potential as an antibiotic alternative for treating diabetic bacterial ulcers.

3. Conclusion

In conclusion, we synthesized a GOx-POD DEM bionanocatalyst Au@CuBCats. Via the DEM cascading catalysis by AuNPs and copper single atoms, the glucose can be catalyzed in situ to generate OH without extra energy input. Notably, the unique copper single atoms coordinated by one oxygen and two nitrogen atoms (CuN₂O₁) exhibit better POD catalytic performance than natural HRP. Further DFT calculations were performed to understand the catalytic mechanism and reveal the advantage of the CuN₂O₁ structure over other copper single-atom sites as both the dissociation of H₂O₂ and desorption of *OH are kinetically accessible. In vitro antibacterial results demonstrated that bionanocatalysts could induce significant bacterial reduction against the MDR bacterial strains *MRSA* and ESLP *E. coli*. In our in vivo study of bacterial diabetic ulcers in a rabbit ear model, the Au@CuBCats group exhibited rapid 100% recovery of the ulcer without any remaining inflammation lesion, suggesting the bionanocatalyst's outstanding therapeutic efficacy and biosafety. This work provides a proof of concept of a multi-enzyme mimetic bionanocatalyst serving as an MDR bacterial diabetic ulcer treatment. We also believe that this work will offer inspirations for designing the antibiotic-free bactericidal system and bionanocatalytic cascading medicines.

4. Experimental Section

Reagents: The chemical reagents including the cell culture materials were provided by commercial sources. All the reagents were of analytical grade and were used without further purification. ESLP *E. coli* was clinically isolated from patients in Charité and *MRSA* (ATCC 43 300) was purchased from American Type Culture Collection. Ultrapure water (18.2 M Ω ; Millipore Co., USA) was applied in all experiments.

Instruments: STEM and EDX Mapping images were recorded by a JEOL JEM-ARM 200F scanning transmission electron microscope equipped with a cold field emission electron source, a DCOR probe corrector (CEOS GmbH), a 100 mm² JEOL Centurio EDX detector microscope. SEM images were obtained by using SU8030 scanning electron microscope (Hitachi). XAS spectra at the copper K-edge were collected at the BESSY synchrotron (Berlin, Germany) at beamlines KMC-3. The UV absorption spectra were recorded by M200 P Infinite PRO microplate reader (Tecan). The fluorescent spectra were measured by Fluorescence Spectrometer FP-6500 (Jasco). The fluorescence images were taken with Leica TCS SP8 CARS fluorescence confocal microscope.

Synthesis of CuBCats: Typically, 145 mg of copper nitrate hydrate and 1.044 g of chloranilic acid were separately dissolved in 50 mL methanol to get metal and ligand solution, respectively. Then, the metal solution was fast poured into the ligand solution under a high-speed magnetic stirring. The reaction was kept overnight. The products (CuCA precursors) were then washed with ethanol for three times by centrifugation and dried in an oven at 65 °C. Afterwards, the CuCA precursors were mixed with the

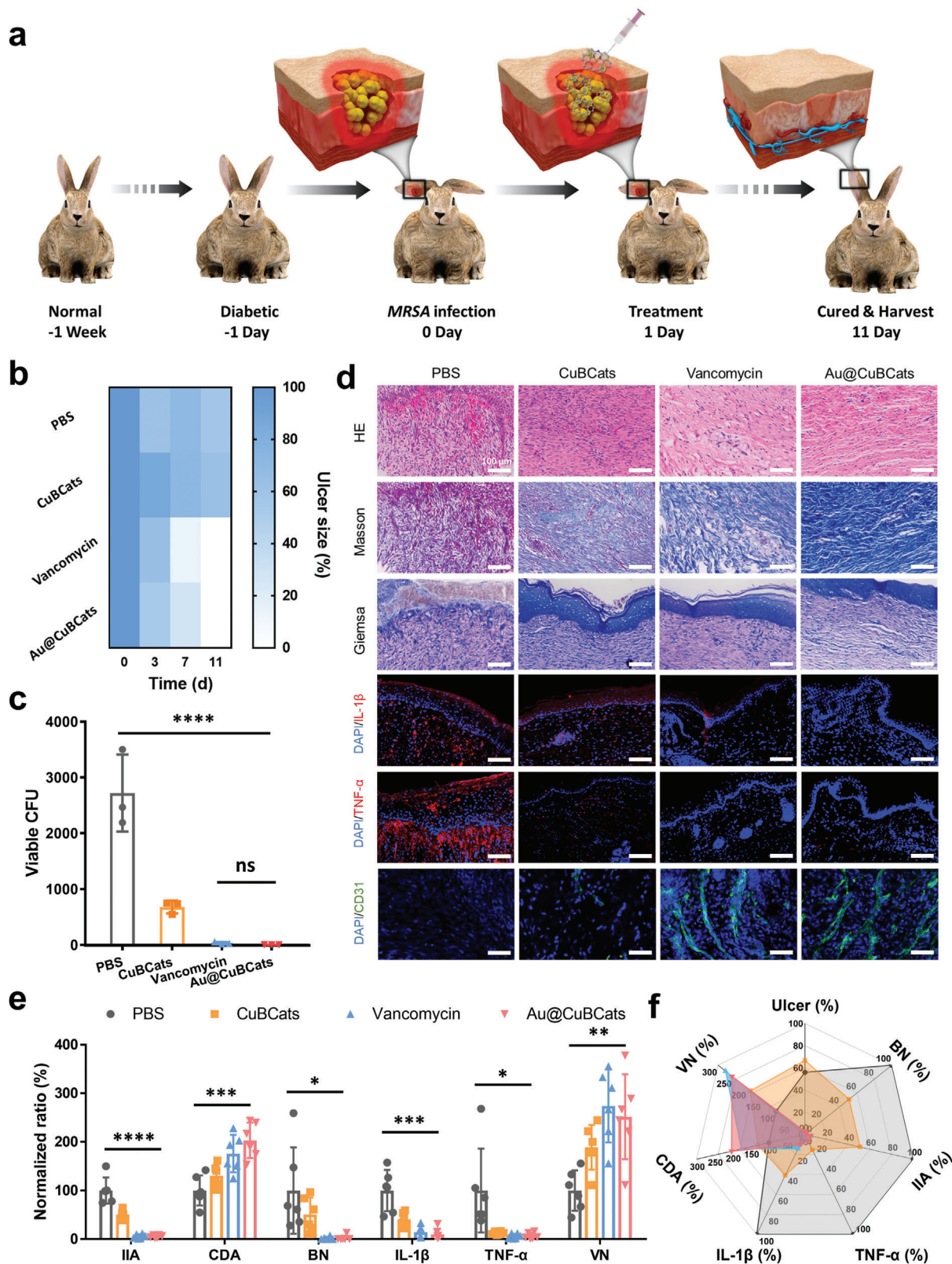


Figure 5. In vivo diabetic ulcer treatment with Au@CuBCats. a) Schematic illustration of the experimental flow. b) Ulcer size ratios with different treatments at days 0, 3, 7, and 11. c) Viable MRSA CFU on ulcer after 11 days of treatment. d) Immunohistochemical studies, and e) corresponding statistical analysis (normalized to PBS group) of diabetic ulcer collected from rabbit at day 11. Scale bar: 100 μ m. f) Overall performance of PBS, CuBCats, vancomycin, and Au@CuBCats in the in vivo diabetic ulcer treatment. The data are estimated from six fluorescent images by ImageJ. * $p < 0.05$; ** $p < 0.01$; *** $p < 0.001$; **** $p < 0.0001$ by multiple t test for data in (c) and (e), ns represents no significant difference.

same mass amount of DCD in corundum boat and then subjected to a 900 °C-pyrolysis step for 3 h in a tube furnace, followed by an acid etching step using 1 M HCl under 90 °C overnight. Finally, the products were washed with water for three times by centrifugation and dried in an oven at 65 °C. We selected 900 °C as the carbonization temperature in order to local adjusting the copper single-atom structures. According to previous studies, when choosing 800 °C or a lower temperature for pyrolysis, metal-N₄ single-atom sites could be easily obtained. While a 900 °C carbonization temperature can facilitate the formation of unsaturated metallic single-atom sites, which possessed higher catalytic activities comparing to the symmetric metal-N₄ single-atom sites.^[33–35]

Synthesis of Au@CuBCats: Typically, 1 mg of CuBCats were homogeneously dispersed in 1 mL of chloroauric acid (HAuCl₄) aqueous solution (2 mM) under the assistance of sonication. The oxygen-containing group within CuBCats could coordinate with Au ions via static interaction. Then, 62.5 μL of fresh prepared sodium borohydride aqueous solution (100 mM) was introduced to the above CuBCats-HAuCl₄ solution under vigorous magnetic stirring. The coordinated Au ions could then be in situ reduced on the CuBCats. After three times of water washing and drying, the final products, Au@CuBCats were obtained.

Computational Details: Spin-polarized DFT calculations were performed with the Vienna ab initio Simulation Package (VASP) in the framework of the projector-augmented wave (PAW) method with energy cutoff $E_{\text{cut}} = 600$ eV.^[36,37] Geometry optimizations (including transition states) and frequency analyses were performed with the PBE functional, followed by single-point calculations with the PBE0 functional.^[38] Grimme D3(BJ) dispersion correction with Becke-Johnson damping was applied to account for Van der Waals interactions.^[39]

The RMM-DIIS algorithm was applied for electronic relaxation during geometry optimization while the conjugate gradient algorithm was applied, starting from the PBE wave function, for the single point calculation. The electronic convergence criterion was set to 10⁻⁵ eV. The Gaussian smearing approach with smearing width $\sigma = 0.05$ eV was applied. K-points were sampled using a 3 × 3 × 1 Γ -centered mesh grid. Ionic relaxation steps were performed with the conjugate gradient algorithm with force convergence of 10⁻² eV Å⁻¹. During geometry optimization, all atomic positions and the unit cell shape were optimized at constant unit cell volume (ISIF = 4). Transition states were obtained using the climbing image nudged elastic band (CI-NEB) method using nine images.^[40]

Supporting Information

Supporting Information is available from the Wiley Online Library or from the author.

Acknowledgements

X.F. and Y.G. contributed equally to this work. This work was financially supported by the National Key R&D Program of China (2019YFA0110600), and Deutsche Forschungsgemeinschaft (DFG) of Germany through grants from the Collaborative Research Centers (SFB) 765 and 1449. The authors are grateful for the support of Benjamin Allen in polishing the language of the manuscript. X.F., F.Y., and L.W. acknowledge the support from China Scholarship Council (CSC). J.L.L. acknowledged support from the Elsa-Neumann Scholarship and the computing resources of Norddeutscher Verbund für Hoch- und Höchstleistungsrechnung (HLRN). Prof. C.C. thanks the support from the National Natural Science Foundation of China (Nos. 52161145402 and 52173133), the Sichuan Science and Technology Program (No. 2021YFH0087), the 1-3-5 Project for Disciplines of Excellence, West China Hospital, Sichuan University (No. ZYJC21047), the innovation project of Med-X Center for Materials, Sichuan University (No. MCM202102), the State Key Laboratory of Polymer Materials Engineering (No. sklpme2021-4-02). The authors thank Li Li, Fei Chen, and Chunjuan Bao of the Institute of Clinical Pathology, Sichuan University, for processing histological staining and BiosupraMol for providing SEM and CLSM. All animal experiments were performed by following the animal

ethical standard from Animal Ethics Committee in West China Hospital, Sichuan University, Chengdu, China, with approval number 2021024A.

Open access funding enabled and organized by Projekt DEAL.

Conflict of Interest

The authors declare no conflict of interest.

Data Availability Statement

The data that support the findings of this study are available from the corresponding author upon reasonable request.

Keywords

cascade catalysis, copper single-atom catalysts, diabetic ulcers, enzyme-mimetic bionanocatalysts, multi-drug resistant bacteria

Received: February 20, 2023

Revised: April 3, 2023

Published online:

- [1] Y. Zheng, S. H. Ley, F. B. Hu, *Nat Rev Endocrinol* **2018**, *14*, 88.
- [2] P. Zimmet, K. G. Alberti, D. J. Magliano, P. H. Bennett, *Nat Rev Endocrinol* **2016**, *12*, 616.
- [3] T. Wang, Y. Li, E. J. Cornel, C. Li, J. Du, *ACS Nano* **2021**, *15*, 9027.
- [4] Y. Liang, M. Li, Y. Yang, L. Qiao, H. Xu, B. Guo, *ACS Nano* **2022**, *16*, 3194.
- [5] C. M. Wong, K. H. Wong, X. D. Chen, *Appl. Microbiol. Biotechnol.* **2008**, *78*, 927.
- [6] Y. Deng, X. Ouyang, J. Sun, X. Shi, Y. Li, Y. K. Chan, W. Yang, S. Peng, *Bioact Mater* **2022**, *25*, 748.
- [7] T. Huang, B. Yuan, W. Jiang, Y. Ding, L. Jiang, H. Ren, J. Tang, *J. Mater. Chem. B* **2021**, *9*, 6190.
- [8] Y. Zhu, J. Zhang, J. Song, J. Yang, Z. Du, W. Zhao, H. Guo, C. Wen, Q. Li, X. Sui, L. Zhang, *Adv. Funct. Mater.* **2020**, *30*, 1905493.
- [9] C. Zhang, L. Zhang, W. Wu, F. Gao, R.-Q. Li, W. Song, Z.-N. Zhuang, C.-J. Liu, X.-Z. Zhang, *Adv. Mater.* **2019**, *31*, 1901179.
- [10] C. Fang, Z. Deng, G. Cao, Q. Chu, Y. Wu, X. Li, X. Peng, G. Han, *Adv. Funct. Mater.* **2020**, *30*, 1910085.
- [11] W. Xu, L. Jiao, Y. Wu, L. Hu, W. Gu, C. Zhu, *Adv. Mater.* **2021**, *33*, 2005172.
- [12] G. Zhang, Y. Ji, X. Li, X. Wang, M. Song, H. Gou, S. Gao, X. Jia, *Adv. Healthc Mater* **2020**, *9*, 2000221.
- [13] X. Wan, H. Zhang, W. Pan, N. Li, B. Tang, *Chem. Commun.* **2021**, *57*, 5402.
- [14] Y. Hu, S. Bai, X. Fan, F. Zhou, B. Chen, S. Tan, H. Xu, A. Pan, S. Liang, Y. He, *Biomater. Sci.* **2022**, *10*, 2358.
- [15] C. Wu, K. Schwibbert, K. Achazi, P. Landsberger, A. Gorbushina, R. Haag, *Biomacromolecules* **2017**, *18*, 210.
- [16] Y. Zhu, J. Zhang, J. Song, J. Yang, Z. Du, W. Zhao, H. Guo, C. Wen, Q. Li, X. Sui, *Adv. Funct. Mater.* **2020**, *30*, 1905493.
- [17] C. J. Miller, Y. Chang, C. Wegeberg, C. J. McKenzie, T. D. Waite, *ACS Catal.* **2021**, *11*, 787.
- [18] Q. Wang, J. Chen, H. Zhang, W. Wu, Z. Zhang, S. Dong, *Nanoscale* **2018**, *10*, 19140.
- [19] J. Wang, R. Huang, W. Qi, R. Su, B. P. Binks, Z. He, *Appl. Catal., B* **2019**, *254*, 452.
- [20] D. Bobo, K. J. Robinson, J. Islam, K. J. Thurecht, S. R. Corrie, *Pharm. Res.* **2016**, *33*, 2373.

- [21] Y. Lin, Z. Li, Z. Chen, J. Ren, X. Qu, *Biomaterials* **2013**, *34*, 2600.
- [22] X. Lu, S. Gao, H. Lin, L. Yu, Y. Han, P. Zhu, W. Bao, H. Yao, Y. Chen, J. Shi, *Adv. Mater.* **2020**, *32*, 2002246.
- [23] Y. Sun, S. Mu, Z. Xing, J. Guo, Z. Wu, F. Yu, M. Bai, X. Han, C. Cheng, L. Ye, *Adv. Mater.* **2022**, *34*, 2206208.
- [24] Y. Cai, J. Fu, Y. Zhou, Y.-C. Chang, Q. Min, J.-J. Zhu, Y. Lin, W. Zhu, *Nat. Commun.* **2021**, *12*, 586.
- [25] H. Luo, L. Lari, H. Kim, S. Hérou, L. C. Tanase, V. K. Lazarov, M.-M. Titirici, *Nanoscale* **2022**, *14*, 910.
- [26] B. Xu, H. Wang, W. Wang, L. Gao, S. Li, X. Pan, H. Wang, H. Yang, X. Meng, Q. Wu, L. Zheng, S. Chen, X. Shi, K. Fan, X. Yan, H. Liu, *Angew. Chem., Int. Ed.* **2019**, *58*, 4911.
- [27] M. Huo, L. Wang, H. Zhang, L. Zhang, Y. Chen, J. Shi, *Small* **2019**, *15*, 1901834.
- [28] L. Gao, J. Zhuang, L. Nie, J. Zhang, Y. Zhang, N. Gu, T. Wang, J. Feng, D. Yang, S. Perrett, X. Yan, *Nat. Nanotechnol.* **2007**, *2*, 577.
- [29] P. Cheng, H. Wang, X. Shi, *Nanoscale* **2020**, *12*, 3050.
- [30] C. Mao, W. Jin, Y. Xiang, Y. Zhu, J. Wu, X. Liu, S. Wu, Y. Zheng, K. M. C. Cheung, K. W. K. Yeung, *Adv. Funct. Mater.* **2022**, *32*, 2202887.
- [31] X. Fan, X. Wu, F. Yang, L. Wang, K. Ludwig, L. Ma, A. Trampuz, C. Cheng, R. Haag, *Angew. Chem., Int. Ed.* **2022**, *61*, e202113833.
- [32] L. Li, S. Cao, Z. Wu, R. Guo, L. Xie, L. Wang, Y. Tang, Q. Li, X. Luo, L. Ma, C. Cheng, L. Qiu, *Adv. Mater.* **2022**, *34*, 2108646.
- [33] S. Ma, Z. Han, K. Leng, X. Liu, Y. Wang, Y. Qu, J. Bai, *Small* **2020**, *16*, 2001384.
- [34] C. Yan, H. Li, Y. Ye, H. Wu, F. Cai, R. Si, J. Xiao, S. Miao, S. Xie, F. Yang, *Energy Environ. Sci.* **2018**, *11*, 1204.
- [35] W. Zheng, J. Yang, H. Chen, Y. Hou, Q. Wang, M. Gu, F. He, Y. Xia, Z. Xia, Z. Li, *Adv. Funct. Mater.* **2020**, *30*, 1907658.
- [36] G. Kresse, J. Hafner, *Phys. Rev. B* **1993**, *47*, 558.
- [37] G. Kresse, J. Furthmüller, *Comput. Mater. Sci.* **1996**, *6*, 15.
- [38] J. P. Perdew, K. Burke, M. Ernzerhof, *Phys. Rev. Lett.* **1996**, *77*, 3865.
- [39] S. Grimme, S. Ehrlich, L. Goerigk, *J. Comput. Chem.* **2011**, *32*, 1456.
- [40] G. Henkelman, B. P. Uberuaga, H. Jónsson, *Chem. Phys.* **2000**, *113*, 9901.

ADVANCED FUNCTIONAL MATERIALS

Supporting Information

for *Adv. Funct. Mater.*, DOI 10.1002/adfm.202301986

A Copper Single-Atom Cascade Bionanocatalyst for Treating Multidrug-Resistant Bacterial Diabetic Ulcer

Xin Fan, Yang Gao, Fan Yang, Jian Liang Low, Lei Wang, Beate Paulus, Yi Wang, Andrej Trampuz, Chong Cheng* and Rainer Haag**

Supporting Information

©Wiley-VCH 2023

69451 Weinheim, Germany

A Copper Single-Atom Cascade Bionanocatalyst for Treating Multidrug-Resistant Bacterial Diabetic Ulcer

Xin Fan, Yang Gao, Fan Yang, Jian Liang Low, Lei Wang, Beate Paulus, Yi Wang, Andrej Trampuz*, Chong Cheng*, and Rainer Haag*

Supporting Information

XAFS measurements and simulations. X-ray absorption spectroscopy (XAS) at the Cu K-edge were performed at beamline KMC-3 at the BESSY-II synchrotron (Helmholtz Center Berlin, Germany) using a set-up including a Si[111] double-crystal monochromator, a 13-element energy-resolving Si-drift detector (RaySpec) for X-ray fluorescence monitoring, and DXP-XMAP pulse-processing electronics (XIA). Samples were held at 20 K in a liquid-helium cryostat (Oxford). The energy axis of the monochromator was calibrated (accuracy ± 0.1 eV) using the K-edge spectrum of copper foil (fitted reference energy of 8979 eV in the first derivative spectrum). The spot size on the samples was ca. 1.5 x 2.0 mm (vertical x horizontal) as set by a focusing mirror and slits. X-ray fluorescence spectra were collected using a continuous scan mode of the monochromator (scan duration ~ 10 min). 3 scans were averaged (1-2 scans per sample spot) for signal-to-noise ratio improvement. XAS data were processed (dead-time correction, background subtraction, normalization, self-absorption correction) to yield XANES and Cu-EXAFS spectra using our earlier described procedures and in-house software.^[1] k^3 -weighted EXAFS spectra were simulated with in-house software and phase functions from FEFF9. The range of the fits was 2.3-10.3 Å, and the amplitude reduction factor (S_0^2) was 0.89. The errors represent the 68% confidence interval of the respective fit parameter in all EXAFS fit tables. The obtained R_f value of the fits are given for the distance range of interest (1-5 Å of reduced distance).

GOx-mimetic activity of Au@CuBCats. To evaluate the GOx-mimetic activity of Au@CuBCats, we tested the glucose consumption, the pH changing and the H₂O₂ generation after certain time of incubation.

For the glucose consumption experiment, typically, 100 μL of Au@CuBCats aqueous dispersion (1 mg/mL) was mixed with 100 μL of glucose solution (1 mg/mL), and 3,5-dinitrosalicylic acid (DNS) method was used to evaluate the glucose concentration. In brief, after a 2.5-hour incubation, 0.6 mL of DNS reagent was added to above solution, which was then heated at 100 $^{\circ}\text{C}$ for 5 minutes and quickly transferred to cool water for 20 minutes. The free GOx (2U/mL) and DI water groups served as comparison.

For pH changing monitoring, Au@CuBCats aqueous dispersion was added into glucose solution, which was dissolved in PBS (0.5 mM, initial pH=7.2). The final concentrations of Au@CuBCats and glucose were 50 $\mu\text{g}/\text{mL}$ and 100 mM, respectively. pH value was recorded with a real-time pH meter.

For H_2O_2 generation experiment, a H_2O_2 assay kit (PierceTM) was employed, which is based on the oxidation of ferrous ions (Fe^{2+}) to ferric ions (Fe^{3+}) by peroxides and the Fe^{3+} then combine a xylenol orange to form a purple-colored complex with the maximum absorbance at 560 nm. In brief, the reaction solution was centrifuged at 14,800 r.p.m. for 5 min and the supernatants were collected. Finally, the supernatants and detection solution were mixed for 30 min at room temperature and then measured using a microplate reader. The level of H_2O_2 in products was calculated according to a standard concentration curve with triplicate experiments.

•OH generation activity of the bionanocatalysts. Terephthalic acid (TA) was used as a fluorescent probe that easily reacts with •OH to form a highly fluorescent product, 2-hydroxy terephthalic acid (HA). In a typical procedure, 150 μg of the bionanocatalysts were dispersed in 1.5 mL of PBS (0.5 mM, pH~7.2). Then, the dispersions were mixed with 1.5 mL of 6 mM TA solution containing 200 μM H_2O_2 (or 2 mM glucose) for 12 h in the dark, and finally, the changes in the 435 nm fluorescence emission peak were recorded using a Fluorescence Spectrometer.

Peroxidase-mimetic activity. To monitor the peroxidase-like property of the bionanocatalysts, the 3,3',5,5'-tetramethylbenzidine (TMB) molecular probe was utilized, and reactions were carried out in 0.1 mL acetate buffer solution (0.1 M, pH = 4.0), and the final concentrations of TMB, H_2O_2 , and CuBCats were 1 mM, 100 μM , and 50 $\mu\text{g}/\text{mL}$, respectively. After 5 min reaction time, photos were taken, and the UV-vis absorption spectra were measured by a microplate reader.

For the measurement of Au@CuBCats with dual-enzyme mimetic cascading catalytic performance, the Au@CuBCats were dispersed in PBS (0.5 mM, initial pH=7.2) that containing glucose. Then, the TMB was firstly dissolved in DMSO and then diluted to Au@CuBCats-PBS solution. The final

concentrations for Au@CuBCats, glucose and TMB were fixed to 50 µg/mL, 1 mM and 0.1 mM, respectively. Finally, the absorption at 652 nm was measured by a microplate reader at different incubation times.

The steady-state kinetic assay was performed at room temperature. For kinetic parameters, the experiments were carried out in 100 µL NaAc buffer containing 50 µg/mL CuBCats, 832 µM TMB, and a series of concentrations of H₂O₂ ranging from 0 to 1000 mM. The absorbances of all reactions were monitored in a time-scan mode at 652 nm through a microplate reader, and the Michaelis–Menten constant was calculated according to the Michaelis–Menten saturation curve by GraphPad Prism 7.0 (GraphPad Software).

GSH depletion test. The consumption of GSH was detected with a 5,5'-Dithiobis-(2-nitrobenzoic acid) (DTNB) probe by UV–vis spectroscopy. The bionanocatalysts were mixed with GSH and DTNB in PBS (pH 7.2) at room temperature in the cuvette. The final concentrations of bionanocatalysts, GSH and DTNB were fixed to 50 µg/mL, 0.1 mM and 0.1 mM, respectively. At different points, the absorbance at 410 nm of the mixed solution was recorded by UV–vis spectrophotometer. In this experiment, PBS served as negative control and H₂O₂ served as the positive control and the consumption of GSH was calculated as the following equation, where A(t), A(Pos), and A(Neg) represent the absorbance at 410 nm of bionanocatalysts group, positive control group and negative control group at time t, respectively.

$$\text{Loss of GSH}(\%) = \left(1 - \frac{A(t) - A(\text{Pos})}{A(\text{Neg}) - A(\text{Pos})}\right) \cdot 100\%$$

For the intracellular GSH consumption, we used an assay kit (ab112132, abcam) to evaluate the intracellular GSH levels. Briefly, we diluted the overnight *MRSA* culture by PBS to 10⁷ CFU/mL. Then, we introduced the Au@CuBCats with a final concentration of 50 µg/mL to the bacterial solution and incubated them in a 37 °C oven for 4 h. Afterwards, we strictly followed the instructions of the assay kit to label the bacterial cell by a thiol-dye. The bacterial solution without dye-labeling served as a negative control and the bacterial solution without materials served as positive control. Finally, a flow cytometer was used to evaluate the fluorescence intensity of bacterial solution.

***In vitro* planktonic bacterial killing tests.** Typically, the Au@CuBCats were firstly dispersed in LB media. Then, 100 µL of sample dispersions with a series of dilution times and glucose with the final

concentration of 1 mg/mL were introduced into 100 μ L of $\sim 10^5$ CFU/mL bacterial suspensions. The suspensions were incubated at 37 °C for 4 h. The experimental groups of PBS, glucose, glucose + GOx (2U/mL as a final concentration), and glucose + CuBCats served as a comparison. At last, the bactericidal ratio for the samples under different conditions was studied via agar plate counting. The bacterial suspensions were diluted and cultured on agar plates for 12 h to count the bacterial colonies. Meanwhile, SEM was utilized to observe the morphologies of bacteria after different treatment.

***In vitro* antibiofilm tests.** Typically, we introduced 200 μ L of *MRSA* solution (10^6 CFU/mL) to each well in 96-well plate and cultured them in 37°C oven for 48 hours to obtain biofilms attaching on the bottoms of well. Afterwards, for each well, 100 μ L of Au@CuBCats-PBS solution with different concentrations and glucose with final concentration of 1 mg/mL were placed and incubated in 37°C oven overnight. The biofilms without Au@CuBCats were considered as control group. Next, to remove the Au@CuBCats, the biofilms were gently washed 3 times by PBS and stained by 0.1% crystal violet for 15 minutes in room temperature. Again, the biofilms were gently washed by RO water to remove the excess dye. After drying in room temperature, the crystal violet in the bottom of each well was redissolved by 100 μ L of ethanol, and finally the optical density of each well at 595 nm was analyzed by microplate reader.

Bacterial intracellular ROS level. We used 2',7'-Dichlorofluorescein diacetate (DCF-DA, Sigma-Aldrich) to study the bacterial intracellular ROS level induced by bionanocatalysts. The bacterial cells with final concentration of 10^8 CFU/mL were treated with different groups for 4 h. Afterwards, the treated bacterial cells were washed with PBS for 3 times by centrifugation, followed by being stained with 10 μ M of DCF-DA for 30 min in the dark. The fluorescent bacterial cells were observed with confocal microscope and the fluorescent intensity was quantified by the Image J software.

Hemolytic experiment. Typically, the PBS-diluted red blood cells (RBCs) were mixed with different concentrations of Au@CuBCats in centrifuge tubes. 1% Triton X-100-treated RBCs were considered as the positive control, and PBS-dispersed RBCs were considered as the negative control. All the experimental groups were incubated at 37 °C with shaking for 3 h and then centrifuged at 6000 rpm for 5 min. The absorbance of supernatant was measured at 545 nm by microplate reader.

Cytotoxicity test. Human skin keratinocyte cell line HaCaT was chosen as model cell line to investigate the cells toxicity of the bionanocatalysts. HaCaT cells were grown in Eagle's minimal essential medium (DMEM) supplemented with 10% fetal bovine serum, 4.5 g/L glucose, 2 mM L-

glutamine, 100 mg/ml streptomycin, and 100 units/ml penicillin) in a 96-well plate at 37 °C and 5% CO₂. The cytotoxicity was then measured via CCK-8 assay according to the manufacturer's instruction. Briefly, we seeded the cells in 96-well plates (~ 10⁴ cells/well) and cultured them for 24 hours in oven. Then, different concentrations of Au@CuBCats diluted by DMEM were introduced to wells and cultured with cells for 24 hours in oven. Afterwards, we gently washed the cells by PBS for 2 times to remove the Au@CuBCats and refilled the wells by 100 μL of DMEM. Next, 10 μL of CCK-8 reagent was introduced to each well and the cells were cultured for 2 hours before their optical density being measured by a microplate reader at OD 460 nm. Also, the cell regrowth after exposing to materials for the next two days was recorded by same CCK-8 assay. The cells without adding materials at day 1 were considered as control.

***In vivo* rabbit's ear bacterial diabetic ulcer model.** To assess the therapeutic effects of the bionanocatalysts, we established a diabetic ulcer model. All the studies on these animals were performed by following the animal ethical standard from Animal Ethics Committee in West China Hospital, Sichuan University, Chengdu, China with approval number 2021024A. Male New Zealand white rabbits (3.5-4 kg) were used in the study. The animals were 3-4 months of age. Rabbits were housed in individual cages, with a 12-h light/dark cycle and controlled temperature and humidity. Rabbits were fed a standard chow and water ad libitum. Typically, to establish the diabetic rabbit model, the rabbits were firstly anesthetized after adaptive feeding, and hair was shaved off the back of the ears. Then, Alloxan (150 mg/kg) (Sigma-Aldrich) was made up in 30 mL of saline and administered via an ear vein using an intravenous cannula at a rate of 1.5 mL/min. After treatment, water containing glucose was provided for 24 h to prevent hypoglycemia. Blood glucose levels were measured daily with a glucose strip after the injection and were considered diabetes when blood glucose levels stabilized above 300 mg/dL (16.67 mol/L). Insulin therapy was administered if the animal lost weight and had "high" (> 33 mmol/L) glucose readings using insulin glargine.

To create bacterial diabetic ulcer, the diabetic rabbits were anesthetized after 4 weeks of hyperglycemia. Three wounds were then created on each ear using sterile, disposable 6 mm punch biopsies. The wounds were created and the dermis was exposed to bare cartilage. Then 0.5 mL MRSA bacterial suspension (1×10⁸ CFU/mL) was dropped on the wounds. After being infected for 1 day, the ulcers formed with festering.

The typical treatment procedure was as follows: 100 μL of Au@CuBCats (10 mg/mL) was added to

the ulcers. PBS and vancomycin (16 $\mu\text{g}/\text{mL}$) were also used as a contrast. After 11 days of treatment, the ulcers were cut off and fixed with 10% formaldehyde solution for histological analysis including H&E, Masson, Giemsa, TNF- α , IL-1 β , and CD31 staining. Fluorescence images were observed by automatic microscope (Olympus, IX83).

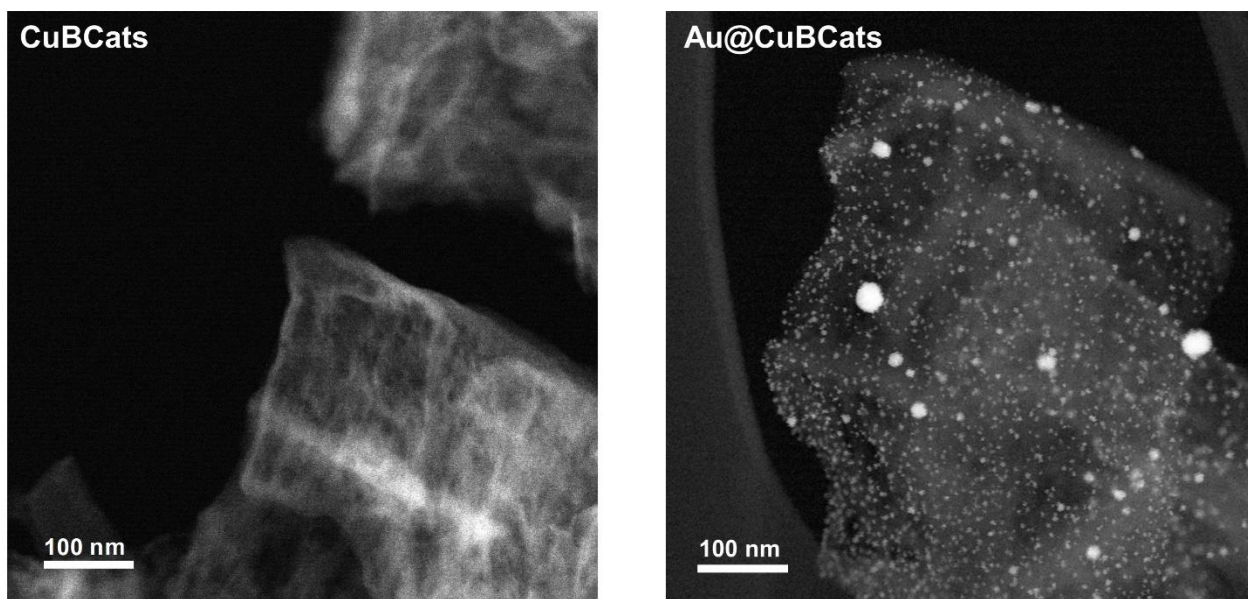


Figure S1. STEM images of CuBCats and Au@CuBCats.

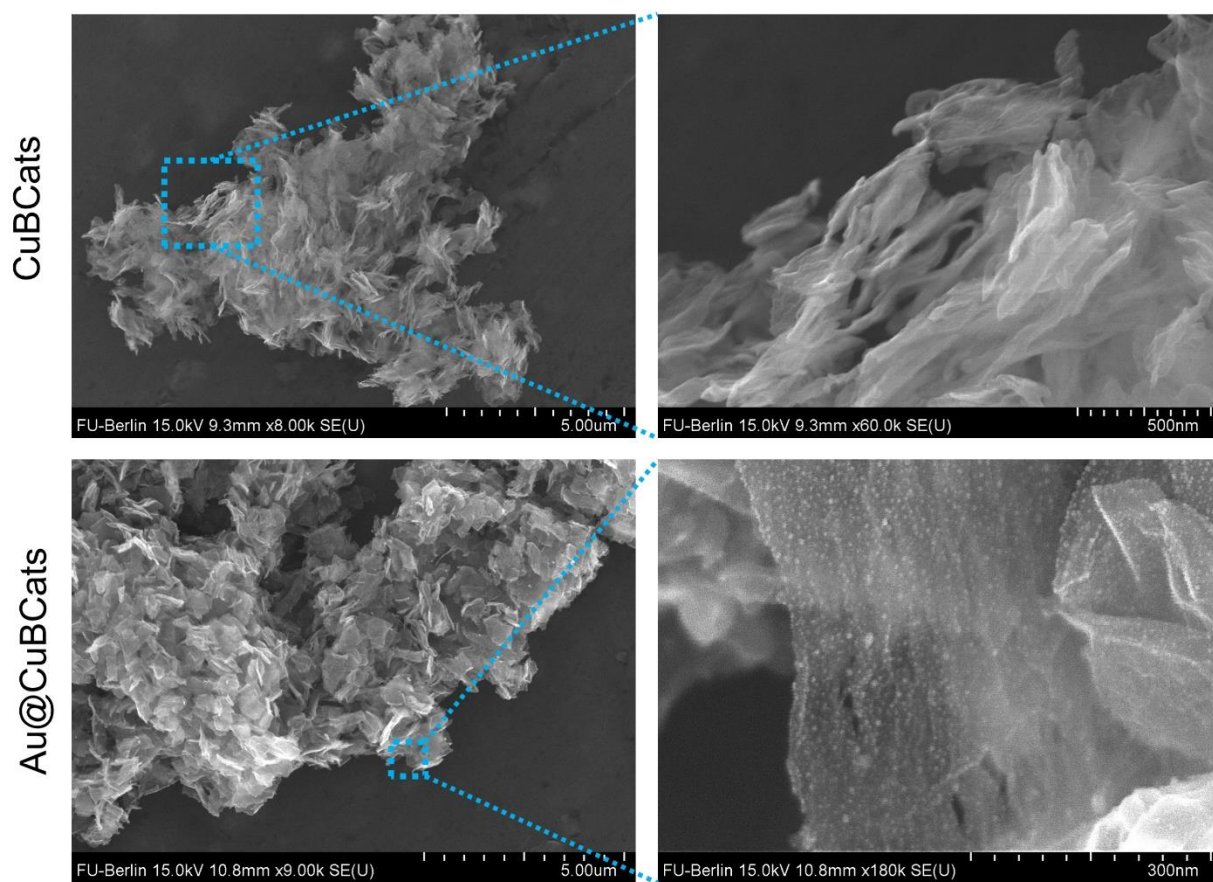


Figure S2. SEM images of CuBCats and Au@CuBCats.

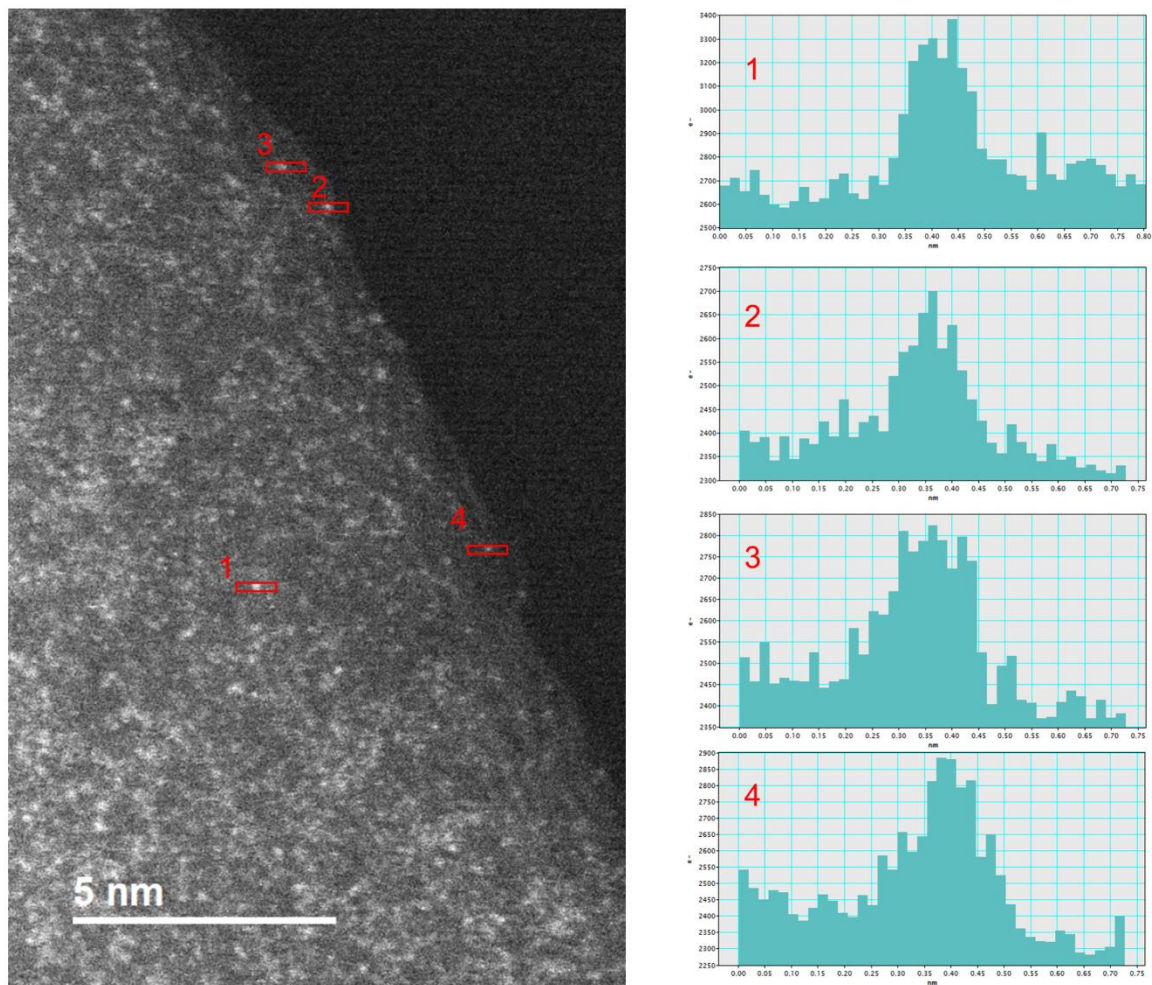
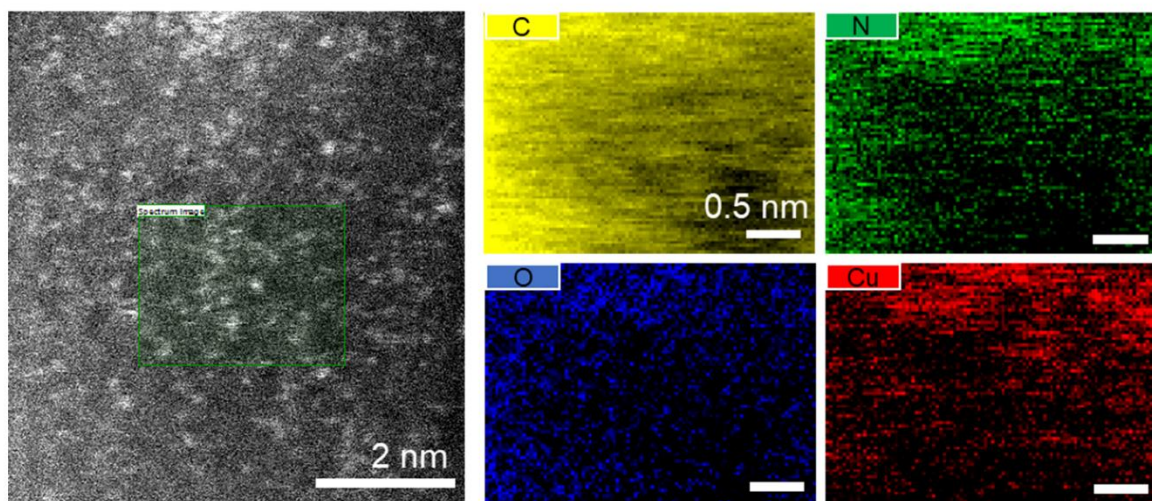
a**b**

Figure S3. (a) High-resolution STEM image of CuBCats with highlighted copper single atoms and corresponding intensity profiles. (b) EDS mapping of CuBCats.

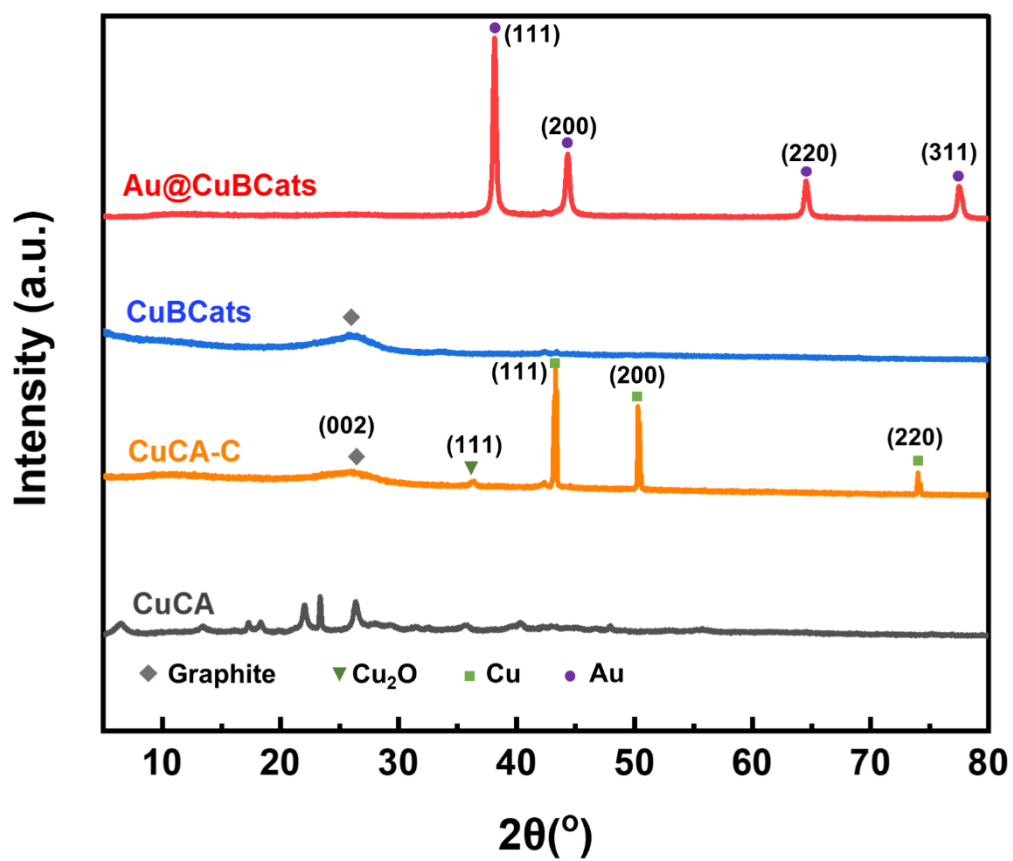


Figure S4. XRD patterns of CuCA, CuCA-C, CuBCats, and Au@CuBCats. CuCA-C is the CuBCats without acid etching.

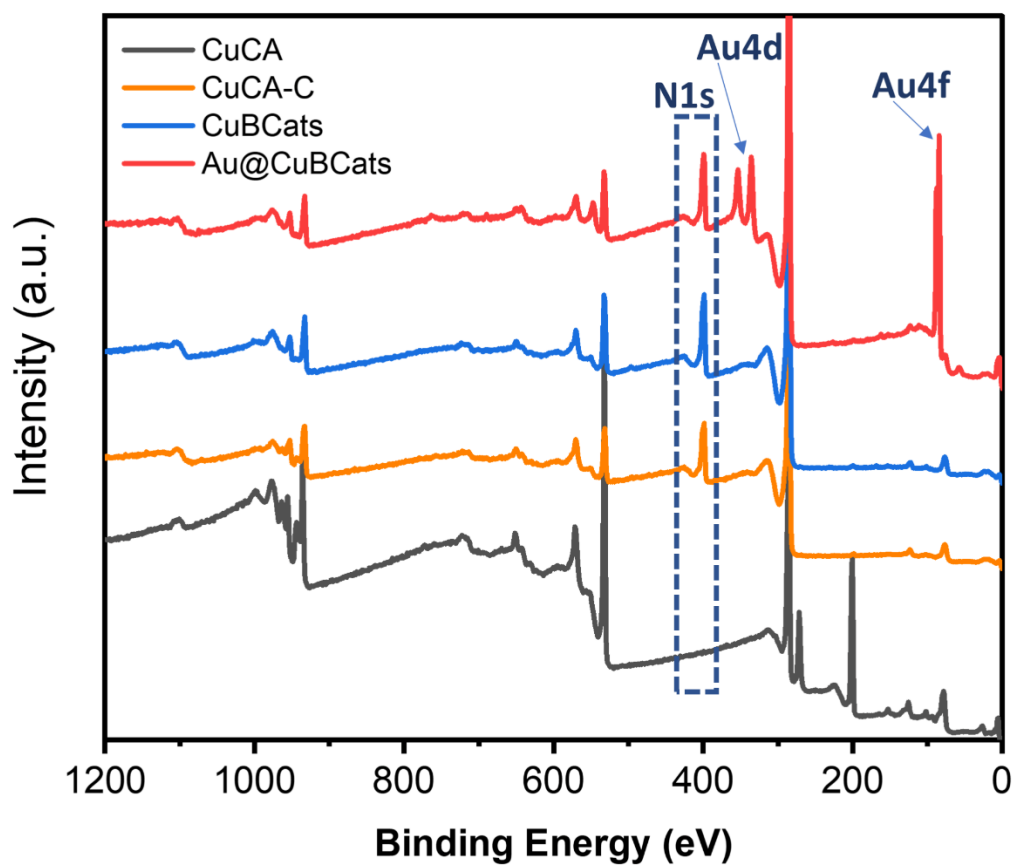


Figure S5. XPS survey of CuCA, CuCA-C, CuBCats and Au@CuBCats.

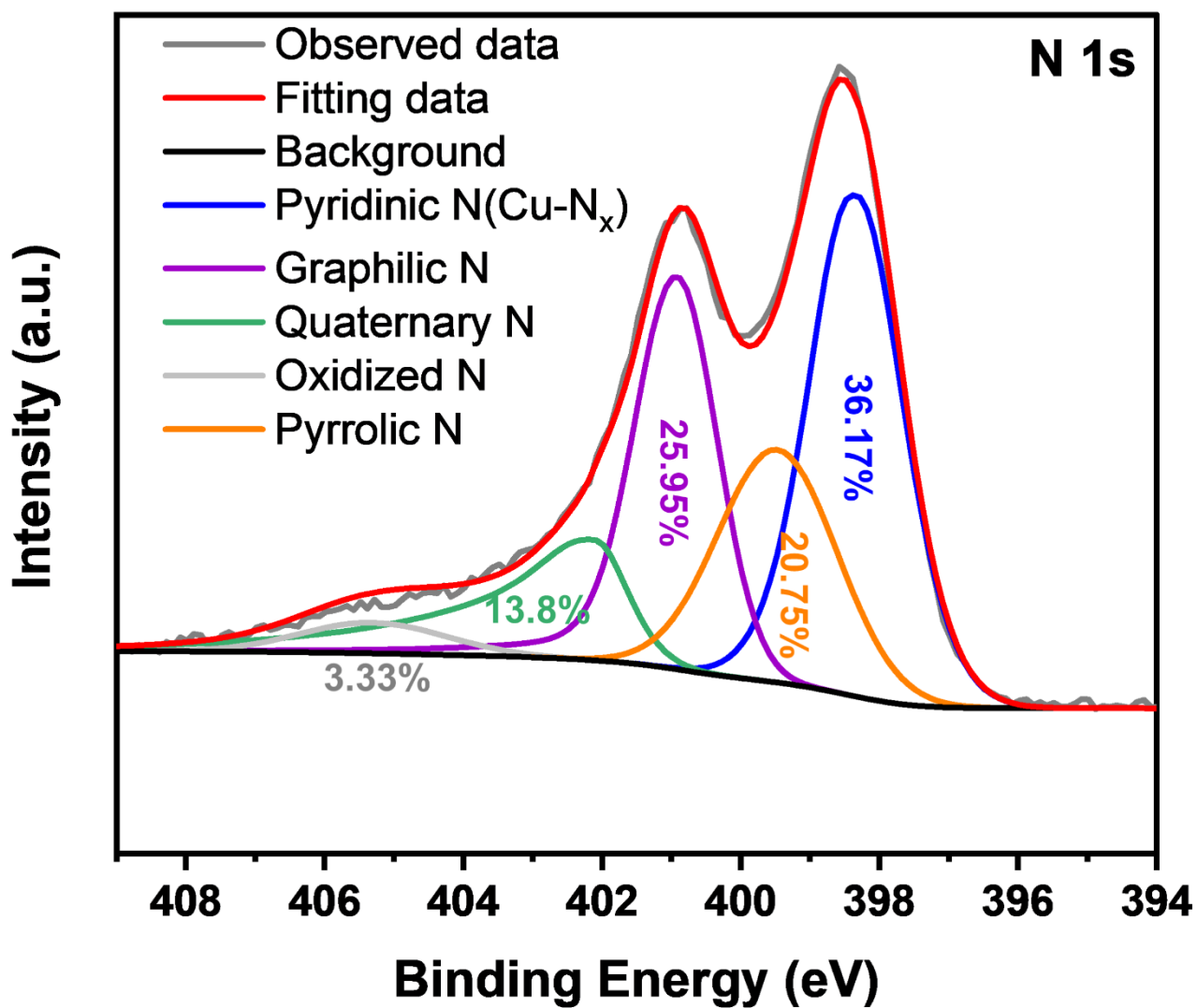


Figure S6. High-resolution XPS N1s spectra of Au@CuBCats.

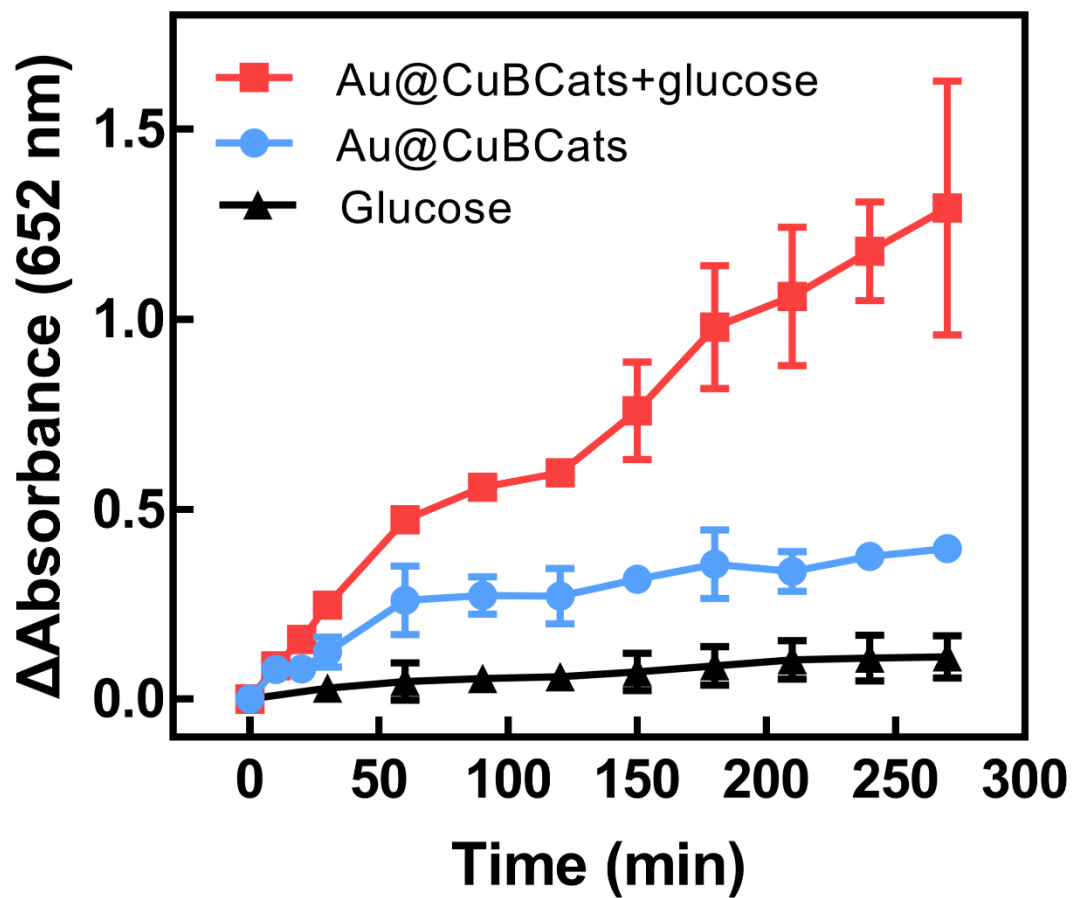


Figure S7. Time-dependent absorbance changes at 652 nm as a result of the catalyzed oxidation of TMB.

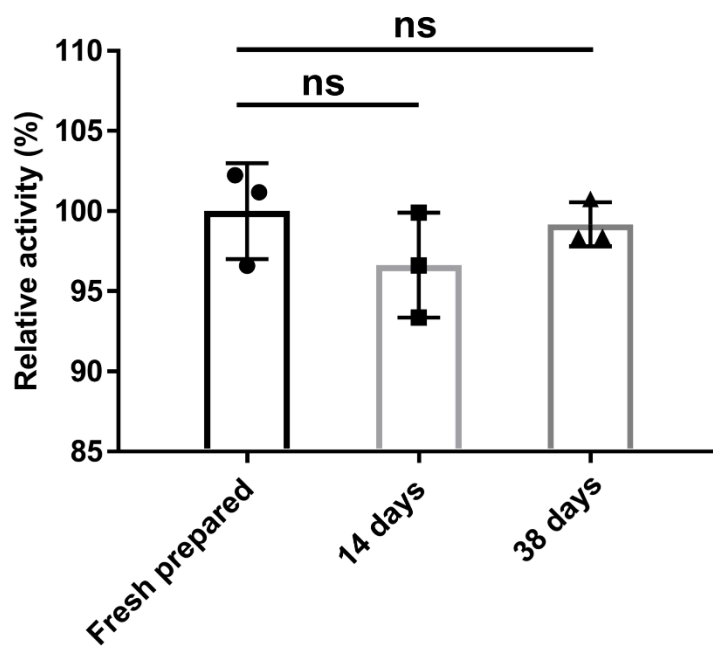


Figure S8. Relative catalytic activities of fresh prepared Au@CuBCats, 14-day-aged and 38-day-aged

room-temperature stored Au@CuBCats. The activities were determined by the absorbance at 652 nm (oxidized TMB peak) with the presence of Au@CuBCats and glucose. The final concentrations of Au@CuBCats, TMB, and glucose were fixed to 50 $\mu\text{g/mL}$, 0.1 mM and 1 mM, respectively. ns represents no significant difference.

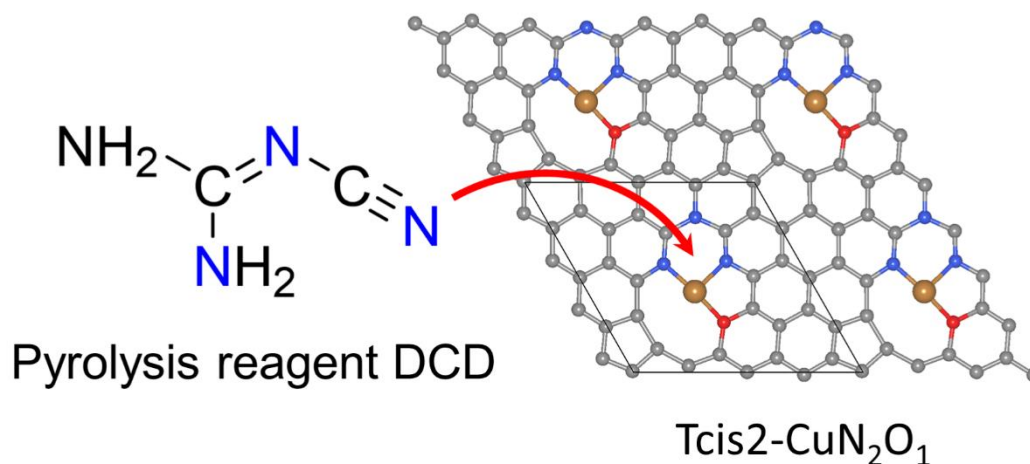


Figure S9. Schematic illustration of how DCD may play a role in facilitating the formation of N-C-N-C-N structure.

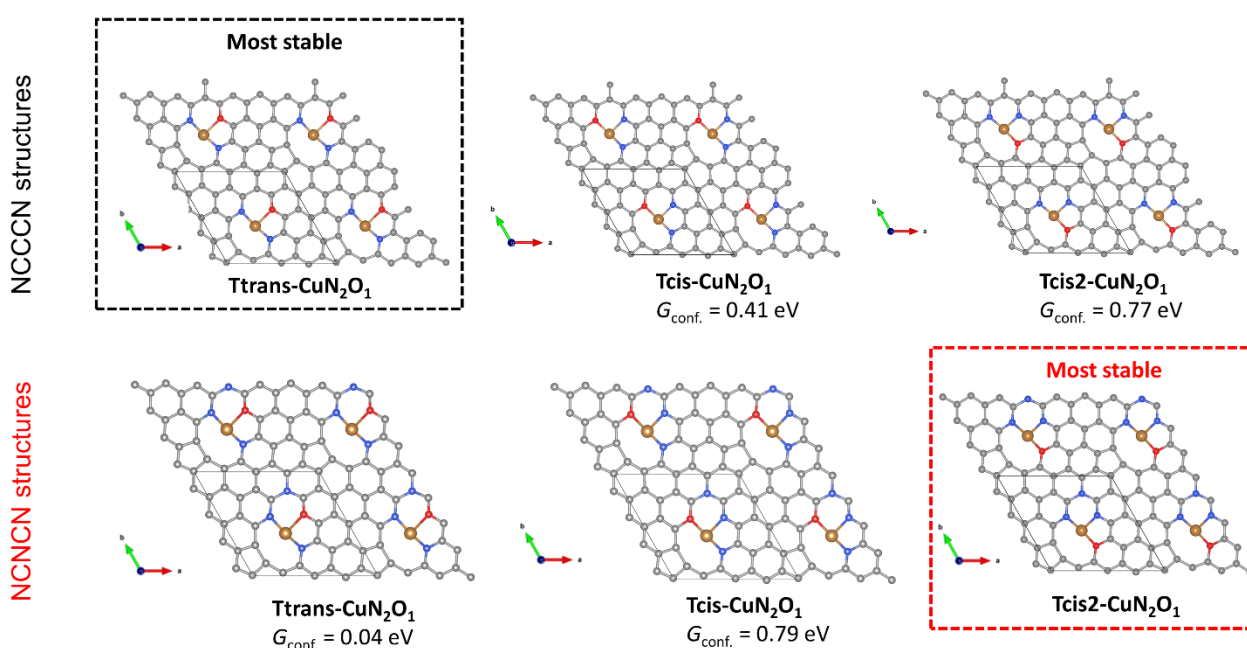


Figure S10. Possible arrangements of CuN₂O₁ motifs derived from a hexagonal 4x4 supercell of graphene with addition N dopant (bottom) and without (top). The conformational free energy of each

motif G_{conf} . is shown with reference to the respective most stable structure.

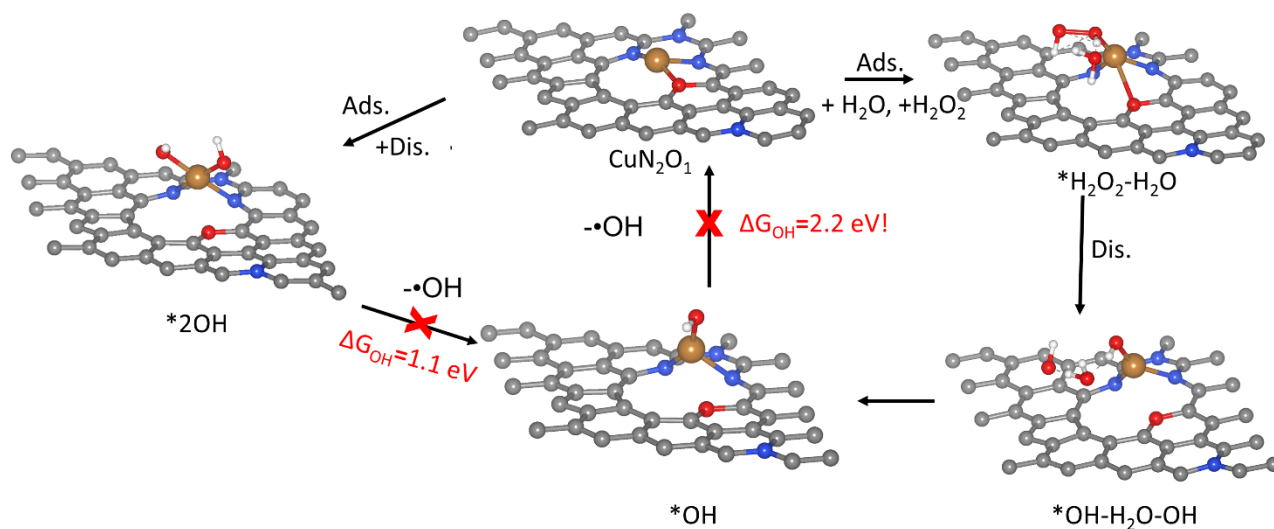


Figure S11. Scheme of alternative reaction mechanisms involving the unfeasible desorption of OH radical from the Cu center. The proposed mechanism differs from the mechanism on the right in the final desorption step of OH.

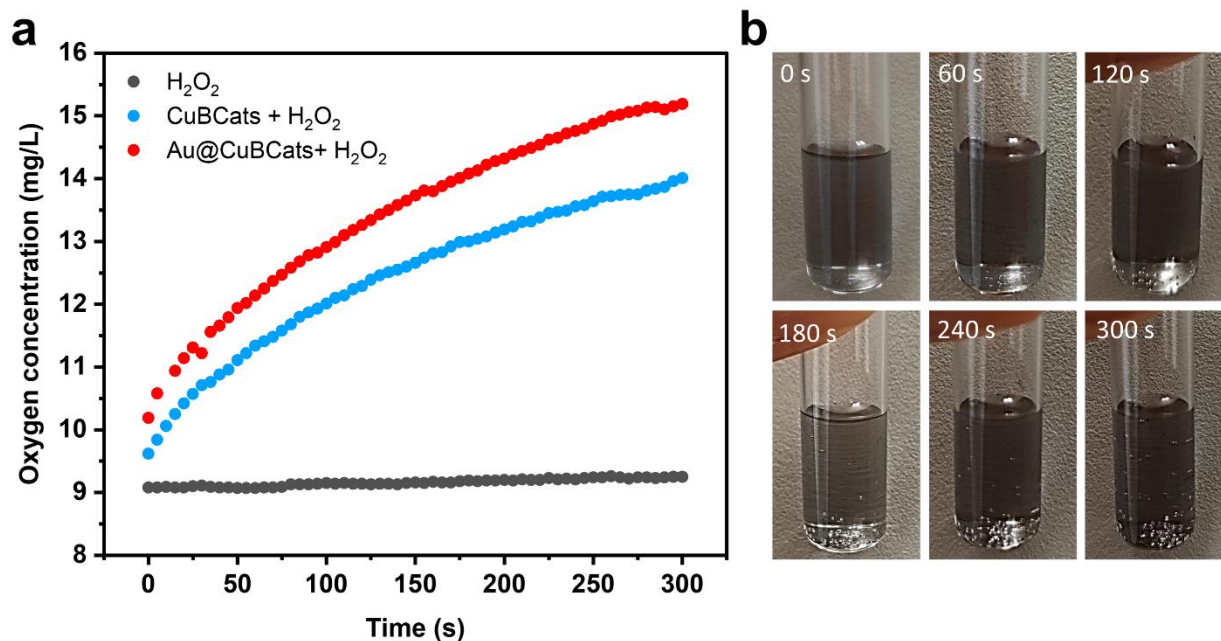


Figure S12. (a) The variation of dissolved oxygen concentrations of H₂O₂, CuBCats + H₂O₂ and Au@CuBCats + H₂O₂ in NaAC/HAc buffer. The final concentration of H₂O₂, CuBCats and Au@CuBCats were fixed to 100 mM, 50 $\mu\text{g/mL}$ and 50 $\mu\text{g/mL}$, respectively. (b) The typical images of oxygen generation of Au@CuBCats + H₂O₂ group over 300 seconds.

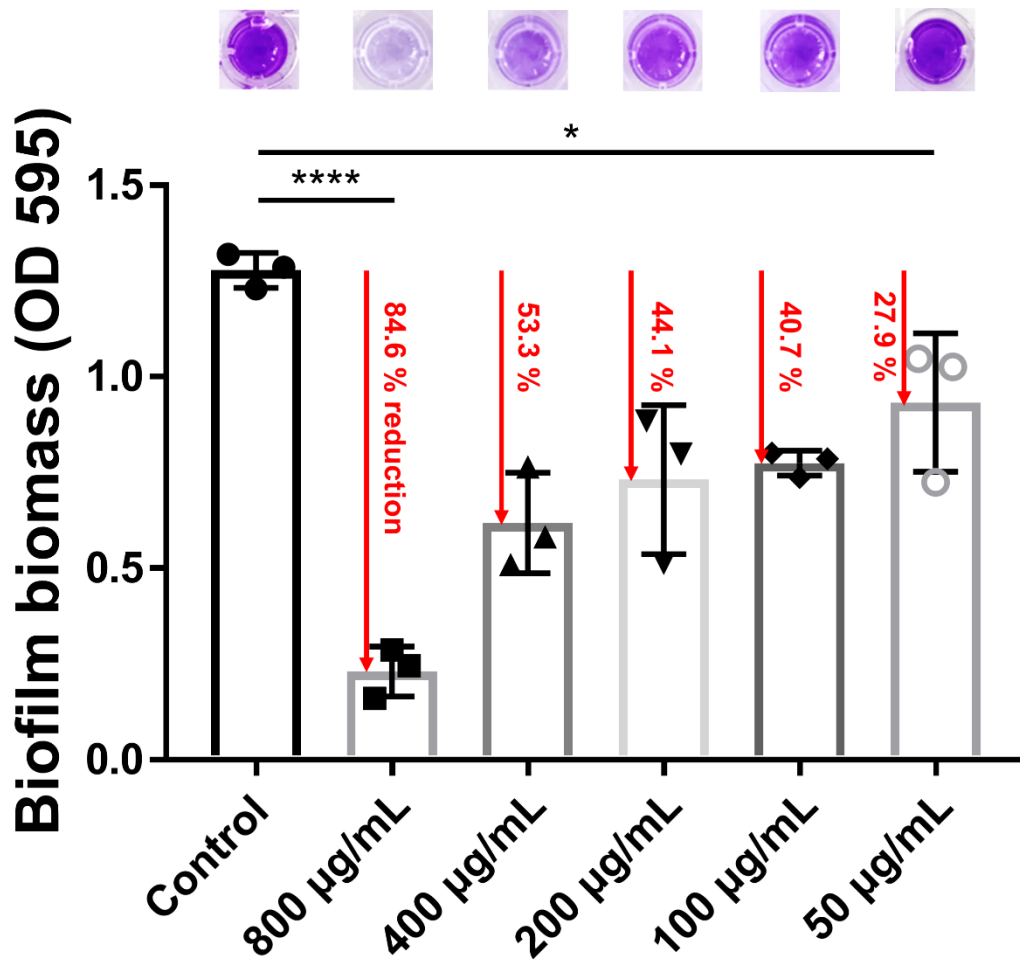


Figure S13. Biofilm biomass after treatment of different concentrations of Au@CuBCats in the presence of glucose with the final concentration of 1 mg/mL. * $P < 0.05$; **** $P < 0.0001$ by multiple t tests for data.

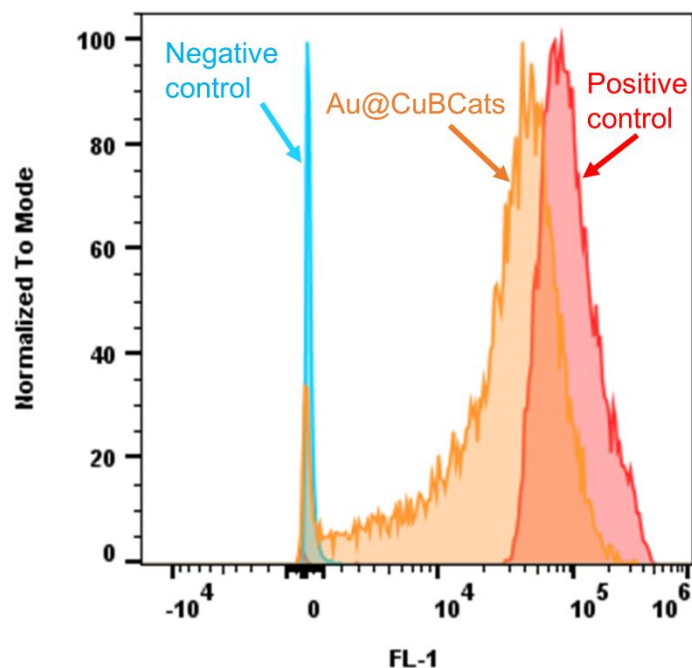


Figure S14. MRSA's intracellular GSH changes before-and-after being treated by Au@CuBCats. Samples were analyzed by flow cytometer at Ex/Em=490/520 nm (FL-1 Channel). The final concentration of Au@CuBCats was fixed to 50 $\mu\text{g/mL}$.

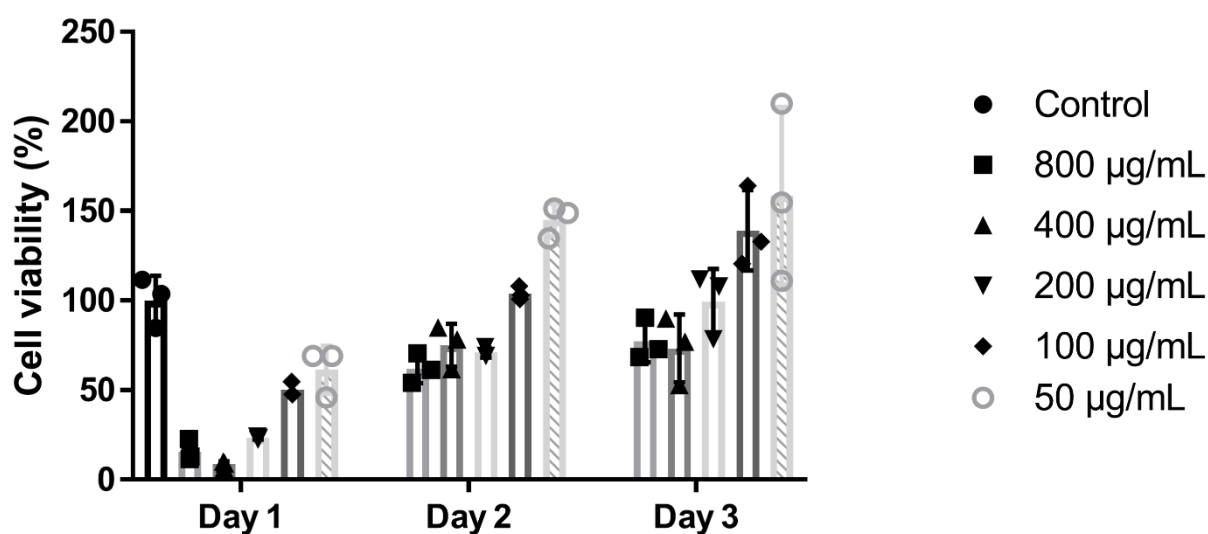


Figure S15. CCK-8 assay to reveal the HaCaT cells viability after being treated by different concentrations of Au@CuBCats. The cells without adding materials at 1 day were considered as control.

As a result, the decreases of cell viability were noticed after incubation with Au@CuBCats for 1 day, attributable to ROS generation from Au@CuBCats under the high glucose concentration (~ 4.5 g/L) in DMEM that we used. While after the Au@CuBCats being washed away, the significant cell regrowth

was noticed at day 2 and day 3, providing the evidence that the cells could recover soon after treatment. The full recovery (~100% cell viability) can be noticed when the materials' concentration below 200 $\mu\text{g}/\text{mL}$ at day 3.

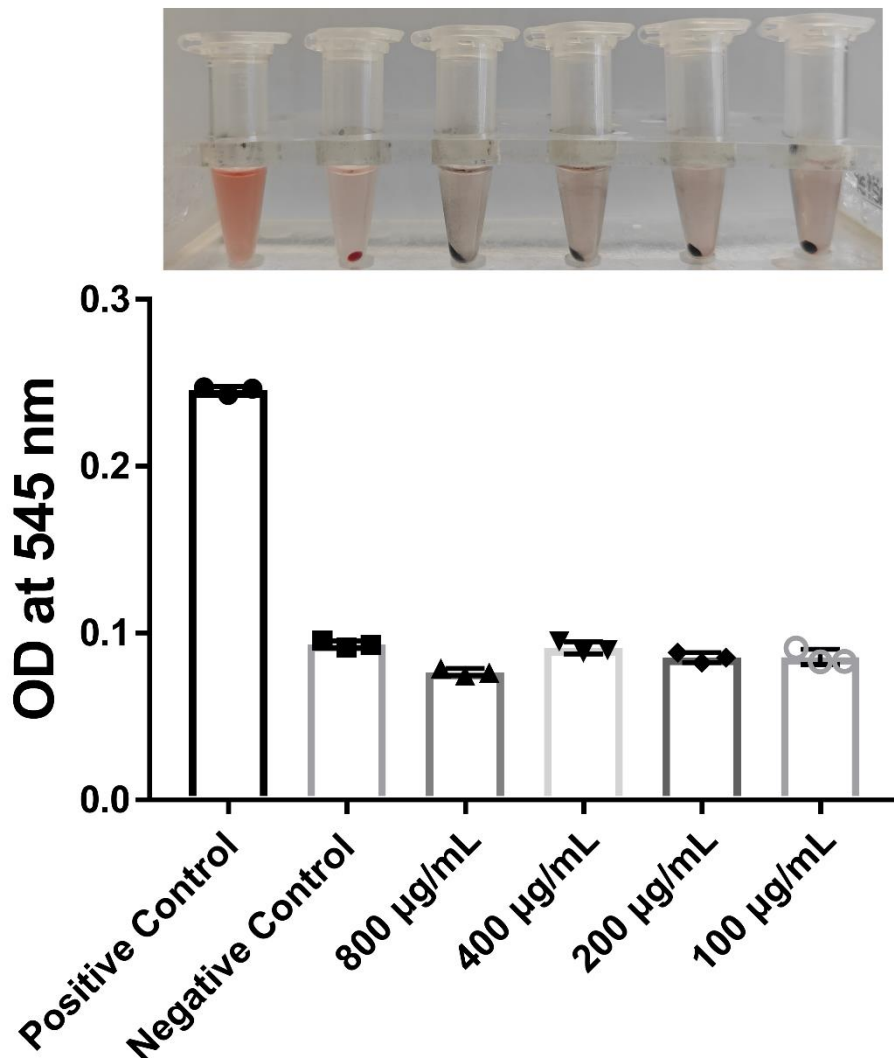


Figure S16. Hemolysis effect of Au@CuBCats under different concentrations. Triton X-100-treated red blood cells (RBCs) served as positive control and PBS-treated RBCs served as negative control.

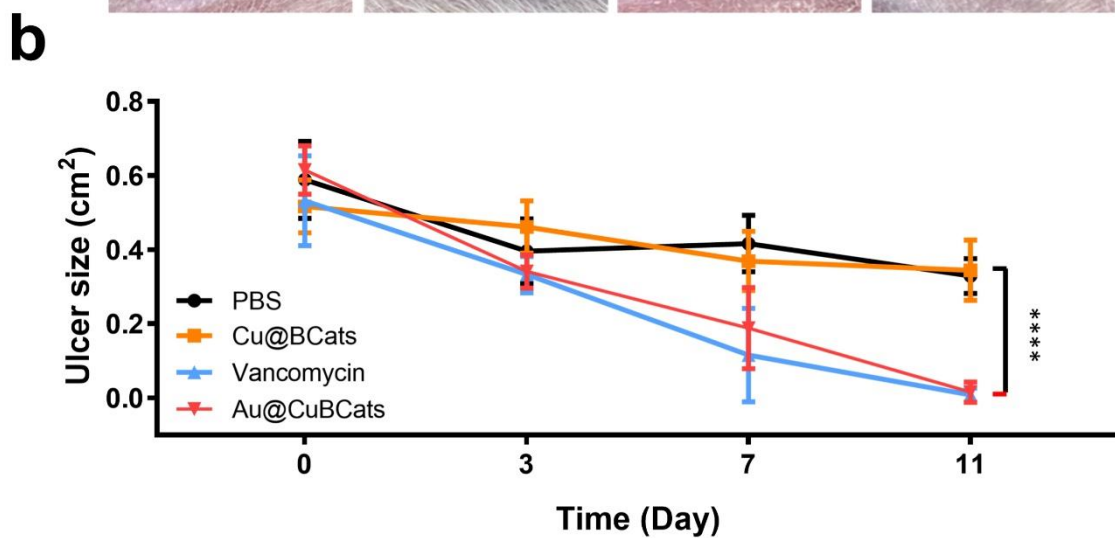
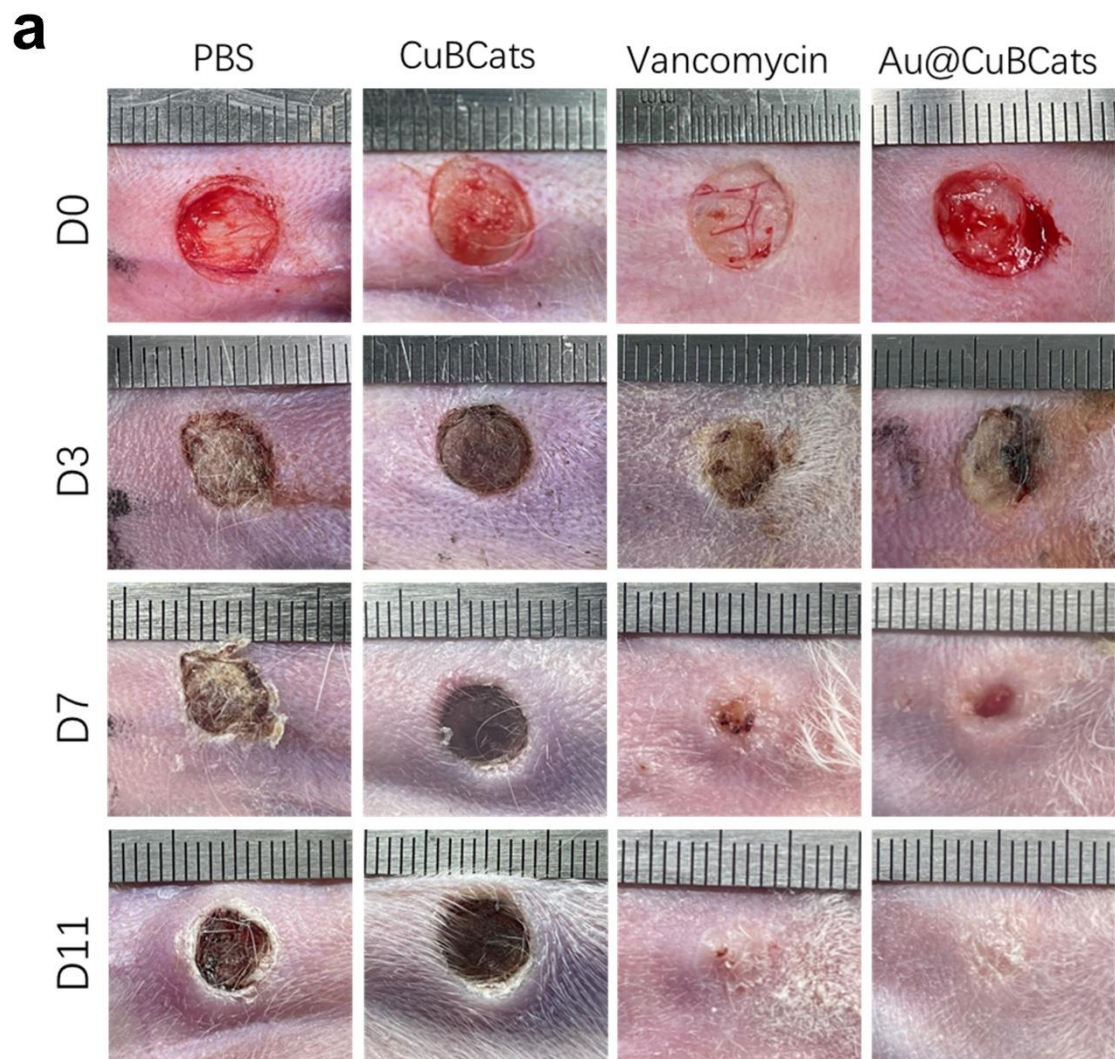


Figure S17. (a) Typical ulcer photos and (b) wound size curves at different day after treatment. The data are presented as mean \pm SD, n=6. *P < 0.05; **P < 0.01; ***P < 0.001; ****P < 0.0001 by multiple t tests.

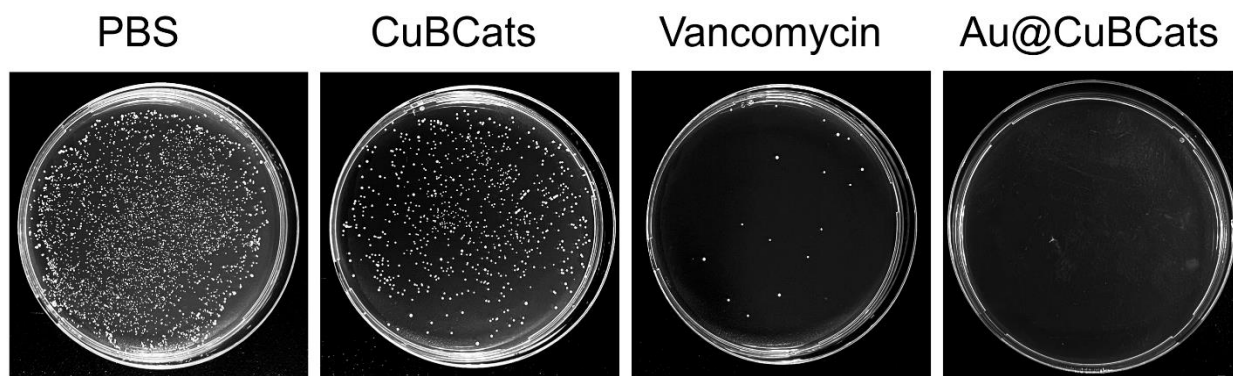


Figure S18. Typical agar plate photos for the remaining *MRSA* colonies in the ulcer after different treatment on day 11.

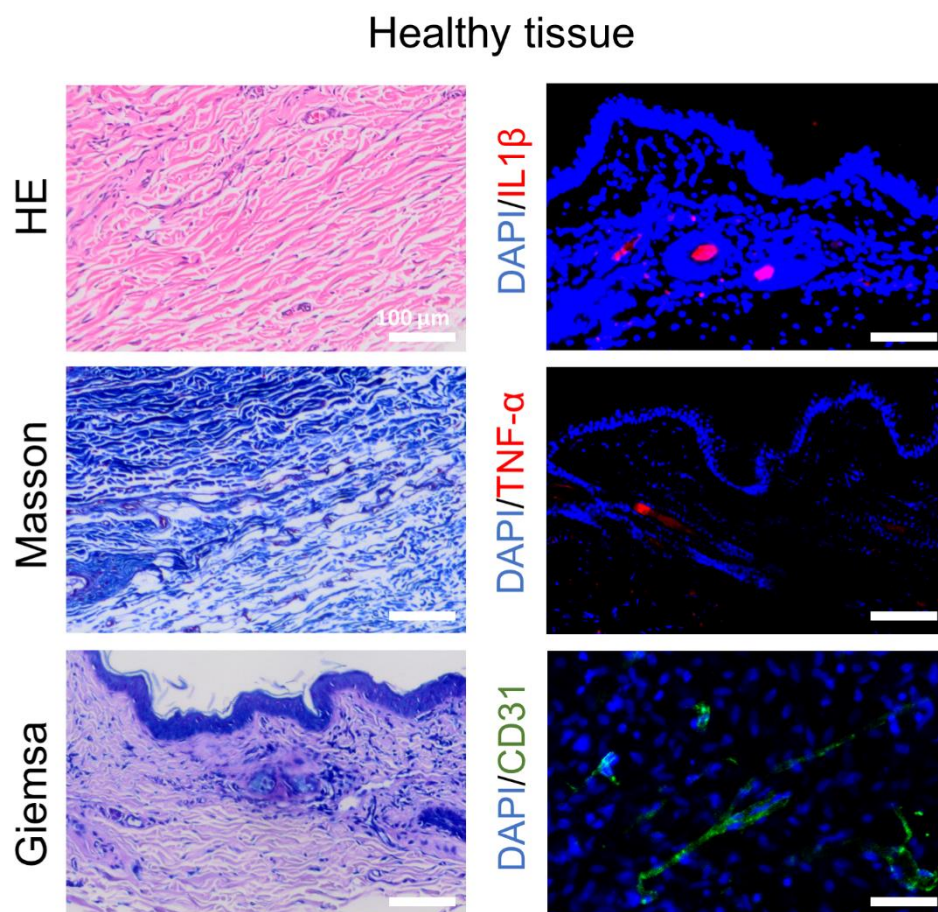


Figure S19. Histological staining of healthy rabbit ear's tissue. Scale bar: 100 μm.

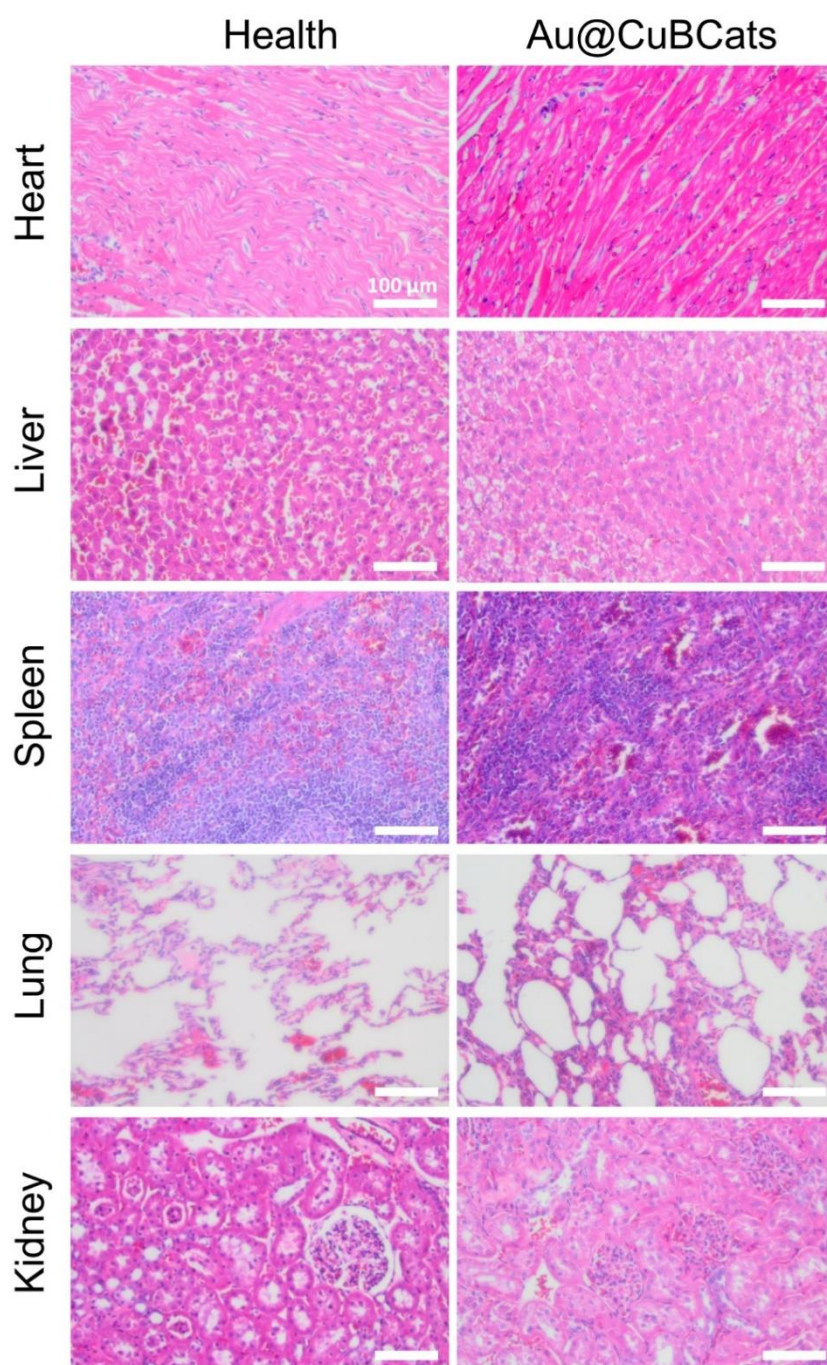


Figure S20. Typical H&E staining images of major organs for healthy rabbits and Au@CuBCats treated rabbits. Scale bar: 100 μm .

Table S1. Atomic ratio of samples

Sample	Atomic ratio (%)					
	Carbon	Nitrogen	Oxygen	Copper	Chlorine	Gold
CuCA	56.45	-	25.65	4.57	11.76	-
CuCA-C	83.55	10.36	4.71	1.38	-	-
CuBCats	82.73	10.96	5.44	0.87	-	-
Au@CuBCats	82.48	10.41	4.60	0.83	-	1.68

Table S2. Best EXAFS fitting parameters at the Cu K-edge.

Sample	path	CN	R(Å)	$\sigma^2(\text{Å}^2)$	ΔE_0 (eV)	R_f
Au@CuBCats	Cu-N	2.07	1.889	0.004	9.4	23.9
	Cu-O	0.91	1.908	0.004		

CN: coordination numbers; *R*: bond distance; σ^2 : Debye-Waller factors; ΔE_0 : the inner potential correction; R_f : goodness of fit.

Table S3. EXAFS fitting data with fixed coordination number of Cu-N and Cu-O at the Cu K-edge.

Structure	path	CN	R(Å)	$\sigma^2(\text{Å}^2)$	ΔE_0 (eV)	R_f
CuN ₁ O ₂	Cu-N	1*	1.802	0.010	9.1	41.8
	Cu-O	2*	1.928	0.010		
CuN ₃	Cu-N	3*	1.923	0.009	11.0	26.5
CuO ₃	Cu-O	3*	1.901	0.009	9.5	26.2

CN: coordination numbers; *R*: bond distance; σ^2 : Debye-Waller factors; ΔE_0 : the inner potential correction; R_f : goodness of fit. * The coordination number is fixed during the fitting. Compared to the best-fitting result (Table S1), CuN₁O₂, CuN₃ and CuO₃ model fits not that well with experimental spectrum of Au@CuBCats (judging from R_f).

References

- [1] H. Dau, P. Liebisch, M. Haumann, *Anal. Bioanal. Chem.* **2003**, 376, 562.

4. Summary and outlook

The thesis is focused on designing advanced NCMs for overcoming the increasing problems caused by MDR bacteria. Owing to the highly efficient ROS-producing antibacterial ability, the NCMs show great potential in combating MDR bacterial infection. To achieve satisfactory therapeutic effects, it is of vital importance to further increase the biosafety by localizing the ROS in bacterial infection sites or get rid of the addition of toxic substrate. In this thesis, by rational designing the compositions, a series of advanced NCMs have been successfully synthesized for overcoming the MDR bacterial infection.

In the first project, a nanohook-equipped NCM, Ni@Co-NC, was designed for localized NIR-assisted MDR bacterial biofilm eradication. The unique nanohook-like CNTs on the surface endowed the NCM with inherent bacterial binding ability, which increased bactericidal efficacy and meanwhile confined the ROS in bacterial infection sites. Besides, thanks to the acidic preferential catalytic effect, Ni@Co-NC only produced toxic $\bullet\text{OH}$ in biofilm microenvironment (pH~5.5) and kept uninjurious in physiologic pH (~7.4). Under irradiation of a NIR laser, Ni@Co-NC was able to convert light to heat, which synergistically promoted the bactericidal efficacy. As a result, no recurrence was observed for both *in-vitro* and *in-vivo* biofilm after treatment with Ni@Co-NC. It is believed that the proposed Ni@Co-NC can be a promising medicine for treating MDR bacterial topical infections.

In the second project, a bacteriophage-based NCM, QD@Phage was designed for anti-MDR-bacteria-targeting therapy. Inheriting the bacterial targeting infectivity of phage, the QD@Phage was able to target host bacteria. Afterwards, the QD locally generated ROS to further enhance bactericidal activity under irradiation of visible light. As a result of the synergistic bactericidal modalities, by over 99.9% and over 99% reduction for planktonic bacteria and biofilm, respectively, were noticed after treatment with QD@Phage. The application as a wound disinfectant has been verified by *in-vivo* experiments, which showed that QD@Phage effectively eliminated the bacterial

colonization in wound and accelerated the wound healing. This project provides an inspiration for designing highly bacteria-targeted NCM. It is also expected that more bacteriophage-based NCMs with NIR-responsiveness or ultrasound-responsiveness can be successfully developed by using the proposed method, so that deep MDR bacterial infection can also be easily handled in near future.

In the third project, a GOx-POD dual-enzyme-mimetic NCM, Au@CuBCats was synthesized for combating MDR bacterial diabetic ulcers. The Au@CuBCats was able to first catalyze the glucose to generate H₂O₂, then in situ converted the H₂O₂ to bactericidal •OH, thus controlling the glucose and bacteria level in diabetic ulcers in the same time. The DFT study confirmed the better POD-mimetic property of the proposed copper single-atom CuN₂O₁ structure than other state-of-art copper single-atom sites (CuN₄ and CuN₃), since a whole reaction path from initiating dissociation of H₂O₂ to •OH releasing are kinetically accessible. The *in vitro* antibacterial experiments confirmed the robust bacterial killing effect of Au@CuBCats against both gram-positive and gram-negative MDR bacterial strains. Furthermore, *in vivo* MDR bacterial diabetic ulcer models demonstrated the Au@CuBCats significantly promoted the ulcer healing without leading to inflammation. It is believed that this multi-enzyme mimetic NCM has great potential in treating MDR bacterial diabetic ulcers.

In summary, the thesis carefully studied not only the antibacterial effect *in vitro* and *in vivo*, but also the biosafety of three advanced NCMs. Besides, the catalytic performance and antibacterial mechanisms of each NCM have been systematically discussed. Proved by three projects, the NCM have a great potential in achieving safe *in vivo* MDR-bacterial infection eradication. Also, it is anticipated that this thesis provides new inspirations for the next-generation NCM-based antibacterial medicines.

5. Zusammenfassung und Ausblick

Diese Arbeit konzentriert sich auf die Entwicklung neuartiger NCMs zur Bewältigung der zunehmenden Probleme, die durch MDR-Bakterien verursacht werden. Aufgrund der hocheffizienten ROS-produzierenden antibakteriellen Fähigkeit zeigen die NCMs großes Potenzial bei der Bekämpfung von MDR-Bakterieninfektionen. Um eine zufriedenstellende therapeutische Wirkung zu erzielen, ist es von entscheidender Bedeutung, die Biosicherheit weiter zu erhöhen, indem die ROS an bakteriellen Infektionsherden lokalisiert werden oder auf die Zugabe von toxischen Substraten verzichtet wird. In dieser Arbeit wurde durch rationales Design der Zusammensetzungen eine Reihe von neuartiger NCMs erfolgreich synthetisiert, um die bakterielle MDR-Infektion zu überwinden.

Im ersten Projekt wurde ein mit Nanohaken ausgestattetes NCM, Ni@Co-NC, für die lokalisierte NIR-unterstützte Eradikation von MDR-Bakterien-Biofilmen entwickelt. Die einzigartigen nanohakenartigen CNTs auf der Oberfläche verliehen dem NCM eine inhärente bakterielle Bindungsfähigkeit, die die bakterientötende Wirksamkeit erhöhte und gleichzeitig die ROS in den bakteriellen Infektionsstellen einschränkte. Dank der sauren präferentiellen katalytischen Wirkung produzierte Ni@Co-NC toxisches $\bullet\text{OH}$ nur in der Biofilm-Mikroumgebung (pH~5,5) und blieb bei physiologischem pH (~7,4) unschädlich. Bei Bestrahlung mit einem NIR-Laser konnte Ni@Co-NC Licht in Wärme umwandeln, was die bakterientötende Wirkung synergistisch förderte. Infolgedessen wurde nach der Behandlung mit Ni@Co-NC kein Wiederauftreten des Biofilms *in vivo* und *in vitro* beobachtet. Es wird postuliert, dass das Ni@Co-NC ein vielversprechender Wirkstoffkandidat zur Behandlung von bakteriellen MDR-Infektionen ist.

Im zweiten Projekt wurde ein auf Bakteriophagen basierendes NCM, QD@Phage, für eine gegen MDR-Bakterien gerichtete Therapie entwickelt. Der QD@Phage übernahm die bakterielle Infektiosität des Phagen und war in der Lage, Wirtsbakterien anzusprechen. Anschließend erzeugten die QD lokal ROS, um die bakterientötende Aktivität unter Bestrahlung mit sichtbarem Licht weiter zu verstärken. Als Ergebnis der

synergistischen bakteriziden Modalitäten wurde nach der Behandlung mit QD@Phage eine Reduktion von über 99,9% bei planktonischen Bakterien und über 99% bei Biofilmen festgestellt. Die Anwendung als Wunddesinfektionsmittel wurde durch *in-vivo* Experimente verifiziert, die zeigten, dass QD@Phage die bakterielle Besiedlung in der Wunde wirksam beseitigten und die Wundheilung beschleunigten. Dieses Projekt bietet eine Inspiration für die Entwicklung des bakterienspezifischen NCM. Es wird erwartet, dass mehr Bakteriophagen-basierte NCMs mit NIR- oder Ultraschall-Empfindlichkeit erfolgreich mit unserer Methode entwickelt werden, so dass tiefe bakterielle MDR-Infektionen in naher Zukunft auch leicht behandelt werden.

Im dritten Projekt wurde ein GOx-POD dual-enzym-mimetisches NCM, Au@CuBCats, zur Bekämpfung von MDR-bakteriellen diabetischen Geschwüren synthetisiert. Au@CuBCats konnten zunächst die Glukose katalysieren, um H₂O₂ zu erzeugen, und dann *in situ* das H₂O₂ in bakterientötendes •OH umzuwandeln, wodurch der Glukose- und Bakterienpiegel in diabetischen Geschwüren gleichzeitig kontrolliert wurde. Die DFT-Studie bestätigte die bessere POD-mimetische Eigenschaft der vorgeschlagenen CuN₂O₁-Struktur im Vergleich zu anderen einatomigen Kupferstrukturen, da der gesamte Reaktionsweg von der beginnenden Dissoziation von H₂O₂ bis zur Freisetzung von •OH kinetisch zugänglich ist. Die *in vitro* antibakteriellen Experimente bestätigten die robuste bakterientötende Wirkung von Au@CuBCats gegen beide MDR-Bakterienstämme. Außerdem zeigten *in-vivo*-Versuche, dass Au@CuBCats die Heilung von diabetischen Geschwüren signifikant fördern, ohne Entzündungen zu verstärken. Es wird davon ausgegangen, dass dieses mimetische Multienzym NCM ein großes Potenzial für die Behandlung von MDR-bakteriellen diabetischen Geschwüren hat.

Zusammenfassend hat diese Arbeit nicht nur die antibakterielle Wirkung *in vitro* und *in vivo* untersucht, sondern sie auch die biologische Sicherheit von neuartigen NCMs bewertet. Außerdem wurden die katalytischen Eigenschaften und die antibakteriellen Mechanismen der einzelnen NCM systematisch diskutiert. In drei erfolgreiche

Projekten wurde gezeigt, dass die NCM ein großes Potenzial für die sichere Beseitigung von MDR-Bakterieninfektionen haben. Es wird erwartet, dass diese Arbeit neue Inspirationen für die nächste Generation von antibakteriellen Medikamenten auf NCM-Basis liefert.

6. References

- [1] D. M. Monack, A. Mueller, S. Falkow, *Nature Reviews Microbiology* **2004**, 2, 747-765.
- [2] S. Doron, S. L. Gorbach, *International Encyclopedia of Public Health* **2008**, 273.
- [3] M. I. Hutchings, A. W. Truman, B. Wilkinson, *Current opinion in microbiology* **2019**, 51, 72-80.
- [4] J.-P. Pirnay, T. Ferry, G. Resch, *FEMS Microbiology Reviews* **2022**, 46, fuab040.
- [5] N. Chakraborty, D. Jha, I. Roy, P. Kumar, S. S. Gaurav, K. Marimuthu, O.-T. Ng, R. Lakshminarayanan, N. K. Verma, H. K. Gautam, *Journal of Nanobiotechnology* **2022**, 20, 375.
- [6] K. Sauer, P. Stoodley, D. M. Goeres, L. Hall-Stoodley, M. Burmølle, P. S. Stewart, T. Bjarnsholt, *Nature Reviews Microbiology* **2022**, 20, 608-620.
- [7] C. A. Fux, J. W. Costerton, P. S. Stewart, P. Stoodley, *Trends in Microbiology* **2005**, 13, 34-40.
- [8] J. W. Costerton, P. S. Stewart, E. P. Greenberg, *Science* **1999**, 284, 1318-1322.
- [9] K. M. G. O'Connell, J. T. Hodgkinson, H. F. Sore, M. Welch, G. P. C. Salmond, D. R. Spring, *Angewandte Chemie International Edition* **2013**, 52, 10706-10733.
- [10] B. K. English, A. H. Gaur, *Hot topics in infection and immunity in children VI* **2010**, 73-82.
- [11] D. Sharma, L. Misba, A. U. Khan, *Antimicrobial Resistance & Infection Control* **2019**, 8, 76.
- [12] H. Wu, C. Moser, H.-Z. Wang, N. Høiby, Z.-J. Song, *International Journal of Oral Science* **2015**, 7, 1-7.
- [13] H. Kresse, M. J. Belsey, H. Rovini, *Nature Reviews Drug Discovery* **2007**, 6, 19-20.
- [14] A. Sulakvelidze, Z. Alavidze, J. G. Morris Jr, *Antimicrobial agents and chemotherapy* **2001**, 45, 649-659.
- [15] Y. Yang, L. Ma, C. Cheng, Y. Deng, J. Huang, X. Fan, C. Nie, W. Zhao, C. Zhao, *Advanced Functional Materials* **2018**, 28, 1705708.
- [16] M. Yang, S. Qiu, E. Coy, S. Li, K. Załęski, Y. Zhang, H. Pan, G. Wang, *Advanced Materials* **2022**, 34, 2106314.
- [17] J. Roy, V. Pandey, I. Gupta, H. Shekhar, *ACS Biomaterials Science & Engineering* **2021**, 7, 5326-5338.
- [18] Y. Li, X. Liu, B. Li, Y. Zheng, Y. Han, D.-f. Chen, K. W. K. Yeung, Z. Cui, Y. Liang, Z. Li, S. Zhu, X. Wang, S. Wu, *ACS Nano* **2020**, 14, 8157-8170.
- [19] M. Qi, X. Ren, W. Li, Y. Sun, X. Sun, C. Li, S. Yu, L. Xu, Y. Zhou, S. Song, *Nano Today* **2022**, 43, 101447.
- [20] Y. Liu, S. Ding, J. Shen, K. Zhu, *Natural product reports* **2019**, 36, 573-592.

- [21] N. Yang, H. Guo, C. Cao, X. Wang, X. Song, W. Wang, D. Yang, L. Xi, X. Mou, X. Dong, *Biomaterials* **2021**, 275, 120918.
- [22] G. Qing, X. Zhao, N. Gong, J. Chen, X. Li, Y. Gan, Y. Wang, Z. Zhang, Y. Zhang, W. Guo, Y. Luo, X.-J. Liang, *Nature Communications* **2019**, 10, 4336.
- [23] R. L. Auten, J. M. Davis, *Pediatric research* **2009**, 66, 121-127.
- [24] S. J. Labrie, J. E. Samson, S. Moineau, *Nature Reviews Microbiology* **2010**, 8, 317-327.
- [25] J. Chen, F. Wang, Q. Liu, J. Du, *Chemical communications* **2014**, 50, 14482-14493.
- [26] M. Cloutier, D. Mantovani, F. Rosei, *Trends in biotechnology* **2015**, 33, 637-652.
- [27] K. M. O'Connell, J. T. Hodgkinson, H. F. Sore, M. Welch, G. P. Salmond, D. R. Spring, *Angewandte Chemie International Edition* **2013**, 52, 10706-10733.
- [28] M. Wegener, M. J. Hansen, A. J. Driessen, W. Szymanski, B. L. Feringa, *Journal of the American Chemical Society* **2017**, 139, 17979-17986.
- [29] A. Sirelkhatim, S. Mahmud, A. Seeni, N. H. M. Kaus, L. C. Ann, S. K. M. Bakhori, H. Hasan, D. Mohamad, *Nano-micro letters* **2015**, 7, 219-242.
- [30] Z.-m. Xiu, Q.-b. Zhang, H. L. Puppala, V. L. Colvin, P. J. Alvarez, *Nano letters* **2012**, 12, 4271-4275.
- [31] Y. Xia, X. Fan, H. Yang, L. Li, C. He, C. Cheng, R. Haag, *Small* **2020**, 16, 2003010.
- [32] C. Nie, L. Ma, H. Luo, J. Bao, C. Cheng, *Smart materials in medicine* **2020**, 1, 48-53.
- [33] Y. Yang, X. Wu, C. He, J. Huang, S. Yin, M. Zhou, L. Ma, W. Zhao, L. Qiu, C. Cheng, *ACS applied materials & interfaces* **2020**, 12, 13698-13708.
- [34] C. Nie, L. Ma, S. Li, X. Fan, Y. Yang, C. Cheng, W. Zhao, C. Zhao, *Nano Today* **2019**, 26, 57-97.
- [35] B. Yang, Y. Chen, J. Shi, *Advanced Materials* **2019**, 31, 1901778.
- [36] M. Zhao, N. Zhang, R. Yang, D. Chen, Y. Zhao, *Advanced Healthcare Materials* **2021**, 10, 2001897.
- [37] X. Fan, F. Yang, J. Huang, Y. Yang, C. Nie, W. Zhao, L. Ma, C. Cheng, C. Zhao, R. Haag, *Nano Letters* **2019**, 19, 5885-5896.
- [38] Z. Wang, T. Xia, S. Liu, *Nanoscale* **2015**, 7, 7470-7481.
- [39] F. Vatansever, W. C. de Melo, P. Avci, D. Vecchio, M. Sadasivam, A. Gupta, R. Chandran, M. Karimi, N. A. Parizotto, R. Yin, *FEMS microbiology reviews* **2013**, 37, 955-989.
- [40] P. Liu, M. Huo, J. Shi, *CCS Chemistry* **2021**, 3, 2445-2463.
- [41] Q. Xin, H. Shah, A. Nawaz, W. Xie, M. Z. Akram, A. Batool, L. Tian, S. U. Jan, R. Boddula, B. Guo, *Advanced Materials* **2019**, 31, 1804838.
- [42] D. Hu, Y. Deng, F. Jia, Q. Jin, J. Ji, *Acs Nano* **2019**, 14, 347-359.
- [43] Y. Gao, J. Wang, M. Chai, X. Li, Y. Deng, Q. Jin, J. Ji, *ACS nano* **2020**, 14, 5686-5699.

- [44] X. Fan, F. Yang, C. Nie, L. Ma, C. Cheng, R. Haag, *Advanced Materials* **2021**, 33, 2100637.
- [45] Y. Tao, E. Ju, J. Ren, X. Qu, *Advanced Materials* **2015**, 27, 1097-1104.
- [46] J. Shan, X. Li, K. Yang, W. Xiu, Q. Wen, Y. Zhang, L. Yuwen, L. Weng, Z. Teng, L. Wang, *ACS nano* **2019**, 13, 13797-13808.
- [47] R. Li, N. D. Mansukhani, L. M. Guiney, Z. Ji, Y. Zhao, C. H. Chang, C. T. French, J. F. Miller, M. C. Hersam, A. E. Nel, *ACS nano* **2016**, 10, 10966-10980.
- [48] H. Sun, N. Gao, K. Dong, J. Ren, X. Qu, *ACS nano* **2014**, 8, 6202-6210.
- [49] B. Xu, H. Wang, W. Wang, L. Gao, S. Li, X. Pan, H. Wang, H. Yang, X. Meng, Q. Wu, *Angewandte Chemie* **2019**, 131, 4965-4970.
- [50] Y. Long, L. Li, T. Xu, X. Wu, Y. Gao, J. Huang, C. He, T. Ma, L. Ma, C. Cheng, *Nature Communications* **2021**, 12, 6143.
- [51] F. Natalio, R. André, A. F. Hartog, B. Stoll, K. P. Jochum, R. Wever, W. Tremel, *Nature nanotechnology* **2012**, 7, 530-535.
- [52] X. He, F. Tian, J. Chang, X. Bai, C. Yuan, C. Wang, A. Neville, *ACS Sustainable Chemistry & Engineering* **2020**, 8, 6744-6752.
- [53] C. Mao, Y. Xiang, X. Liu, Z. Cui, X. Yang, Z. Li, S. Zhu, Y. Zheng, K. W. K. Yeung, S. Wu, *ACS Nano* **2018**, 12, 1747-1759.
- [54] H. Lin, Z. Lin, K. Zheng, C. Wang, L. Lin, J. Chen, J. Song, *Advanced Optical Materials* **2021**, 9, 2002177.
- [55] K. Deng, C. Li, S. Huang, B. Xing, D. Jin, Q. Zeng, Z. Hou, J. Lin, *Small* **2017**, 13, 1702299.
- [56] J. Mou, T. Lin, F. Huang, H. Chen, J. Shi, *Biomaterials* **2016**, 84, 13-24.
- [57] Y. Ding, C. Du, J. Qian, C.-M. Dong, *Nano letters* **2019**, 19, 4362-4370.
- [58] L. Tan, J. Li, X. Liu, Z. Cui, X. Yang, S. Zhu, Z. Li, X. Yuan, Y. Zheng, K. W. Yeung, *Advanced Materials* **2018**, 30, 1801808.
- [59] D. Sun, X. Pang, Y. Cheng, J. Ming, S. Xiang, C. Zhang, P. Lv, C. Chu, X. Chen, G. Liu, *ACS nano* **2020**, 14, 2063-2076.
- [60] H. Abou Oualid, O. Amadine, Y. Essamlali, I. M. Kadmiri, H. El Arroussi, M. Zahouily, *Nanoscale Advances* **2019**, 1, 3151-3163.
- [61] Q. Xu, S. Chen, L. Jiang, C. Xia, L. Zeng, X. Cai, Z. Jin, S. Qin, W. Ding, Q. He, *National Science Review* **2023**, nwad063.
- [62] Y. Zeng, Q. Ouyang, Y. Yu, L. Tan, X. Liu, Y. Zheng, S. Wu, *Small Methods* **2023**, 7, 2201248.
- [63] Q. Ouyang, Y. Zeng, Y. Yu, L. Tan, X. Liu, Y. Zheng, S. Wu, *Small* **2023**, 19, 2205292.
- [64] X. Pang, Q. Xiao, Y. Cheng, E. Ren, L. Lian, Y. Zhang, H. Gao, X. Wang, W. Leung, X. Chen, *ACS nano* **2019**, 13, 2427-2438.
- [65] K. Herget, P. Hubach, S. Pusch, P. Deglmann, H. Götz, T. E. Gorelik, I. y. A. Gural'skiy, F. Pfitzner, T. Link, S. Schenk, *Advanced Materials* **2017**, 29, 1603823.

- [66] D. Campoccia, L. Montanaro, C. R. Arciola, *International Journal of Molecular Sciences* **2021**, 22, 9100.
- [67] L. Montanaro, A. Poggi, L. Visai, S. Ravaioli, D. Campoccia, P. Speciale, C. R. Arciola, *The International journal of artificial organs* **2011**, 34, 824-831.
- [68] M. Okshevsky, R. L. Meyer, *Critical reviews in microbiology* **2015**, 41, 341-352.
- [69] F. Xu, Q. Lu, P.-J. J. Huang, J. Liu, *Chemical Communications* **2019**, 55, 13215-13218.
- [70] Z. Chen, H. Ji, C. Liu, W. Bing, Z. Wang, X. Qu, *Angewandte Chemie* **2016**, 128, 10890-10894.
- [71] Z. Liu, F. Wang, J. Ren, X. Qu, *Biomaterials* **2019**, 208, 21-31.
- [72] D. Hu, H. Li, B. Wang, Z. Ye, W. Lei, F. Jia, Q. Jin, K.-F. Ren, J. Ji, *ACS nano* **2017**, 11, 9330-9339.
- [73] L. Gao, Y. Liu, D. Kim, Y. Li, G. Hwang, P. C. Naha, D. P. Cormode, H. Koo, *Biomaterials* **2016**, 101, 272-284.
- [74] Y. Liu, P. C. Naha, G. Hwang, D. Kim, Y. Huang, A. Simon-Soro, H.-I. Jung, Z. Ren, Y. Li, S. Gubara, *Nature communications* **2018**, 9, 2920.
- [75] A. Gupta, R. Das, G. Yesilbag Tonga, T. Mizuhara, V. M. Rotello, *ACS nano* **2018**, 12, 89-94.
- [76] L. Gao, K. Fan, X. Yan, *Theranostics* **2017**, 7, 3207.
- [77] Y. Zhong, X. T. Zheng, S. Zhao, X. Su, X. J. Loh, *ACS nano* **2022**, 16, 19840-19872.
- [78] Y. Zhang, P. Sun, L. Zhang, Z. Wang, F. Wang, K. Dong, Z. Liu, J. Ren, X. Qu, *Advanced functional materials* **2019**, 29, 1808594.
- [79] N. Ninan, A. Forget, V. P. Shastri, N. H. Voelcker, A. Blencowe, *ACS applied materials & interfaces* **2016**, 8, 28511-28521.
- [80] G. Guo, H. Zhang, H. Shen, C. Zhu, R. He, J. Tang, Y. Wang, X. Jiang, J. Wang, W. Bu, *ACS nano* **2020**, 14, 13391-13405.
- [81] R. M. Anderson, R. M. May, *Infectious diseases of humans: dynamics and control*, Oxford university press, **1991**.
- [82] C. Ge, R. Wu, Y. Chong, G. Fang, X. Jiang, Y. Pan, C. Chen, J. J. Yin, *Advanced Functional Materials* **2018**, 28, 1801484.
- [83] X. Zhang, G. Li, G. Chen, D. Wu, X. Zhou, Y. Wu, *Coordination Chemistry Reviews* **2020**, 418, 213376.
- [84] X. Liu, Z. Yan, Y. Zhang, Z. Liu, Y. Sun, J. Ren, X. Qu, *Acs Nano* **2019**, 13, 5222-5230.
- [85] T. Li, J. Li, Q. Pang, L. Ma, W. Tong, C. Gao, *ACS applied materials & interfaces* **2019**, 11, 6789-6795.
- [86] Z. Zhao, Y. Huang, W. Liu, F. Ye, S. Zhao, *ACS Sustainable Chemistry & Engineering* **2020**, 8, 4481-4488.
- [87] S. Gao, H. Lin, H. Zhang, H. Yao, Y. Chen, J. Shi, *Advanced Science* **2019**, 6, 1801733.

- [88] X. Liu, Y. Pan, J. Yang, Y. Gao, T. Huang, X. Luan, Y. Wang, Y. Song, *Nano Research* **2020**, 13, 653-660.
- [89] A. R. Deshmukh, H. Aloui, B. S. Kim, *Chemical Engineering Journal* **2021**, 421, 127859.
- [90] Y. Ding, H. Xu, C. Xu, Z. Tong, S. Zhang, Y. Bai, Y. Chen, Q. Xu, L. Zhou, H. Ding, *Advanced Science* **2020**, 7, 2001060.
- [91] Y. Sang, W. Li, H. Liu, L. Zhang, H. Wang, Z. Liu, J. Ren, X. Qu, *Advanced Functional Materials* **2019**, 29, 1900518.
- [92] Y. Yang, X. Wu, L. Ma, C. He, S. Cao, Y. Long, J. Huang, R. D. Rodriguez, C. Cheng, C. Zhao, *Advanced Materials* **2021**, 33, 2005477.
- [93] H. Song, Y. Ahmad Nor, M. Yu, Y. Yang, J. Zhang, H. Zhang, C. Xu, N. Mitter, C. Yu, *Journal of the American Chemical Society* **2016**, 138, 6455-6462.
- [94] Z. Ma, J. Li, Y. Bai, Y. Zhang, H. Sun, X. Zhang, *Chemical Engineering Journal* **2020**, 399, 125787.
- [95] S. Xu, S. Bhatia, X. Fan, P. Nickl, R. Haag, *Advanced Materials Interfaces* **2022**, 9, 2102315.
- [96] K. Kingwell, *Nature Reviews. Drug Discovery* **2015**, 14, 515.
- [97] M.-Y. Wu, L. Chen, Q. Chen, R. Hu, X. Xu, Y. Wang, J. Li, S. Feng, C. Dong, X.-L. Zhang, Z. Li, L. Wang, S. Chen, M. Gu, *Advanced Materials* **2023**, 35, 2208578.
- [98] F. L. Nobrega, M. Vlot, P. A. de Jonge, L. L. Dreesens, H. J. E. Beaumont, R. Lavigne, B. E. Dutilh, S. J. J. Brouns, *Nature Reviews Microbiology* **2018**, 16, 760-773.
- [99] X. He, Y. Yang, Y. Guo, S. Lu, Y. Du, J.-J. Li, X. Zhang, N. L. C. Leung, Z. Zhao, G. Niu, S. Yang, Z. Weng, R. T. K. Kwok, J. W. Y. Lam, G. Xie, B. Z. Tang, *Journal of the American Chemical Society* **2020**, 142, 3959-3969.
- [100] C. M. Courtney, S. M. Goodman, J. A. McDaniel, N. E. Madinger, A. Chatterjee, P. Nagpal, *Nature materials* **2016**, 15, 529-534.
- [101] M. Clauss, A. Trampuz, O. Borens, M. Bohner, T. Ilchmann, *Acta biomaterialia* **2010**, 6, 3791-3797.
- [102] J. Lawrence, J. Bull, *Engineering in medicine* **1976**, 5, 61-63.
- [103] J. Ouyang, X. Ji, X. Zhang, C. Feng, Z. Tang, N. Kong, A. Xie, J. Wang, X. Sui, L. Deng, *Proceedings of the National Academy of Sciences* **2020**, 117, 28667-28677.
- [104] Z. Tu, H. Qiao, Y. Yan, G. Guday, W. Chen, M. Adeli, R. Haag, *Angewandte Chemie* **2018**, 130, 11368-11372.
- [105] M. Huo, L. Wang, Y. Wang, Y. Chen, J. Shi, *ACS nano* **2019**, 13, 2643-2653.
- [106] H. Dau, P. Liebisch, M. Haumann, *Analytical and Bioanalytical Chemistry* **2003**, 376, 562-583.

7. Appendix

7.1. Publications

First and co-first author:

1. **Xin Fan**¹, Yang Gao¹, Fan Yang, Jian Liang Low, Lei Wang, Beate Paulus, Yi Wang, Andrej Trampuz*, Chong Cheng*, and Rainer Haag*, A copper single-atom cascade bionanocatalyst for treating multidrug-resistant bacterial diabetic ulcer, *Adv. Funct. Mater.*, 2023, Accepted.
2. Lei Wang¹, **Xin Fan**^{1*}, Mercedes Gonzalez Moreno, Tamta Tkhilaishvili, Weijie Du, Xianlong Zhang, Chuanxiong Nie, Andrej Trampuz*, and Rainer Haag*, Photocatalytic quantum dot-armed bacteriophage for combating drug-resistant bacterial infection, *Adv. Sci.*, 2022, 9, 2105668.
3. **Xin Fan**, Xizheng Wu, Fan Yang, Lei Wang, Kai Ludwig, Lang Ma, Andrej Trampuz*, Chong Cheng*, and Rainer Haag*, A Nanohook-equipped bionanocatalyst for localized near-infrared-enhanced catalytic bacterial disinfection, *Angew. Chem. Int. Ed.*, 2022, 61, e202113833.
4. **Xin Fan**, Fan Yang, Chuanxiong Nie, Lang Ma, Chong Cheng, Rainer Haag, Biocatalytic Nanomaterials: A New Pathway for Bacterial Disinfection, *Adv. Mater.* 2021, 2100637.

Co-author:

5. Shaohui Xu, Sumati Bhatia, **Xin Fan**, Philip Nickl, Rainer Haag, Glycosylated MoS₂ sheets for Capturing and Deactivating *E. coli* Bacteria: Combined Effects of Multivalent Binding and Sheet Size, *Adv. Mater. Interfaces*, 2022, 9 (9), 2102315.
6. Yong Hou, Wenyan Xie, **Xin Fan**, Peng Tang, Leixiao Yu, Rainer Haag, "Raspberry" Hierarchical Topographic Features Regulate Human Mesenchymal Stem Cell Adhesion and Differentiation via Enhanced Mechanosensing, *ACS Appl. Mater. Interfaces* 2021, 13, 46, 54840–54849.
7. Yi Xia, **Xin Fan**, Hua Yang, Ling Li, Chao He, Chong Cheng, Rainer Haag, ZnO/Nanocarbons-Modified Fibrous Scaffolds for Stem Cell-based Osteogenic Differentiation, *Small*, 2020, 16 (38), 2003010.

7.2. Curriculum Vitae

For reasons of data protection, the curriculum vitae is not published in the electronic version.

Declaration of independence

Hereby, I certify that the work presented in this thesis has not previously been submitted for a degree nor has it been submitted as part of requirements for a degree except as fully acknowledged within the text.

I also certify that the thesis has been written by me. Any help that I have received in my research work and the preparation of the thesis itself has been acknowledged. In addition, I certify that all information sources and literature used are indicated in the thesis.

Xin Fan